École Doctorale 353 - Sciences pour l'ingénieur
Spécialité : mécanique et physique des fluides

THÈSE DE DOCTORAT

présentée par

Zhenhai ZOU

en vue de l'obtention du grade de

Docteur de l'Université d'Aix-Marseille

Étude de l'éjection de grains hors d'un cylindre pressurisé

Soutenue le 16 Octobre 2019 devant le jury composé de :

Monsieur	Alain DE RYCK	*Institut Mines - Télécom Albi*	Rapporteur
Madame	Valérie VIDAL	*Laboratoire de Physique, ENS Lyon*	Rapporteur
Monsieur	Philippe GONDRET	*Laboratoire FAST, Université Paris-Sud*	Examinateur
Monsieur	Pierre JOP	*SVI, CNRS/Saint-Gobain*	Examinateur
Monsieur	Philippe LAFON	*IMSIA, EDF*	Examinateur
Monsieur	Iker ZURIGUEL BALLAZ	*Facultad de Ciencias, Universidad de Navarra*	Examinateur
Madame	Pascale AUSSILLOUS	*IUSTI, Université d'Aix-Marseille*	Directrice de Thèse
Monsieur	Pierre-Yves LAGRÉE	*IJLRA, CNRS/Sorbonne Université*	Co-encadrant de Thèse
Monsieur	Pierre RUYER	*IRSN*	Tuteur de Thèse

Laboratoire IUSTI

École Polytechnique Universitaire de Marseille

5, Rue Enrico Fermi, Technopôle de Château-Gombert

13453 Marseille

École Doctorale Sciences pour l'ingénieur : Mécanique, Physique, Micro et Nanoélectronique

5, Rue Enrico Fermi, Technopôle de Château-Gombert

13453 Marseille

Acknowledgement

Firstly, I would like to express my sincere gratitude to my advisors, Pascale Aussillous, Pierre Ruyer and Pierre-Yves Lagrée, for the continuous support of my Ph.D study and related research. Pascale, I am really appreciated for your patience, confidence, optimism, motivation and immense knowledge during these three years. Your guidance helped me in all the time of research and writing of this thesis. Your optimism is particularly impressed for me that will always be a treasure during my whole life. Pierre, thank you for your kindness and patience, also for your support, encouragement and valuable advice whenever I encountered difficulties, you had always the brilliant ideas to provide to me. Your immense knowledge helped me a lot to advance my work. Pierre-Yves, thank you for your unparalleled knowledge. Your help cannot be overestimated and you extended a great amount of assistance to my Ph.D study. The period working with you at l'Institut Jean Le Rond d'Alembert is unforgettable for me. I could not have imaged having better advisors than all you for my Ph.D study.

Besides my advisors, I would like to thank the rest of my thesis committee: Valérie Vidal and Alain De Ryck for reading my manuscript and giving their comments, as well as Philippe Gondret, Iker Zuriguel Ballaz, Pierre Jop and Phillippe Lafon to have accepted to participate in my thesis committee. I would like to express my appreciation for their interest in my research work, as well as for their very encouraging and interesting comments.

Thanks should also go to Rémy mozul, Frédéric Dubois and Stéphane popinet for their valuable support in the numerical simulation.

I am deeply indebted to $SHOC$ team of IUSTI, thanks to Georges, Lazhar and Christian for helping me on the design of experimental setup. Thanks to Sady and Frédéric for the manufacturing, thanks to Nathalie, William and Pierre for the support of electronic aspect.

I would like to thank to l'IRSN, not only for the funding of this thesis, but also for providing me lots of opportunities to discovery the research and the French culture. I also had great pleasure of working with all the colleagues at Cadarache, even though for short period during the thesis days of IRSN and the seminars. Thanks to Fabienne and Jean for their kindness to bring me to the seminar place for several times, thanks to Olivier and Gaétan for the excellent organization, thank to Frédéric and Dubois for their kindness and patience. Finally, thanks to all my colleagues I met at IRSN.

I would also like to extend my deepest gratitude to the GEP team that I feel so honor to work with you. Thanks to Laurence for your kindness and humor that made always energetic. Thanks to Blanche for your interest in Chinese culture and providing me the opportunity to give the Chinese course to students. A big thanks to Olivier, Babette, Yoël, Geoffroy, Maxime, Henri, Bloen for your scientific skills and brilliant ideas when I was stuck in my work. I would like to express my deepest appreciation to all the PhD students and post doctorates of IUSTI, It is an unforgettable memory of staying in such dynamic, friendly and enjoyable group. A special thanks to Yixian, who was the former student of this topic, for helping me a lot at the beginning of my

Résumé de thèse en français

Cette thèse de doctorat a été financée par l'IRSN et motivée par des études de sûreté concernant l'accident d'insertion de réactivité dans une centrale nucléaire de type REP (réacteur nucléaire à eau pressurisée).

Dans un REP, le combustible, matière fissile, est un oxyde polycristallin (d'uranium ou d'un mélange d'uranium et de plutonium, d'une densité d'environ $10^4 kg/m^3$) conditionné sous forme de pastilles cylindriques de diamètre et de hauteur dans la gamme centimétrique, le grain élémentaire étant de l'ordre de quelques microns. Ces pastilles de combustible sont empilées dans une gaine métallique d'environ $500 \mu m$ d'épaisseur pour contenir les produits de fission. L'ensemble, appelé crayon de combustible, mesure environ 4m de long et 1cm de diamètre. Dans le cœur du réacteur, les dizaines de milliers de crayons de combustible sont assemblés les uns à côté des autres autour des grappes de commande et immergés dans de l'eau sous pression à 15.5 MPa.

Avec le temps et notamment en raison des réactions de fission dans le réacteur, les pastilles de combustible se fragmentent et gonflent. Elles sont soumises à des gradients thermiques et de contraintes, à l'irradiation (flux neutronique) et à des réactions de fission (formation de nouveaux composés solides dans la matrice et libération de produits de fission gazeux). La taille des fragments (le plus important étant de l'ordre de quelques millimètres) dépend de la nature du combustible et du taux de combustion qui mesure l'énergie massique fournie par le matériau. Dans la couronne extérieure du combustible, pour un taux de combustion élevé, la taille des grains constituant la matière est réduite (moins de $1 \mu m$) et les fragments peuvent être de l'ordre de $10 \, \mu m$.

L'accident d'insertion de réactivité nucléaire (RIA) est l'un des scénarios considérés dans les études de sûreté des centrales nucléaires de type REP. Ce scénario est initié par l'éjection inattendue d'un groupe de grappes de commande, utilisé pour réguler la réaction de fission à l'échelle d'un assemblage (quelques centaines de crayons). Cette éjection violente provoque une augmentation locale de l'énergie nucléaire pendant quelques dizaines de millisecondes, entraînant une augmentation rapide de la température du combustible. En conséquence, la température et les niveaux de déformation de la gaine de crayon combustible augmentent, entraînant finalement un risque de rupture de cette gaine, dû à l'expansion thermomécanique et au gonflement du combustible. Selon l'étude réalisée par Tanzawa and Fujishiro [1987], un comportement transitoire de la pression interne de la gaine ainsi que la pression à l'intérieur du crayon de combustible a été observé, pour un cas exceptionnel de crayon de combustible remplie d'eau. L'au agit alors comme un promoteur de la rupture de la gaine ainsi que de l'éjection des fragments hors du crayon. Les fragments de combustible et les gaz de fission étant à très haute température (de l'ordre de 2000 K) vont être éjectés par la brèche vers le fluide caloporteur à une température de l'ordre de 600 K [1]. Ainsi, un violent transfert de chaleur se produit entre les fragments de combustible et le fluide caloporteur, entraînant une augmentation soudaine de l'énergie dans l'eau et conduisant à un pic

---

[1] Pour le cas de Tanzawa, la température était d'environ 300 K.

de pression initié par une vaporisation rapide. Ces phénomènes d'augmentation de pression et de vaporisation du fluide pourraient induire d'autres endommagements.

La violence de la mise en contact dépend notamment du débit d'éjection des fragments de combustible, qui contrôle la cinétique de transfert d'énergie entre le combustible chaud et le fluide caloporteur. Cette dynamique d'éjection est gouvernée par la taille et la géométrie de la brèche, la pression initiale du gaz à l'intérieur du crayon de combustible (de l'ordre de plusieurs dizaines à plusieurs centaines de bar au-dessus de la pression du cœur dans le cas où le crayon est accidentellement partiellement remplie d'eau) et la taille des fragments combustibles, qui détermine leur capacité à traverser la brèche. Cependant, la compréhension de cette dynamique d'éjection reste limitée, du fait qu'il est inconcevable d'observer directement ce phénomène dans des crayons combustibles lors des essais RIA (Ruyer [2012]).

Le scénario RIA est étudié à l'aide d'essais dédiés pour lesquels une section de crayon de combustible est soumise à un pic de puissance (Ishikawa and Shiozawa [1980], Fuketa et al. [1997]). Lors de certains essais RIA, la rupture de la gaine du crayon de combustible a été observée et les fragments de combustible ont été éjectés suite à cette rupture menant à des pressurisations et des vaporisation violentes au sein de la cellule d'essai. Fuketa et al. [1997] ont montré que les particules de combustible collectées sont fortement fragmentées : 90% de particules (en masse) sont inférieures à $500\mu m$, et plus de 50% de particules (en masse) sont inférieures à $50\mu m$.

La rupture de la gaine d'un crayon de combustible est aussi envisagée dans le scénario d'accident dit de perte de réfrigérant primaire (APRP). Dans ce scénario, on suppose une rupture de la boucle primaire du caloporteur, une vidange partielle du caloporteur et une perte de pression du fluide associé : la pression du gaz de fission contenu dans le crayon de combustible n'a plus de contre-réaction externe et entraîne ainsi un gonflement de la gaine à une température haute et sa rupture éventuelle. Dans ce cas, du fait de l'absence du fluide caloporteur entourant le crayon de combustible, l'interaction entre le combustible et le fluide caloporteur ne se produira pas et le débit de fragments de combustible hors du crayon est d'une importance secondaire. Néanmoins, la quantité potentielle des fragments de combustible hors du crayon a des conséquences radiologiques.

Ces deux situations accidentelles pourraient conduire (même si dans le cas de RIA, les études de sûreté assurent l'intégrité de la gaine) à la rupture de la gaine et la fragmentation du crayon de combustible. Pour mieux comprendre les conséquences potentielles d'une rupture de la gaine, l'IRSN vise à évaluer le mouvement du combustible dans le crayon de combustible et la quantité de combustible qui peut être dispersée dans le cœur. Ainsi, la connaissance de l'écoulement d'un milieu fragmenté confiné dans un réservoir cylindrique avec un orifice latérale, sous l'action motrice de la gravité et de l'écoulement de gaz pressurisé, a un intérêt particulier dans l'étude de ces scénarios d'accident. Dans le cas spécifique du RIA, nous cherchons à comprendre plus précisément ce qui détermine le débit de fragments du crayon de combustible vers le fluide caloporteur à l'instant de la rupture.

Les fragments d'un crayon de combustible sont complexes à caractériser et à représenter. Dans

cette étude, ils sont idéalisés par un milieu granulaire dense composé par des billes monodisperses. La forme sphérique des ces billes minimise le contact entre les particules par rapport aux matériaux fragmentés et il est donc supposé que le débit de ces milieux surestimera celui du matériau réel. Nous étudierons également le cas des particules de sable ayant une forme plus angulaire. Le combustible fragmenté a une distribution granulométrique relativement large, nous discutons aussi brièvement du cas d'un mélange bidisperse pour déduire le rôle potentiel de la distribution granulometrique du milieu.

Afin de modéliser la dynamique de l'éjection de gaz et de particules suite à la rupture d'un crayon de combustible nucléaire, nous avons choisi d'étudier une configuration simplifiée à l'échelle du laboratoire, en considérant le débit d'éjection d'un milieu granulaire hors d'un silo cylindrique. Ce travail fait suite à la thèse de Zhou [2016], qui portait sur le rôle d'un débit d'air constant et ainsi que le rôle de la position latérale de l'orifice sur le débit de vidange. Dans ce travail, nous nous concentrerons sur le rôle de l'écoulement instationnaire du gaz pressurisé et sur l'influence du fluide environnant sur le débit de vidange. Cette étude vise à déterminer les paramètres qui gouvernent le débit de vidange des milieux granulaires, d'abord par l'approche expérimentale. Ensuite, nous analysons la capacité d'une modélisation continue à deux phases avec un modèle rhéologique frictionnel pour la phase granulaire afin de reproduire la phénoménologie que nous observons expérimentalement.

Dans le chapitre 2, nous proposons une description de l'état des connaissances concernant l'écoulement des milieux granulaires denses et leur couplage avec un écoulement fluide. En particulier, nous nous concentrons sur le cas de la vidange d'un silo qui est analogue à la configuration d'intérêt.

Concernant le rôle de la position latérale de l'orifice, qui correspond à la géométrie d'un crayon rompu, dans le chapitre 3, nous avons d'abord étudié le rôle de l'accélération et de la friction (interne et latérale) sur le débit de vidange d'un milieu granulaire en utilisant une géométrie non conventionnelle (mais pertinente vis-à-vis du problème du crayon combustible) : un silo rectangulaire avec un fond incliné qui se termine par un orifice latéral. Expérimentalement, nous avons fait varier différents paramètres: la taille de l'orifice D, le diamètre des particules d_p, l'épaisseur du silo W et l'angle d'inclinaison du font du silo θ_i. Une simulation continue avec une rhéologie frictionnelle $\mu(I)$ a été réalisée pour reproduire les observations expérimentales. Nous avons montré que le débit de vidange du milieu granulaire est contrôlé par deux phénomènes. Pour un orifice latéral avec un fond horizontal, deux régimes d'écoulement existent en fonction du rapport d'aspect D/W et résultant de la concurrence entre le frottement des parois et le frottement interne. Ceci contrôle l'orientation de l'écoulement granulaire à la sortie. Deux régimes d'écoulement ont également été identifiés dans la géométrie d'intérêt lors de la variation de l'inclinaison du fond. Pour les petits angles d'inclinaison, l'écoulement granulaire n'est pas perturbé par le fond et l'orientation de la ligne de courant centrale à la sortie est contrôlée par le rapport d'aspect D/W. Le second régime d'écoulement est observé pour les grands angles d'inclinaison où l'orientation

de l'écoulement granulaire est imposée par l'inclinaison du fond. Nous avons ensuite montré que l'orifice correspond à une zone où les particules accélèrent, l'énergie potentielle étant transférée en énergie cinétique. Cependant, ce transfert qui détermine la norme de la vitesse au centre de l'orifice (et le débit) est très sensible à la géométrie du silo, à la rhéologie granulaire et aux conditions limites. Enfin, nous avons proposé un modèle phénoménologique qui prédit le débit de particules hors d'un silo rectangulaire avec un fond incliné en fonction du rapport d'aspect de l'orifice avec un bon accord dans les régimes asymptotiques.

Deuxièmement, dans le chapitre 4, nous avons étudié expérimentalement la vidange d'un silo cylindrique couplé avec une surpression d'air imposée au sommet de la colonne granulaire. Nous avons observé qu'une surpression d'air maintenue constante générait une augmentation temporelle du débit de particules ainsi qu'une augmentation du débit d'air au cours du temps. Nous avons montré que cette évolution était associée au fait que la hauteur de la colonne granulaire diminue lors de la vidange. Suite aux travaux menés par Zhou [2016], qui a étudié la vidange stationnaire d'un silo avec injection d'un débit de gaz constant au sommet du silo, nous avons montré que le débit de vidange des milieux granulaire peut être décrit par une loi de Hagen-Beverloo modifiée : le gradient de pression du gaz à la sortie agit comme une force supplémentaire au terme moteur de la gravité. Nous avons validé que la force d'interaction entre le gaz et le milieu granulaire peut être bien décrite par loi de résistance de Darcy-Forchheimer. Dans la gamme de pression de gaz explorée, nous avons montré que la phase fluide se détend instantanément, ce qui signifie que le terme inertiel peut être négligé par rapport à la force d'interaction entre les deux phases. Ensuite, nous avons proposé un modèle analytique basé sur une modélisation continue à deux phases avec une rhéologie frictionnelle $\mu(I)$ pour le milieu granulaire et la loi de Hagen-Beverloo modifiée avec la loi de résistance de Darcy-Forchheimer entre deux phases qui explique assez bien les observations expérimentales. En outre, nous avons montré que le couplage fluide-grain dépend principalement de la perméabilité du milieu granulaire. Le modèle est valable pour tous les types de particules, à savoir les particules sphériques de verre ou de céramique, les particules de sable ayant une forme plus angulaire ainsi que le mélange bidisperse si nous considérons le diamètre de Sauter. Finalement, nous avons entièrement résolu la modélisation continue à l'aide de simulations numériques dans une configuration axisymétrique tridimensionnelle et nous avons validé la plupart des hypothèses du modèle analytique.

Dans le cas industriel, le gaz pressurisé et le milieu granulaire sont soudainement (à la suite de la rupture de la gaine) en contact avec un domaine à faible pression, ce qui ajoute un processus instationnaire aux écoulements. Pour être plus réaliste avec la configuration d'intérêt, dans le chapitre 5, nous avons effectué une étude sur l'effet d'une rupture instantanée de l'orifice d'un silo cylindrique. Une rupture rapide d'une feuille d'aluminium à un niveau de pression critique d'environ 3 bar a permis de simuler cette rupture soudaine. Trois périodes de vidange ont été observées pendant la vidange du silo : la période de l'établissement du gradient de pression de gaz, la période de vidange de gaz pressurisé et la période de vidange stationnaire. Nous avons

constaté que le temps caractéristique d'établissement du gradient de pression de gaz dépend particulièrement de la perméabilité du milieu granulaire: il est d'autant plus court que le milieu granulaire est plus perméable. Ensuite, au cours de la période de vidange de gaz pressurisé, nous avons d'abord observé un débit de particules très élevé, correspondant à une vitesse de particules élevée à la sortie. Ensuite, le débit de vidange diminue rapidement avec la pression du gaz au sein du silo pour atteindre la période de vidange stationnaire. Cette période de vidange stationnaire correspond à un silo fermé avec un contre-courant de gaz. Pour décrire l'ensemble de la vidange, nous avons développé un modèle unidimensionnel qui prend en compte la compressibilité de l'air, qui donne une assez bonne prédiction des observations expérimentales. Ensuite, nous avons résolu numériquement une modélisation complète continue à deux phases en considérant un fluide compressible et une rhéologie granulaire. Ce modèle reproduit bien les observations expérimentales et permet de valider une partie des hypothèses du modèle unidimensionnel analytique. Finalement, une instabilité du jet granulaire à la sortie du silo a été observée pour les particules les plus petites et nous avons discuté du mécanisme qui pourrait conduire à de tels phénomènes.

Dans la situation d'intérêt (scénario RIA), le crayon de combustible est immergé dans l'eau sous pression, les fragments de combustible chauds sont éjectés dans un liquide. Pour étudier l'influence du liquide environnant sur le débit de vidange du milieu granulaire, nous avons réalisé une étude de vidange d'un silo en immergeant la sortie du silo dans l'eau, avec trois configurations d'injection de gaz. En outre, des particules hydrophobes ont également été utilisées pour imiter l'effet de la température chaude des fragments ce qui induit la présence d'une couche de gaz vaporisé autour d'eux. Dans le cas d'un débit d'air constant au sommet du silo, nous avons montré que le débit de particules n'est pas modifié par le liquide environnant, mais que ce dernier applique une surpression hydrostatique à la sortie par rapport la pression atmosphérique. Dans le cas d'une pression du gaz imposée au sommet du silo, nous avons montré que le modèle unidimensionnel développé pour le cas avec une sortie dans l'air est toujours valable si nous prenons en compte la surpression hydrostatique. Enfin, avec une rupture instantanée de la sortie immergée dans l'eau, nous avons montré que cette surpression hydrostatique est négligeable par rapport à la pression interne du silo et le modèle développé pour le cas avec une sortie dans l'air reste valable. En outre, nous avons proposé une prévision du débit de vidange des fragments de combustible dans le cas du RIA.

Cette thèse de doctorat apporte plusieurs éléments pour modéliser l'écoulement granulaire avec un orifice latéral ou inférieur couplé avec un écoulement du gaz instationnaire. Par ailleurs, de nombreuses questions ont pu être mises en lumière au cours de ce travail.

- Au cours de l'étude de l'effet du fond incliné sur le débit de vidange, la modélisation continue s'est avérée être le bon cadre pour décrire le débit de vidange d'un milieu granulaire hors d'un silo, et dans les travaux futurs, elle permettra de réaliser une étude paramétrique complète de l'influence des paramètre rhéologiques sur le débit prévu analytiquement dans différentes géométries, sans avoir recours à des expériences particulières. En effet les

modèles analytiques de débit (loi de Beverloo) permettent de déterminer les lois d'échelle mais conservent un caractère empirique dépendant a priori des paramètres géométriques et des propriétés des matériaux. L'utilisation des simulations continues en calibrant mieux les paramètres rhéologiques du modèle $\mu(I)$ à partir d'expériences plus simples apportent ainsi une réelle avancée pour la prédiction des effets géométriques d'un silo sur sa vidange. En particulier, ces résultats peuvent avoir un intérêt pratique compte tenu de l'effet de l'angle de la trémie pour un silo industriel. De plus, nous avons observé un comportement différent entre les expériences 2D mono-couche et les simulations discrètes, notamment pour la norme de la vitesse au centre de l'orifice. Pour comprendre cette différence, il faut envisager d'autres simulations discrètes, par exemple, une simulation tridimensionnelle complète qui prend en compte le frottement sur les parois avant et arrière.

- Pour la vidange d'un silo avec une rupture instantanée de l'orifice, nous avons montré que le temps caractéristique d'établissement du gradient de pression de gaz τ dépend non seulement de la perméabilité du milieu granulaire (que nous avons fait varier), mais aussi, théoriquement de la hauteur initiale de la colonne granulaire h_p^0 et de la densité de gaz ρ_f. Par conséquent, des expériences supplémentaires, par exemple en variant h_p^0 ou en utilisant un gaz plus dense, pourraient être considérées comme une perspective pour valider davantage la loi d'échelle de τ. Du point de vue de la simulation numérique, une simulation complète à deux phases en considérant la phase fluide comme un milieu compressible pourrait être envisagée pour valider le modèle. Pour expliquer précisément l'instabilité du jet granulaire à la sortie au tout début de la rupture de l'orifice, plus des travaux expérimentaux doivent être effectués, par exemple, en variant plus largement les dimensions du silo et de l'orifice pour établir les conditions d'occurence de cette instabilité.

- Concernant la vidange d'un silo avec une sortie immergée dans l'eau et sans injection de gaz, nous avons observé un débit constant pour les petits particules indépendamment du niveau d'eau dans le réservoir, contrairement au cas des grosses particules où nous avons observé un effet d'histoire associé au niveau d'eau dans le réservoir. Ce comportement est intéressant à étudier expérimentalement et théoriquement, par exemple en contrôlant plus précisément la propriété de surface du milieu granulaire, en variant la taille de l'orifice et en maintenant le niveau d'eau constant dans le réservoir pendant la vidange.

- Sur la base de ce travail de thèse, nous avons clairement identifié le rôle de la compressibilité de gaz, des gradients de pression de gaz près de l'orifice, de la perméabilité du milieu granulaire, de la géométrie de crayon cylindrique, de la taille et de la position de l'orifice, ainsi que de l'environnement extérieur sur le débit de vidange du milieu granulaire hors d'un silo pressurisé. Ce travail permet de disposer d'une base solide pour développer l'évaluation de l'éjection de fragments de combustible dans un cas RIA. Néanmoins, certains aspects sont

encore assez approximatifs dans la représentation du combustible fragmenté en tant qu'un milieu granulaire en raison de sa large distribution granulométrique et de sa compaction élevée que nous n'avons pas représenté de manière réaliste. Plus d'études expérimentales et théoriques sont nécessaires pour approcher ce matériau.

Contents

Chapter 1

Introduction

This PhD thesis was funded by IRSN, the french institute of research on nuclear safety and was motivated by safety studies concerning the reactivity insertion accident of power plant of type PWR.

In a pressurized water nuclear reactor (PWR), the fuel, fissile material, is a polycrystalline oxide (of uranium or a mixture of uranium and plutonium, with a density of about $10^4 kg/m^3$) packaged in the form of cylindrical pellets of diameter and height in the centimeter range as shown on the right of Figure 1.1, the elementary grain being of the order of a few micrometers. These fuel pellets are stacked in a metal cladding about $500\mu m$ thick to contain the fission products. The set, called the fuel rod, is about $4m$ long and $1cm$ diameter for each one. In the reactor, the fuel rods are assembled next to each other around the control clusters, as shown on the left part of Figure 1.1, and immersed in pressurized water at $15.5MPa$ within the reactor core.
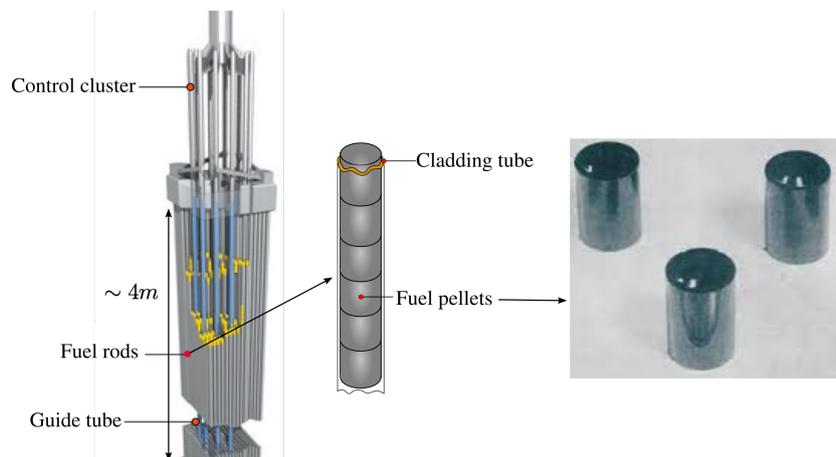
Figure 1.1: Schematic view of fuel rod assembly.

With time and in particular due to the fission reactions within the reactor, the fuel pellets fragment and swell. As illustrated in Figure 1.2, they are subjected to thermal and mechanical gradients, irradiation (neutron flux) and fission reactions (formation of novel solid compounds within the matrix and release of gaseous fission products). The size of the fragments (the most

important being of the order of a few mm) depends on the nature of the fuel and the combustion rate (also referred as burnup) which measures the mass energy provided by the material. In the outermost ring of the fuel, for a high combustion rate, the size of the grains constituting the material is reduced (less than $1\mu m$) together with the fragment size.
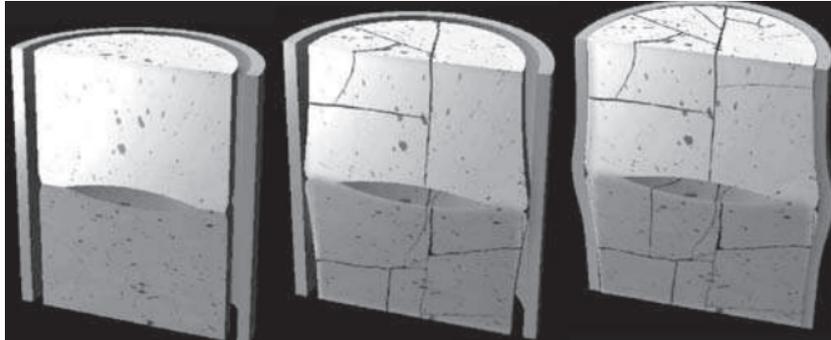
Figure 1.2: Schema of the deformation of the fuel pellet in the form of diabolo, its fracture and the subsequent deformation of the metal cladding during the irradiation

The reactivity insertion accident (RIA) is one of the scenarios considered in the safety studies of power plant of type PWR. This scenario is initiated by an unexpected ejection of a control rods cluster, used to regulate the fission reaction. This violent ejection causes a local increase of the nuclear power for a few tens of milliseconds (see the bottom part in Figure 1.3a), causing a rapid increase of the fuel temperature. As a consequence, the temperature and the deformation levels of the fuel rod cladding rise, ultimately leading to a risk of the rupture of this cladding, due to the thermomechanical expansion and swelling of the fuel. A transient behavior of the cladding internal pressure is illustrated on the upper part of Figure 1.3a, following the study carried out by Tanzawa and Fujishiro [1987], for an exceptional case of a fuel rod filled water, which is considered as a powerful driving source for the fuel fragment ejection. The middle part of Figure 1.3a illustrates the evolution of the pressure within the center fuel rod. Figure 1.3b illustrates the sequence of events that can occur following this failure: the fuel fragments and the fission gas both being at very high temperature (in the order of $2000K$) are ejected through the breach and toward the surrounding coolant fluid at a temperature of around $600K$[1]. Thus, a violent heat transfer occurs between the fuel fragments and the coolant fluid. The sudden increase of energy in the water leads to a pressure peak followed by its rapid vaporization. These phenomena of the peak pressure and the fluid vaporization could induce further damage.

The violence of this contact depends particularly on the ejection rate of the fuel fragments, because it controls the kinetics of the energy transfers between the hot fuel and the coolant fluid. This ejection dynamics is governed by the size of the breach, the initial pressure of the fission gas within the fuel rod (in the order of several tens to several hundred bar above the core pressure for the case when the rod is accidentally partially filled by water) and the size of the fuel fragments,

---

[1]In the Tanzawa case, temperature is around $300K$
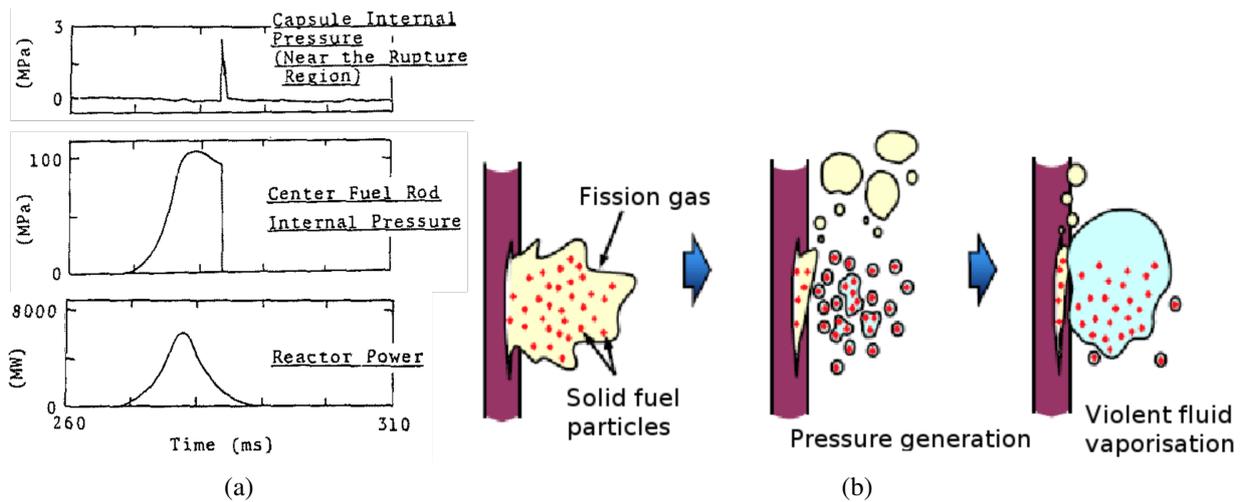
Figure 1.3: (a) Transient behavior of pressure and reactor power under RIA condition (Tanzawa and Fujishiro [1987]). (b) Schematic view of the sequence of coupled phenomena during a reactivity insertion accident (RIA).

which determines their ability to pass through the breach. However, the understanding of this ejection dynamic remains limited, as the direct observation of this phenomenon during RIA testing of the fuel rods is inconceivable (Ruyer [2012]).

The RIA scenario is studied using dedicated tests for which a fuel rod section is subjected to a power peak. See for example the work carried out by Ishikawa and Shiozawa [1980] and Fuketa et al. [1997]. After a RIA test, the failure of fuel cladding is observed as shown in Figure 1.4a, and fuel fragments are ejected, as displayed in Figure 1.4b. The size distribution of fuel fragments is illustrated in Figure 1.4c, which denotes that the collected fuel particles are highly fragmented: in the case of a power peak $131 cal/g$, 90% of particles (by mass) are less than $500 \mu m$, and more than 50% of particles (by mass) are less than $50 \mu m$.

The failure of the cladding of fuel rod is also envisaged in the so-called loss of primary coolant accident scenario, namely LOCA or APRP (Accident par Perte de Réfrigérant Primaire). In this context, a breach in the primary coolant loop, a partial discharge of the coolant and a loss of the associated fluid pressure are assumed: the pressure of the fission gas contained in the fuel rod no longer has any external counter-reaction and thus lead to a swelling of the cladding at high temperature and to its eventual rupture, shown in Figure 1.5. But in this case, due to the absence of the liquid water surrounding the rod, the fuel-coolant interaction will not occur and the flow rate of the fuel fragments leaving the rod is of secondary importance. Nevertheless the potential amount of the fuel fragments dispersed out of the rod has radiological consequences.

Both of these two accidental situations could lead (even if in the RIA case, safety studies ensure clad integrity) to a failure of the cladding tube and also the fragmentation of fuel rod. To better understand potential consequence of rod failure even, IRSN aims evaluating the movement of fuel within the rod and the amount of fuel that can be spread in the core. Therefore, the knowledge
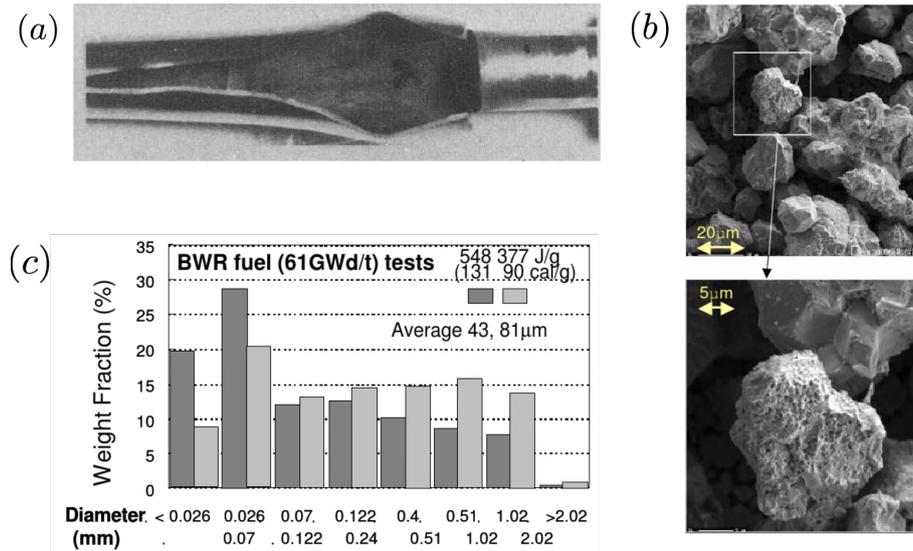
Figure 1.4: (a) RIA tests (Ishikawa and Shiozawa [1980]): A part of the fuel rod with a lateral breach after the cladding failure. (b, c) A sample of the fuel fragments observed under a microscope and its size distribution (Nakamura et al. [2002]).

of the flow of a fragmented media confined in a cylindrical reservoir with a lateral outlet, under the double action of gravity and pressurized gas flow, has a particular interest in the study of these accident scenarios. In the specific case of RIA, we seek to understand more precisely the flow rate of the fragments out of the fuel rod into the coolant fluid.

The fragmented nuclear material is complex to characterize and represent, but in this study it is idealized as a dense granular media composed by monodisperse beads. The spherical shape of those beads minimizes the contact between the particles with respect to fragments materials and it is therefore assumed that the flow rate of such media will overestimate that of the real media. We will also study the case of sand particle having a more angular shape. The fragmented fuel has a relatively wide particle size distribution, so we will discuss briefly the case of a bidisperse mixture to infer the potential role of the size distribution.

In order to model the dynamics of the gas and particle ejection following the rupture of a nuclear fuel rod, we chose to study a simplified configuration at the laboratory scale, considering the discharge flow of a granular media out of cylindrical silos. This work follows the PhD thesis of Zhou [2016], who focused on the role of a steady air flow rate and those of the lateral position of the orifice on the granular discharge flow rate. In this work, we will focus on the role of an unsteady pressurized air flow and the influence of surrounding water on the discharge flow rate. This study seeks to determine the parameters that govern the discharge flow rate of the granular media, firstly through experimental work. Then, we analyze the ability of a two phase continuum modelling with a frictional rheological model for the granular phase to reproduce the phenomenology that we observe experimentally.

In the following chapter, we propose a presentation of the state of knowledge concerning the

(a)   (b)
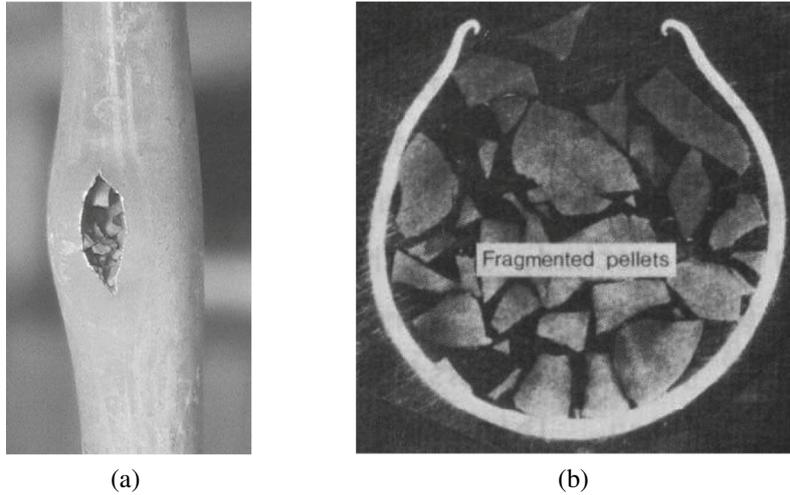
Figure 1.5: LOCA test (simulation of a swelling situation): (a) rupture of the cladding and (b) fragmented pellets, pictures taken by Karb et al. [1983]

flow of dense granular media and its coupling with a fluid flow. In particular, we focus on the case of the discharge of a silo which is analogous to the configuration of interest. In chapter 3, we will focus on the position of the orifice, considering a rectangular silo and investigating how the internal geometry drives the discharge flow of the granular media. In chapter 4, we will investigate a simple configuration considering the unsteady discharge of granular media from a cylindrical silo assisted by a constant gas pressure at its top, without surrounding liquid (the discharge takes place into air). Then in chapter 5, we will discuss the discharge of a cylindrical silo initially pressurized and with an instantaneous rupture of the outlet which represents a more realistic configuration relatively with the hypothetical accident situation. Finally in chapter 6, we will focus on the role of the surrounding liquid on the discharge flow rate.

Chapter 2

State of the art

In this chapter, we present a brief description of the state of knowledges concerning the flow of dense dry granular media, the fluid-grain coupling and the discharge of a silo.

2.1 Flow of dense granular media

2.1.1 Definition and example of granular media

$$
\begin{array}{ccc}
\text{Colloid} & \text{Powder} & \text{Granular media}
\end{array}
$$
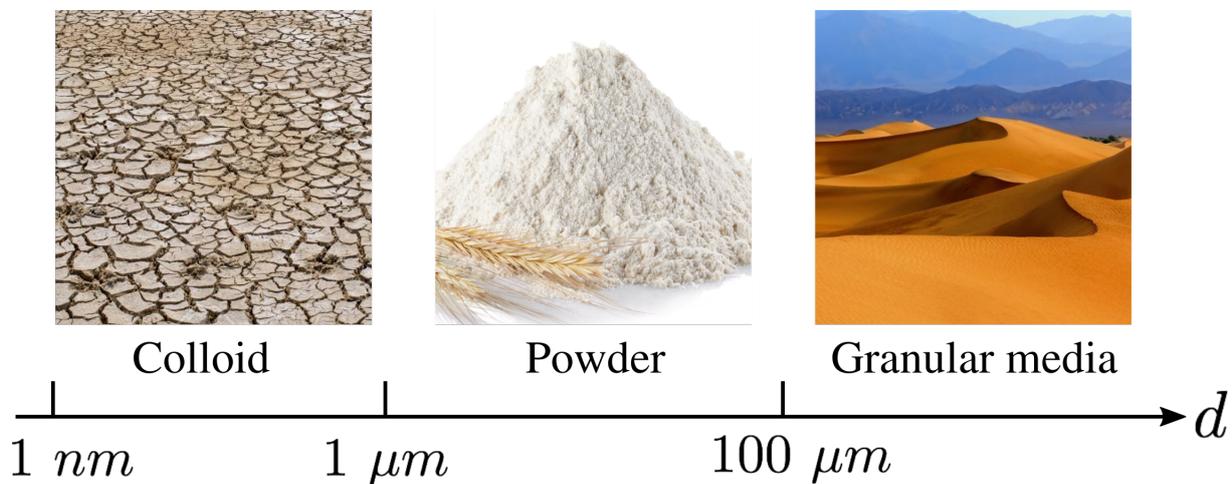
Figure 2.1: A physical classification of divided media as a function of the particle size.

A granular media is a collection of macroscopic solid particles, typically larger than $100\mu m$ (Brown and Richards [1970], Nedderman [1992],Guyon Etienne [1994], Duran [1997], Rao and Nott [2008], Andréotti et al. [2011]). This limit corresponds to the case where the cohesive forces, the moisture effect and also the thermal agitation are negligible with respect to the contact forces. A typical example of granular media is the sand dunes, as shown in Figure 2.1. Finer particles, typically with a particle size between $1\mu m$ and $100\mu m$, form powder like for example the wheat flour. In this case, the van der Waals interactions, the moisture effects and the role of air are often

predominant. For even smaller particles, like in the mud with a size between $1nm$ and $1\mu m$, the thermal agitation is no longer negligible (W.B. Russel [1989]).

Granular media are present in daily life, in many industrial sectors or natural phenomena in geophysics. For example, as a cereal grain, rice is the most widely consumed staple food for a large part of the world's human population, especially in Asia. Granular media accompanies the whole life of rice, as shown in Figure 2.2. Rice seeds in the form of grains are grown on the terraced fields composed principally by mud and sand, which allow to decrease both erosion and surface runoff. Then the rice grains are obtained by passing through the rice thresher, removing the husks from the rice seeds, and finally we obtain a bowl of cooked rice, ready for eating. The understanding of the behavior of granular media plays an important role on the soil for the agronomy soil, also for improving the efficiency of rice threshers.

Rice thresher
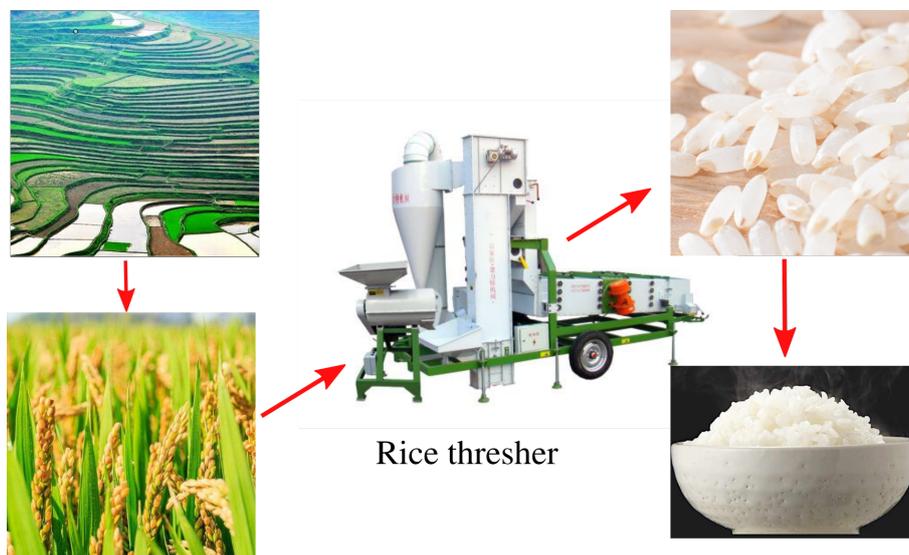
Figure 2.2: Role of granular media during the whole life of rice

Numerous studies on the rheology of a dry granular media have been carried out since the last thirty years and allow to establish the constitutive laws that can describe their behavior in various cases (Andréotti et al. [2011]). In the following parts, we will present the flow of dry granular media and the rheology for describing this type of flow.

2.1.2 Flow of a dry granular media

A granular medium behaves very differently depending on the mode of solicitation (Jaeger et al. [1996]). Figure 2.3a, extracted from Forterre and Pouliquen [2008], illustrates an experiment representing a granular flow obtained by pouring the grains on a pile of particles. Here, we can clearly distinguish three regions: the first region has a solid like behavior, located at the bottom of the pile where the grains remain motionless; the second region is observed above the solid region (see the zone framed by the white dashed lines), in which a dense granular media flows and

behaves as a liquid; the third region is observed at the surface of the pile, the so-called gaseous region, in which the particles bounce forming a diluted and agitated media. These behaviors are also observed simply by manipulating sand by hands (see Figure 2.3b). In the case of the discharge of a silo, which is analog of our configuration of interest, the flow is dense. Therefore, we concentrate on this regime in the following study.

<div align="center">(a)   (b)</div>
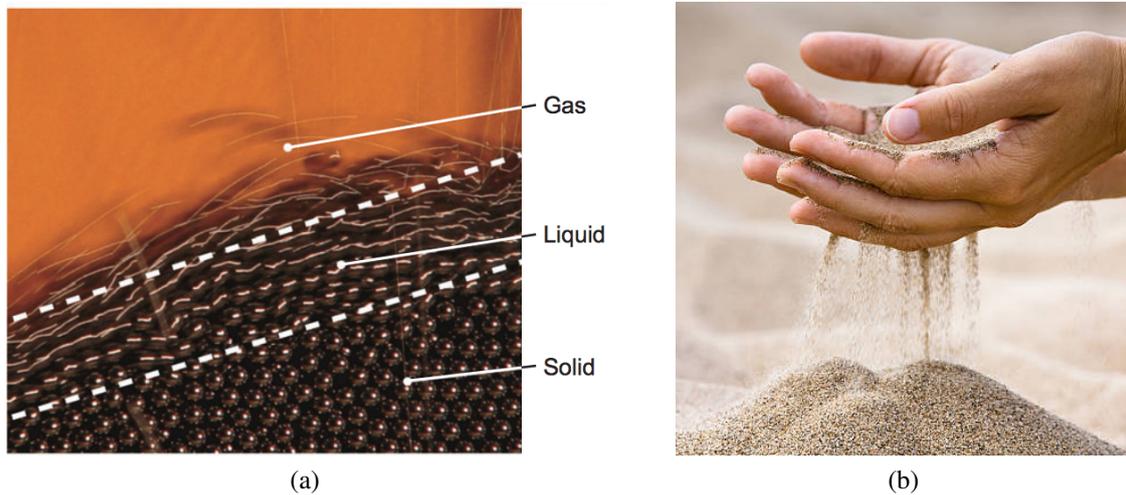
Figure 2.3: Granular media exists in several states: solid, liquid and gas (a) particles poured as a pile (Forterre and Pouliquen [2008]). (b) sand manipulated by hands.

One of main question studying the dense granular flow is to understand how the material flows under the effect of stress, i.e. the rheology. From a microscopic point of view, at the grain scale, the behavior of a granular media is intimately linked to the interactions between the particles that propagate the stresses through the media. Discrete numerical simulation methods calculating the individual movement of each grain and determining the contact forces become an important tool in the study of the behavior of granular media, see for example Radjai and Dubois [2011]. They give informations that are difficult to access experimentally, such as grain forces or contact distribution. On the other hand, and despite the increasing power of computers, these discrete methods remain very costly in terms of computing time and are also limited to small number of particles. However, for the purpose of modelling the dense granular flow, it is not always necessary to describe all the particles states.

2.1.3 Rheology of dry granular media

Since the 1990s, a large amount of research have been carried out, including experimental, numerical and theoretical studies, for understanding the behavior of dense granular flow. From a macroscopic point of view, the granular flow can be characterized by two basic properties. On one hand, the granular media has to be submitted to a certain stress for flowing. Consequently a static stack of granular media does not have a horizontal surface, as it is commonly observed for a pile

Figure 2.4: A pile of sand.

of sand as illustrated in Figure 2.4. A maximal angle can be reached, from which the particles start to flow, noted as θ_c. This observation can be compared to the problem of a frictional block placed on an inclined plane, where the block starts to slide when the inclination angle reaches a critical value, regardless of the size of the block. Then a coefficient of friction of the material can be defined as $\mu_s = \tan \theta_c$. The stability criterion of a granular media is thus a frictional criterion, being related to the maximal angle of the sand pile that can be constructed. On the other hand, when the material starts to flow, the stress depends on the shear rate and cannot be described by a simple Coulomb law.

To study the rheology of a dense granular media, a simple planar shear flow of granular media was considered as illustrated in Figure 2.5a. A granular media composed of spherical particles of diameter d_p and density ρ_p, is confined between two rough plates by an imposed pressure p^p on the top plate. The bottom plate remains motionless, and the top plate moves with a velocity of V. Thus, a constant shear rate is applied $\dot{\gamma} = V/L$, where L is the distance between two plates.
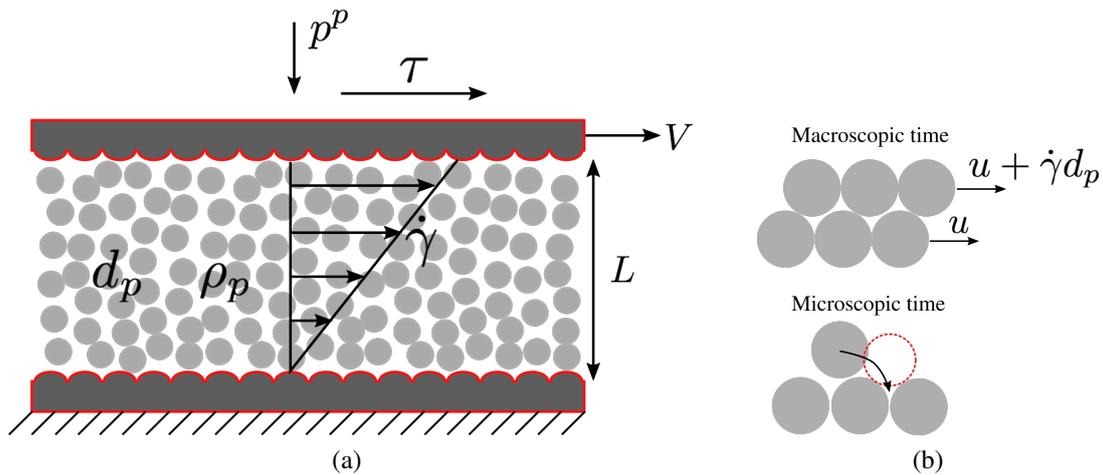
Figure 2.5: (a) Two-dimensional planar shear. (b) Physical interpretation of the inertial number I with a macroscopic and a microscopic times, extracted from Andréotti et al. [2011].

In the absence of gravity, for a stationary and uniform flow, da Cruz et al. [2005] have shown that the behavior of this system can be described by a single dimensionless number (using dimen-

sional arguments), called the inertial number and given by equation 2.1.

$$I = \frac{\dot{\gamma} d_p}{\sqrt{p^p/\rho_p}} \tag{2.1}$$

The inertial number can be interpreted as the ratio between two characteristic times, $I = t_{micro}/t_{macro}$, where:

- The microscopic rearrangement time, $t_{micro} = d_p/\sqrt{p^p/\rho_p}$, represents the time for a particle to fall into the well between its neighbors under the effect of the confinement pressure p^p, as shown on the bottom part of Figure 2.5b.

- The macroscopic deformation time, $t_{macro} = 1/\dot{\gamma}$, corresponds to the time for a particle to pass through the neighboring particle under the shear effect, as shown on the upper part of Figure 2.5b.

The inertial number allows to classify the different granular flow regimes. The very small inertial numbers (typically less than 10^{-3}) correspond to a quasi-static regime. In contrast, the large values of I ($\gtrsim$ 0.1) correspond to the fast and diluted regime. The dense flow regime is between them, corresponding to the range $10^{-3} \lesssim I \lesssim 0.1$.

Thanks to a dimensional analysis in the planar shear configuration, a friction law relationship can be written between the tangential stress and the normal stress, with an effective coefficient of friction that depends on the shear rate and on the confinement pressure through the number I, as follows:

$$\tau^p = \mu(I)p^p \tag{2.2}$$

(a)   (b)
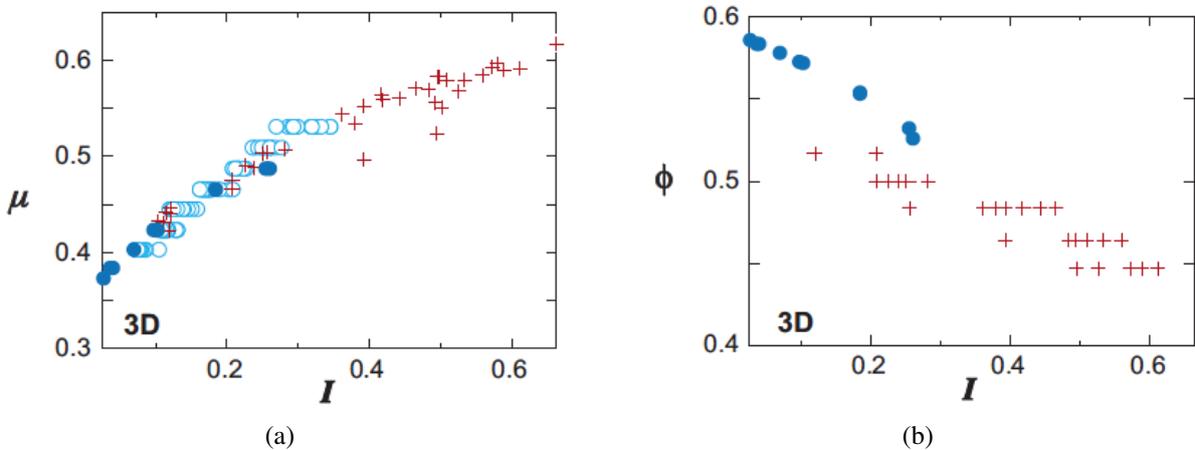
Figure 2.6: (a) friction coefficient μ and (b) volume fraction ϕ as a function of the inertial number in three configurations: inclined plane experiments ($\circ$), inclined plane simulation ($\bullet$) and planar shear experiments ($+$), extracted from Forterre and Pouliquen [2008].

Figure 2.6a illustrates the friction coefficient $\mu = \tau^p/p^p$ versus the inertial number I, for experimental and numerical studies in several configurations. All the points corresponding to different flow conditions overlay which suggests that there is an unique local rheology, intrinsic to material (MIDI [2004]). The friction coefficient increases with the number I. Additionally, Figure 2.6b shows that the volume fraction ϕ depends on the number I:

$$\phi = \phi(I) \tag{2.3}$$

It decreases as I increases, denoting that the granular media tends to dilate under shear. Several authors (see for example Pouliquen and Forterre [2002], Forterre and Pouliquen [2003], MIDI [2004] Jop et al. [2005]), proposed an empirical expression for the friction law $\mu(I)$, and for the volume fraction $\phi(I)$:

$$\mu(I) = \mu_1 + \frac{\mu_2 - \mu_1}{I_0/I + 1} \quad \text{and} \quad \phi = \phi_{max} - (\phi_{max} - \phi_{min})\, I \tag{2.4}$$

The parameters μ_1, μ_2, I_0, ϕ_{max} and ϕ_{min} depend on the material used, typically for monodispersed glass particles, $\mu_1 = 0.4$, $\mu_2 = 0.65$, $I_0 = 0.3$, $\phi_{max} = 0.64$ and $\phi_{min} = 0.4$ (Lagrée et al. [2011], Staron et al. [2012, 2014]).

To describe more complex tridimensional flows, Jop et al. [2005] have generalized the friction law. Assuming incompressible flow and isotropic pressure, they propose the following constitutive law for the relationship between the stress tensor and the strain rate tensor:

$$\sigma_{ij} = -p^p \delta_{ij} + \tau_{ij}^p$$
$$\tau_{ij} = \eta_{eff}\dot{\gamma}_{ij} \quad \text{with} \quad \eta_{eff} = \frac{\mu(I)p^p}{|\dot{\gamma}|} \tag{2.5}$$

where $\dot{\gamma}_{ij} = \left(\partial u_i^p/\partial x_j\right)$ is the strain-rate tensor and $|\dot{\gamma}| = \sqrt{\frac{1}{2}\dot{\gamma}_{ij}\dot{\gamma}_{ij}}$ is the second invariant of the strain-rate tensor. In this formulation, the granular media is described as a non-Newtonian visco-plastic incompressible fluid with an effective viscosity η_{eff}. This local visco-plastic rheology given by the equation 2.5, has been successfully applied to more complex granular flow than the planar shear. For example, it was used to describe the granular flows on a heap (Jop et al. [2006], Chauchat and Médale [2014]), the appearance of surface waves in a flow on an inclined plane (Forterre [2006]), the collapse of a column of grains on a horizontal plane (Lacaze and Kerswell [2009], Lagrée et al. [2011]) as well as the discharge of silo (Staron et al. [2012, 2014], Zhou et al. [2017]). Jop et al. [2005] have also successfully described the granular flow influenced by the presence of solid walls, taking into account the parietal friction. Moreover, this rheology may be extended to the cohesive materials by introducing a Coulomb cohesion term in the yield criterion (Brewster et al. [2005], de Ryck [2008], Gu et al. [2014]).

However, some important characteristics can not be predicted by this simple approach. For example, within the quasi-static limit (solid/liquid transition), the starting and stopping properties

of the flow are poorly described, as well as the existence of spatial correlations that introduce a non-locality. Many models are now trying to introduce these ingredients (Pouliquen and Forterre [2009], Kamrin [2010], Bouzid et al. [2013]). The liquid/gas transition is also poorly captured. When a layer of grain is inclined above a certain critical angle, it is observed that the layer accelerates and leaves the dense regime to enter a fast and diluted regime (Börzsönyi and Ecke [2006]). Finally, this local rheology $\mu(I)$ generates instabilities for low and high values of I during the numerical resolution (Barker et al. [2015]).

Despite these limitations, previous successes in the use of rheology $\mu(I)$ in the study of the discharge of a silo and considering the parietal friction encourage us to test the validity of this continuum modelling for our study.

2.2 Fluid-Grain coupling

Grain and fluid mixtures are widely used in many industrial sectors, for example in the construction industry for base materials such as concrete or cement. The role of the fluid phase becomes important when the fluid-grain interaction force is sufficient to equilibrate the contact forces. This is particularly the case for granular media immersed in a liquid with a comparable density (inducing a buoyancy force) or with high viscosity. Otherwise a gas at high relative velocity provides also strong drag force, such as in the fluidized beds.

In the case of numerical discrete methods, the interstitial fluid flow has to be solved to describe the coupling. For example, Amarsid [2015] simulated the fluid flow with the Lattice Boltzman method coupled with the resolution of the contact dynamics. However, it is very costly in term of computing time particularly for simulating a realistic tridimensional two-phase flow. In contrast, a continuum approach has a great advantage for describing such system. Two-phase continuum modelling are widely used in the description of fluidized bed flows or suspensions (Jackson [2000], Duru et al. [2002], Sundaresan [2003]). Following this approach, several recent studies have shown that the flows of granular media immersed in a fluid can be described in a two-phase continuum modelling using a frictional rheology for the granular phase. These studies deal, for example, with underwater avalanches (Cassar et al. [2005], Pailha and Pouliquen [2009], Bouchut et al. [2016]), dam breaks (Roche et al. [2008], Rondon [2011]), dense suspensions (Boyer et al. [2011]), erosion of particle bed (Ouriemi et al. [2009], Chauchat and Médale [2010], Aussillous et al. [2013], Revil-Baudard and Chauchat [2013]), or a discharge of a silo with injection of air (Zhou [2016]).

The following subsections will present the formalism of the two-phase equations, as well as the relationships proposed by different authors for closing these equations.

2.2.1 Two-phase equations

We consider a granular media of mass density ρ_p immersed in a liquid phase with a viscosity η, and a mass density ρ_f. The approach describes the two phases as two continuous medias. The mass and momentum conservation equations for the two phases are obtained by an averaging process on both phases on an elementary volume δV that is large compared to the scale of the particle size, and small relatively to the scale of the macroscopic flow (Jackson [2000]):

$$\frac{\partial(1-\phi)}{\partial t} + \frac{\partial((1-\phi)u_i^f)}{\partial x_i} = 0 \tag{2.6}$$

$$\frac{\partial\phi}{\partial t} + \frac{\partial(\phi u_i^p)}{\partial x_i} = 0 \tag{2.7}$$

$$\rho_f(1-\phi)\left[\frac{\partial u_i^f}{\partial t} + u_j^f\frac{\partial u_i^f}{\partial x_j}\right] = \frac{\partial\sigma_{ij}^f}{\partial x_j} - f_i + (1-\phi)\rho_f g_i \tag{2.8}$$

$$\rho_p\phi\left[\frac{\partial u_i^p}{\partial t} + u_j^p\frac{\partial u_i^p}{\partial x_j}\right] = \frac{\partial\sigma_{ij}^p}{\partial x_j} + f_i + \phi\rho_p g_i \tag{2.9}$$

Notice that σ_{ij}^f and σ_{ij}^p are the stress tensors which apply respectively on the fluid and the granular phases, u^p and u^f represent the averaged velocity respectively for the granular and the fluid phases and ϕ is the volume fraction of the granular materials. Additionally, f_i represents the resulting average fluid-grain interaction force. The averaging process gives formal expressions of σ_{ij}^f, σ_{ij}^p and f_i, however these complex formulas, which involve integrals on the surface of the grains and sums on the particles, do not allow to express them by average quantities. In the next part, we will present empirical closure relationships which were proposed in the litterature.

2.2.2 Fluid-grain interaction force f_i

The first closure concerns the interaction force between the fluid phase and the granular phase which can be decomposed in two parts: the buoyancy force $\phi\frac{\partial\sigma_{ij}^f}{\partial x_j}$ and the drag force linked to the relative velocities between two phases f_{ti} (Jackson [2000], Andréotti et al. [2011], Simonin et al. [2016]).

$$f_i = \phi\frac{\partial\sigma_{ij}^f}{\partial x_j} + f_{ti} \tag{2.10}$$

Several empirical relationships exist to describe the drag force. Darcy's law is widely used to describe a fluid flowing through a porous media, and it can be expressed as:

$$f_{ti} = \beta_l\eta\left(1-\phi\right)^2\left(u_i^f - u_i^p\right) \tag{2.11}$$

where β_l is the inverse of the permeability of the porous media. For a porous media composed of monodisperse spheres of diameter d_p, an empirical expression of β_l can be given by the Kozeny-

Carman formula:

$$\beta_l = \frac{150\phi}{(1-\phi)^3 d_p^2} \tag{2.12}$$

Generally, this law is used to determine the drag force in the case of a granular media immersed in a fluid phase (Ouriemi et al. [2009], Pailha and Pouliquen [2009], Rondon [2011]). However, Darcy's law is only valid for flows in the viscous regime around the particles meaning a small particle Reynolds number, $Re_p = \rho_f(u^f - u^p)d_p/\eta$ according to the experimental studies carried out by Hassanizadeh and Gray [1987]. For the case of large particle Reynolds number, the inertial aspect of the fluid flow should be taken into account for estimating the drag force. The most used relationship was proposed by Forchheimer [1901] and Ergun [1952]:

$$f_{ti} = \eta(1-\phi)^2(u_i^f - u_i^p)\left[\beta_l + (1-\phi)\beta_i Re_p \frac{u_i^f - u_i^p}{\mid u_i^f - u_i^p \mid}\right] \tag{2.13}$$

with $\beta_l = \frac{150\phi^2}{(1-\phi)^3 d_p^2}$ and $\beta_i = \frac{1.75\phi}{(1-\phi)^3 d_p^2}$, and the first term corresponds to the Darcy's law (equation 2.11). This relation called the Darcy-Forchheimer law is particularly used for the fluidized beds (Dalloz-Dubrujeaud et al. [2000], Peirano et al. [2002]), and also for the discharge of a silo with a steady injection of air (Zhou [2016]) close to our configuration of interest.

2.2.3 Stress tensor of the fluid phase σ_{ij}^f

The stress tensor of the fluid phase σ_{ij}^f can be decomposed between an isotropic pressure term and a deviatoric component:

$$\sigma_{ij}^f = -p^f \delta_{ij} + \tau_{ij}^f \tag{2.14}$$

Several authors proposed a Newtonian formulation related to the mixture velocity $U_i = (1-\phi)u_i^f + \phi u_i^p$ for describing the rheological behavior of fluid phase (Jackson [2000], Ouriemi et al. [2009], Aussillous et al. [2013]):

$$\tau_{ij}^f = \eta_{eff}\left(\frac{\partial U_i}{\partial x_j} + \frac{\partial U_j}{\partial x_i}\right) \tag{2.15}$$

where η_{eff} represents an effective viscosity which depends on ϕ. However, in many configurations, this deviatoric term is negligible with respect to the interaction drag force between the fluid and granular phases since the gradient of U is relatively small at the flow scale with respect to the one at the interstitial scale (Cassar et al. [2005], Pitman and Le [2005], Pailha and Pouliquen [2009], Zhou [2016]), leading to:

$$\sigma_{ij}^f \simeq -p^f \delta_{ij} \tag{2.16}$$

2.2.4 Stress tensor of granular media σ_{ij}^p

In the configuration of underwater avalanche, Cassar et al. [2005] has shown that the local visco-plastic rheology, given by equations 2.4 and 2.5 is still valid when modifying the definition of I. Indeed the presence of the fluid can modify the falling time of a particle, as demonstrated by Courrech du Pont et al. [2003] in the configuration of a rotating drum, revealing three regimes of flow:

- In the free-fall regime, the fluid-induced drag is negligible during its short fall, corresponding to the case of dry granular flow as in our configuration of interest. The microscopic time corresponds to a free fall, $t_{micro}^{free-fall} \sim d_p/\sqrt{p^p/\rho_p}$.

- In the viscous regime, the particle reaches quickly its terminal velocity controlled by the equilibrium between the viscous drag and the confinement pressure, giving the microscopic viscous time, $t_{micro}^{visc} \sim \eta_f/p^p$.

- In the turbulent regime, the particle also reaches its terminal velocity, which is now controlled by the turbulent drag and the confinement pressure, giving the microscopic turbulent time, $t_{micro}^{turb} \sim d_p/\sqrt{p^p/(\rho_f C_d)}$, where C_d represents a drag coefficient, of magnitude 1.
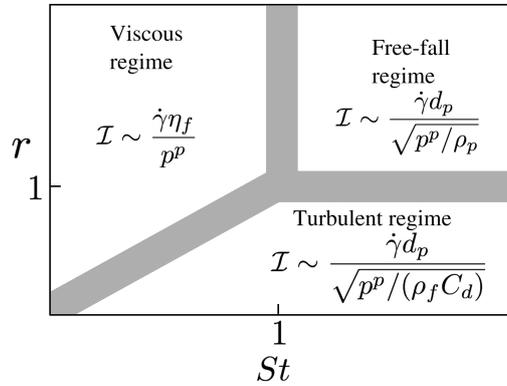
Figure 2.7: Diagram of different flow regimes in the plane (St, r), extracted from Andréotti et al. [2011].

The transition between these different regimes is controlled by two dimensionless numbers: the Stokes number $St = \frac{d\sqrt{p^p\rho_p}}{\eta_f}$, which compares the free fall time to the viscous time and the density ratio $r = \frac{\rho_p}{\rho_f C_d}$, which compares the free fall time to the turbulent time. The different flow regimes and the definitions of $\mathcal{I}$ are shown in Figure 2.7, in the plane (St, r).

The two-phase continuum modelling with $\mathcal{I}^{visc}$ in the visco-plastic granular rheology was successfully used to describe several configurations (Cassar et al. [2005], Doppler et al. [2007], Ouriemi et al. [2009], Pailha and Pouliquen [2009], Boyer et al. [2011], Aussillous et al. [2013]).

2.2.5 Virtual mass approach

Considering an unsteady fluid flow in a porous media, several experimental studies have shown that it exists a phase shift between the fluid pressure drop and its velocity (Gu and Wang [1991], Hall et al. [1995]), which results from the inertia of the accelerated fluid flow. The unsteady Darcy-Forchheimer equation should be taken into consideration:

$$R_f \frac{\partial u_i^f}{\partial t} = -\frac{\partial p^f}{\partial x_i} - \eta(1-\phi)u_i^f \left[\beta_l + (1-\phi)\beta_i Re_p \frac{u_i^f}{\mid u_i^f \mid} \right] \tag{2.17}$$

Where R_f takes into account a virtual mass effect, introduced by Sollitt and Cross [1972]: the acceleration of the fluid particles in the vicinity of an obstacle provides an additional resistance to the flow. It has been emphasized in the literature (Gu and Wang [1991], Hall et al. [1995], Rajagopal [2007], Zhu et al. [2014]). C_{vm} is an empirical virtual mass coefficient, Lowe et al. [2008] has determined C_{vm} by measuring the phase and amplitude of the flow in a porous media, comparing with the value in the literature, which are in the range of $0.5 \le C_{vm} \le 2.0$.

2.3 Discharge of a silo

The discharge of silo has been widely studied due to the great interest for industrial applications, such as the agri-food sector and the pharmaceutical industry. Since the pioneering work carried out by Hagen [1852], a large amount of research deals with the discharge of silo with an experimental approach (see for example Beverloo et al. [1961], Nedderman et al. [1982], Tüzün et al. [1982], Mankoc et al. [2007], Janda et al. [2012], Zuriguel et al. [2014], Rubio-Largo et al. [2015], Zhou et al. [2015]) and with a numerical approach (see for example Hirshfeld and Rapaport [2001], Rycroft et al. [2006], Hilton and Clearly [2011], Staron et al. [2012, 2014], Zhou [2016]).

2.3.1 Static of a silo: Janssen model

In 1895, Janssen measured the pressure at the bottom of a silo filled with corn (see the original article of Janssen translated by Sperl [2006]). He observed that, unlike what happens with a liquid, the pressure seems to saturate when an increasing mass of corn is poured into the silo. He then developed a simple model to predict the distribution of stresses, considering a cylindrical silo of diameter D, filled with a granular media of density ρ_p and a bulk volume fraction ϕ (see Figure 2.8a). He made the following three assumptions:

- The vertical stress σ_{zz} is supposed to be uniform in the cylinder section.

- The granular media is about to slide, meaning that the friction on the side walls is fully mobilized. Thus, there is a upward tangential stress at the side walls, $\tau = \mu_w \sigma_{rr}$, where
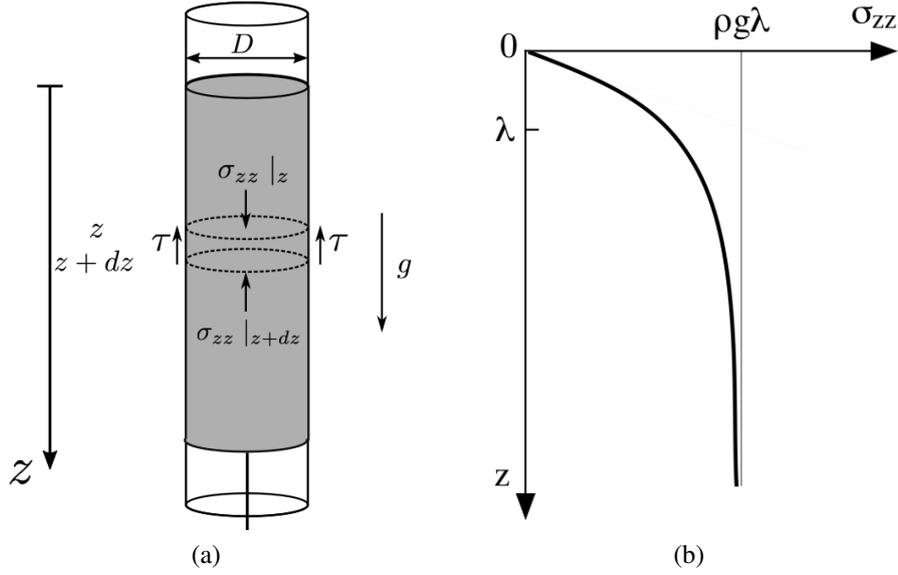
Figure 2.8: Janssen model for determining the stress distribution in a silo (Andréotti et al. [2011]). (a) schema of the silo. (b) Evolution of the vertical normal stress as a function of depth.

μ_w is the coefficient of friction wall-grain and σ_{rr} is the normal horizontal stress at the side walls.

- The normal horizontal stress is proportional to the normal vertical stress: $\sigma_{rr} = K\sigma_{zz}$, where K is a constant value.

With these assumptions, the force equilibrium on a slice of granular media reads:

$$\frac{d\sigma_{zz}}{dz} = \rho_p g - \frac{4K\mu_w}{D}\sigma_{zz} \tag{2.18}$$

Equation 2.18 is integrated knowing that the stress is zero at the top of the granular media surface ($z = 0$), giving the stress distribution along the vertical position:

$$\sigma_{zz} = \phi\rho_p g\lambda\left(1 - e^{-z/\lambda}\right) \tag{2.19}$$

where $\lambda = D/(4\mu_w K)$ represents a characteristic length. This solution is displayed in Figure 2.8b. We notice that the pressure increases linearly as $\sigma_{zz} = \phi\rho_p gz$, for $z \ll \lambda$, and it saturates to a constant value $\sigma_{zz} = \phi\rho_p g$, for $z \gg \lambda$. For the latter case, the excess weight is fully supported by the friction on the side walls. This model was validated experimentally by several authors (Vanel et al. [2000], Ovarlez et al. [2003]).

2.3.2   Regimes of silo discharge

Three regimes of silo discharge can be distinguished depending on the ratio between the outlet size D and the particle size d_p.

- Jamming regime: for relatively small ratio $D/d_p < 4$, the discharge flow is quickly blocked, the particles forming an arch above the outlet as shown in Figure 2.9a. Injection of energy (blowing, shaking or tapping) is required to break the blocking arch and restart the flow (To et al. [2001], Zuriguel et al. [2005], Mankoc et al. [2009], Janda et al. [2009]).

- Intermediate regime: for the silo with an intermediate ratio, the flowing and the blocking phases follow each other during the discharge period (Pennec et al. [1996]).

- Continuous regime: for a sufficiently large ratio, the discharge flow becomes continuous. In this continuous regime, we observe various flow regions within the silo, as illustrated in Figure 2.9b that shows a velocity field obtained by a two-dimensional continuous simulation (Zhou [2016]). We observe that at the upper part of the silo, the granular flow is homogeneous along the cross section (small velocity gradient), and the streamlines of the flow are purely vertical. A constriction of the streamlines with an acceleration of the flow is observed at the zone near the outlet (for $z \lesssim 3D$). In addition, we observe stagnant zones nearby the bottom borders of the silo.
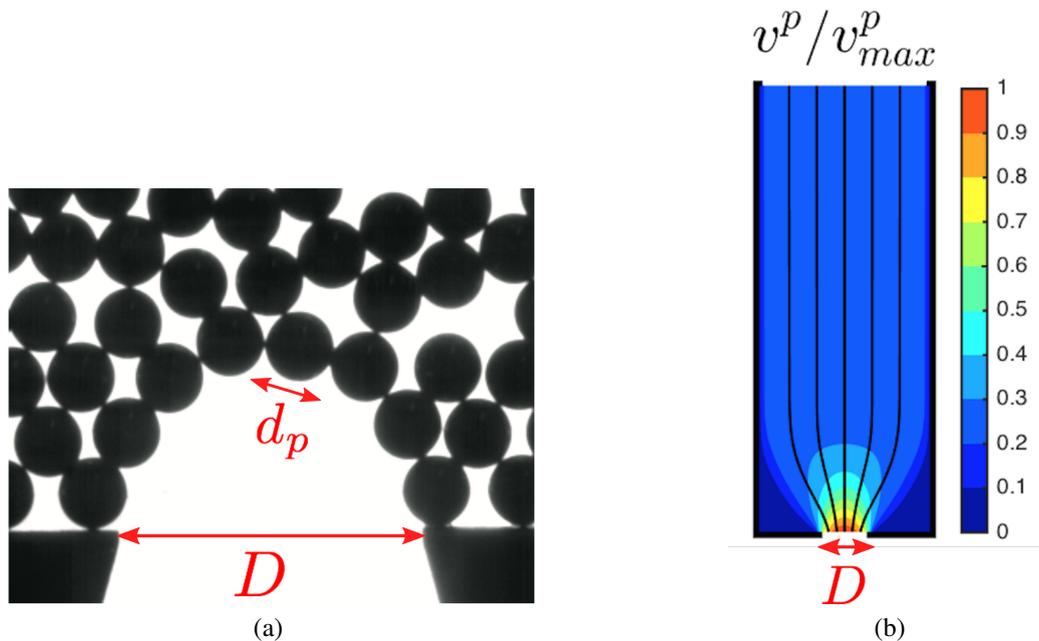
Figure 2.9: (a) Photograph of a blocking arch formed above the outlet, extracted from Janda et al. [2008]. (b) Velocity field of a two-dimensional continuous simulation of a silo discharge, extracted from Zhou [2016]

2.3.3 Discharge flow rate

A remarkable property of the discharge of a silo, is that the flow rate is constant over time, independently on the remaining granular media height in the silo contrary to the case of a liquid. This property can be partly explained by the Janssen model: the stress that controls the flow at the orifice is independent of the granular height. However, even if this pressure shielding effect still exists under the flowing conditions (Bertho et al. [2003], Perge et al. [2012]), several experimental studies have shown that the flow rate is independent of the pressure at the silo bottom (Aguirre et al. [2011], Perge et al. [2012]).

(a)   (b)
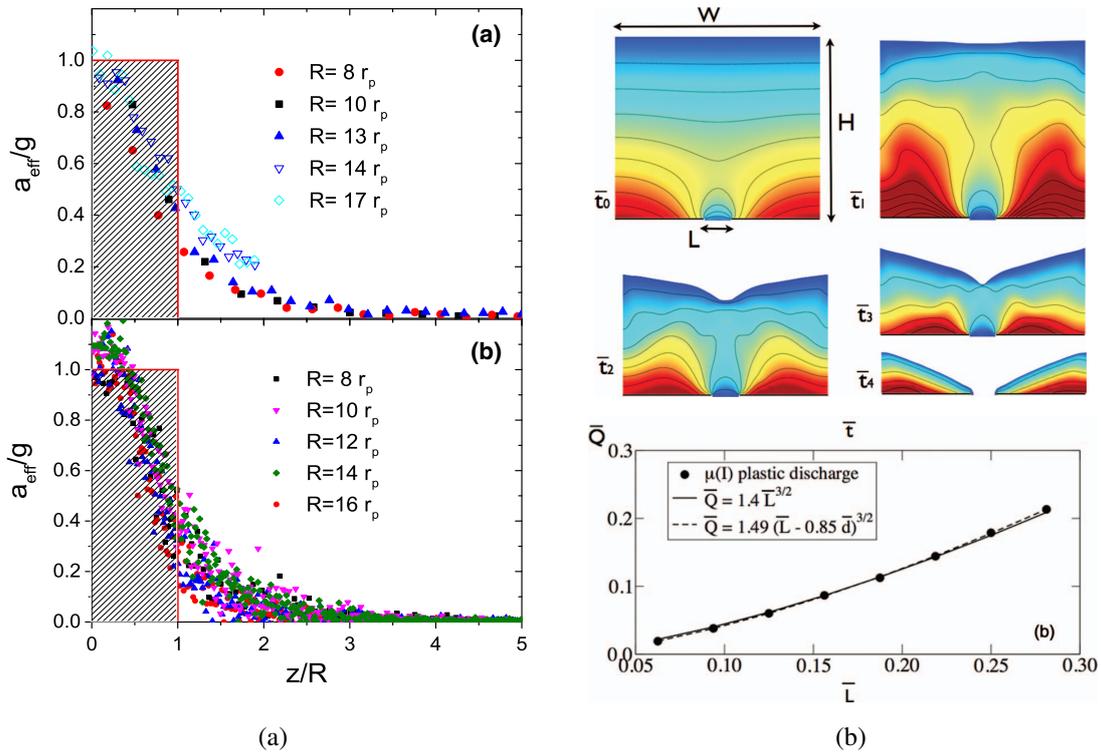
Figure 2.10: Discharge of silos: (a) measurements of the particle acceleration above the outlet (Rubio-Largo et al. [2015]). The superior figure is obtained by a two-dimensional experiment and the inferior figure is obtained by a 3D discrete simulation. (b) Two-dimensional continuum simulation with a frictional rheology by Staron et al. [2012]. The superior figure shows the granular pressure fields at various moments and the inferior figure illustrates the discharge flow rate of the granular media as a function of the outlet size.

Moreover experimental studies show that the flow rate does not depend on the silo width as long as it is sufficiently large compared to the outlet size (Nedderman [1992]). Based on these observations, a dimensional analysis of the problem can be conducted to estimate the discharge flow rate. If neither the granular height, the silo size, nor the particle size impacts the discharge flow rate, the only relevant remaining length to scale the flow rate is therefore the size of the outlet D. The single driving force being the gravitational acceleration, the discharge velocity v of the

particle scales as:

$$v \propto \sqrt{gD} \tag{2.20}$$

The discharge flow rate Q is then obtained by multiplying this velocity by the outlet surface, and by taking into account the specific density of the granular media: $\phi_b \rho_p$, leading for a circular orifice:

$$Q = C \rho_p \phi_b \sqrt{gD^5} \tag{2.21}$$

where ρ_p is the density of granular media, ϕ_b is the bulk volume fraction and C is an empirical coefficient of magnitude approximate 1. To interpret this behavior, Hagen [1852] and Brown and Richards [1970] proposed that it exists a dynamical arch of characteristic size of order of magnitude D. Underneath this dynamical arch, the particles are in free-fall in gravity. This concept can be adapted to rectangular silo of thickness W, the orifice being of size D spanning with the thickness (Janda et al. [2012], Benyamine et al. [2014]), lead to:

$$Q = c_D \rho_p \phi_b W \sqrt{gD^3} \tag{2.22}$$

Thanks to the development of new experimental techniques and numerical simulations means this hypothesis has been recently questioned. Experimentally and with discrete simulations, Janda et al. [2012] and Rubio-Largo et al. [2015] have shown that the granular medium remains dense and that the particles do not exactly undergo a free fall but accelerated continuously from zero to g on a typical length of D above the outlet.

Recently several authors have studied numerically the discharge of silo, by implementing the visco-plastic rheology $\mu(I)$ in the continuous simulation code (Staron et al. [2012, 2014], Dunatunga and Kamrin [2015], Davier and Bertails-Descoubes [2016], Zhou et al. [2017]). They showed that this continuous modelling reproduced well the flow rate scaling of equation 2.21 (see Figure 2.10b). The frictional properties of granular media considered as a continuous media therefore explains this behavior.

2.3.4 Dilation of particles at the outlet

A slight dependency of the discharge flow rate on the particle size was found by several authors (Hagen [1852], Beverloo et al. [1961]) for small D/d_p, Hagen [1852] noted that the particles at the border would partially lose their velocities and disrupt their neighbors. Beverloo et al. [1961] proposed to describe this slight dependency of the particle size by:

$$Q = C \rho_p \phi_b \sqrt{g \left(D - k d_p \right)^5} \tag{2.23}$$

where k is a coefficient that depends both on the silo geometry and the granular material. Brown and Richards [1965] explained this correlation by the existence of an "empty annulus" close to the
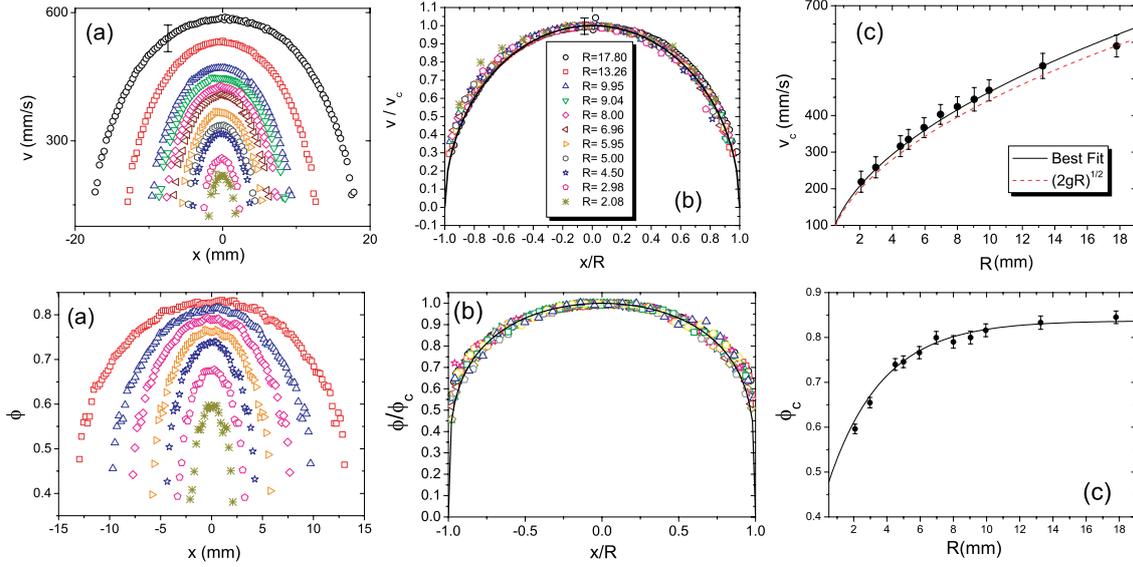
Figure 2.11: Velocity and volume fraction profiles at the outlet of a two-dimensional silo, extracted from Janda et al. [2012].

borders of the outlet.

Recently, based on experimental measurements of the discharge of a two-dimensional silo (filled by a monolayer of particle), Janda et al. [2012] have shown that the velocity and the volume fraction profiles at the outlet are self-similar, as shown in Figure 2.11, and they can be respectively expressed as $v(x) = v_0(1 - (x/R)^2)^{0.5}$ and $\phi(x) = \phi_0(1 - (x/R)^2)^{0.22}$, where x represents the horizontal position and v_0 and ϕ_0 are respective the velocity and the volume fraction at the center of outlet.

Concerning the volume fraction at the center of outlet ϕ_0, Mankoc et al. [2007], Janda et al. [2012] and Benyamine et al. [2014] have shown experimentally that the granular media tends to dilate for maintaining the discharge flow for a small ratio D/d_p. They proposed an empirical expression for the dilation at the outlet:

$$\phi_0 = \xi_\phi \phi_b \left[1 - \alpha e^{-\beta \frac{D}{d_p}} \right] = \xi_\phi \phi_b G \left(\frac{D}{d_p} \right) \tag{2.24}$$

where ϕ_b is the initial volume fraction and ξ_ϕ, α and β are fitting parameters.

Furthermore, Janda et al. [2012] have shown that the velocity of the particles at the center of the outlet depends only on the outlet size D:

$$v_0 = \sqrt{\gamma g D} \tag{2.25}$$

with $\gamma = 1.1$. Based on the self-similar profiles of the velocity and of the volume fraction at the

40

outlet and considering equations 2.24 and 2.25, the discharge flow rate can be expressed as:

$$Q = c_D \phi_b \rho_p G\left(\frac{D}{d_p}\right) S_0 \sqrt{gD} = c_D \phi_b \rho_p \left[1 - \alpha e^{-\beta \frac{D}{d_p}}\right] S_0 \sqrt{gD} \qquad (2.26)$$

where S_0 represents the outlet surface and c_D is a constant. This expression gives a good adjustment of experimental results (Benyamine et al. [2014], Zhou et al. [2017]) for the discharge of rectangular or cylindrical silos, and of two-dimensional discrete simulations results (Percier [2013], Zhou et al. [2015]).

2.3.5 Effect of the outlet position

Few studies concern the discharge of a silo with a lateral orifice. With a cylindrical or square lateral orifice, Chang et al. [1991] and Zhou [2016] have shown that equation 2.21 stays valid but with a lower value (about half) of the coefficient C.
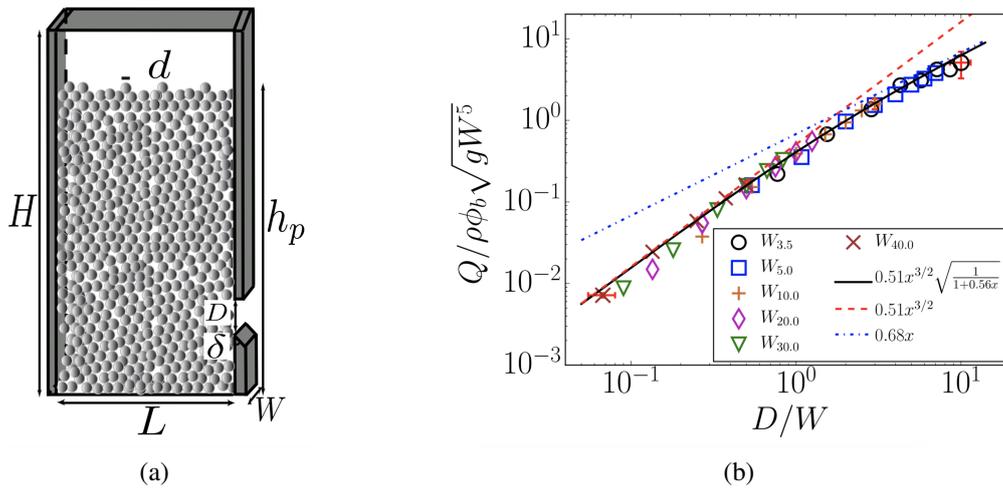
Figure 2.12: Figures extracted from Zhou et al. [2017]. (a) Schematic apparatus of the rectangular silo with a lateral outlet. (b) Dimensionless mass flow rate $Q/\rho_p \phi_b \sqrt{gW^5}$ as a function of aspect ratio D/W.

Modelling a fuel rod cladding break by a rectangular lateral orifice of height D and width W, in a cylindrical or a rectangular silo (see Figure 2.12a), Zhou et al. [2017] identified two granular flow regimes. As shown in Figure 2.12b for a rectangular silo, the first discharge flow regime observed for small outlet aspect ratio $D/W < 2$, corresponds to the Hagen-Beverloo law $Q \sim W D^{3/2}$. The second regime is observed for thin silos ($D/W > 2$), where the discharge flow rate then scales as $Q \sim W^{3/2} D$. These authors has shown that these two-regimes of discharge can be simulated thanks to a continuum model for the granular media with the frictional rheology $\mu(I)$ in 2D computations where the wall friction force (along the front and behind walls of the silo) is accounted for from a Hele-Shaw point-of-view. In those simulations, it has first been observed

that norm of the velocity on the central streamline does not depend on the lateral friction:

$$U_0 = c_E \sqrt{gD} \tag{2.27}$$

Which suggests that the potential energy is transferred to kinetic energy in the outlet area. Then, it has been observed that friction term acts mainly on the orientation of the internal flow of the granular media. For lateral aperture, the granular flow, that is accelerated by the vertical gravity, has to rotate toward aperture. The more the wall friction term is (the thinner the silo is), the less is the inclination of the flow, and therefore the flow-rate toward horizontal (normal to the aperture). Hence, a reduction of mass flow rate was observed as well as a new regime controlled by the thickness of silo W. The authors proposed an empirical model to predict the angle of inclination θ_0 of the central streamline at the orifice relative to the horizontal:

$$\cos \theta_0 = \frac{c_{\theta_0}}{\sqrt{1 + \gamma D/W}}. \tag{2.28}$$

where c_{θ_0} and γ are numerical constant. Thus the mass flow rate as a function of the aperture aspect ratio reads:

$$\frac{Q}{\rho_p \phi_b \sqrt{gW^5}} = c_{lat} \frac{(D/W)^{3/2}}{\sqrt{1 + \gamma D/W}} \tag{2.29}$$

where c_{lat} is a numerical constant which can take into account the particle diameter which is seemed to play only a role in the volume fraction of the outlet area. However there is still little understanding of the physical process leading to this scaling that is related to the internal friction in the silo.

2.3.6 Effect of air flow

The aim of this thesis being to study the discharge flow rate of fuel fragments coupled with a pressurized gas flow, let us review the understanding of the role of the gas flow on the ejection dynamics. The gas flow can be used either to assist or resist the granular flow corresponding respectively to the case of a co-current air flow (de Jong [1969], de Jong and Hoelen [1975], Altenkirch and Eichhorn [1981], Nedderman et al. [1983]), or to the case of a counter-current air flow (Crewdson et al. [1977], Altenkirch and Eichhorn [1981], Hsiau et al. [2010], Hilton and Clearly [2011]). The air flow is fully correlated with the pressure field within the silo (Resnick et al. [1966], de Jong [1969], Nedderman et al. [1983]). To model the coupling of the granular discharge with the air flow, many authors modified the Hagen-Beverloo law (equation 2.23) by adding a pressure gradient term to the gravitational driving force (Crewdson et al. [1977]):

$$Q = Q_0 \left[1 + \frac{1}{\rho_p \phi_b g} \frac{dp}{dr} \mid_0 \right]^{1/2} \tag{2.30}$$

Here, $\frac{dp}{dr}\big|_0$ represents the pressure gradient on the outlet zone, i.e. over a length of approximately $r = D/2$ and Q_0 represents the discharge flow rate without gas injection, given by the Hagen-Beverloo law. This pressure gradient accounts for the fluid-grain interaction force, that influences the discharge flow rate.

In the context of the RIA, Zhou [2016] proposed a first study of the role of the gas flow using a simplified configuration. They carried out an experimental and numerical study on the discharge of silo with an imposed air flow rate at the silo top, corresponding to a steady discharge flow for a bottom or a lateral orifice. Using equation 2.30 with Q_0 given by Janda et al. [2012] (equation 2.26), they developed an analytical model in the framework of the two-phase continuum modelling where the gas pressure gradient at the outlet is determined by the Forchheimer resistance law (equation 2.13). They introduced the mean velocity of the granular flow at the outlet $u^p(z \approx 0) = Q/S_0\phi_0\rho_p$ and that of the mixture $U(z \approx 0) = Q_{air}/S_0$, where Q_{air} is the steady injected volumetric flow rate and Q is the steady discharge mass flow rate of granular media. ϕ_0 represents the volume fraction of particle at the outlet and S_0 is the outlet section. They obtained

$$\frac{\partial p^f}{\partial z}(z \approx 0) = \eta_f\beta_l\frac{Q_{air} - Q/(\phi_0\rho_p)}{S_0} + \rho_f d_p\beta_i\left(\frac{Q_{air} - Q/(\phi_0\rho_p)}{S_0}\right)\left|\frac{Q_{air} - Q/(\phi_0\rho_p)}{S_0}\right| \quad (2.31)$$

with $\beta_l = \frac{150\phi_0^2}{(1-\phi_0)^3 d_p^2}$ and $\beta_i = \frac{1.75\phi_0}{(1-\phi_0)^3 d_p^2}$ corresponding to the Kozeny-Carman model. The flow rate is thus given by following:

$$Q = Q_0\left[1 + \frac{\eta\beta_l(\phi_0, d_p)}{\phi_0\rho_p g S_0}\left(Q_{air} - \frac{Q}{\phi_0\rho_p}\right) + \frac{\rho_f d\beta_i(\phi_0, d_p)}{\phi_0\rho_p g S_0^2}\left(Q_{air} - \frac{Q}{\phi_0\rho_p}\right)\left|Q_{air} - \frac{Q}{\phi_0\rho_p}\right|\right]^{1/2} \quad (2.32)$$

where Q_0 represents the discharge flow rate of particles without gas injection. Equation 2.32 can be considered as a quadratic equation linking the mass flow rate of particles Q with the air volumetric flow rate Q_{air}, namely $Q = f(Q_{air})$. For convenience, they introduced the notations

$$\bar{Q} = \frac{Q}{Q_0} \quad \text{and} \quad \tilde{Q} = \frac{\phi_0\rho_p Q_{air}}{Q_0} \quad (2.33)$$

$$\mathcal{N}_{l0} = \frac{\eta_f\beta_l(\phi_0, d_p)Q_0}{\phi_0^2\rho_p^2 g S_0} \quad \text{and} \quad \mathcal{N}_{i0} = \frac{\rho_f d_p\beta_i(\phi_0, d_p)Q_0^2}{\phi_0^3\rho_p^3 g S_0^2} \quad (2.34)$$

Dimensionless $\bar{Q}$ and $\tilde{Q}$ flow rates are normalized by the discharge flow rate in absence of fluid interaction Q_0, respectively for granular flow rate and air flow rate. In addition, a definition of sign was also introduced

$$\pm = \frac{\tilde{Q} - 1}{|\tilde{Q} - 1|} \quad (2.35)$$

whose value is $+1$ for the case of co-current flow and -1 for the case of counter-current flow. The transition, i.e. the change of sign corresponds to the singular value when $Q_{air} = Q/\phi_0\rho_p$, meaning that the air volume flow rate is exactly equal to the volumetric granular flux ejected through the
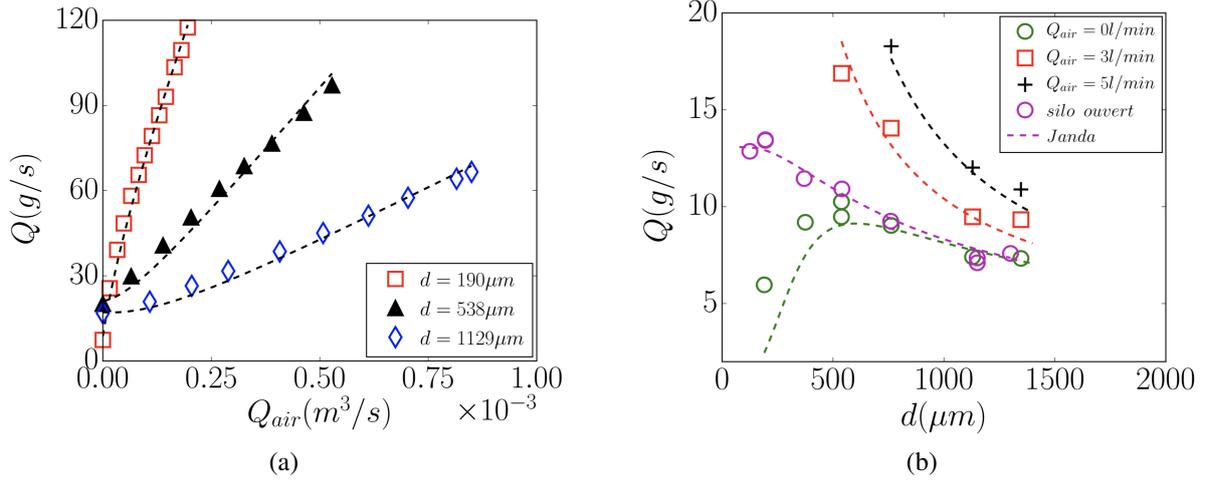
Figure 2.13: Figures extracted from Zhou [2016]. (a) Mass flow rate of particles Q versus the volumetric flow rate of air Q_{air}. (b) Mass flow rate versus the particle diameter for different volumetric flow rate of air. The lines represent equation 2.37.

outlet, leading to a discharge of silo driven by gravity, as $Q = Q_0$. Therefore, equation 2.32 can be rewritten under a simple form as following:

$$(1 \mp \mathcal{N}_{i0}) \bar{Q}^2 + (\mathcal{N}_{l0} \pm 2\mathcal{N}_{i0}\tilde{Q}) \bar{Q} - (1 + \mathcal{N}_{l0}\tilde{Q} \pm \mathcal{N}_{i0}\tilde{Q}^2) = 0 \qquad (2.36)$$

The discriminant Δ of this quadratic equation on $\bar{Q}$ is strictly positive so there are two distinct roots, however, the single positive root of this quadratic equation on $\bar{Q}$ is the solution of problem due to the fact that the negative one would correspond to particles entering the silo which has no physical meaning. Therefore, the solution is:

$$\bar{Q} = \frac{(\mp 2\mathcal{N}_{i0}\tilde{Q} - \mathcal{N}_{l0}) + \sqrt{\Delta}}{2(1 \mp \mathcal{N}_{i0})} \quad \text{with} \quad \Delta = \mathcal{N}_{l0}^2 + 4(1 + \mathcal{N}_{l0}\tilde{Q}) \pm 4\mathcal{N}_{i0}(\tilde{Q}^2 - 1) \qquad (2.37)$$

Using the volume fraction at the outlet ϕ_0 deduced from Q_0 in this solution, Zhou [2016] obtained a fairly good agreement between this steady analytical model and the experiments as shown in Figure 2.13. For a lateral orifice, they showed that the model stays valid replacing g by κg where $\kappa = \left(\frac{c_{Dl}}{c_D}\right)^2$ takes into account the inclination of the granular streamlines. Finally, using continuum simulation, they have shown that the two-phase modelling with the frictional rheology for the granular phase reproduces well the observed behavior in the Darcy regime.

2.3.7 Effect of surrounding liquid

During the hypothetical accident, the fuel fragments will be ejected out of the cladding, and towards the surrounding coolant, namely pressurized water. Very few studies concern the discharge of a dry granular media from a silo into a liquid. The grain/air/water interface at the outlet generates capillary depression (J.Bear [1972]):

$$p_c = \frac{4\gamma \cos \theta^*}{d_p} \tag{2.38}$$

where γ represents the surface tension between the liquid and the air, θ^* is the contact angle and d_p is the particle diameter. For a static granular media, this depression may induce a water motion (see Figure 2.14a). For the case of $\theta^* < 90°$, the capillary depression is positive, which conducts a rising water level inside the granular media, until an equilibrium state: $p_c = \rho g \left(h_{wet} - h_{water} \right)$, where h_{wet} is the level of water in the granular media and h_{water} is the water level in the tank. Oppositely, for the case of $\theta^* > 90°$, the capillary depression becomes negative, a lower water level compared to that of tank is found due to the hydrophobic property of the particles.
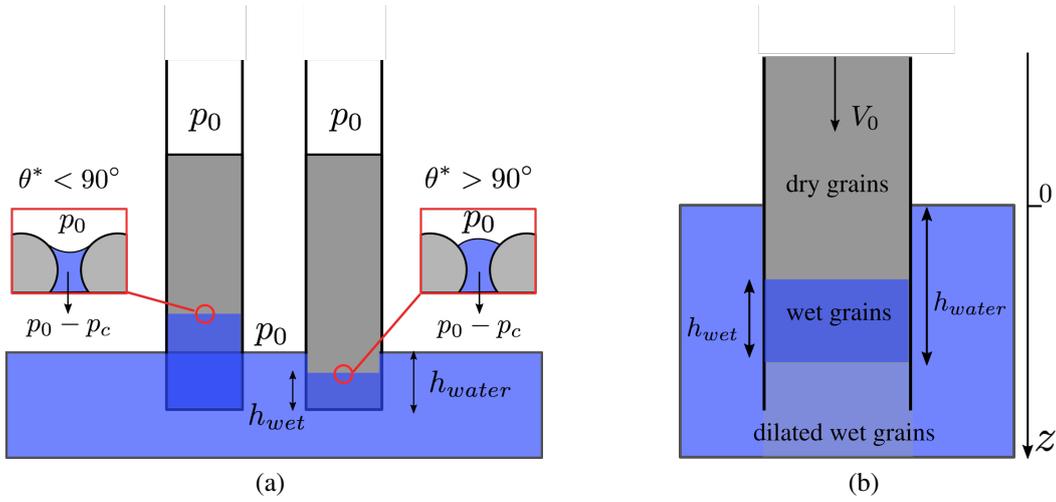
Figure 2.14: (a) schematic view of an experiment of capillary rise in a granular column. (b) schematic view of an impregnation of a granular jet in water (Saingier [2018]).

Saingier [2018] proposed to model the impregnation of a dense granular jet in water by the immersion of a porous media at a constant velocity V_0 (see Figure 2.14b). For a porous media translated at the velocity V_0, they have shown that the imbibition front can be modeled using the Darcy-Forchheimer law:

$$(1 - \phi)\boldsymbol{u}^p \left[1 + (1 - \phi) \frac{\rho \beta_i d_p}{\eta \beta_l} |\boldsymbol{u}^p| \right] = -\frac{\boldsymbol{\nabla} p - \rho \boldsymbol{g}}{\eta \beta_l} \tag{2.39}$$

For a granular jet, using a 1D model, they supposed that the stationary jet velocity corresponds to the critical velocity where the Darcy drag is not sufficient enough to compensate the apparent weight of the materials:

$$u_c = \frac{d_p^2}{180} \left(\frac{1 - \phi}{\phi} \right)^2 \frac{\Delta \rho g}{\eta} = \frac{u_{Stokes}}{10} \left(\frac{1 - \phi}{\phi} \right)^2 \tag{2.40}$$

with $u_{Stokes} = \left(d_p^2 / 18 \right) \Delta \rho g / \eta$.

2.4 Conclusion

This presentation of the state of knowledge concerning the two-phase flow shows that there is no model available to predict the flow rate of the fuel fragments in the configuration of interest.

We have seen that these flows are the result of the dynamics of grain-grain contact, gravity and grain-fluid interaction. While all these elements can be represented at the grain scale (the subject of discrete numerical simulations), there is no more macroscopic modelling based solely on the physical properties of the media. The discharge of a silo remains empirically modelled, i.e. without all the coefficients of Hagen-Beverloo law being linked to the physical mechanisms. Nevertheless, continuum modelling, based on the frictional rheology, makes it possible to predict certain dynamics in a phenomenologically satisfactory way, such as the silo discharge or the influence of parietal friction. Moreover, a two-phase continuum modelling with this granular rheology allows to describe the coupling between fluid and grain and to predict the discharge flow rate of a silo with gas injection in a steady regime. In this thesis, we are now interested in unsteady situation when the gas flow rate is not constant or when the outlet suddenly opens, without or with a surrounding liquid. We will also investigate how the internal geometry drives the discharge flow rate of granular media for a lateral orifice. The approach of this work is first to determine experimentally the role of the different parameters (silo outlet size, particle size, gas internal pressure). Then we will examine the ability of the two-phase continuum modelling with a granular frictional rheology to predict the observed silo discharge.

In the next chapter, we will focus on the role of the lateral position of the orifice, studying how the internal geometry of the silo may drive the discharge flow.

Chapter 3

Discharge of a silo with lateral orifice: role of the silo geometry versus friction

To study the RIA case, since the fuel rod mostly fails by lateral opening of its clad, Zhou [2016] have considered a non conventional geometry with a lateral orifice. They have identified a specific flow regime where friction along the lateral walls as well as the geometry of the stagnant zone and the inclination of the granular flow seem to be intimately coupled. Moreover, they have shown that a continuum modelling with a granular frictional rheology and taking into account the lateral friction reproduces the experimental behaviors. This study questions the concept of the free fall arch, as being the phenomenological explanation of the Hagen-Beverloo law (equation 2.21 in chapter 2).

Following this work, we propose to identify the relative role of the acceleration and the friction (internal and lateral) on the discharge flow rate of a granular media from a rectangular silo, by varying the internal geometry thanks to an inclined bottom which ends up at a lateral outlet. The granular materials, experimental setup and silo configuration will be presented in section 3.1. We performed experiments where we measured independently the mass flow rate and the velocity profiles, norm and inclination. The experiment results are presented in section 3.2, first for a monolayer flow then for a 3D flow, together with a simple analytical model. In section 3.3 we propose a more complete continuum modeling with a frictional rheology described by a $\mu(I)$ constitutive law and taking into account the wall friction. We confront the experiments with those continuum simulations and we deduce an analytical model that predicts the discharge flow rate of particles from a rectangular silo with an inclined bottom according to its outlet aspect ratio.

3.1 Experimental setup

3.1.1 Silo configuration

To study how internal silo geometry drives the granular flow, we perform laboratory experiments corresponding to silos with a finite thickness and an inclined bottom. Figure 3.1a illustrates the rectangular silo (of height H = 1m, width L = 10cm and thickness W that can be varied) made of two thin vertical glass plates separated on the sides by Plexiglas plates. The right hand side separator delimits the top part of the outlet and has a bevel of 45. The bottom of the silo is inclined thanks to a triangular Plexiglas plate with an inclined angle θ_i relative to the horizontal which can be varied from $0°$ to $80°$. Figure 3.1b illustrates three examples of inclined bottom with respective angle of $60°$, $40°$ and $20°$. Those inclined triangular bottoms end up at the lateral outlet defining the outlet size D.

(a) Rectangular silo

(b) Inclined bottom
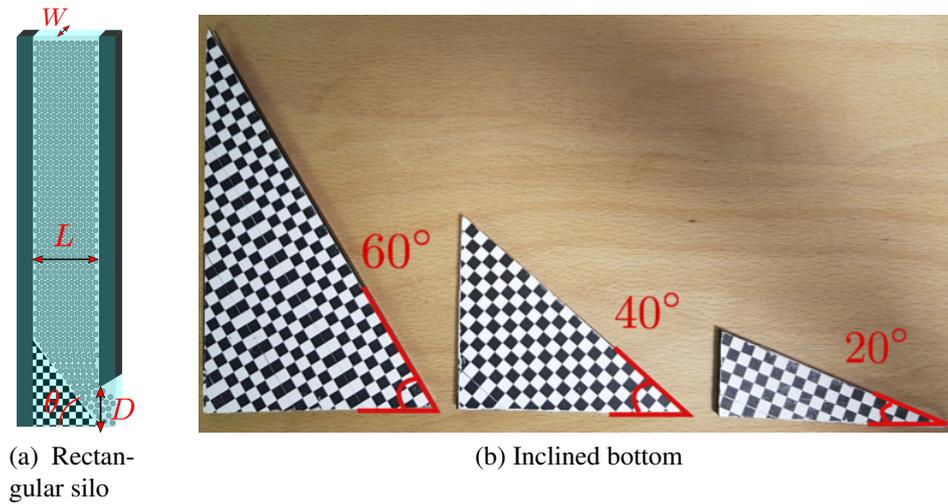
Figure 3.1: Silo configuration.

The whole set of geometrical data is given in Table 3.1.

D	W	θ_i (deg)
$[10; 20; 30; 40; 50]$ mm	$[5; 10]$ mm	$[0; 20; 40; 60; 70; 80]$

Table 3.1: Geometrical parameters for the performed runs, the dimensions are defined in Figures 3.1.

3.1.2 Granular media

We use smooth spherical glass particles with density $\rho_p = 2500 kg/m^3$ provided by $Potter \& Ballotini$. All the particles are sieved and can be considered as monodisperse in size with a little dispersion about $\pm 10\%$ to avoid crystallization effect. The images displayed in Figure 4.2a are obtained by a Digital Microscope of brand $HIROX\ RH-2000$, illustrating a sample of glass particles of mean size $d_p = 550\ \mu m$, where the corresponding size distribution is illustrated in Figure 4.2b. The size distributions are fitted by a gaussian distribution law, as follow:

$$f(d_p, \sigma, d_m) = \frac{1}{\sqrt{2\pi\sigma^2}} e^{-\frac{(d_p - d_m)}{2\sigma^2}} \tag{3.1}$$

where d_m is the mean particle size and σ is the standard deviation.
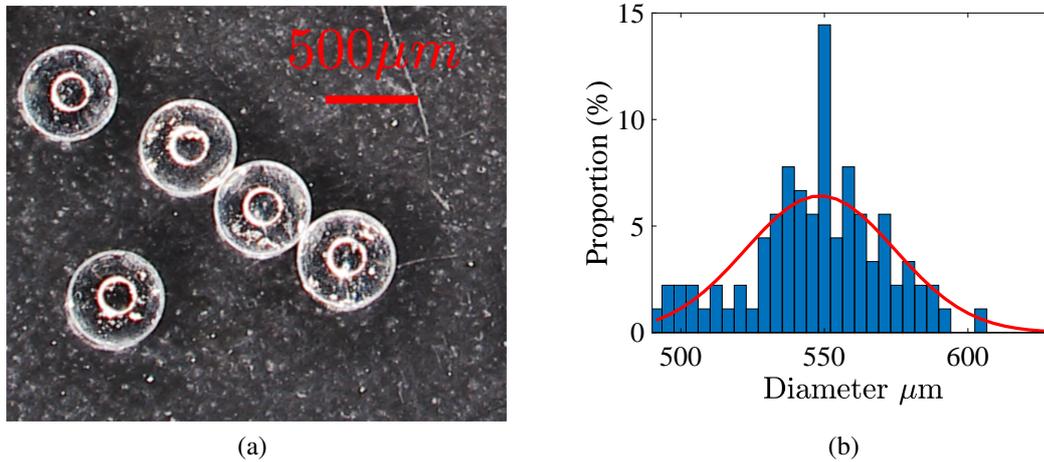
Figure 3.2: (a) Visual aspect and (b) analysis of the dispersion in size of a sample of particles with a mean diameter value $538\mu m$. The red line represent the equation 3.1, with $d_m = 538\mu m$ and $\sigma = 26\mu m$.

Table 3.2: Characteristic of granular media.

	Glass particles	Ceramic particles
d_p (μm)	190; 375; 538; 762; 1129; 1347	4170

We also use spherical ceramic beads with a diameter $d_p = 4170\mu m$ and a density $\rho_p = 6000 kg/m^3$ (provided by $SiLibeads$) in the thinner silo to study the flow of a mono-layer case, with a silo thickness of 5mm. The characteristic of the experimental granular media is provided in Table 3.2.

3.1.3 Measurements and post-processing

As shown in Figure 3.3, the experimental setup consists on the rectangular silo, a high speed camera, a light source, an electronic balance (Mettler Toledo 6002S) and a computer which permits the acquisition of the balance and the camera. Once the silo filled with a mass m_p of particles, the column height h_p is measured. Then the outlet is quickly opened manually and the grains falling out of the silo are collected in a vessel whose temporal evolution of the mass is recorded using the electronic balance with a precision of 0.1g at 20Hz. Each experiment is repeated twice to validate the reproducibility of the process.
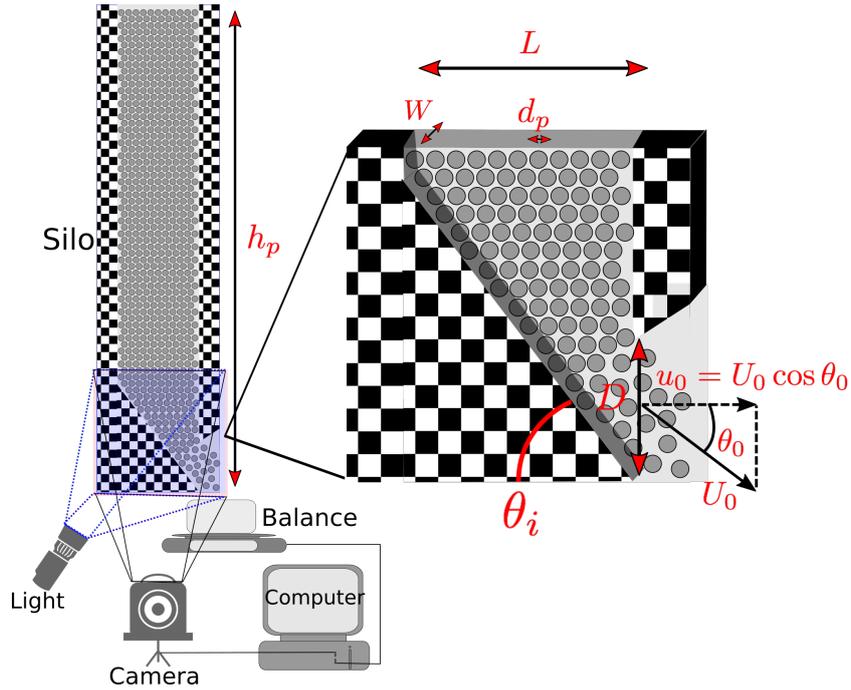
Figure 3.3: Experimental setup.

Several quantities are measured during the discharge of silo thanks to the experimental instruments, the initial bulk particle volume fraction ϕ_b, the mass flow rate of particles Q, the velocity field around the outlet and the particle volume fraction for the mono-layer flow.

a. Initial bulk particle volume fraction ϕ_b

The initial bulk particle volume fraction reads:

$$\phi_b = 2m_p/[W\rho_p L(2h_p - Ltan\theta_i)] \tag{3.2}$$

In Figure 3.4, we plot the initial bulk particle volume fraction versus the mean size of the glass particles. The horizontal dispersion is determined by the distribution of the particle size and the vertical dispersion is defined by the standard deviation of particle volume fraction: $\sigma_{\phi_b} =$

$\sqrt{\sum_{i=1}^{n}(\phi_b - \bar{\phi_b})^2/(n-1)}$. All the values are close to 0.6, and we observed that the volume fraction increases slightly with the particle size. Additionally, we find that the thinner silo ($W = 5$mm) gives a slightly more compact granular column.
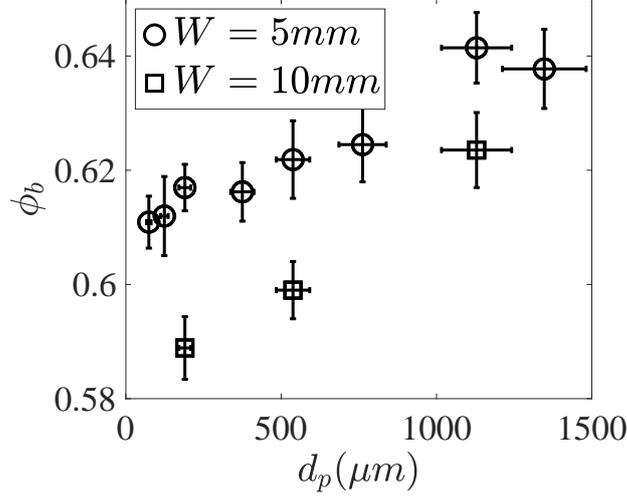
Figure 3.4: Initial bulk particle volume fraction ϕ_b as a function of the mean particle size for the glass particles.

b. Mass flow rate

During the silo discharge, the particles are ejected continuously through the outlet and then collected by a metal vessel placed over the electronic balance. Figure 3.5a shows a typical temporal evolution of the mass. The instantaneous mass flow rate is obtained by post processing the local slope of the mass versus time during $\delta t = 1$s, given by: $Q_i = (m(t + \delta t) - m(t))/\delta t$. A typical temporal evolution of the mass flow rate is illustrated in Figure 3.5b. We observe that similarly to the case of a flat bottom, the mass flow rate reaches rapidly a stationary value. The dashed line represents the mean mass flow rate Q during this stationary period. The dispersion of mass flow rate is evaluated by the standard deviation, $\sigma_Q = \sqrt{\sum_{i=1}^{n}(Q_i - Q)^2/(n-1)}$, where n represents the number of the points used to calculate the mean value of mass flow rate. For clarity, in most of the graph only some error bars are shown.

c. Velocity field

In the experiment, the motion of the particles at the front plate is recorded using a High-Speed camera (Photron FASTCAM APX RS with a SIGMA zoom 24-70 mm f2.8) with a spatial resolution of 1024×1024 at a rate of 250 frames per second. The pictures are taken at the bottom of
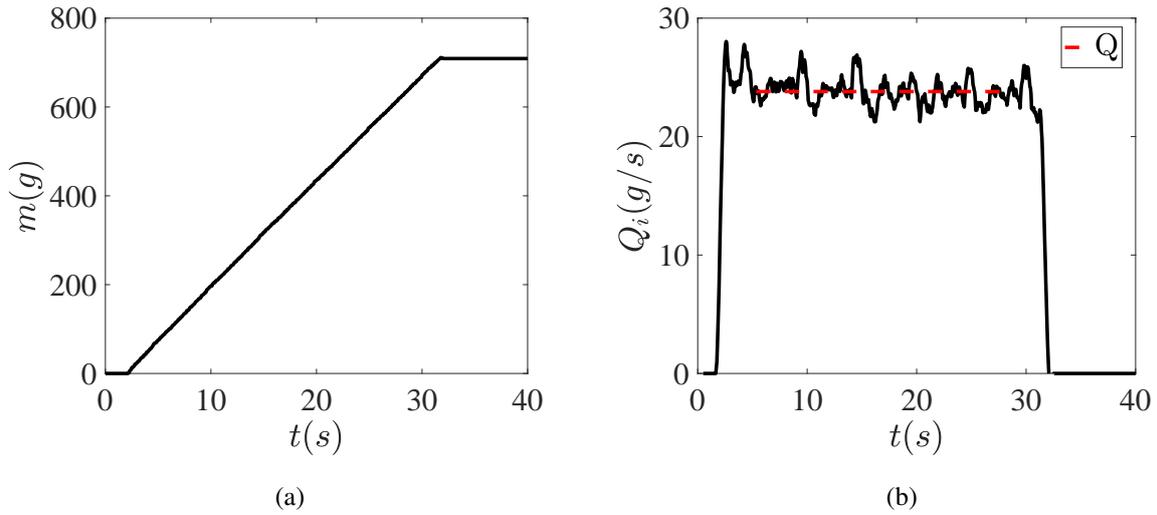
Figure 3.5: Discharge of a silo for W = 5mm, D = 20mm, d_p = $538\mu m$ and θ_i = $60°$. (a) mass versus time. (b) Instantaneous mass flow rate versus time. The red dashed line represents the mean discharge flow rate during the stationary period.

the silo and are approximately 15 cm wide to permit both a good visualization of the flow around the outlet and good resolution of the particle imaging (see Figure 3.6a). Particle velocities are measured by particle image velocimetry (PIV) using the MATLAB software DPIVsoft developed by Meunier and Leweke [2003]. In practice, this involves using a square interrogation region having a size S_{ir} = 32 pixels, with 60 boxes in both the horizontal and vertical direction. The local particle displacement at each node for each pair of consecutive images is measured using a direct cross-correlation. The velocities are built up by taking the average on 9 pairs of consecutive images which are picked up every 0.04 s during the steady-state period of discharge. The error is given by one standard error. The spatial resolution of the measurement (given by the height of the interrogation region) is approximate 5 mm while the velocity resolution (given by the choice of the image pairs) is approximate 0.04 m/s. Due to the spatial resolution, we were not able to obtain the velocity fields for the small particles ($d_p < 500\mu m$) or for the small outlet size ($D\cos\theta_i < 5mm$).

An example of the magnitude of the velocity field, U, for D = 40mm, W = 5mm, d_p = $538\mu m$ and θ_i = $60°$ is shown in Figure 3.6b, where the red line represents the silo edges. The velocity profiles for the vertical component far from the outlet and the horizontal component at the outlet are shown in Figure 3.6c.

Each experiment being done twice, we verify the reproducibility of the method and remove data when the difference between the measured velocities at the centre of the outlet for the same condition is more than double. We also removed data for which the standard deviation of the velocity at centre of the outlet is higher than the magnitude of this velocity.

(a)   (b)   (c)
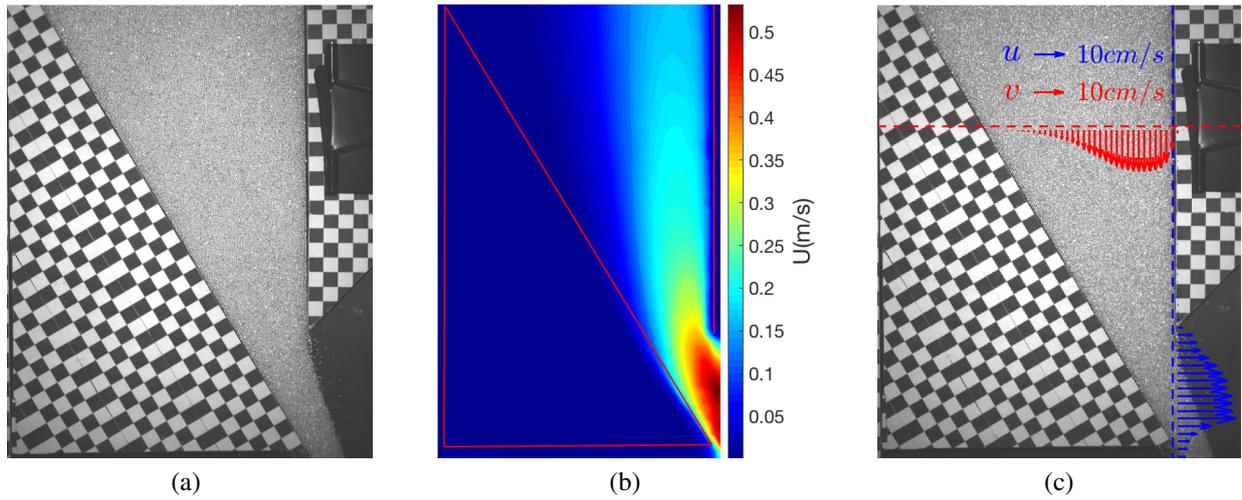
Figure 3.6: A typical analysis of the velocity field for $D = 40$mm, $W = 5$mm, $d_p = 538\mu m$ and $\theta_i = 60°$. (a) snapshot by the high-speed camera. (b) velocity magnitude field. (c) vertical velocity profile far from the outlet (red arrows) and horizontal velocity profile at the outlet (blue arrows).

d. Particle volume fraction for the mono-layer flow

A mono-layer discharge of silo is performed using the ceramic particles of diameter $d_p = 4170\mu m$ in a silo of thickness $W = 5$mm. A typical image is shown in Figure 3.7a. In this case, we can compute the particle volume fraction using a threshold value. The digital images of the silo discharge film are binarized, as shown in Figure 3.7b, with only two possible values for each pixel: 1 for white and 0 for black. An image representing the particle volume fraction is then obtained by

(a)   (b)   (c)
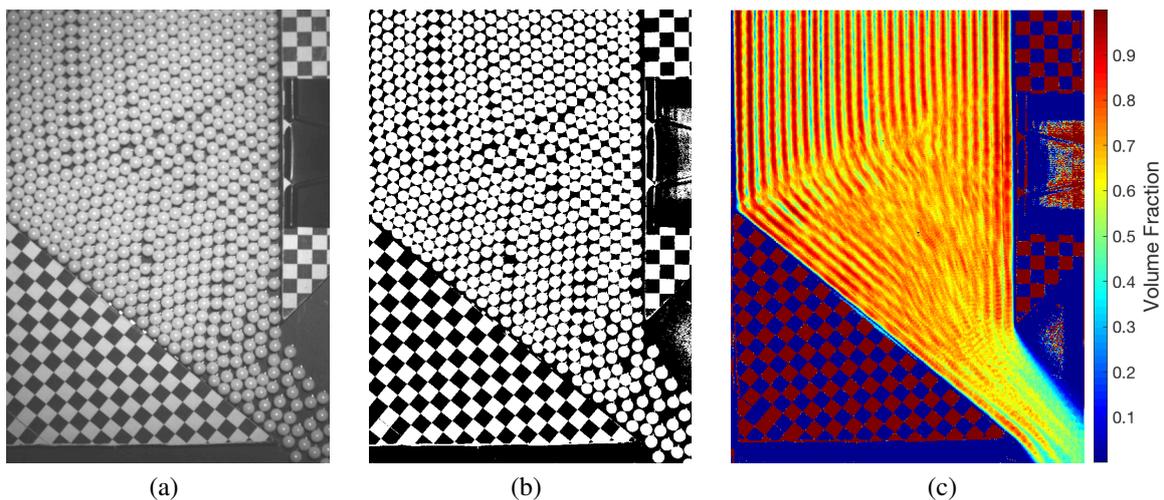
Figure 3.7: (a) Snapshot of the silo discharge in the case of a mono-layer for $D = 40$mm and $\theta_i = 40°$. (a) original image (b) binarized image (c) map of the volume fraction field.

averaging 100 consecutive binarized images corresponding to 0.4s during the stationary discharge period, as shown in Figure 3.7c. Then we scale the pixel value in this image by using the bulk

volume fraction evaluated by averaging the image on a zone far from the the outlet, and measured independently as shown in section 3.1.3a. Finally, we averaged the value on the same boxes than for the PIV processing.

3.2 Experimental results

To study the influence of the bottom inclination angle on the mass flow rate of the discharge from a silo, we first focus on the simplest 2D case corresponding to the mono-layer flow (particles of diameter $d_p = 4170 \mu$m in a silo of thickness $W = 5$ mm). Then we will study the more general 3D flow in a finite rectangular silo.

3.2.1 Experimental mono-layer flow

To understand the role of the bottom inclination on the silo discharge for a mono-layer flow, we will first discuss the observation on the flow rate, then we will interpret its variation thanks to the Particle Image Velocimetry results which will allow us to propose a simple model.

a. Mass flow rate

In chapter 2, we presented the Hagen-Beverloo law (Hagen [1852], Beverloo et al. [1961], Tighe and Sperl [2007]) for describing the discharge flow rate of granular media from silo with a bottom orifice. For our configuration of a rectangular silo of thickness W, with an outlet of size D spanning with the thickness, the particle mass flow rate writes:

$$Q = c_D \phi_b \rho_p W \sqrt{gD^3}. \tag{3.3}$$

Figure 3.8a shows the particles mass flow rate as a function of the inclination angle θ_i for various aperture sizes. In each case we observe that increasing the inclination of the bottom first tends to slightly increase the flow rate (till $\approx 40°$), then we observe a sharp decrease. For a 2D flow at a given angle θ_i, we expect the Hagen-Beverloo equation 3.3 to be valid, then in Figure 3.8b we have plotted the dimensionless mass flow rate $Q/\rho_p \phi_b \sqrt{gW^5}$ as a function of the dimensionless outlet size D/W varying the bottom inclination. We observe that each curve can be effectively adjusted by equation 3.3, with a fitting parameter c_D obtained using the least squares method. Figure 3.8c show this parameter plotted versus the bottom inclination angle. We recover the described behavior with a slow increase of c_D followed by a sharp decrease when increasing θ_i.

To understand this behavior we can now observe the velocities fields.
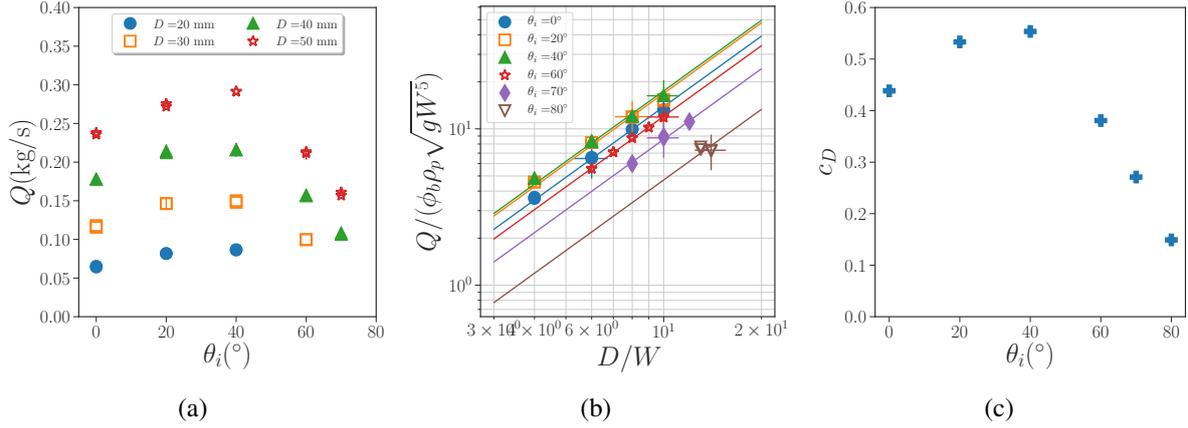
Figure 3.8: Mono-layer flow: (a) Mass flow rate of particles as a function of the bottom angle of inclination θ_i for several outlet sizes D. (b) Mass flow rate of particles made dimensionless by $\phi_b \rho_p \sqrt{gW^5}$ versus the dimensionless outlet size D/W. The full lines represents the Hagen-Beverloo equation 3.3 with the fitting parameters c_D plotted in (c) versus the θ_i.

b. Velocities fields

The 2D velocity fields of the granular flow at the front wall of the silo are shown in Figure 3.9 for $\theta_i = 40°$ (a,b) and $\theta_i = 0°$ (c,d). In Figure 3.9(a,c) we have drawn the streamlines (calculated for velocities higher than 0.01 m/s). We can see that for the $\theta_i = 40°$ case, all the particles are flowing and that there is no stagnant zone contrary to the horizontal bottom case $\theta_i = 0$. In this case, a large slipping zone close to the outlet is also observed. For both cases, the flow is vertical far from the outlet then rotates at the vicinity of the outlet. For the $\theta_i = 40°$ case, the streamlines at the outlet appear to be quite aligned with the bottom.
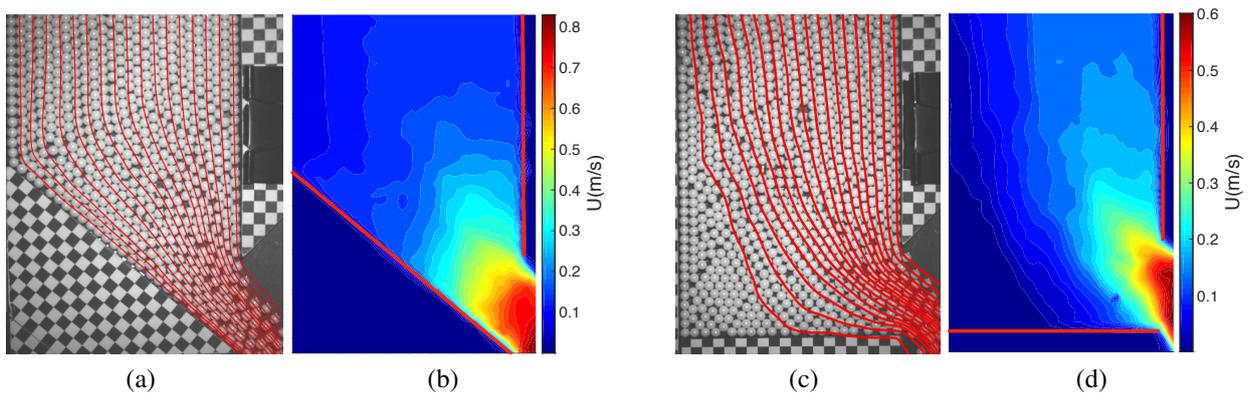
Figure 3.9: (a, c) Streamlines and (b, d) velocity magnitude fields for the mono-layer experiment with $D = 40$mm, $\theta_i = 40°$ for (a, b), and $\theta_i = 0°$ for (c, d).

The magnitude of the velocity in the front plane is illustrated by a color field in Figure 3.9(b, d) for the same data. It clearly illustrates the flow behavior along the silo, with a zone of higher

velocities at the very near region of the outlet related to the flow cross section reduction where the particle acceleration is localized. We will then focus on the flow velocity profiles at the outlet.
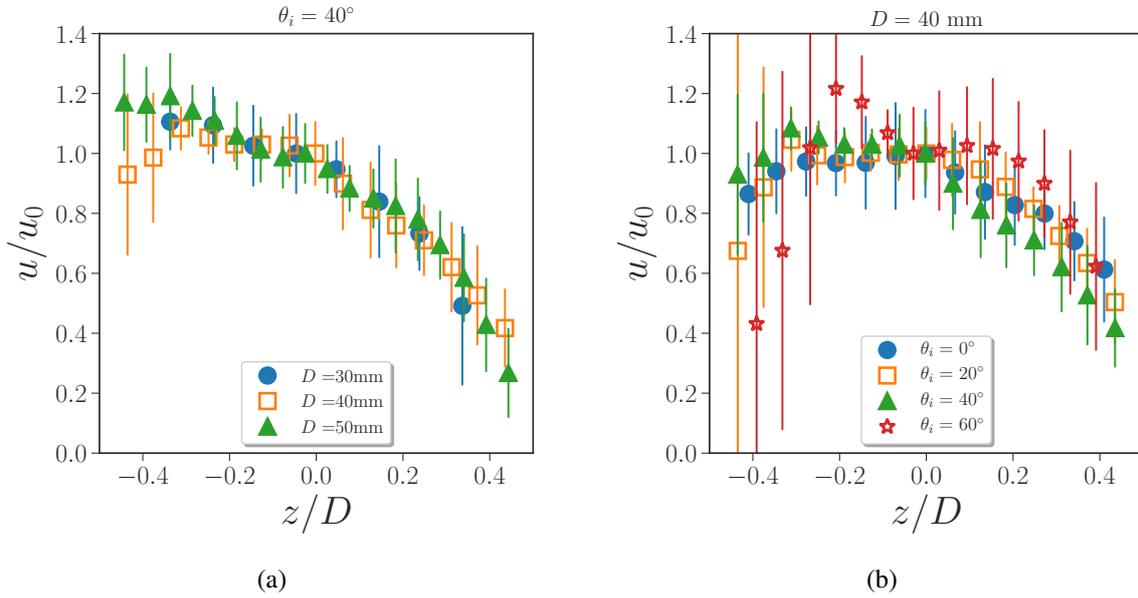
Figure 3.10: Horizontal velocity profiles at the outlet, normalized by the velocity at the center u_0, versus the vertical position normalized by the outlet size z/D for (a) $\theta_i = 40°$ and several outlet sizes D and (b) $D = 40$ mm and several bottom inclinations θ_i. The vertical position, z, is oriented upward and its origin is taken at the centre of the outlet.

The outlet being vertical, the flow rate corresponds to the integral of the horizontal component of the velocity on the outlet surface $Q = \rho_p \int_{-D/2}^{D/2} \int_{-W/2}^{W/2} \phi u \, dy \, dz$, then we focus on this component. Figure 3.10 shows the profiles of the horizontal velocity component at the outlet, normalized by its value at the centre of the outlet, u_0, varying (a) the outlet size D for $\theta_i = 40°$ and (b) the angle of inclination of the bottom θ_i for $D = 40$mm. We first can observe that the horizontal velocity profile exhibits an asymmetry between the top and the bottom of the outlet, certainly mainly due to the sliding of the particles on the inclined bottom. Then we can see that the dimensionless profiles are found to be rather self-similar as observed experimentally by Janda et al. [2012] for a bottom outlet or numerically in a 2D discrete simulation by Zhou et al. [2017] for a lateral outlet. This self similarity is observed whatever the angle inclination of the bottom and the outlet size. The uncertainty of the PIV technique increases when the outlet size D decreases for a given θ_i, and when the inclined angle θ_i increases for a given outlet size D (the minimal cross section $D \cos \theta_i$ decreases). That may explain the deviation of the velocity at the bottom of the outlet ($z/D \approx -0.5$) between the $D = 40$mm case and the $D = 50$mm case in Figure 3.10a, and also the large uncertainty of the velocity profiles for the $\theta_i = 60°$ case in Figure 3.10b.

To infer the degree of self similarity of the horizontal velocity profiles, we plot in Figure 3.11a the averaged value across its profile of the dimensionless horizontal velocity versus the bottom angle of inclination for all the data. We can observe that the experimental data are scattered (in
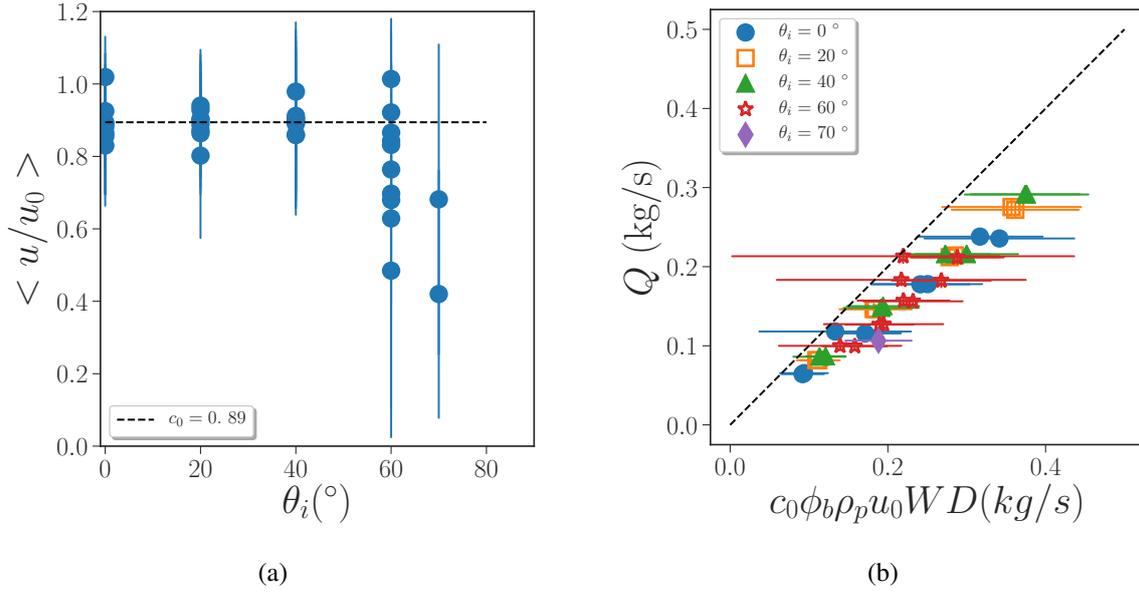
Figure 3.11: (a) Mean value of the normalized horizontal velocity profiles versus the bottom angle of inclination for all the experiments. The horizontal line represents the mean value $c_0 = 0.89$. (b) Experimental flow rate versus $c_0 \phi_b \rho_p u_0 W D$ for all the data. The dashed line represents equation 3.4

particular when θ_i increases) but are well represented by a constant value $c_0 = 0.89$. Thus the integral of the horizontal component of the velocity at the outlet can be well represented by the velocity at the centre of the outlet with $\int_{-D/2}^{D/2} u \, dz = c_0 u_0 D$. If we suppose that the volume fraction at the outlet is constant $\phi \approx \phi_b$, the flow rate reads:

$$Q = c_0 \rho_p \phi_b u_0 W D. \tag{3.4}$$

Figure 3.11b shows the comparison between the flow rate and equation 3.4 for all the data. The experimental data and equation 3.4 appear to be shifted, equation 3.4 over evaluating the flow rate by a factor 1.4. This suggests that the volume fraction cannot be simply evaluated using the bulk volume fraction ϕ_b.

c. Analysis of the particle volume fraction at the outlet

Using the recorded images, we process the volume fraction as can be seen in Figure 3.7b. We observe that the particle being mono-size they tend to crystallize far from the outlet. At the outlet, this order is disturbed due to the converging flow. As described in the literature (Janda et al. [2012], Benyamine et al. [2014], Zhou et al. [2017]), we observe that the particles tend to dilate at the outlet, lowering the volume fraction.

Figure 3.12 show the profiles of the volume fraction across the outlet normalized by its value at the centre of the outlet, ϕ_0, varying (a) the outlet size D for $\theta_i = 40°$ and (b) the angle of
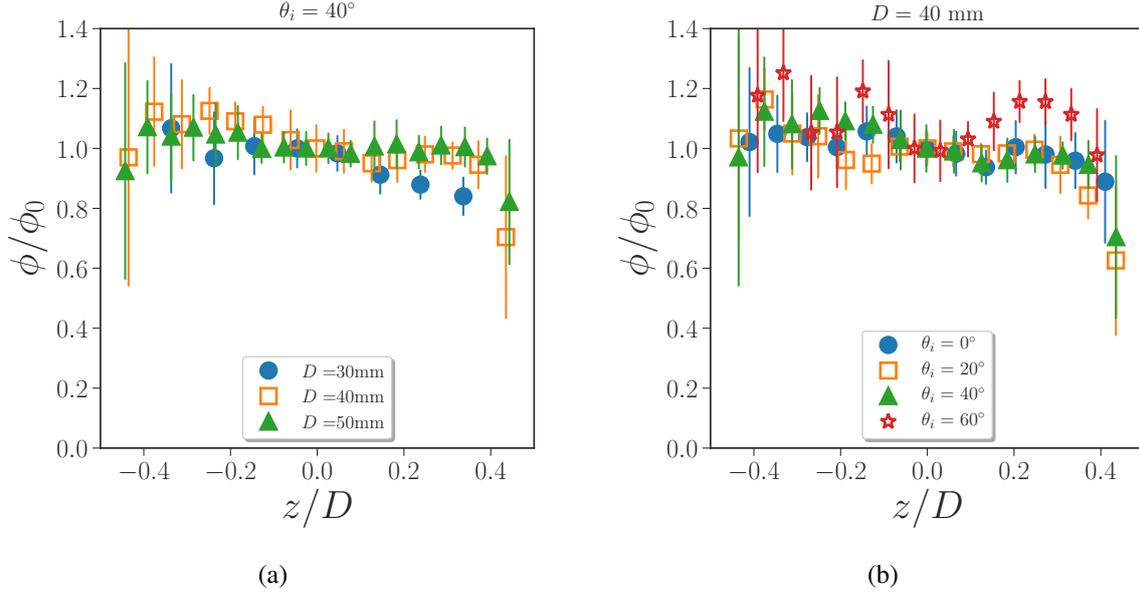
Figure 3.12: Volume fraction profiles at the outlet, normalized by the volume fraction at the center ϕ_0, versus the vertical position normalized by the outlet size z/D for (a) $\theta_i = 40°$ and several outlet sizes D and (b) $D = 40$ mm and several bottom inclinations θ_i.

inclination of the bottom θ_i for $D = 40$mm. We observe that the profiles are relatively flat, with a tiny decrease from the bottom to the top of the outlet. The profiles seem to be rather self-similar varying the outlet size or the bottom inclination.

To predict the flow rate from the images processing, we then first verify in Figure 3.13(a, b) that the quantity ϕu, corresponding to the volume of particle transported, is rather self-similar at the outlet varying the outlet size or the bottom inclination. Then by averaging the profiles we evaluate in Figure 3.13c $c_0 = \int_{-D/2}^{D/2} \phi u/(\phi_0 u_0)dz$ which is found to be rather constant with $c_0 = 0.89$. The volume fraction profile being quite flat, we recover the previous value. Finally in Figure 3.13d we obtain that the flow rate is reasonably given by

$$Q = c_0 \rho_p \phi_0 u_0 W D. \tag{3.5}$$

Using ϕ_0 instead of ϕ_b increases the accuracy of the model without eliminating the dispersion for large angles. The flow rate being controlled by the horizontal component of the velocity at the centre of the outlet u_0, and by the particle volume fraction at the outlet, let us now consider how these variables depend on the control parameters of the experiment.

We first focus on the volume fraction at the centre of the outlet ϕ_0 that we have plotted in Figure 3.14a, normalized by ϕ_b versus the outlet size D normalized by the particle diameter d_p for various bottom inclinations. We can see that the data are scattered but at a given bottom inclination ϕ_0 seems to increase with the number of particle in the aperture. However despite the scattering of the data they do not seem to superimpose when varying θ_i. Following Janda et al. [2012], Benyamine

58
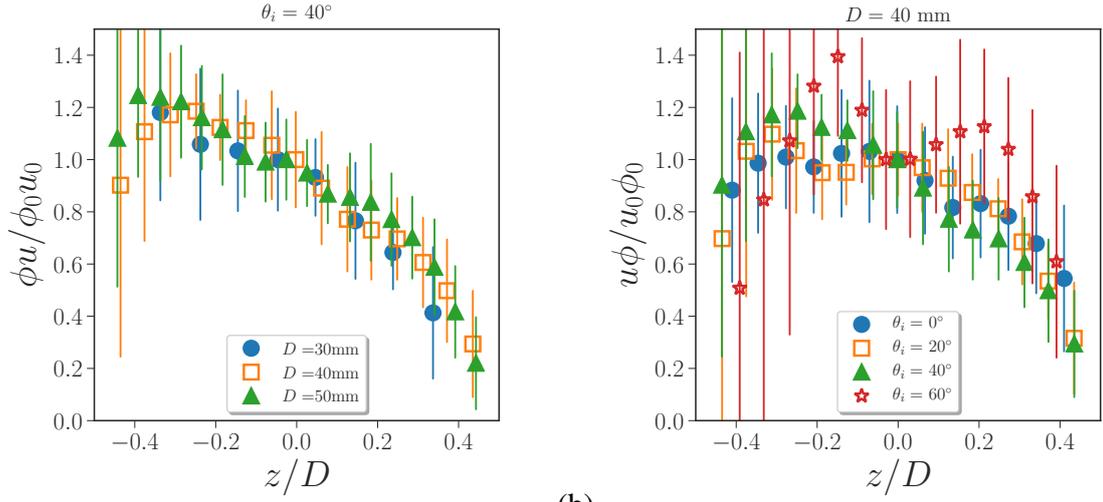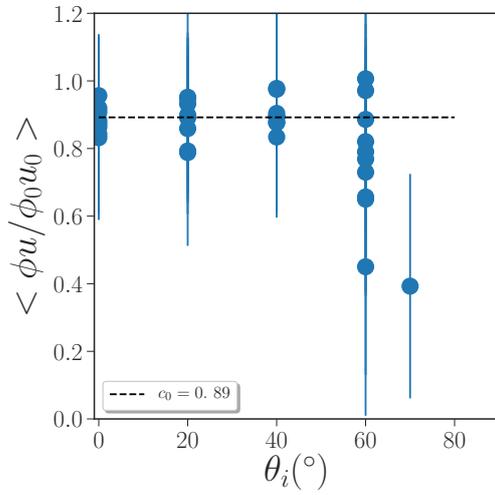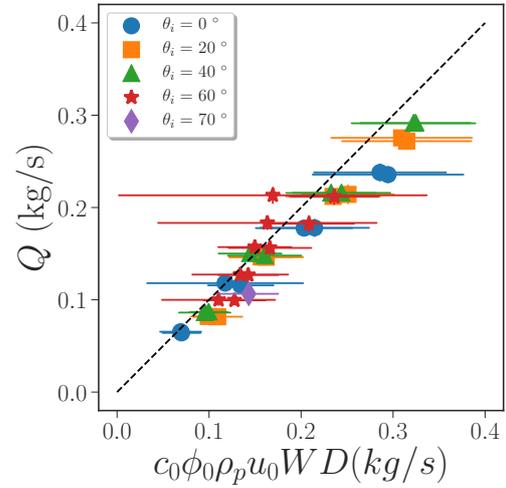
Figure 3.13: (a, b) Normalized profiles of ϕu the outlet, versus the normalized vertical position z/D for (a) $\theta_i = 40°$ and several outlet sizes D, (b) $D = 40$ mm and several bottom inclinations θ_i. (c) Mean value of the normalized profiles of ϕu versus the bottom angle of inclination for all the experiments. The horizontal line represents the mean value $c_0 = 0.89$. (d) Experimental flow rate versus $c_0 \phi_0 \rho_p u_0 W D$ for all the data. The dashed line represents equation 3.5.

et al. [2014], Zhou et al. [2017], we can expect that the dilation at the outlet is due to a geometrical constrain, the particle diameter not being negligible compare to the outlet size. In the case of a bottom outlet or a lateral outlet, they have shown that the volume fraction at the outlet depends mainly on the number of beads in the aperture D/d_p and is well described by $\phi_0 = \phi_b G(D/d_p)$ where $G(x) = \xi_\phi(1 - \alpha e^{-\beta x})$. However the bottom being inclined the smaller dimension in the silo is not the outlet D but the perpendicular to the bottom which joins the top of the outlet, whose dimension is $D \cos \theta_i$. In Figure 3.14b, we have plotted ϕ_0/ϕ_b versus $D \cos \theta_i/d_p$, we find that the data seem to be less scattered and can be reasonably adjusted by

$$\phi_0 = \phi_b \xi_\phi (1 - \alpha e^{-\beta D \cos \theta_i/d_p}) \tag{3.6}$$

59
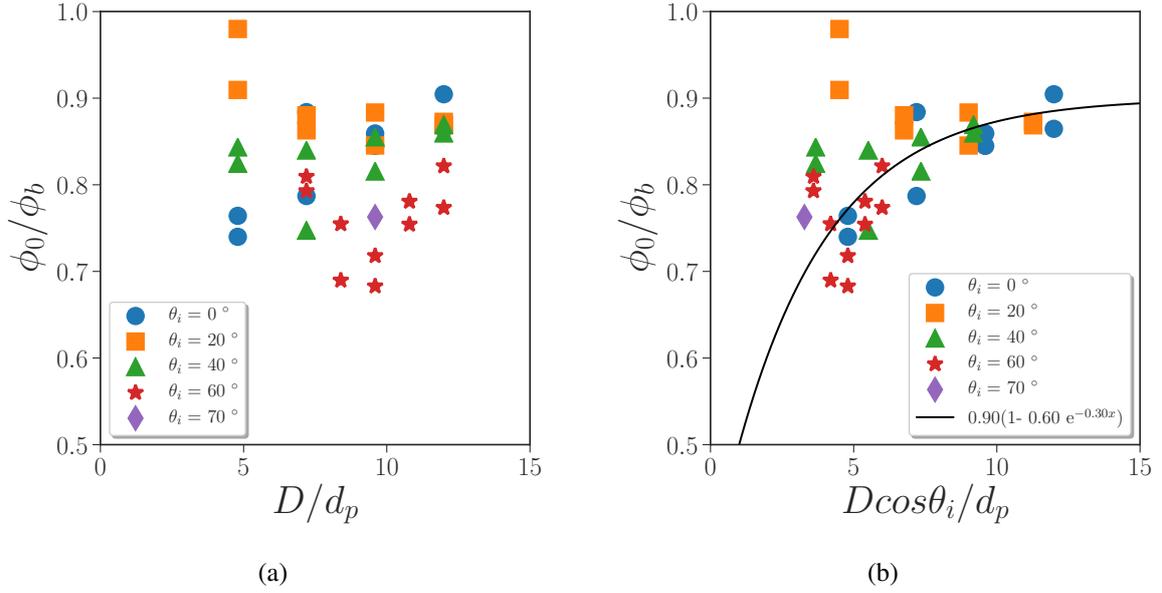
Figure 3.14: Volume fraction at the centre of the outlet ϕ_0 normalized by the bulk volume fraction ϕ_b versus the outlet size D normalized (a) by the particle diameter d_p and (b) by $d_p / \cos \theta_i$, for various bottom inclination. The black line represents equation 3.6.

with $\xi_\phi = 0.9$, $\alpha = 0.6$ and $\beta = 0.3$ in good agreement with the previous work of Zhou et al. [2017]. We can however notice that the variation of ϕ_0 / ϕ_b stays small in the range explored and is a second order effect on the variation of the flow rate with the inclination angle of the bottom.

We now focus on u_0, following Zhou [2016], we decompose it using the inclination of the granular flow and the velocity magnitude.

d.   Central inclination of the granular flow

Following Zhou et al. [2017], we introduce the flow inclination at the outlet by its central value, related to the ratio between the horizontal component of the velocity u_0 and the velocity magnitude U_0 both being evaluated at the center of the outlet ($z = 0$):

$$\cos \theta_0 = \frac{u_0}{U_0} \tag{3.7}$$

We can first focus on the role of the inclination of the bottom of the silo, θ_i, on the inclination of the flow at the central streamline, θ_0, as illustrated on Figure 3.15. In Figure 3.15a, $\cos \theta_0$ is plotted versus the outlet size D for various bottom inclinations, there is clearly a strong correlation. We observe that for a given bottom inclination the streamline inclination does not depend on D, meaning that θ_i totally determines θ_0. In Figure 3.15b we have plotted the mean value (corresponding to the dashed horizontal lines in Figure 3.15a) versus the cosine of the angle of the bottom inclination.

We observe that except for the horizontal bottom ($\theta_i = 0$) the inclination of the flow is strongly

(a)　　　　　　　　　　　　　　　　　　(b)
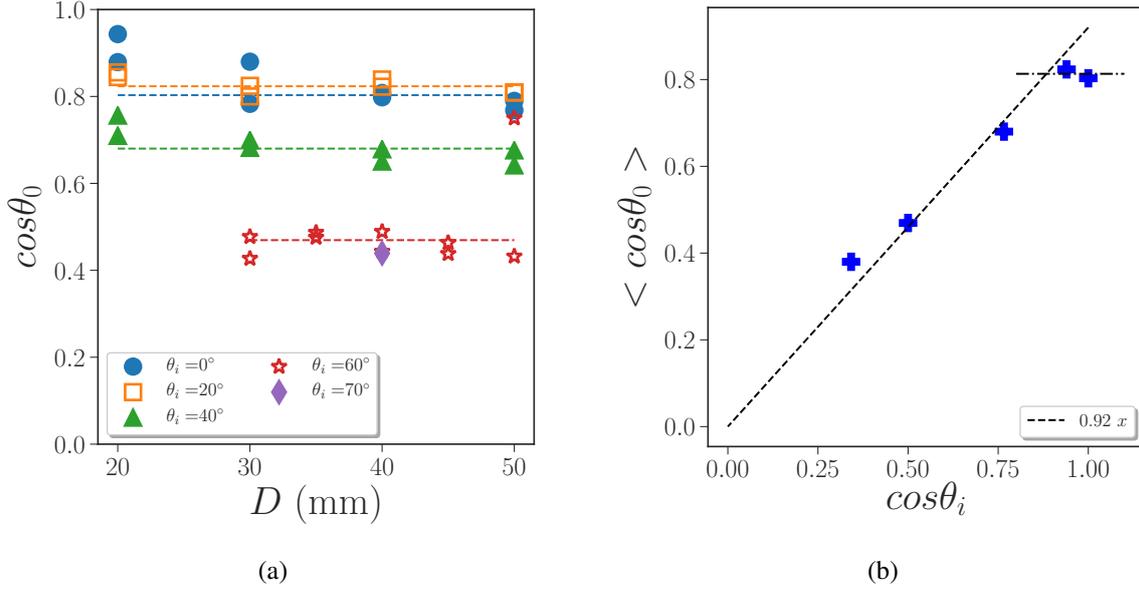
Figure 3.15: (a) Inclination of the central streamline at the outlet, $\cos\theta_0$ versus the outlet size D for various inclination of the bottom of the silo. The dashed lines represent the mean value plotted in (b) versus $\cos\theta_i$. The dashed black line represents equation 3.8 with $\zeta = 0.92$ and the dashed dotted line represent $\cos\theta_0^f = 0.81$.

correlated to the bottom inclination, the cosine of both angles being well adjusted by a linear function:

$$\cos\theta_0 = \zeta \cos\theta_i \qquad (3.8)$$

with $\zeta = 0.92$ (see the dashed line in the figure). To understand this correlation we have plotted in Figure 3.16 the normalized profiles of the angle of inclination of the streamlines at the outlet, for the same parameters than Figure 3.10. We observe that these profiles are self-similar, whatever the outlet size and the bottom inclination. The shape of the profiles can be idealized by a linear decrease from the bottom to the top of the outlet where the flow is expected to be mainly vertical. This linear trend starts from the imposed bottom inclination which explains the linear equation 3.8. For small bottom inclination, the central streamline seems to reach a constant inclination that we denote θ_0^f.

e.　Criterion for a threshold inclination leading to a stagnant zone

This regime of constant inclination may be due to the presence of an angle of avalanche due to the internal friction and generating a stagnant zone. While the bottom inclination stays below this angle, it will not influence the flow. If we suppose that the flow in unperturbed by the bottom while the central streamline angle generated by the bottom inclination is smaller than those by a
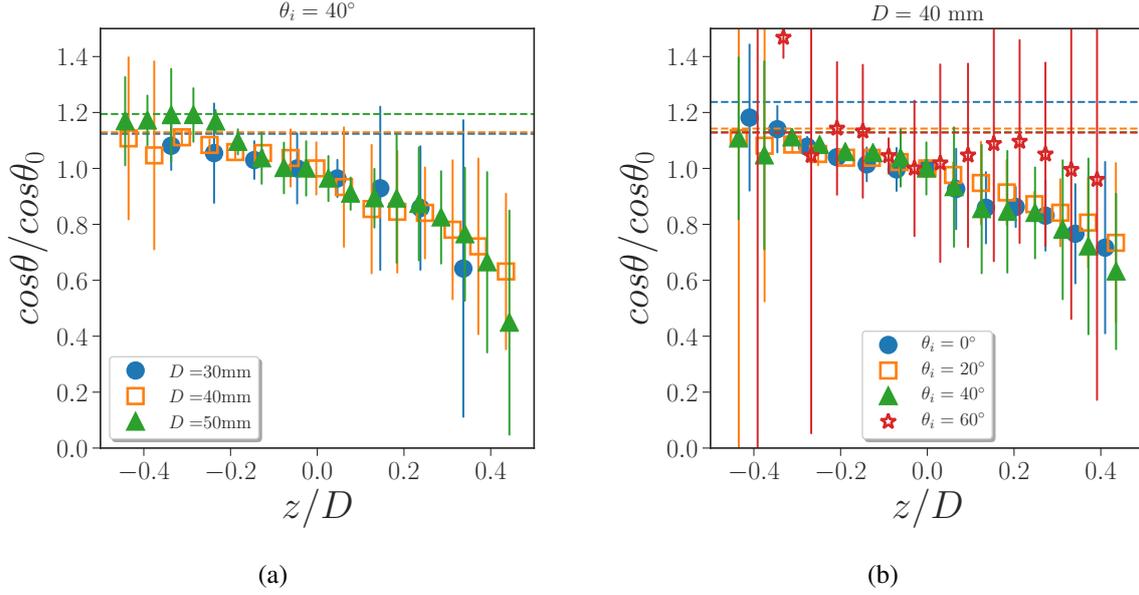
Figure 3.16: (a) profiles of the cosine of the angle of inclination at the outlet, normalized by the cosine of the angle of inclination of the central streamline of the outlet θ_0, versus the vertical position normalized by the outlet size z/D for (a) $\theta_i = 40°$, and several outlet size D and (b) $D = 40$ mm and several bottom inclination θ_i. The horizontal dashed line corresponds to the imposed angle of inclination $\cos \theta_i / \cos \theta_0$.

flat bottom, $\theta_0 < \theta_0^f$, we obtain a model for the streamline angle at the centre of the outlet:

$$\text{if} \quad \theta_i < \theta_c, \qquad \cos \theta_0 = \cos \theta_0^f \qquad \text{else} \qquad \cos \theta_0 = \zeta \cos \theta_i \qquad (3.9)$$

where we denoted $\theta_c \approx 28°$ the critical angle at which the transition occurs:

$$\theta_c = \arccos(\cos \theta_0^f / \zeta) \qquad (3.10)$$

This model suggests that when the bottom inclination increases above a threshold, the central streamline inclination will be controlled by the bottom inclination and not anymore by the internal friction. Thus the flow rate will tend to decrease with inclination with respect to the flat bottom case, the flow being less horizontal.

f. Velocity magnitude

We now turn to the magnitude of the velocity. Figure 3.17 shows the normalized profiles of the magnitude of the velocity for the same parameters than Figure 3.10. We observe that these profiles are also quite self-similar, whatever the outlet size or the bottom inclination.

In Figure 3.18a the normalized magnitude of the velocity of the central streamline is plotted versus the normalized outlet size for various bottom inclinations. As observed numerically by
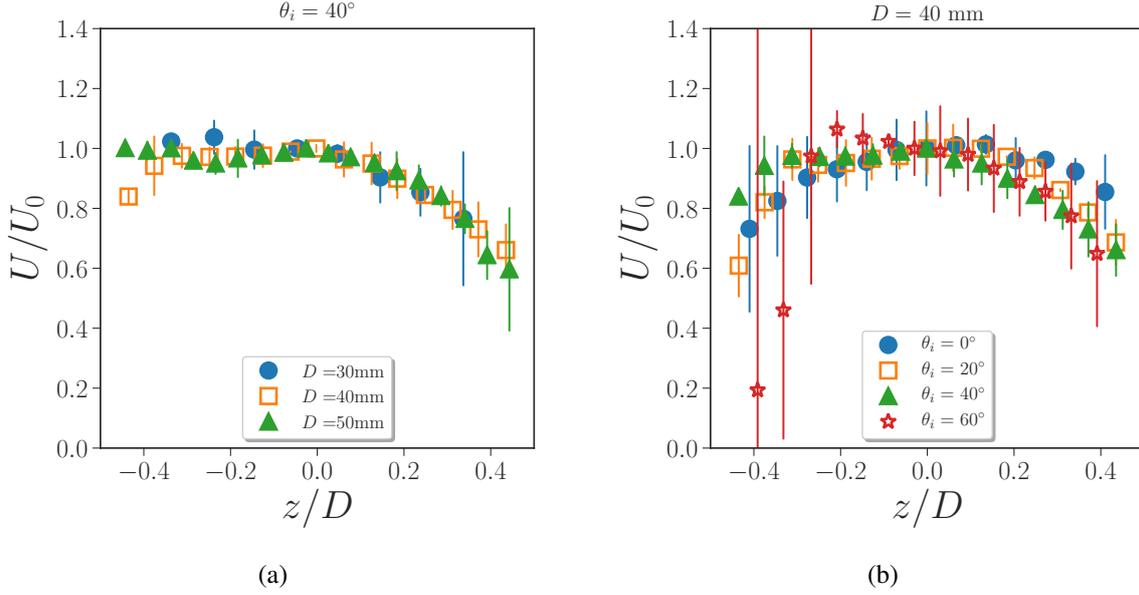
Figure 3.17: (a) Magnitude of the velocity profiles at the outlet, normalized by the magnitude of the velocity at the central outlet U_0, versus the vertical position normalized by the outlet size z/D for (a) $\theta_i = 40°$, and several outlet size D and (b) $D = 40$ mm and several bottom inclination θ_i.

Zhou et al. [2017] for a lateral orifice ($\theta_i = 0°$), the velocity magnitude is well adjusted by a square root variation with respect to the opening size given by:

$$U_0 = c_E^i \sqrt{gD} \tag{3.11}$$

However the fitting parameter c_E^i appears to depend on the bottom inclination in this new configuration and increasing with θ_i, in the range $[0.8, \ 1.2]$.

The scaling law in $\sqrt{D}$ suggests that velocity magnitude U_0 is controlled by a transfer from the potential energy to kinetic energy in the characteristic length of the outlet size. When the flow orientation is controlled by the bottom inclination, the flow rotation is constrained not only by internal friction but also by wall interaction and the inclination at the central streamline is given by equation 3.8. When reaching the dense granular zone, at a distance $s \approx D$, the potential energy then depends on the orientation of the streamline, $E_p \approx \rho_p g \sin \theta_0 s$. This potential energy is transfer to a kinetic energy at the outlet $E_k \approx \rho_p U_0^2$ thus giving :

$$U_0 = c_E \sqrt{gD \sin \theta_0}, \tag{3.12}$$

which predicts an increase of the velocity with the bottom inclination as seen in Figure 3.18a. In Figure 3.18b we have plotted the normalized velocity $U_0/\sqrt{gd_p}$ versus $\sqrt{gD \sin \theta_0}$ for all the data and we observe a good collapse. The data are well adjusted by equation 3.12 with $c_E = 1.27$. This effect tends to counter balance a little bit the effect of the inclination of the streamline on the flow
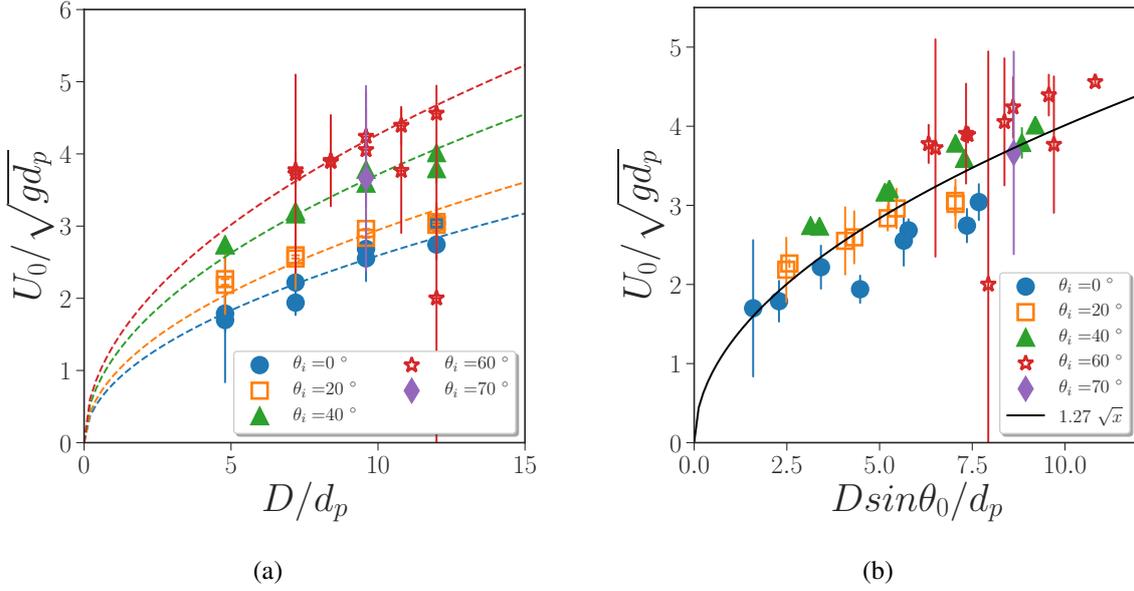
Figure 3.18: Magnitude of the velocity profiles at the centre of the outlet, U_0, normalized by $\sqrt{gd_p}$ versus the outlet size D normalized by (a) d_p and (b) $d_p/sin\theta_0$ for several outlet inclinations θ_i. The dashed and full lines represent square root fit with each adjustable coefficient obtained by the least squares method.

rate.

g. A simple model for the flow rate variation with respect to the inclination

From all the previous analysis, it is possible to deduce a model for the flow-rate dependence on the bottom inclination of the silo. Using equations 3.6, 3.8, 3.9, 3.10 and 3.12 we can write:

$$\text{if} \quad \theta_i < \theta_c \qquad \frac{Q}{\rho_p \phi_b G(\frac{D\cos\theta_i}{d_p})DW\sqrt{gD}} = c_D$$

$$\text{else if} \quad \theta_i > \theta_c \qquad \frac{Q}{\rho_p \phi_b G(\frac{D\cos\theta_i}{d_p})DW\sqrt{gD}} = c_\theta \cos\theta_i\sqrt{\sin\theta_i} \qquad (3.13)$$

with $G(x) = \xi_\phi(1 - \alpha e^{-\beta x})$, $\theta_c = \arccos\left(\cos\theta_0^f/\zeta\right)$, $c_\theta = c_0 c_E \zeta$ and $c_D = c_0 c_E \cos\theta_0^f \sqrt{\sin\theta_0^f}$. For the large bottom inclination and the large outlet size, equation 3.13 can be simplified to give $Q/(\rho_p\phi_b DW\sqrt{gD}) = c_\theta \cos\theta_i$.

In Figure 3.19 we compare the model given by equations 3.13 with (a) the mass flow rate normalized by $\rho_p\phi_b G(\frac{D\cos\theta_i}{d_p})DW\sqrt{gD}$ and (b) mass flow rate Q, both plotted versus the bottom angle of inclination. The agreement is fairly good, except for small angle of inclination where the model predicts a plateau below θ_c and not a slight increase with θ_i.

Even if this simple model does not capture finely this specific behavior, it is able to predict the main physical mechanism of the influence of the bottom inclination on the flow rate for a 2D
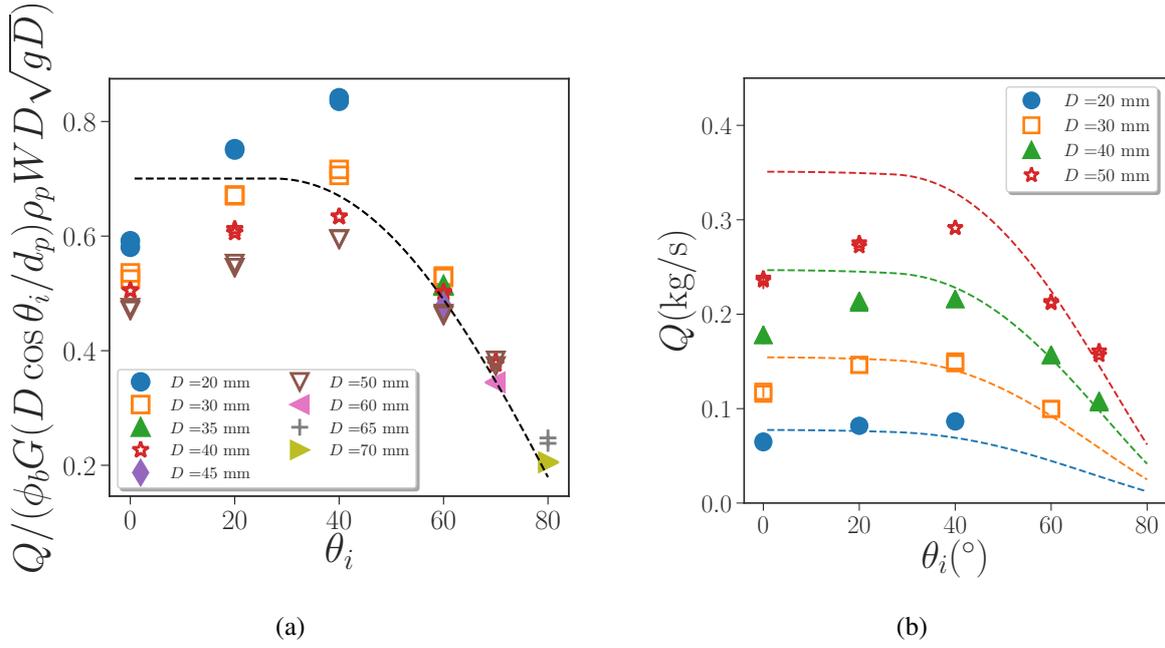
Figure 3.19: (a) Mass flow rate normalized by $\rho_p \phi_b G(\frac{D\cos\theta_i}{d_p})DW\sqrt{gD}$ and (b) Mass flow rate, versus the bottom angle of inclination. The dashed lines represent equations 3.13 with $\xi_\phi = 0.9$, $\alpha = 0.6$, $\beta = 0.3$, $\zeta = 0.92$, $c_E = 1.27$, $c_0 = 0.89$, $\theta_c = 28°$, $\cos\theta_0^f = 0.81$.

mono-layer flow.

To be able to study the role of the friction between the grains and the bottom wall, we have carried in appendix A a discrete simulation of a 2D flow. The DEM simulation reproduces most of the behavior observed except for the variation of U_0 with θ_i. This kind of simulation may be a really interesting tool to see the effect of the grain and wall parameters (μ_p and μ_w) on the flow rate and to obtain more informations than in the experiment (stress field).

In the next section we will study how the finite size of the silo can change the observed behaviors.

3.2.2 3D flow

We will now focus on the experiments performed with one of the smallest particles having the velocity fields resolved, $d_p = 538\mu$m and follow the same approach than for the 2D mono-layer flow.

a. Mass flow rate

Following the work carried out by Zhou et al. [2017] presented in chapter 2, for a rectangular silo with a flat bottom and with presence of a lateral outlet, the flow rate obeys:

$$\frac{Q}{\rho_p \phi_b \sqrt{gW^5}} = c_D \frac{(D/W)^{3/2}}{\sqrt{1 + \gamma D/W}} \tag{3.14}$$

Figure 3.20a shows the particle mass flow rate as a function of the inclination angle θ_i for a given aperture size and various silo thicknesses. In these 3D flow we observe a large plateau where the mass flow rate does not seem to depend on the inclination of the bottom. However, we can observe a small increase in this plateau zone if we do not consider the limit $\theta_i = 0$, specially for bigger particles (data not shown). Then above a critical angle, which seems to depends on the silo thickness, the mass flow rate starts to decrease. The critical angle at which the flow rate decrease initiates seems much larger than for the 2D case. Indeed, for a narrow silo of thickness $W = 5$mm the inclination of the bottom does not influence the flow for angle as large as $60°$.
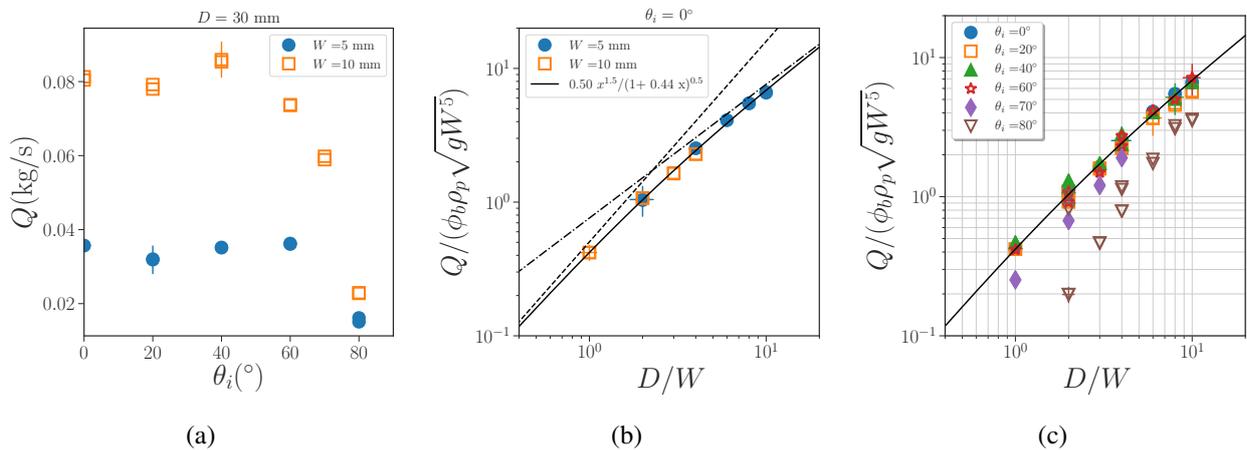
Figure 3.20: Experiments with $d_p = 538\mu$m: (a) Mass flow rate of particles as a function of the angle of inclination θ_i for $D = 30$mm. (b,c) Mass flow rate made dimensionless by $\phi_b \rho_p \sqrt{gW^5}$ versus the dimensionless outlet size D/W (b) for an horizontal bottom $\theta_i = 0$ and (c) for all the bottom inclinations θ_i explored. The solid line represents equation 3.14 with $c_D = 0.5$ and $\gamma = 0.44$. The dash line represents the Hagen-Beverloo equation 3.3 with $c_D = 0.5$ and the dotted-dashed line represents the linear asymptotic regime of equation 3.14 for $D/W >> 1$.

For the low angle, the value of the plateau is given by the value at $\theta_i = 0$, which corresponds

to the study of Zhou et al. [2017]. Following this work, we have plotted in Figure 3.20b the dimensionless mass flow rate $Q/\rho_p\phi_b\sqrt{gW^5}$ as a function of the aspect ratio $\mathcal{A} = D/W$ for the zero inclination bottom silos ($\theta_i = 0°$). As predicted by Zhou et al. [2017], the flow rate can be adjusted by equation 3.14 (black line) with respectively $c_D = 0.5$ and $\gamma = 0.44$, in good agreement with the values reported in Zhou et al. [2017].

We thus recover that the granular flow can be separated into two regimes. For a small aperture aspect ratio $D/W \ll 1$, on the left part of Figure 3.20b the results can be adjusted by the Hagen-Beverloo law 3.3 (dashed line) corresponding to a flow controlled by the internal friction. The second regime of granular flow is observed for a large aperture aspect ratio $D/W \gg 1$, on the right part of Figure 3.20b where the results can be adjusted by a linear law, corresponding to a flow controlled by the wall friction. The transition between these two regimes occurs around $D/W \approx 2$. The experiments are mainly done in the transition zone between the two regimes.

The effect of the bottom inclination can then be observed using this representation in Figure 3.20c where the dimensionless flow rate $Q/(\phi_b\rho_p\sqrt{gW^5})$ is plotted versus the aperture aspect ratio D/W for all the data. We observe that for a large range of inclination angles the data are super-imposed. Then increasing θ_i, we observe a deviation which appears first for the smaller aperture aspect ratio. In the following part, we will observe the velocities fields obtained experimentally.

b. Velocities fields
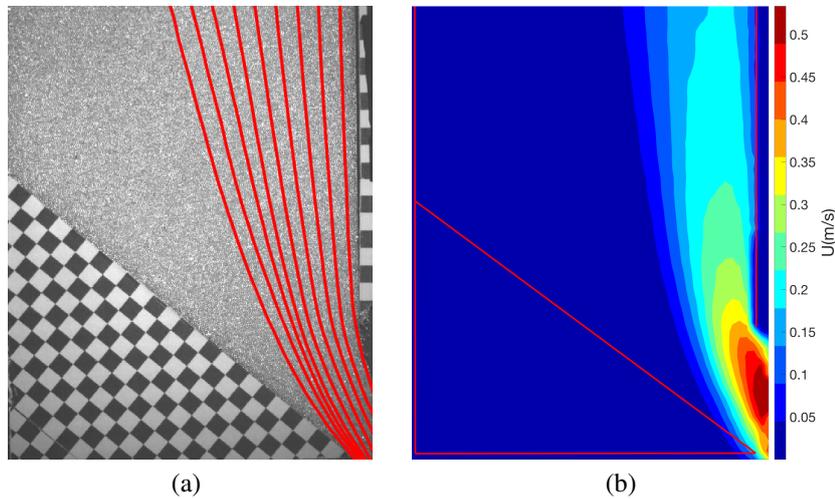
Figure 3.21: (a) Streamlines and (b) velocity magnitude field for $W = 5mm$, $d_p = 538mm$, $D = 40mm$ and $\theta = 40°$.

The 2D velocity fields of the granular flow at the front wall of the silo is shown in Figure 3.21 for $\theta = 40°$ for the thinner experimental silo with $W = 5mm$, $D = 40mm$ and $d_p = 538\mu m$. In Figure 3.21a we have drawn nine streamlines (calculated for velocities higher than 0.01 m/s). We can see that the flow is quasi-vertical far from the outlet and then rotates at the vicinity of the

outlet. Note that under the conditions of this experiment, the inclination of the streamlines at the outlet appears to be higher than the inclination of the bottom of the silo. We can also observe a large stagnant zone located on the left hand side part of the silo, whereas for the mono-layer case, the stagnant zone disappears for the same angle (see Figure 3.9b).

The magnitude of the velocity in the front plane is illustrated by a color field in Figure 3.21b for the same data. It clearly illustrates the flow behavior along the silo, with again a stagnant zone on the left hand side part (although we imposed a significant angle of inclination), and a zone of higher velocities at the very near region of the outlet related to the flow cross section reduction where the particle acceleration is localized. This $\theta_i = 40°$ case is more qualitatively similar to the $\theta_i = 0°$ case of the mono-layer flow (see Figure 3.9d).

The persistency of a dead zone even in the $\theta_i = 40°$ case explains that the flow rate is only affected by the bottom inclination for large angle with respect to the monolayer case (see the plateau in Figure 3.20a). Small inclination of the bottom only suppresses particles within the dead zone, that would have no interaction with the flow. It therefore does not impact the flow-rate. For larger bottom inclination, the flowing zone is constrained by the silo geometry which affects the flow orientation and decreases the discharge flow-rate. To test this hypothesis, we will focus on the flow velocity at the centre of the outlet but first let us verify that the image processing is successful in predicting the flow rate. The particles are sufficiently small compared to the outlet dimensions ($D \cos \theta_i / d_p > 10$) to suppose the volume fraction at the outlet is given by $\phi_0 \approx \phi_b$ (see Figure 3.14b), then if the profile of the horizontal velocity is self-similar, the flow rate should read:

$$Q = c_0 \rho_p \phi_b u_0 W D. \tag{3.15}$$

(a) (b) (c)
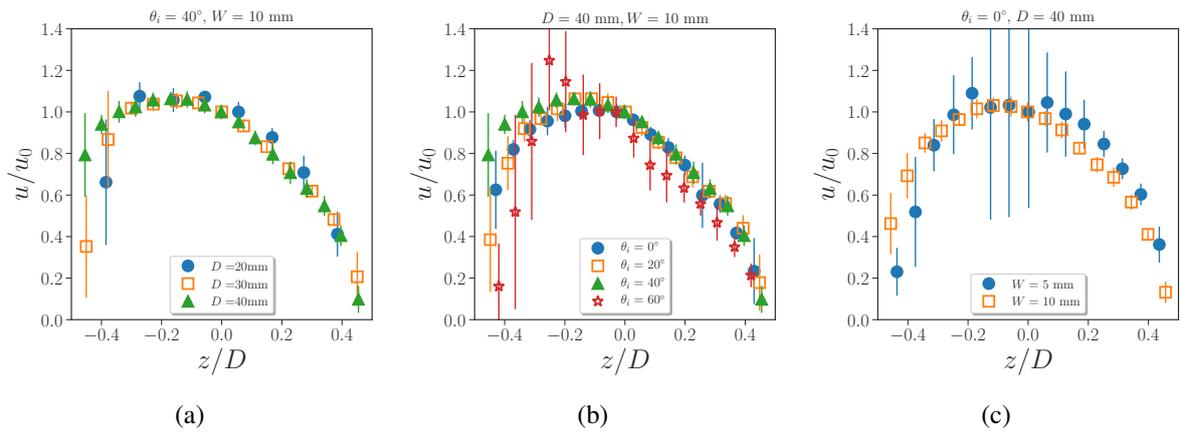
Figure 3.22: (a) Horizontal velocity profiles at the outlet, normalized by the velocity at the centre u_0, versus the vertical position normalized by the outlet size z/D for the experiments with $d_p = 538 \ \mu$m with (a) $\theta_i = 40°$, $W = 10$mm and several outlet sizes D, (b) $D = 40$ mm, $W = 10$mm and several bottom inclinations θ_i, (c) $\theta_i = 0°$, $D = 40$mm and several silo thicknesses W. The vertical position, z, is oriented upward and its origin is taken at the centre of the outlet.

Figure 3.22 shows the profiles of the horizontal velocity component at the outlet, normalized by its value at the centre of the outlet, u_0 for $d_p = 538$ μm, varying (a) the outlet size D, (b) the angle of inclination of the bottom θ_i and (c) the thickness of the silo W, for each graph the other parameters being kept constant. From these graphs, we can conclude that these profiles are indeed rather self-similar when varying all the experimental parameters. We can also observe that the horizontal velocity profile exhibits an asymmetry between the top and the bottom of the outlet but slightly smaller than in the mono-layer case (see Figure 3.10).

Figure 3.23a shows the averaged value across its profile of the dimensionless horizontal velocity versus the bottom angle of inclination for all the data. We can observe that the experimental data are scattered (in particular when θ_i increase) but are well centered around a constant mean value $c_0 = 0.79$. Finally Figure 3.23b shows the comparison between the experimental flow rate obtained from the balance measurement and equation 3.15 obtained from the image processing. We can see that the agreement is fairly good, with a small discrepancy in the experiments for the larger silo ($W = 10$mm, opened symbols), which may be due to 3D effects (inducing a velocity variation across the thickness of the silo). This effects would tend to reduce the velocity at the front wall leading to equation 3.15 slightly underestimating the flow rate.
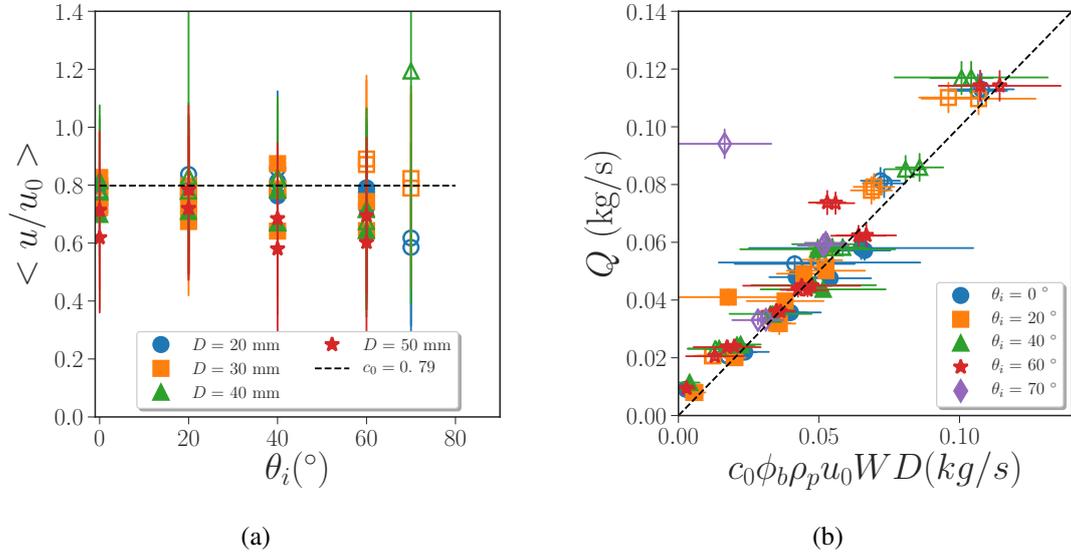
Figure 3.23: Experimental results for $d_p = 538$ μm, $W = 5$mm (closed symbols), $W = 10$mm (opened symbols) and various outlet sizes: (a) Mean value of the normalized horizontal velocity profiles versus the bottom angle of inclination. The horizontal line represents the mean value $c_0 = 0.79$. (b) Flow rate versus $c_0 \phi_b \rho_p u_0 W D$. The dashed line represents the equation $y = x$.

We can now turn to the study of the flow properties at the centre of the outlet and following the previous part we will focus on the magnitude of the velocity U_0 and its inclination θ_0 with $\theta_0 = \arccos(u_0/U_0)$.

c. Flow properties at the centre of the outlet: towards a simple model

The variation of the inclination of the central streamline with the bottom inclination is shown in Figure 3.24a for $d_p = 538$ μm, $D = 30$mm and for the two silo thicknesses studied. We recover that for large bottom inclinations θ_i (small $cos\theta_i$) the inclination of the flow is strongly correlated to the bottom inclination, following:

$$\cos\theta_0 = \zeta \cos\theta_i \qquad (3.16)$$

with $\zeta = 0.9$, this value being very similar to the one deduced for the mono-layer analysis. Looking at the normalized profiles of the angle of inclination of the streamlines at the outlet, plotted in Figure 3.25 for the same parameters than Figure 3.22, we observe that these profiles are self-similar, whatever the outlet size, the bottom inclination or the silo thickness. Similarly to the mono-layer flow, the shape of the profiles can be mainly represented by a linear decrease from the bottom of the outlet to the top of the outlet where the flow is mainly vertical. For large bottom inclination the linear trend tends to start from the imposed bottom inclination which explains the linear equation 3.16. For low bottom inclination, the linear trend tends to start from an higher inclination than the imposed bottom inclination. In these cases the flow is not perturbed by the bottom and its inclination is the same than for a flat bottom and depends on D/W as can be seen in Figure 3.24a where $\cos\theta_0$ tends to a plateau which depends on the silo thickness W.

(a) (b)
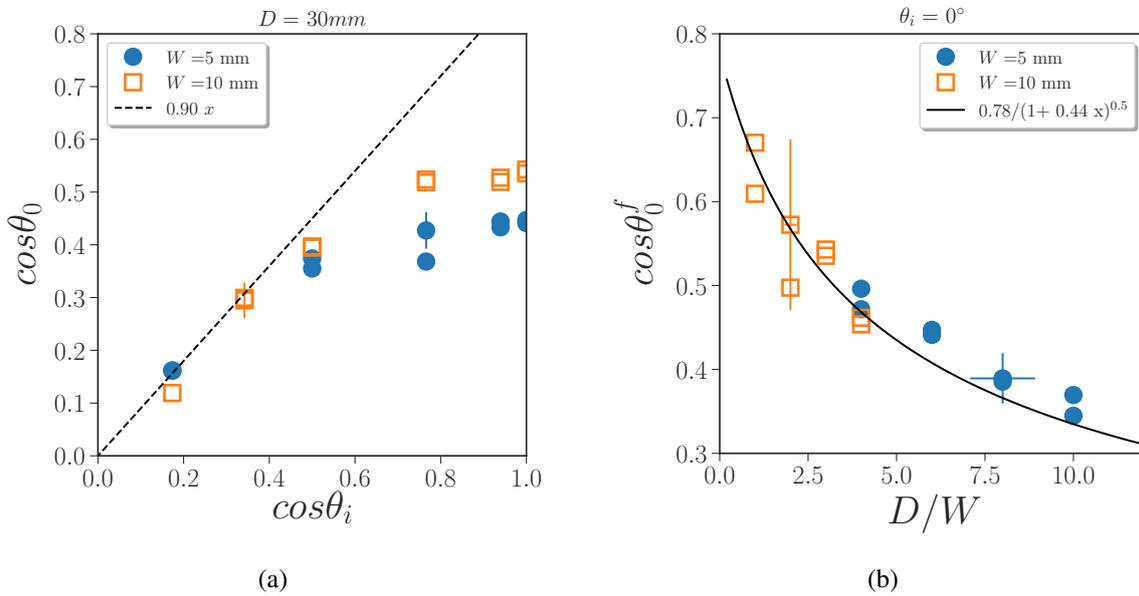
Figure 3.24: Experiments with $d_p = 538\mu$m: (a) Inclination of the central streamline at the outlet, $\cos\theta_0$, versus the inclination of the bottom of the silo, $\cos\theta_i$ for $D = 30$mm. The dashed line represents equation 3.16 with $\zeta = 0.9$. (b) Inclination of the central streamline at the outlet, $\cos\theta_0$, for an horizontal bottom, $\theta_i = 0°$, versus the aspect ratio of the aperture D/W. The full line represents equation 3.17 with $c_{\theta_0} = 0.78$ and $\gamma = 0.44$.
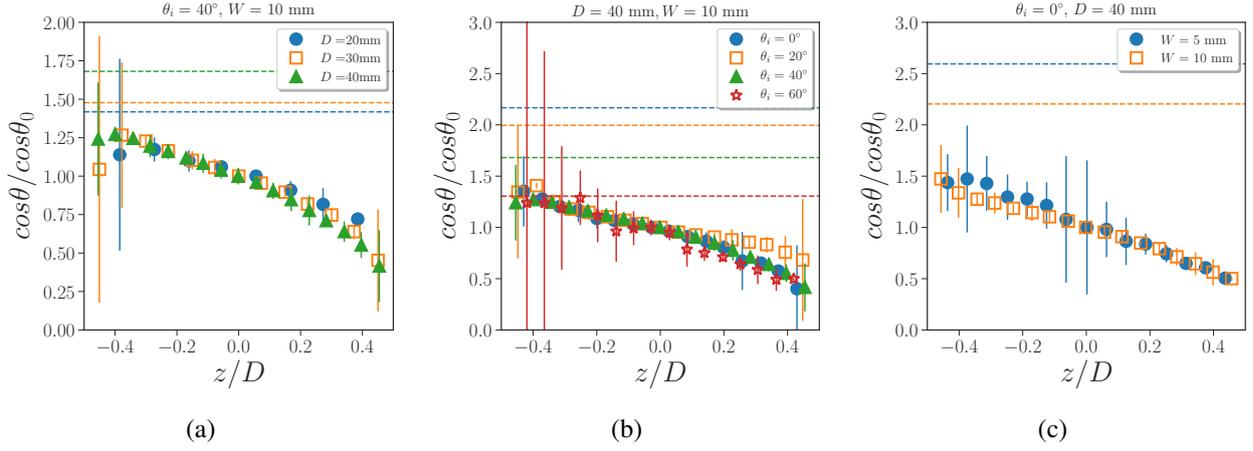
Figure 3.25: (a) profiles of the cosine of the angle of inclination at the outlet, normalized by the cosine of the angle of inclination of the central streamline of the outlet θ_0, versus the vertical position normalized by the outlet size z/D for $d_p = 538$ μm with (a) $\theta_i = 40°$, $W = 10$mm and several outlet sizes D, (b) $D = 40$ mm, $W = 10$mm and several bottom inclinations θ_i, (c) $\theta_i = 0°$, $D = 40$mm and several silo thicknesses W. The horizontal dashed lines correspond to the imposed angle of inclination $\cos\theta_i / \cos\theta_0$.

We thus will denote θ_0^f the angle of inclination of the central streamline at the outlet when the flow is not perturbed by the inclined bottom. We measure its value using a flat bottom with a lateral aperture as shown in Figure 3.24b versus the outlet aspect ratio D/W. As predicted by Zhou et al. [2017] we observe that the inclination clearly scales with D/W and is well adjusted by equation 3.17:

$$\cos\theta_0^f = \frac{c_{\theta_0}}{\sqrt{1 + \gamma D/W}}. \tag{3.17}$$

with $c_{\theta_0} = 0.78$ and $\gamma = 0.44$ where c_{θ_0} was obtained by the least squares method keeping the same γ than in the scaling of the flow-rate observed in Figure 3.20b. This measurement confirms experimentally that the frictions (internal and on the wall) control the inclination of the streamlines and the presence of a stagnant zone for an horizontal bottom.

If we suppose that the flow is unperturbed by the bottom while the streamline angle generated by the bottom inclination is smaller than those by a flat bottom, $\theta_0 < \theta_0^f$ we can generalize the model obtained previously for 2D flow giving the streamline angle at the centre of the outlet:

$$\text{if} \quad \theta_i < \theta_c, \quad \cos\theta_0 = \frac{c_{\theta_0}}{\sqrt{1 + \gamma\frac{D}{W}}} \quad \text{else} \quad \cos\theta_0 = \zeta\cos\theta_i \tag{3.18}$$

where we denoted θ_c the critical angle at which the transition occurs:

$$\theta_c = \arccos\left(\frac{c_{\theta_0}}{\zeta\sqrt{1 + \gamma D/W}}\right) \tag{3.19}$$

In Figure 3.26 we compare equation 3.18 (dashed line and black line) with the experimental
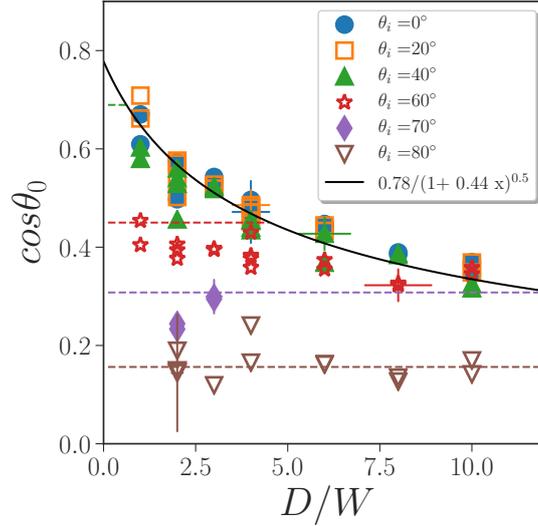
Figure 3.26: Inclination of the central streamline at the outlet, $\cos \theta_0$, for all the bottom inclinations, versus the aspect ratio of the aperture D/W for the experiments with $d_p = 538 \, \mu$m. The full and dashed lines represent equation 3.18 with $c_{\theta_0} = 0.78$, $\gamma = 0.44$ and $\zeta = 0.9$.

results. The agreement is fairly good even if this simple model does not describe finely the transition between the two regimes (see for example the data for $\theta_i = 60°$). This model shows that the transition between a flow controlled by the bottom inclination and a free flow from a lateral aperture strongly depends on D and W on such confined silo. When the central streamline inclination is controlled by the bottom inclination, the flow rate tends to decrease, the flow being less horizontal.

We now turn to the magnitude of the velocity. Figure 3.27 shows the normalized profiles of the magnitude of the velocity for the same parameters than in Figure 3.22. We observe again that those profiles are quite self-similar, whatever the outlet size, the bottom inclination or the silo thickness and are nearly symmetrical. In Figure 3.28 we study how the magnitude of the velocity of the central streamline on the outlet depends on various parameters. Figure 3.28a corresponds to the horizontal bottom for various silo thicknesses W. As observed numerically by Zhou et al. [2017], the velocity magnitude does not seem to depend on the silo thickness and is well adjusted by a square root variation with respect to the opening size given by equation 3.11, $U_0 = c_E \sqrt{gD}$, with $c_E = 0.78$. We observe the same behavior for the case where the inclination of the central streamline is controlled by the bottom inclination as shown in Figures 3.28b with a coefficient $c_E = 0.85$ on the same order of magnitude. Finally Figure 3.28c corresponds to all the data varying bottom inclination. The data are a bit scattered, but as observed numerically by Zhou et al. [2017], the velocity magnitude seems not to depend on the silo thickness and is well adjusted by a square root variation with respect to the opening size given by equation 3.11 with $c_E = 0.84$.

This scaling is not the same than observed in the mono-layer case (equation 3.12). However due to the silo confinement, the central streamline is already quite inclined even for a flat bottom,
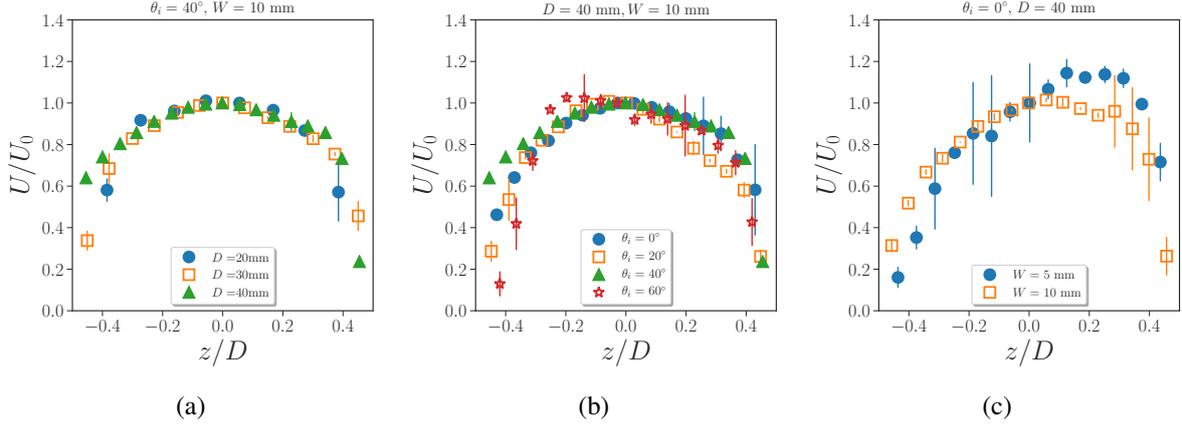
Figure 3.27: Magnitude of the velocity profiles at the outlet, normalized by the magnitude of the velocity at the centre U_0, versus the vertical position normalized by the outlet size z/D for $d_p = 538~\mu m$ and (a) $\theta_i = 40°$, $W = 10$mm and several outlet sizes D, (b) $D = 40$ mm, $W = 10$mm and several bottom inclinations θ_i, (c) $\theta_i = 0°$, $D = 40$mm and several silo thicknesses W.

and the measurement are relatively scattered. If we plot the data versus $gD\sin\theta_0/d_p$ the collapse of the data is comparable and the agreement with a square root law is reasonable in both cases (data not shown). This experiment does not allow to conclude on this point, but the similarity of the scaling for the flat bottom between the flow rate (equation 3.15) and the cosine of the angle of inclination of the central streamline (equation 3.17), suggesting that $U_0 \propto Q/\cos\theta_0^f$ should not depend on W thus on θ_0^f. This may be due to the fact that the stagnant zone boundary has a curvature and does not reduce to a constant inclination angle line (see Figure 3.21). Therefore when reaching the dense granular zone, at a distance $s \approx D$, the flow is nearly vertical, leading to a potential energy $E_p \approx \rho_p g s$, which tends to equilibrate the kinetic energy at the outlet $E_k \approx \rho_p U_0^2$ thus giving equation 3.11.

We can finally write the model for the flow-rate dependence on the geometry of the silo using equations, 3.7, 3.11 and 3.15 to 3.19:

$$\text{if} \quad \theta_i < \theta_c: \qquad \frac{Q}{\rho_p\phi_b DW\sqrt{gD}} = \frac{c_D}{\sqrt{1+\gamma D/W}} \tag{3.20}$$

$$\text{else if} \quad \theta_i > \theta_c: \qquad \frac{Q}{\rho_p\phi_b DW\sqrt{gD}} = \xi_\theta c_D \cos\theta_i \tag{3.21}$$

with $c_D = c_0 c_E c_{\theta_0}$, $\xi_\theta = \zeta/c_{\theta_0}$ and $\theta_c = \arccos(1/\xi_\theta\sqrt{1+\gamma D/W})$. The second case is similar to the asymptotic case of the 2D flow for large bottom inclination (equation 3.13). We can first compare the coefficient $c_D = 0.5$ adjusted on the flow rate for the horizontal bottom (Figure 3.20b) and the value of $c_0 c_E c_{\theta_0} = 0.52$ obtained from the velocity measurement which shows a good agreement.

73
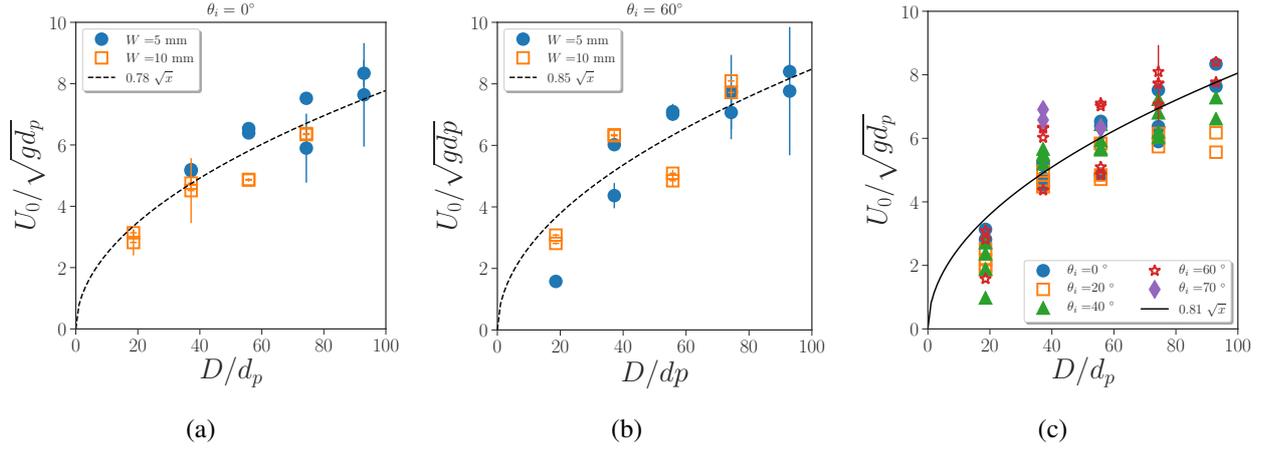
Figure 3.28: Magnitude of the velocity profiles at the centre of the outlet, U_0, normalized by $\sqrt{gd_p}$ versus the normalized outlet size D/d_p for $d_p = 538$ μm and (a) $\theta_i = 0°$, and several silo thicknesses W, (b) $\theta_i = 60°$, and several silo thicknesses W, (c) for all the data. The dashed and solid lines represents square root fit with each adjustable coefficients obtained by the least squares method.
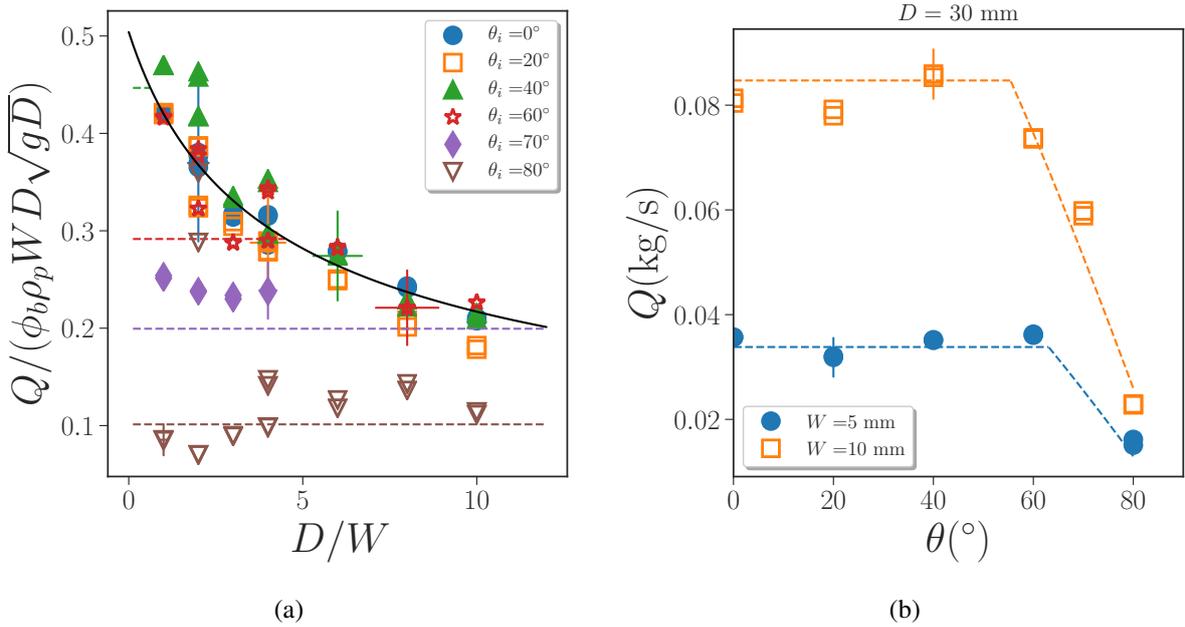
Figure 3.29: Experiments with $d_p = 538$ μm: (a) Mass flow rate normalized by $\rho_p \phi_b DW \sqrt{gD}$ for all the bottom inclination, versus the normalized aperture size D/W. The full line represents equation 3.20 and the dashed lines represent equation 3.21 with $c_D = 0.5$, $\gamma = 0.44$, $c_{\theta_0} = 0.78$, $c_E = 0.84$ and $\zeta = 0.9$. (b) Mass flow rate versus the bottom angle of inclination for $D = 30$mm. The dashed lines represent equation 3.20 and 3.21.

In Figure 3.29 we compare the model given by equations 3.20 and 3.21 with the mass flow rate normalized by $\rho_p \phi_b DW \sqrt{gD}$ plotted versus the normalized aperture D/W. The agreement is fairly good for large bottom inclination ($\theta_i > 60°$) or small bottom inclination ($\theta_i \leq 40°$)

but the model fails to describe the experiments close to the transition between the two regimes. In particular it is interesting to note that for $\theta_i = 60°$, the flow rate stays very closed to the unperturbed flow rate whereas the inclination of the central streamline is already perturbed (see the red stars in Figures 3.29a and 3.26). Even if this simple model does not capture finely this particular behavior, it succeeds to predict the flow rate in the two asymptotic regimes where the flow is controlled either by the silo confinement through the parietal friction or by the inclined bottom. In the next section we will compare this model with the other particles studied.

d.   Comparisons and discussion

In table 3.3 we have summed up the fitting parameters deduced from the balance measurement and image processing for all the particles large enough to perform accurate particle image velocimetry ($d_p \geqslant 375\mu m$).

d_p(μm)	c_D	γ	c_{θ_0}	c_E	ζ	c_0	$c_0 c_E c_{\theta_0}$	ξ_θ
4170 (2D)	0.5	-	0.63	1.27	0.92	0.89	0.71	1.46
1347	0.41	0.28	0.81	0.94	0.92	0.85	0.65	1.14
1129	0.45	0.44	0.86	0.92	0.92	0.81	0.64	1.1
762	0.42	0.28	0.69	0.95	0.92	0.81	0.53	1.3
538	0.5	0.44	0.78	0.84	0.9	0.79	0.52	1.15
375	0.52	0.53	0.81	0.84	0.85	0.83	0.56	1.05

Table 3.3: Experimentally measured fitting parameters.

For particle larger than 1000μm we obtain that $c_0 c_E c_{\theta_0}$ slightly over-evaluate the value of c_D due to a small dilatation of the particles at the outlet. To evaluate the evolution of the flow rate with the bottom inclination, 3 parameters are necessary c_D, γ and ξ_θ. We can deduce the two first using experiments with a horizontal bottom. From table 3.3 we evaluate $\xi_\theta \approx 1.1$ to be rather constant.

In Figure 3.30 we have plotted the flow rate for the smallest particles $d_p = 190\mu$m and compare it with the analytical model given by equations 3.20 and 3.21. We recover a good agreement for the asymptotic regimes (small and large angle) and a discrepancy at the transition for $\theta_i = 60°$ similarly to the $d_p = 538\mu m$ case.
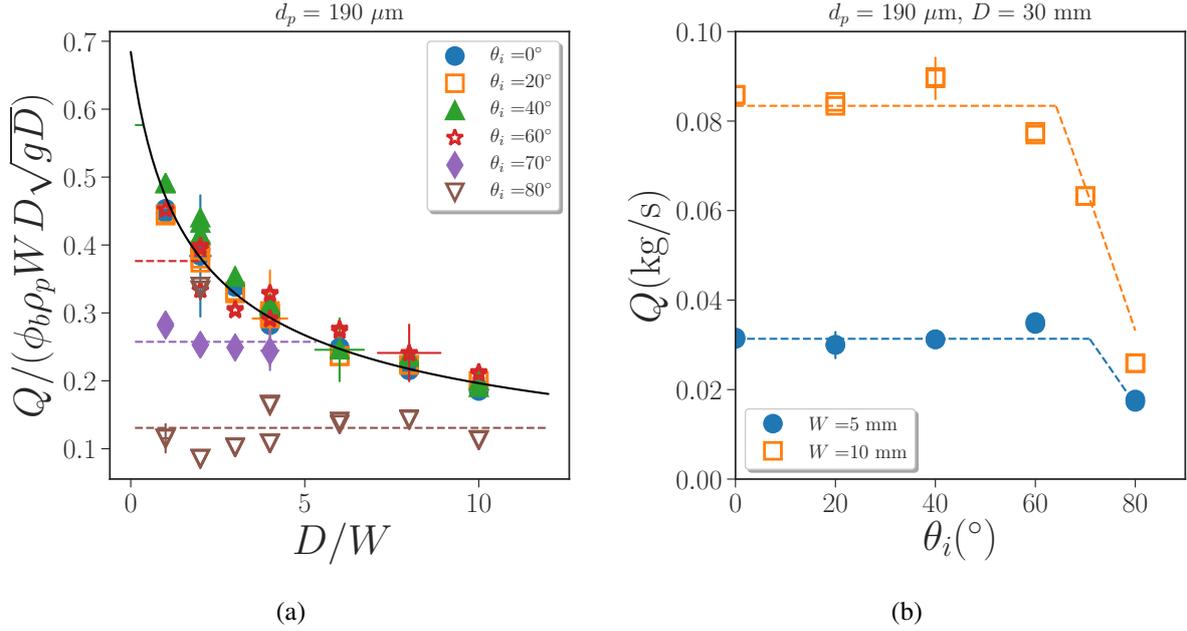
Figure 3.30: Experiments with d_p = 190 μm: (a) Mass flow rate normalized by $\rho_p \phi_b D W \sqrt{gD}$ for all the bottom inclination, versus the normalized aperture size D/W. The full line represents equation 3.20 and the dashed lines represent equation 3.21 with c_D = 0.68, γ = 1.11, ξ_θ = 1.1. (b) Mass flow rate versus the bottom angle of inclination for D = 30mm. The dashed lines represent equation 3.20 and 3.21.

3.2.3 Conclusion

We have investigated experimentally two types of discharge flow out of a silo with a inclined bottom: the mono-layer discharge flow and the 3D discharge flow. Using Particle Image Velocimetry, we identified two flow regimes varying the bottom inclination angle: for small angles of the bottom inclination, the orientation of the granular flow at the outlet is controlled by the friction; for large angles of the bottom inclination, the orientation of the granular flow at the outlet is controlled by the bottom inclination.

We have developed a simple phenomenological model which allows to recover the main feature of the dependance of the flow rate with the bottom inclination in a rectangular silo with a lateral outlet. However the model developed for the 3D flow cannot simply apply to the 2D flow supposing $W = \infty$ and it depends on 3 fitting parameters which are not linked with the properties of the granular media or with the geometry of the silo. To better understand the physical mechanisms which control this discharge flow, we develop a more complete modelling considering the granular media as a continuum media with a viscoplastic frictional rheology (Jop et al. [2006]), that we solve numerically.

3.3 Continuum modelling

3.3.1 Method

Following Zhou et al. [2017] we simulate the discharge flow of a granular media from a rectangular silo considering a non-Newtonian incompressible Navier–Stokes system, averaged across the thickness of the silo:

$$\frac{\partial u_i^p}{\partial x_i} = 0$$

$$\rho \left[\frac{\partial u_i^p}{\partial t} + u_j^p \frac{\partial u_i^p}{\partial x_j} \right] = \frac{\partial \sigma_{ij}^p}{\partial x_j} + \rho g_i + f_{wi}, \quad \text{with} \quad f_{wi} = -2 \frac{\mu_w p^p}{W} \frac{u_i^p}{|u_i^p|} \qquad (3.22)$$

Where f_{wi} represents the depth averaged Coulomb friction on the front and back wall, with a coefficient of friction $\mu_w = 0.1$. The stress tensor of the particle phase $\sigma_{ij}^p = -p^p \delta_{ij} + \tau_{ij}^p$ comes only from direct particle-particle interactions and can be described by a shear-dependant frictional rheology (MIDI [2004], Jop et al. [2005]):

$$\tau_{ij}^p = \eta_p(|\dot{\gamma}|, p^p)\dot{\gamma}_{ij} \quad \text{with} \quad \eta_p(|\dot{\gamma}|, p^p) = \frac{\mu(I)p^p}{|\dot{\gamma}|}, \quad I = \frac{|\dot{\gamma}|d}{\sqrt{p^p/\rho_p}}, \quad \text{and} \quad \mu(I) = \mu_s + \frac{\Delta\mu}{I_0/I + 1}.$$

$$(3.23)$$

where $\dot{\gamma}_{ij} = \partial u_i^p/\partial x_j + \partial u_j^p/\partial x_i$ is the strain-rate tensor with $|\dot{\gamma}| = (0.5\dot{\gamma}_{ij}\dot{\gamma}_{ij})^{0.5}$ its second invariant, and $I_0 = 0.4$, $\mu_1 = 0.4$, and $\mu_2 = 0.68$ are constant which depend upon the particle materials and shapes used.

The equations are made dimensionless using the silo width L as a length scale, $\rho g L$ as a stress scale and $\sqrt{L/g}$ as a time scale. The Navier–Stokes simulations are performed with the free software *Basilisk*[1] which uses a finite-volume projection method. Two phases are presented, a surrounding gas and the granular fluid. The interface between these two phases is tracked with a Volume-Of-Fluid method. The viscosity and density of the surrounding gas are small, so that its influence on the granular flow is minimized. The computational cost is dominated by the solution of two Poisson-Helmholtz problems: a scalar Poisson equation for the pressure necessary to enforce incompressibility and a vector Poisson-Helmholtz equation for the time-implicit discretization of the viscous term. We use a regularization technique to avoid the divergence of the viscosity when the shear becomes too small by replacing η by $\min(\eta, \eta_{max})$ with $\eta_{max} = 100$ a constant large enough, as done successfully in Lagrée et al. [2011], Staron et al. [2012, 2014] and Zhou et al. [2017].

---

[1] http://basilisk.fr

3.3.2 Configuration

a. Boundary conditions

The configuration of the simulation is illustrated in Figure 3.31a. A rectangular silo is chosen with a width L, a height H and a pseudo silo thickness W that determines the scaling of f_{wi}. The granular media is considered as a continuous media and has a initial height of h_p. The outlet of size D is located at the lateral position of silo (right bottom of the silo). The bottom in shape of a triangle starts from the bottom border of outlet and ends up at the left side of silo, with an inclined angle of θ_i.
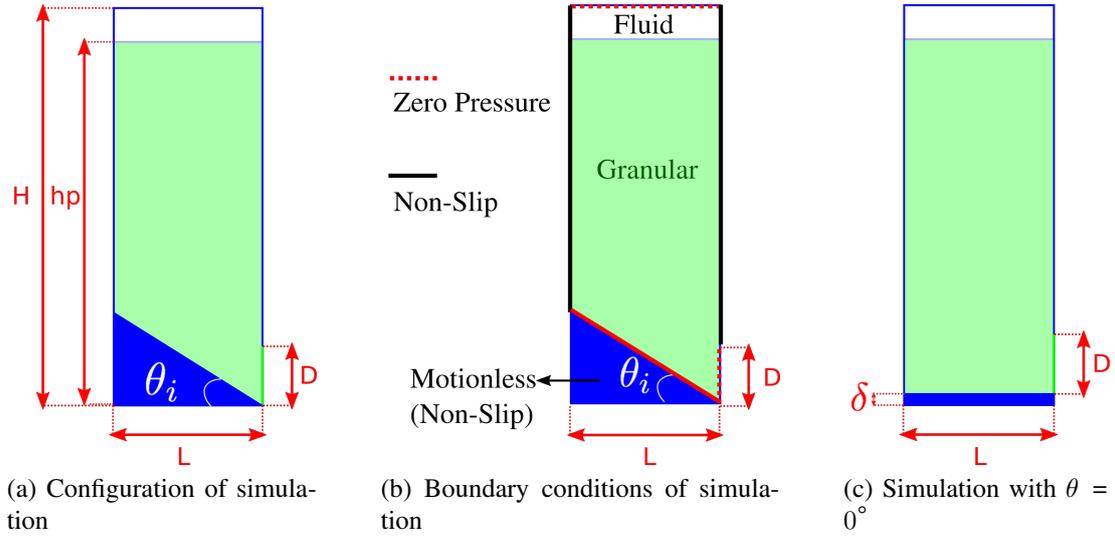
Figure 3.31: Configuration and boundary conditions of the continuum simulations.

(a) Configuration of simulation

(b) Boundary conditions of simulation

(c) Simulation with $\theta = 0°$

Different boundary conditions are applied to the borders of calculation domain, shown in Figure 3.31b:

- On both side walls (black lines in Figure 3.31b), Neumann boundary condition is applied for granular pressure, $\vec{\nabla} p^p \cdot \vec{n} = \vec{0}$, together with a no-penetration condition $\vec{u}^p \cdot \vec{n} = \vec{0}$ and a non-slip condition $\vec{u}^p \cdot \vec{t} = \vec{0}$.

- For the opened boundaries (red dashed lines in Figure 3.31b), at the top of silo and at the outlet, a Dirichlet boundary condition is applied for the granular pressure $p^p = 0$. Additionally, the normal and tangential components of granular velocity possess a Neumann boundary condition, namely $\nabla \left(\vec{u}^p \cdot \vec{n} \right) \cdot \vec{n} = \vec{0}$ and $\nabla \left(\vec{u}^p \cdot \vec{t} \right) \cdot \vec{n} = \vec{0}$.

- For the inclined bottom, we applied a non-slip condition (blue zone in Figure 3.31b). The inclined bottom is considered as an obstacle for the granular flow, so that for each time step of calculation, we impose a motionless condition in this area $u^p = 0$. Specifically, for the simulations with a plat bottom $\theta_i = 0°$, a thin plat layer of motionless area is placed at the

78

bottom of silo with $\delta = 0.125\,L$, allowing to have a similar bottom boundary condition with the other cases.

b. Post-processings

During the simulation, the volume of granular media left inside the silo is computed by following the granular surface every $\Delta t = 0.1\sqrt{L/g}$. In addition, the different fields (velocity, pressure, ...) are saved every $\Delta t = 1\sqrt{L/g}$. Figure 3.32a illustrates an example of the temporal evolution of the granular mass out of the silo during a discharge. The instantaneous mass flow rate of granular medium is determined by: $Q_i(t) = [m(t + \delta t) - m(t)]/\delta t$ with $\delta t = 0.5\sqrt{L/g}$.

(a)

(b)
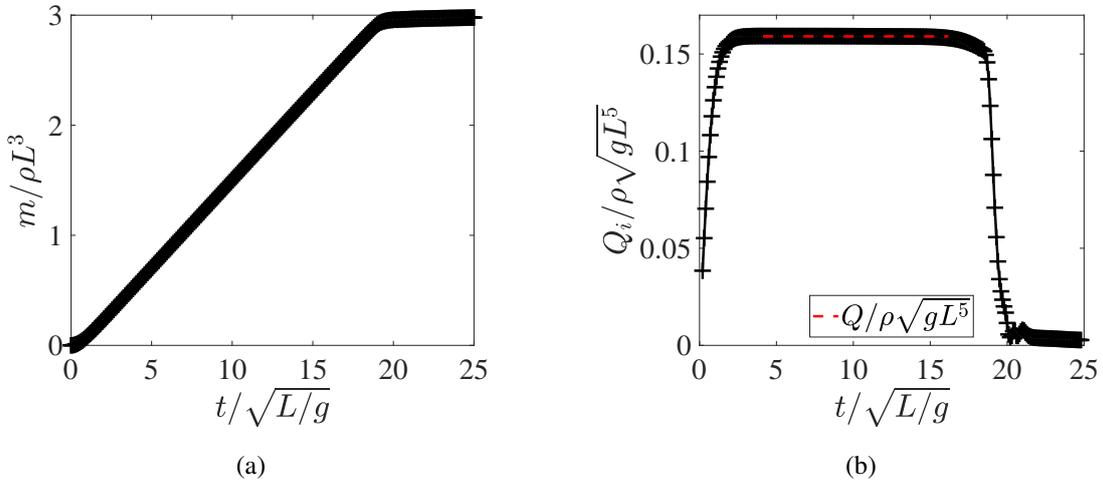
Figure 3.32: Discharge of the silo for a continuum simulation with $D = 0.5L, W = 0.75L$ and $\theta_i = 60°$. Temporal evolutions of (a) the granular mass out of the silo and (b) the instantaneous mass flow rate.

Figure 3.32b shows a typical temporal evolution of the mass flow rate of the granular media $Q_i/\rho\sqrt{gL^5}$ for $D = 0.5L, W = 0.75L$ and $\theta = 60°$. We observe that the mass flow rate reaches rapidly a steady-state regime of discharge, where the red dashed line represents the mean mass flow rate during this stationary period.

c. Computing parameters

To choose the computing parameters including the mesh size, the silo width, the initial granular height and the time step, we carry out a series of simulation, varying the parameters independently. Let us remark that we always observe a slight decrease of Q over time during the stationary phase whatever the parameter choice. This tendency, non consistent with the experimental observations, remains unexplained (it may be due to the regularization technique) but does not affect to a large extent the value of the flow rate. It is therefore neglected in the following analysis.
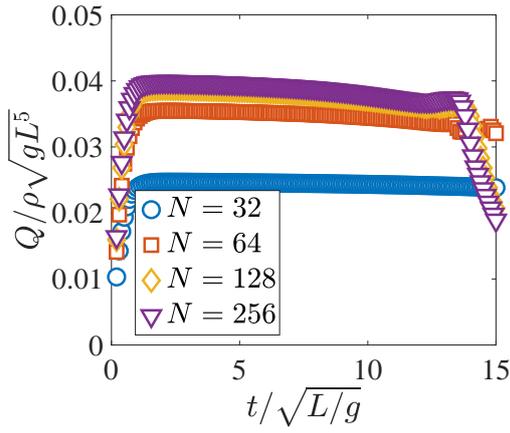
(a) Discharge flow rate $Q/\rho\sqrt{gL^5}$ versus time $t/\sqrt{L/g}$ for $L = 90d$, $D = 14d$, $h_p = 81d$ and $\theta_i = 20°$
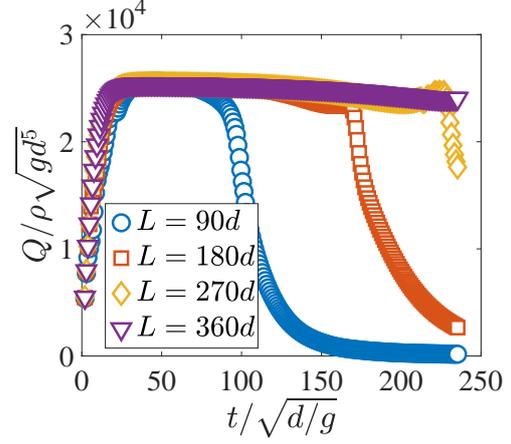
(b) Discharge flow rate $Q/\rho\sqrt{gd^5}$ versus time $t/\sqrt{d/g}$ for $D = 56d$, $h_p = 346d$ and $\theta_i = 20°$
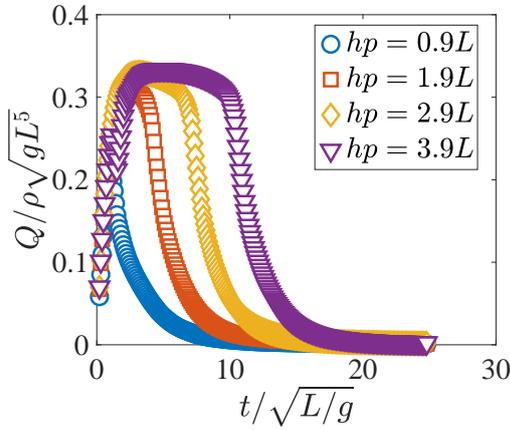
(c) Discharge flow rate $Q/\rho\sqrt{gL^5}$ versus time $t/\sqrt{L/g}$ for $L = 90d$, $D = 56d$, and $\theta_i = 20°$
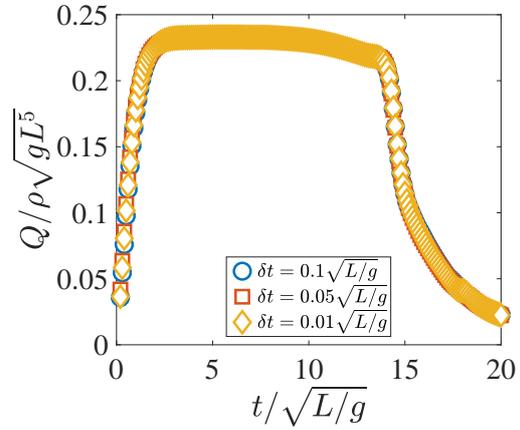
(d) Discharge flow rate $Q/\rho\sqrt{gL^5}$ versus time for $L = 90d$, $D = 45d$, $h_p = 3.9L$ and $\theta_i = 0°$

Figure 3.33: Parametric study for the continuum simulation.

First of all, we focus on the influence of the mesh size on the numerical results, fixing the silo width $L = 90d$, the initial granular column height $h_p = 81d$, the outlet size $D = 14d$ and with a small inclination angle $\theta_i = 20°$. We vary the number of mesh cells along the silo width N, from 32 to 256, and the discharge flow rate $Q/\rho\sqrt{gL^5}$ is illustrated in Figure 3.33a. We observe a beginning of convergence for $N \geq 64$. A deviation of approximately 6% is observed for $N = 64$ with respect to the values obtained for denser meshes. Considering both the computing time and the accuracy of simulation, $N = 64$ is chosen for the following calculations.

Secondly, we concentrate on the influence of the silo width on the discharge flow, with $D = 56d$, $h_p = 346d$ and $\theta_i = 20°$, varying the silo width L from $90d$ to $360d$. The discharge flow rate $Q/\rho\sqrt{gd^5}$ versus time $t/\sqrt{d/g}$ is illustrated in Figure 3.33b. We observe very little influence on the flow rate in the tested range, therefore, $L = 90d$ is used for the following simulations.

Figure 3.33c shows the discharge flow rate $Q/\rho\sqrt{gL^5}$ as a function of time $t/\sqrt{L/g}$, for $D =$

$56d$, $L = 90d$ and $\theta_i = 20°$, for various h_p. We observe that the curves of flow rate begin to superpose when $h_p \geq 1.9L$. It denotes that the initial granular height does not play a role on the flow rate when the silo is filled enough. Thus, for the following simulations, $h_p = 3.9L$ is chosen to obtain a sufficiently long discharge period.

To investigate the influence of time step, a series of simulation for $D = 45d$, $L = 90d$, $h_p = 3.9L$ and $\theta_i = 0°$ is carried out varying the time step, and displayed in Figure 3.33d. We observe that the tested time step has no influence on the mean flow rate and a time step $\delta t = 0.01\sqrt{L/g}$ is applied for the simulations.

The geometrical parameters of the performed runs, for studying the effect of an inclined bottom, are displayed in Table 3.4.

D	W	θ_i (deg)	d_p
$[0.44; 0.5; 0.56; 0.60;$ $0.63; 0.66; 0.69; 0.75]L$	$[0.25; 0.5; 0.75;$ $1.0; 2.0]L$	$[0; 10; 20; 30; 40;$ $50; 60; 70; 80]$	$L/90$

Table 3.4: Geometrical parameters for the performed continuum simulations.

3.3.3 Simulation results

(a)　　　　　　　　(b)　　　　　　　　(c)
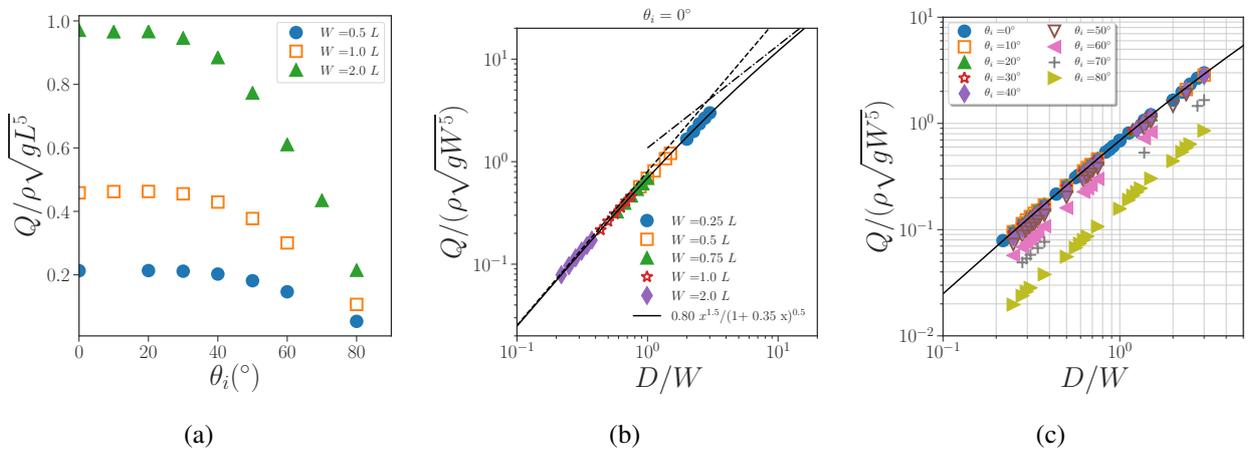
Figure 3.34: Continuum simulations: (a) Mass flow rate of particles as a function of the angle of inclination θ_i and $D = 0.75L$. (b,c) Mass flow rate made dimensionless by $\rho\sqrt{gW^5}$ versus the aspect ratio of the aperture D/W for (b) an horizontal bottom $\theta_i = 0$ and (c) all the bottom inclination θ_i explored. The solid line represents equation 3.14 with $c_D = 0.8$ and $\gamma = 0.35$. The dash line represents the Hagen-Beverloo equation 3.3 with $c_D = 0.8$ and the dotted-dashed line represents the linear asymptotic regime of equation 3.14 for $D/W >> 1$.

Figure 3.34a shows the particles mass flow rate as a function of the inclination angle θ_i for $D = 0.75L$ and various silo thicknesses. We can observe that the continuum model successfully recover the experimental behavior with a large plateau where the mass flow rate does not depend

on the inclination of the bottom followed by a strong decrease above a critical angle which depends on the silo thickness. For the zero inclination bottom silo, the dimensionless flow rate plotted in Figure 3.34b can be adjusted by equation 3.14 (black line) with $c_D = 0.8$ and $\gamma = 0.35$, in good agreement with the values reported in Zhou et al. [2017]. The continuum simulations were mainly performed in the Hagen-Beverloo regime and at the beginning of the transition zone, which add imprecision on the determination of the coefficient γ. Indeed we do not perform simulations for large value of D/W as the code tends to numerically destabilize for small value of W. When increasing the angle of the bottom wall inclination, we recover the same behavior than in the experiment, for small bottom inclination the data are superimposed then the flow rate decreases as can be seen in Figure 3.34c.

We now turn to the observation of the velocity field. Figure 3.35 show the streamlines and velocity fields for $W = 2L$, $D = 0.75L$ for (a, d) the horizontal bottom, (b, e) a small inclination $\theta_i = 20°$ and (c, f) a large inclination $\theta_i = 60°$. Similarly to the experiment we observe that the flow is vertical far from the outlet and rotate close to it, leaving a stagnant zone on the left part of the silo. For small bottom inclination angle this stagnant zone is not perturbed whereas for larger inclination angle the stagnant zone connects to the inclined bottom upward the outlet.
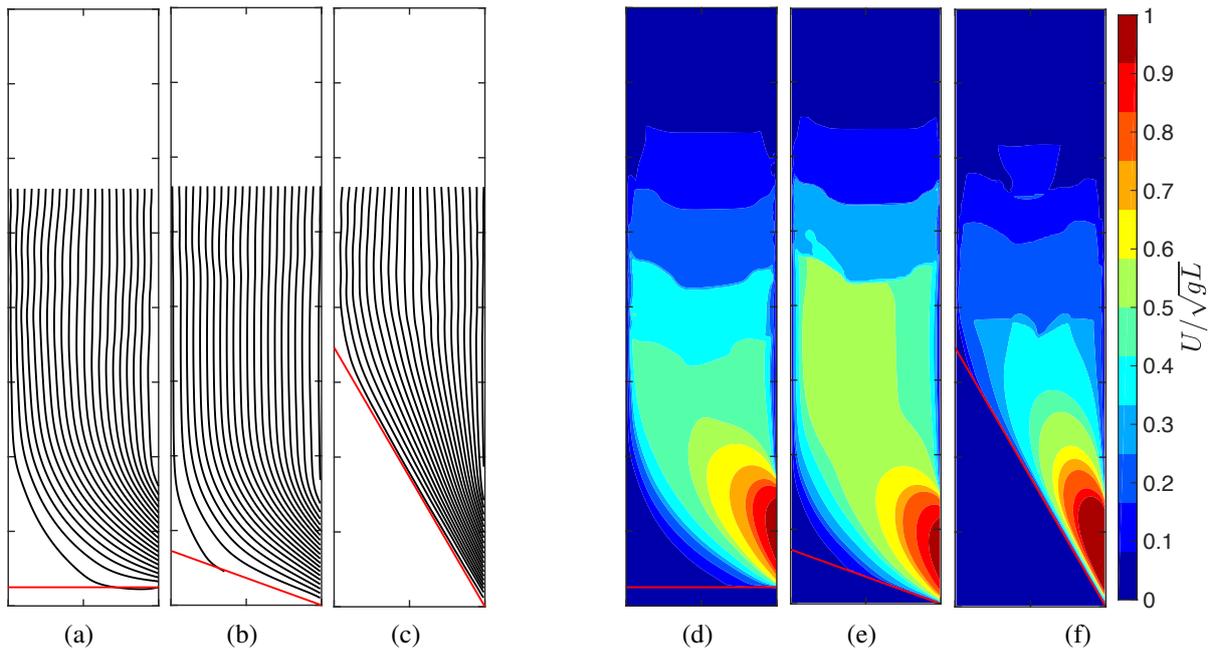
Figure 3.35: (a,b,c) Streamlines and (d,e,f) velocity magnitude fields for the continuum simulations with no slip condition and $W = 2L$, $D = 0.75L$ and (a,d) $\theta = 0°$, (b,e) $\theta = 20°$ and (c,f) $\theta = 60°$.

The horizontal and magnitude dimensionless profiles of the velocity are displayed on Figure 3.36 (a-f). We recover the self similarity of the profiles and the global shape of the profiles, with an asymmetric profile for the horizontal component of the velocity and a more symmetric shape for the magnitude. Concerning the profile of the cosine of the angle of the streamline, plotted in
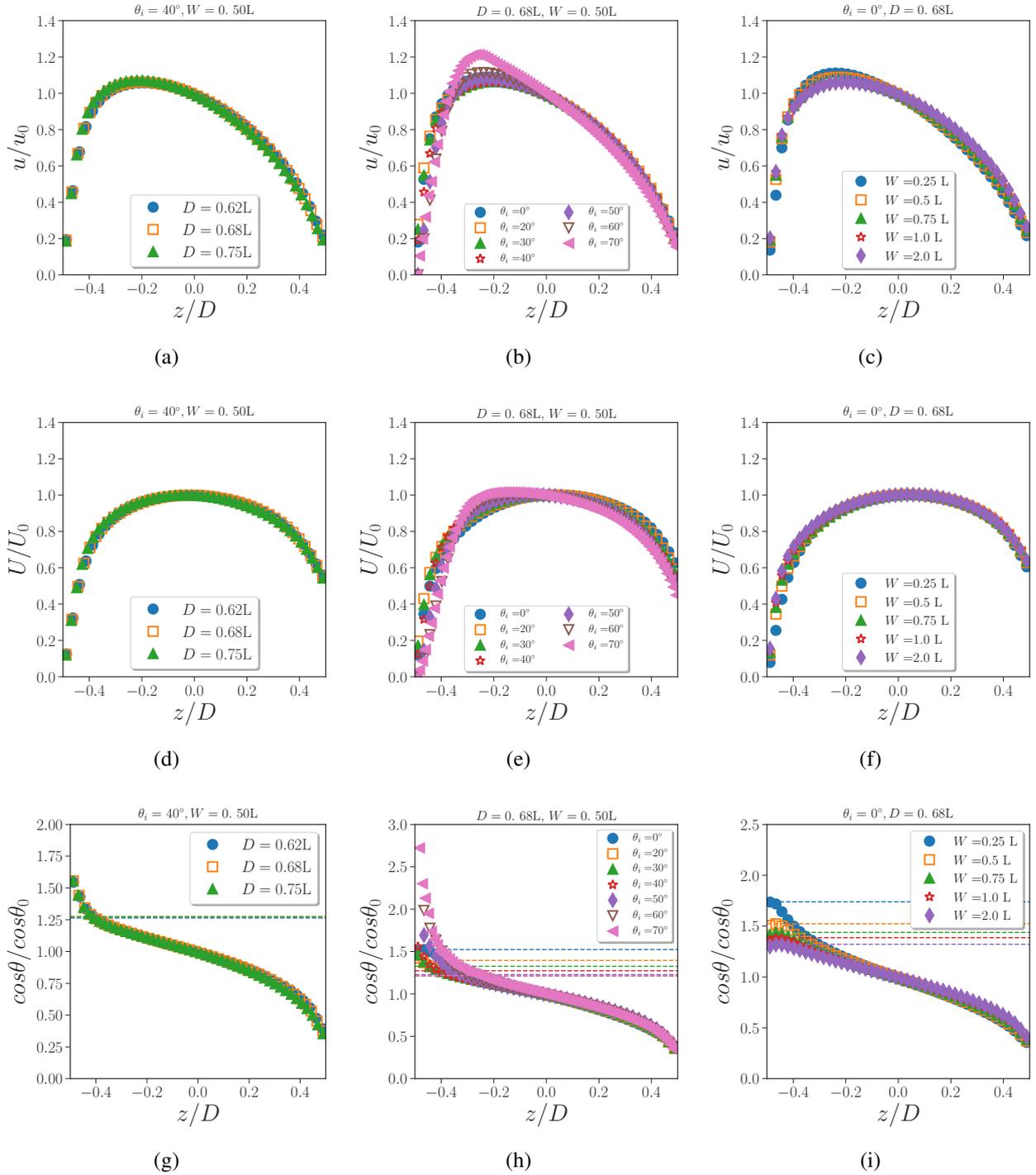
Figure 3.36: Profiles of (a,b,c) the horizontal velocity, (d,e,f) the velocity magnitude and (g,h,i) the cosine of the inclination angle, normalized by their central values of the outlet, with (a,d,g) $\theta_i = 40°$, $W = 0.5L$ and several outlet diameters D, (b,e,h) $D = 0.68L$, $W = 0.5L$ and several outlet inclinations θ_i and (c,f,i) $\theta_i = 0°$, $D = 0.68L$ and several silo thicknesses W.
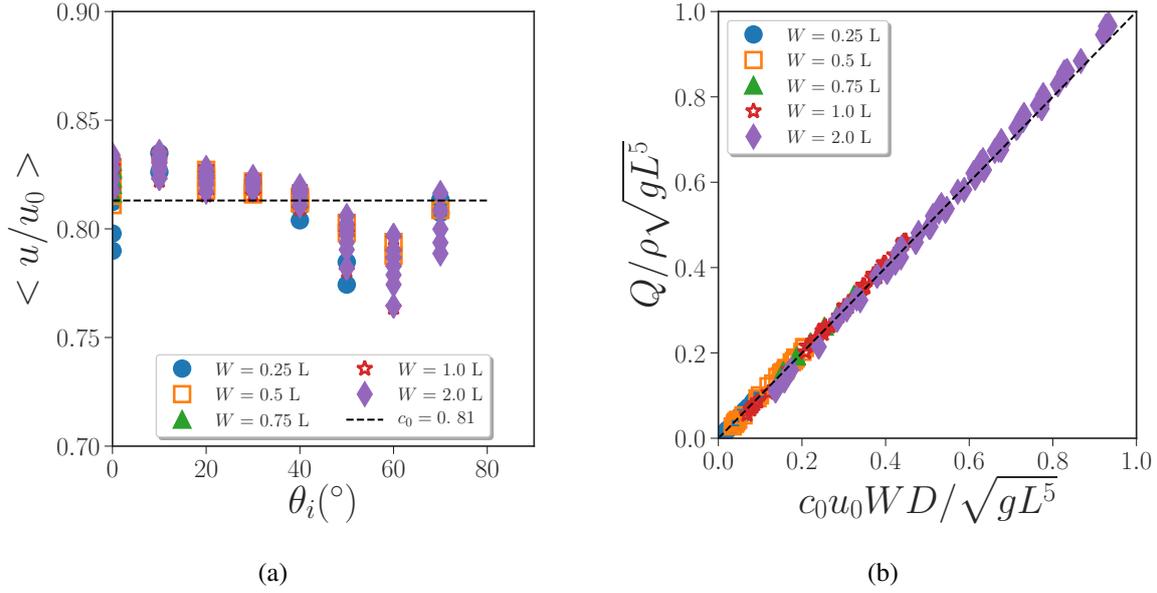
Figure 3.37: (a) Mean value of the normalized horizontal velocity profiles versus the bottom angle of inclination. The horizontal line represents the mean value $c_0 = 0.81$. (b) Flow rate versus $c_0 \phi_b \rho_p u_0 W D$. The dashed line represents the equation $y = x$.

Figure 3.36 (g-i), we also observe a self similarity of the profiles with a linear decrease from the bottom to the top of the outlet, except close to the bottom of the outlet where the inclination of the streamline strongly decreases and can be smaller than the imposed bottom inclination represented by the horizontal dashed lines. This may be due to the pixelation of the bottom interface, which is represented by a staircase. Finally Figure 3.37 shows that equation 3.4 is valid for the continuum simulation. We do not show on this graph the profile obtained with the higher bottom inclination $\theta_i = 80°$ as they are largely scattered in such extreme geometry.

Following the experimental section, we first focus on the inclination of the flow at the central streamline, θ_0, as illustrated on Figure 3.38. Again we recover the same behavior than in the experiment with a regime for large θ_i dominated by the bottom inclination where $\cos \theta_0 = \zeta \cos \theta_i$ with $\zeta = 0.83$ (see Figure3.38a for $D = 0.75L$), and a regime dominated by the friction (internal and on the wall) depending only on the aperture dimensions D and W (see equation 3.17). The inclination of the central streamline is thus well adjusted by equation 3.18 with $c_{\theta_0} = 0.81$ and $\gamma = 0.35$ and $\zeta = 0.83$ as can be seen in Figure3.38b.

Concerning the magnitude of the velocity, for an horizontal bottom as shown by Zhou et al. [2017] the velocity magnitude does not depend on the silo thickness and is well adjusted by a square root variation with respect to the opening size given by equation 3.11 with $c_E^i = 1.19$ (see Figure 3.39a). If we now consider a case where the inclination of the central streamline is controlled by the bottom inclination as shown in Figures 3.39b we can see that the data do not superimpose when varying the silo thickness, the velocity increasing when increasing W. If we consider the variation of the magnitude of the velocity with the bottom inclination plotted in Figure

(a)   (b)
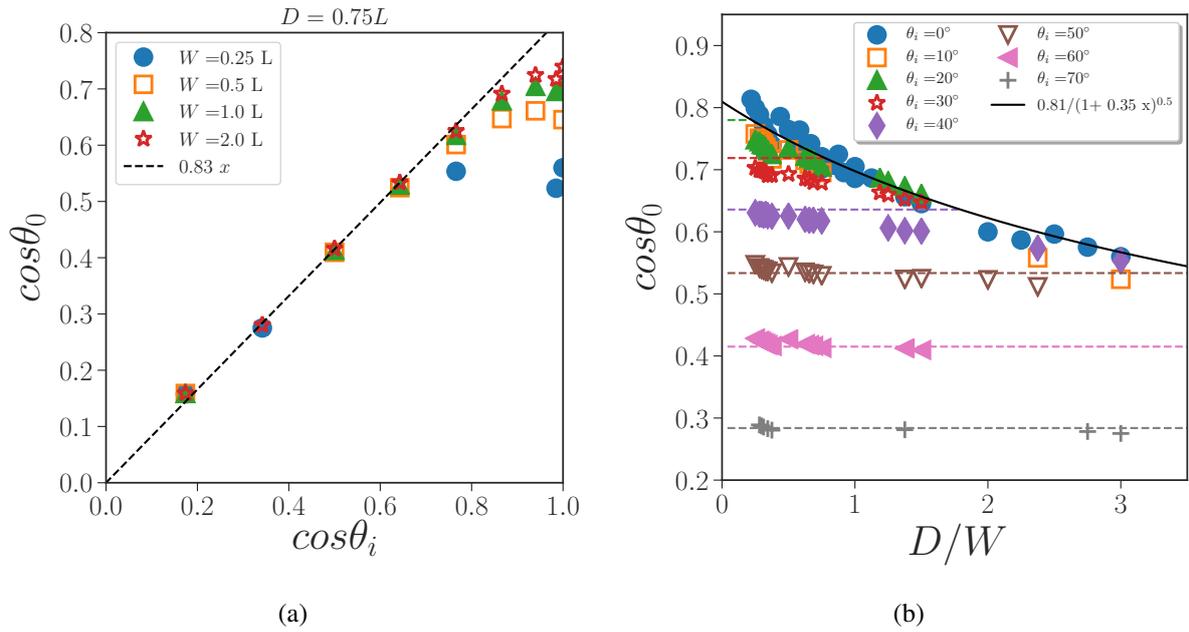
Figure 3.38: Inclination of the central streamline at the outlet, $\cos\theta_0$ (a) versus the inclination of the bottom of the silo, $\cos\theta$ for $D = 0.75L$ where the dashed line represents equation 3.16 with $\zeta = 0.83$, (b) versus the aspect ratio of the aperture D/W for all the bottom inclinations. The full line represents equation 3.17 with $c_{\theta_0} = 0.81$ and $\gamma = 0.35$. The dashed lines represent equation 3.16 with $\zeta = 0.83$.

(a)   (b)   (c)
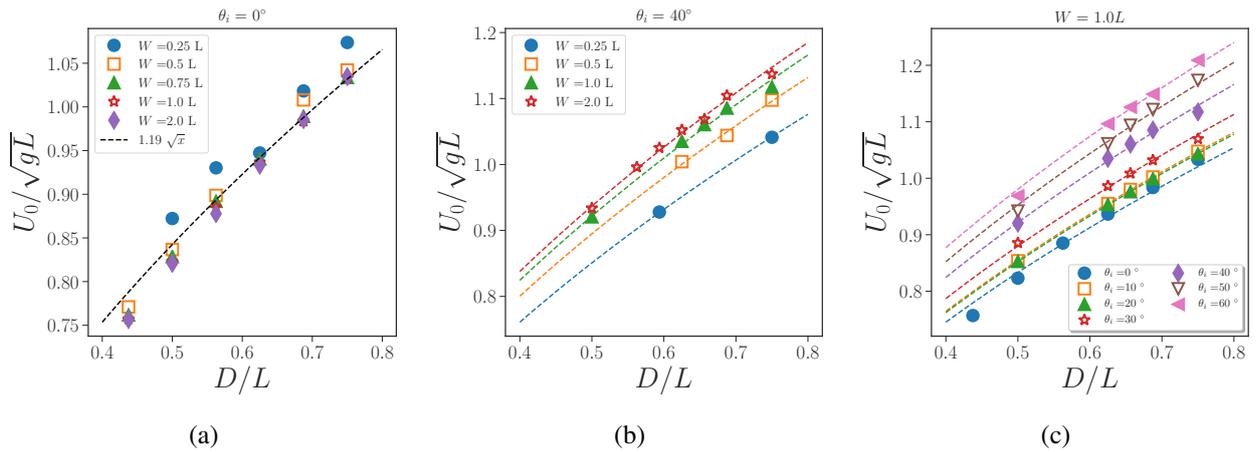
Figure 3.39: Magnitude of the velocity profiles at the centre of the outlet, U_0, normalized by $\sqrt{gL}$ versus the outlet size D normalized by the silo width L for (a) $\theta_i = 0°$, and several silo thickness W, (b) $\theta_i = 40°$, and several silo thicknesses W, and (c) $W = L$ and several outlet inclinations θ_i. The dashed lines represent square root fit with each adjustable coefficients obtained by the least squares method.

3.28c for $W = L$, we observe that the data are superimposed for low θ_i then the velocity increases when increasing θ_i. However each curve is well adjusted by a square root variation as given in equation 3.11, the coefficient c_E now depending on W and θ_i.

This suggests that the flow behavior is not the same when the stagnant zone develops freely or when the flow is confined by the inclined bottom. For a free stagnant zone, the parietal friction controls the angle of inclination of the central streamline θ_0^f at the outlet, which depends on W as given by equation 3.17, but the magnitude of the velocity does not depend on the confinement and is only controlled by the outlet size giving $U_0^f = c_E\sqrt{gD}$. This may be due to the fact that the stagnant zone is curved and when reaching the dense granular zone the flow is nearly vertical. When the flow orientation is controlled by the bottom inclination, the flow is not free to rotate, the inclination at the central streamline is given by equation 3.16 and the magnitude of the velocity follow $U_0 = c_E^i\sqrt{gD\sin\theta_0}$. However Figure 3.39b suggests that c_E^i is not constant and depends on W.
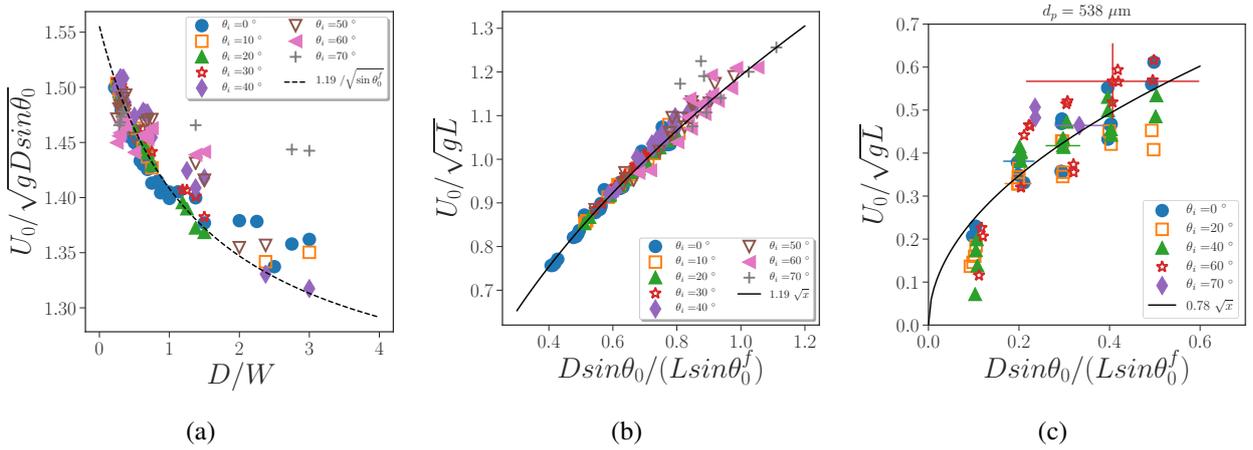
Figure 3.40: (a) Magnitude of the velocity profiles at the centre of the outlet, U_0, normalized by $\sqrt{gD\sin\theta_0}$ versus the outlet aspect ratio D/W for several outlet inclinations θ_i. The dashed line represents equation 3.24 with $c_E = 1.19$. (b, c) Magnitude of the velocity profiles at the centre of the outlet, U_0, normalized by $\sqrt{gL}$ versus the normalized outlet size $D\sin\theta_0/(L\sin\theta_0^f)$, where θ_0^f is given by equation 3.17, for several outlet inclinations θ_i for (b) the continuum simulations and (c) the experiments with $d_p = 538\,\mu$m . The full lines represent equation 3.24 with (b) $c_E = 1.19$ and (c) $c_E = 0.78$.

Let us study how the fitting parameter c_E^i depends on θ_i. To test the evolution of c_E^i, we plot in Figure 3.40a the dimensionless velocity $U_0/(\sqrt{gD\sin\theta_0})$ versus D/W for all the bottom inclinations. Interestingly we observe that all the data superimpose, which allows to match equations 3.11 and 3.12 writing

$$U_0 = c_E\sqrt{gD\frac{\sin\theta_0}{\sin\theta_0^f}}. \tag{3.24}$$

Equation 3.24 is drawn in dashed lines in Figures 3.40a using the value of c_E obtained fitting the

data for a horizontal bottom (Figures 3.39a). The agreement is fairly good, but a more straightforward representation of equation 3.24 is shown in Figure 3.40b where the velocity normalized by $\sqrt{gL}$ is plotted versus a normalized outlet size $D \sin \theta_0 / (L \sin \theta_0^f)$. The data are well superimposed and adjusted by equation 3.24 with $c_E = 1.19$. This observation suggests that when the flow is controlled by the bottom inclination, the parietal friction still played a role controlling the magnitude of the velocity at the outlet. This effect will tend to counterbalance a little bit the decrease of the flow rate due to the strong inclination of the streamlines. In Figure 3.40c we plot the data corresponding to the experiments with $d_p = 538\mu$m in the same representation. The streamline inclination being quite important even for a horizontal bottom, the agreement with equation 3.24 with $c_E = 0.78$ is equivalent to the one previously found in Figure 3.28c.

We can then complete the simple analytical model by considering the effect of the inclined bottom on the granular velocity magnitude at the outlet, in addition to the equations 3.20 and 3.21:

$$\text{if} \quad \theta_i < \theta_c: \qquad \frac{Q}{\rho_p \phi_b DW \sqrt{gD}} = \frac{c_D}{\sqrt{1 + \gamma D/W}} \tag{3.25}$$

$$\text{else if} \quad \theta_i > \theta_c: \qquad \frac{Q}{\rho_p \phi_b DW \sqrt{gD}} = c_\theta \cos \theta_i [(1 - \zeta^2 (\cos \theta_i)^2)]^{1/4} \left[\frac{1 + \gamma D/W}{1 - c_{\theta_0}^2 + \gamma D/W}\right]^{1/4} \tag{3.26}$$

with $c_D = c_0 c_E c_{\theta_0}$, $\theta_c = \arccos(c_{\theta_0}/(\zeta\sqrt{1 + \gamma D/W}))$ and $c_\theta = c_0 c_E \zeta$.
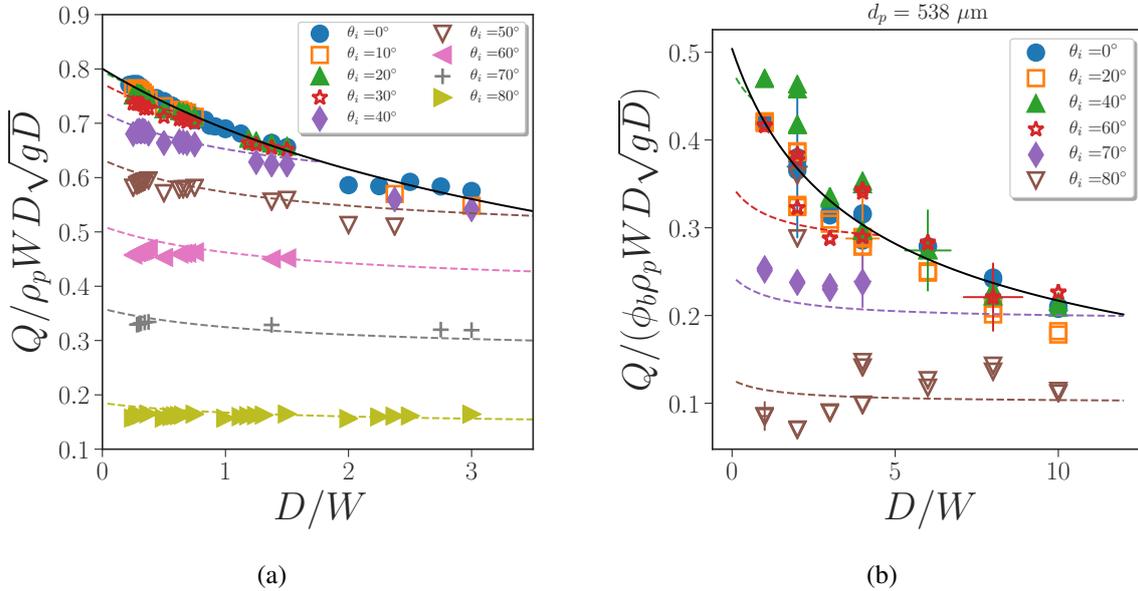
Figure 3.41: Mass flow rate normalized by $\rho_p \phi_b DW \sqrt{gD}$ for all the bottom inclination, versus the normalized aperture size D/W for (a) for the continuum simulations and (b) the experiments with $d_p = 538 \ \mu$m . The full lines represent equation 3.20 and the dashed lines represent equation 3.21 with (a) $c_D = 0.8$, $c_{\theta_0} = 0.81$ and $\gamma = 0.35$ and $\zeta = 0.83$ and (b) $c_D = 0.5$, $c_{\theta_0} = 0.78$, $\gamma = 0.44$ and $\zeta = 0.9$.

In Figure 3.41 we compare the model given by equations 3.25 and 3.26 with the mass flow rate normalized by $\rho_p \phi_b DW\sqrt{gD}$ plotted versus the normalized aperture D/W both for the simulations and the experiments. For the simulations the agreement is very good. For large bottom inclination ($\theta_i > 50°$), the flow rate is completely controlled by the bottom whereas for small inclination ($\theta_i < 20°$) it is controlled by the friction (internal to the granular media and with the walls). In between even when the inclination of the streamline is controlled by the bottom, the model predicts that the flow rate stays close to the unperturbed flow but not as closed as observed in the experiment (red stars in Figure 3.41b). This continuum model appears to reproduce quite well the experimental behavior and allowed us to complete the simple analytical model. However it does not capture finely the transition zone where the flow rate seems to follow the unperturbed law whereas the streamline inclination at the outlet is controlled by the inclination of the bottom. This may be due to the choice of the no slip condition at the bottom, which is not realistic when the flow is perturbed by the bottom inclination.

A study on the effect of the boundary condition is presented in appendix B, supposing a free slip condition at the bottom wall (the other walls keeping a no slip condition). The numerical results show that the main difference compared to the previous condition (non slip at the inclined bottom) occurs for the wall velocity at the bottom of the outlet which is not zero leading to a strong asymmetry of the velocity profile at the outlet. Moreover, using equations 3.16 and 3.17 to describe the flow orientation is very robust where the magnitude of the velocity is found to be sensitive to the boundary condition. Interestingly, we recover a similar behavior than the experiments for the transition zone.

3.3.4 Conclusion and perspectives

We have shown in this section that the continuum modelling contains all the necessary ingredients to predict the effect of an inclined bottom on the flow rate of a granular media discharging from a lateral outlet. Using the simplest no slip boundary condition on the walls, we have seen that the internal friction against both the front and rear wall drive the flow rate for low bottom angle of inclination or low aperture aspect ratio D/W. For higher θ_i the flow inclination is controlled by the bottom inclination whereas the magnitude of the velocity still depends on the internal and wall friction.

All these observations suggest that the different parameters of the model should depend on the rheology of the granular flow, on the silo geometry (inclination of the bottom) and on the boundary conditions on the walls. To better understand the relevant physical mechanism, in future work it will be interesting to simulate the real boundary condition with a Coulomb friction and to develop an analytical model based on the $\mu(I)$ rheology to link the flow rate with the rheological parameters. As an example we performed a first set of simulation to test how the flow rate depends on the rheological parameters μ_s, $\Delta\mu$ and I_0 for a lateral outlet with a horizontal bottom and a no

slip conditions on all the walls. We observe in Figure 3.42 that the flow rate depends strongly on μ_s but poorly on $\Delta\mu$ or I_0. This is consistent with the fact that close to the outlet, the granular flow accelerates strongly, the granular pressure decreases and the momentum equation (equation 3.22) mainly consists on an equilibrium between the acceleration terms and the gravity, independently on the rheological parameters. However μ_s still plays an important role, certainly through the shape of the stagnant zone.
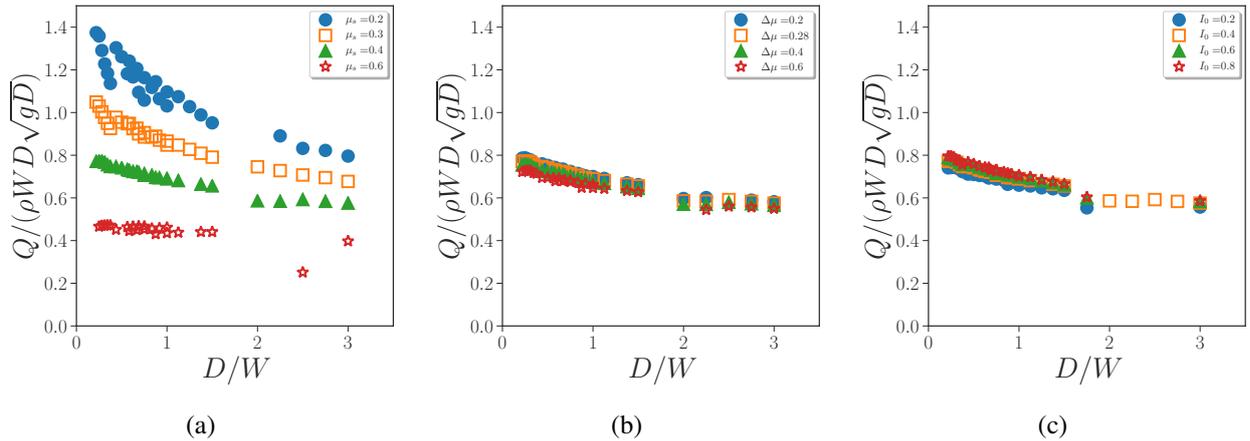
Figure 3.42: Role of the rheological parameters for a lateral outlet an a horizontal bottom with no slip condition: (a) $\Delta\mu = 0.28$, $I_0 = 0.4$ and various μ_s. (b) $\mu_s = 0.4$, $I_0 = 0.4$ and various $\Delta\mu$. (c) $\mu_s = 0.4$, $\Delta\mu = 0.28$ and various I_0.
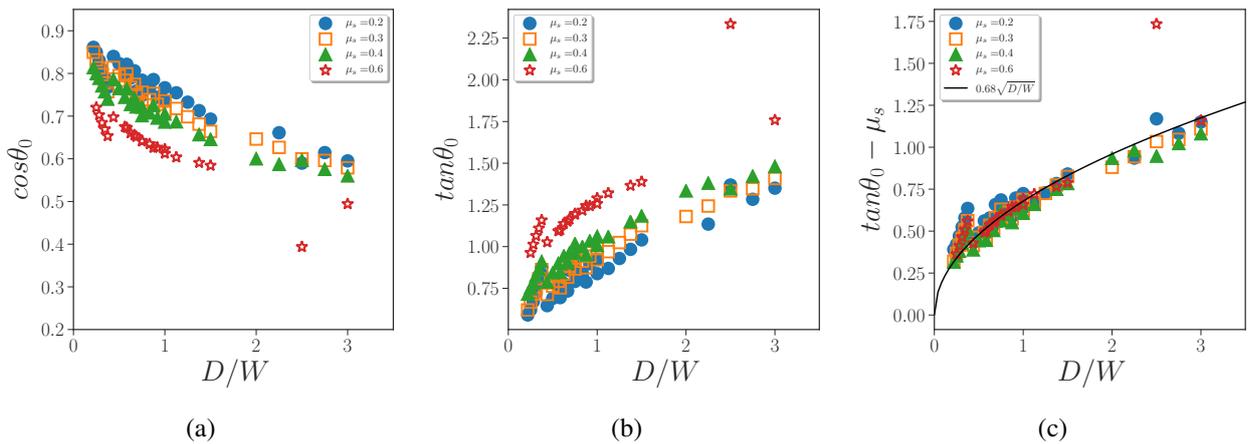
Figure 3.43: Role of the rheological parameters for a lateral outlet an a horizontal bottom with no slip condition and $\Delta\mu = 0.28$, $I_0 = 0.4$ and various μ_s. (a-c) Effect on the inclination angle of the central streamline: (a) $\cos\theta_0$ versus D/W, (b) $\tan\theta_0$ versus D/W and (c) $(\tan\theta_0 - \mu_s)$ versus D/W. The full line represents equation 3.27 with $\gamma_1 = 0.68$.

In Figure 3.43a we can see that the variation of the angle of inclination of the central streamline at the outlet with D/W depends indeed on μ_s: the higher the internal friction, the higher the angle

of inclination. As μ_s represents the tangent of the avalanche angle and should correspond to the tangent of the angle of the stagnant zone for a 2D silo (or large W) we have plotted in 3.43b $\tan\theta_0$ versus D/W. We can see that the curves seems to be shifted when increasing μ_s, so in Figure 3.43c we have plotted $\tan\theta_0 - \mu_s$ versus D/W. The data seem to superimpose in this representation and are well adjusted by a square root suggesting that

$$\tan\theta_0 = \mu_s + \gamma_1\sqrt{D/W} \tag{3.27}$$

with $\gamma_1 = 0.68$. The inclination angle of central streamline depend both on μ_s and μ_w through γ_1.
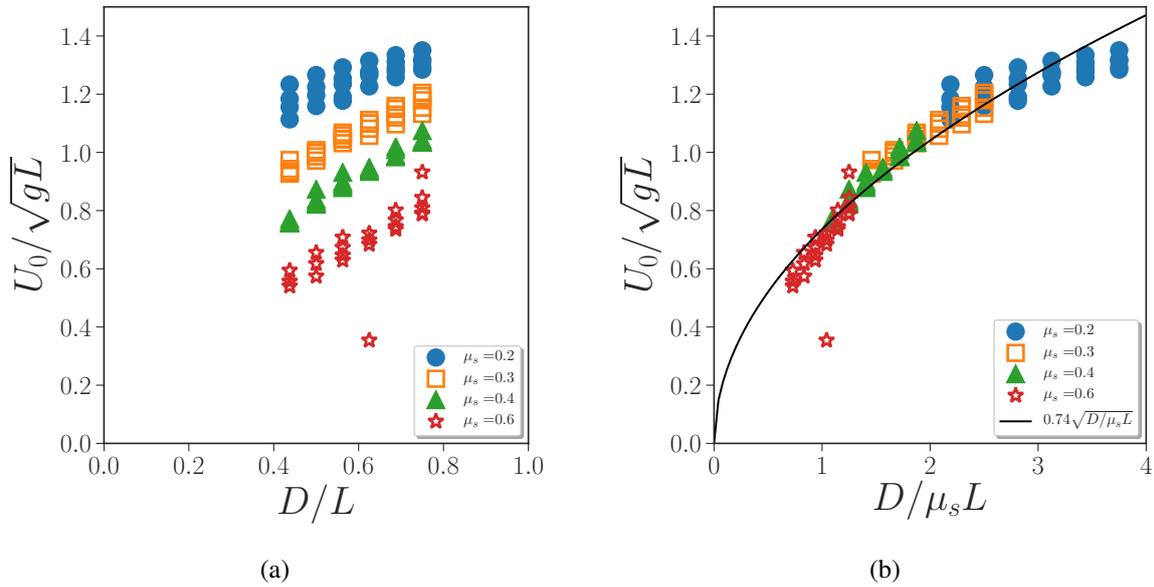
Figure 3.44: Magnitude of the velocity profiles at the centre of the outlet, $U_0/\sqrt{gL}$, versus (a) D/L and (b) $D/\mu_s L$. The full line represents equation: $y = c_E\sqrt{x}$ with $c_E = 0.74$.

In Figure 3.44 we have plotted the magnitude of the velocity at the outlet. We can see that it depends also strongly on μ_s; the higher the friction coefficient, the lower the velocity. The data can be reasonably superimposed if we plot $U_0/\sqrt{gL}$ versus $D/\mu_s L$ and adjusted by a square root law, which may suggest that the characteristic length scale separating the dense regime from the accelerated regime vary with D/μ_s. In future work a full parametric study should be done to characterize the silo discharge and link the adjustable coefficient used to predict the flow rate with the rheological parameters.

3.4 Conclusion

Using a non-conventional geometry (a rectangular silo with an inclined bottom which ends up at a lateral outlet) we have shown thanks to laboratory experiments and continuum simulation with $\mu(I)$ frictional rheology that the flow-rate is controlled by two phenomena and not only by the orifice size like for more conventional silos. For lateral aperture with a horizontal bottom two regimes of flow exist depending on the aperture aspect ratio D/W and resulting from the competition between wall friction and internal friction to control the orientation of the granular flow. For outlet situated at the bottom of the silo, this effect does not affect the flow-rate, the streamline at the center being vertical. In the geometry of interest when varying the bottom inclination two flow regimes have also been identified. For small angles of inclination the flow is not perturbed by the bottom and the central streamline orientation is controlled by the outlet aspect ratio D/W. The second regime is observed for large inclined angles where the flow orientation is imposed by the bottom inclination.

Then we have shown that the outlet corresponds to an area where the grains are accelerated, the potential energy being transferred to kinetic energy. However this balance and thus the magnitude of the velocity at the center of the outlet was found to be quite sensitive to the silo geometry, the granular rheology and the boundary conditions.

Finally, we present a phenomenological model that predicts the discharge flow rate of particles from a rectangular silo with an inclined bottom according to its aperture aspect ratio with a good agreement in the asymptotic regimes.

The continuum modelling was shown to be the good framework to describe the discharge flow of a granular media from a silo, and in future work it will allow to perform a full parametric study of the influence of the rheological parameters on the analytically predicted flow rate in various geometry. It may therefore, reduce the empirical parameters in the flow rate scaling law to the geometrical and materials related parameters that could be inferred from more simple experiments (such the $\mu(I)$ rheological parameters). In particular these results may have practical interest considering the effect of the hopper angle for an industrial silo.

In the next chapter, we will now consider the role of a pressurized gas in the silo discharge, in a more simple cylindrical geometry with a bottom orifice.

Chapter 4

Discharge of silo: coupling with an imposed gas pressure

In this chapter, we will discuss on the effect of an imposed gas pressure on the discharge flow of granular media, through a circular outlet located at the center of the bottom of a cylindrical silo. The experimental system and the performed measurements are presented in the first section. Afterwards, the experimental results is discussed, including a description of both granular flow and gas flow during the silo discharge. Then a quasi-steady analytical model based on a two-phase continuum modelling is developed for describing the behaviors of both the granular phase and the gas phases. Finally, the confrontation between the numerical simulation based on a continuum modelling and the experimental results is presented in the last section.

4.1   Experimental setup

4.1.1   Silo configuration

We choose cylindrical silos of height $H = 0.5$ m, internal diameter $L = [20; 40; 60]$ mm to carry out the study of their discharge with pressurized gases, shown in Figure 4.1. The silo is dismountable and composed of three parts: a top plug which can be removed in order to pour the particles into the silo; a main part in plexiglas with a thickness of 5 mm; a changeable bottom plug with an outlet diameter of $D = [10; 20]$ mm. An o-ring seal is added to the bottom plug to ensure the tightness of the silo (see the right part of Figure 4.1).

The cylindrical silo is instrumented with five pressure taps along the silo wall $P_1 - P_5$ (see the left part of Figure 4.1), all the taps are on the same vertical axis but at different elevations. There are also two taps of air inlet on the top part of the silo, which permit the homogeneous injection of gas.
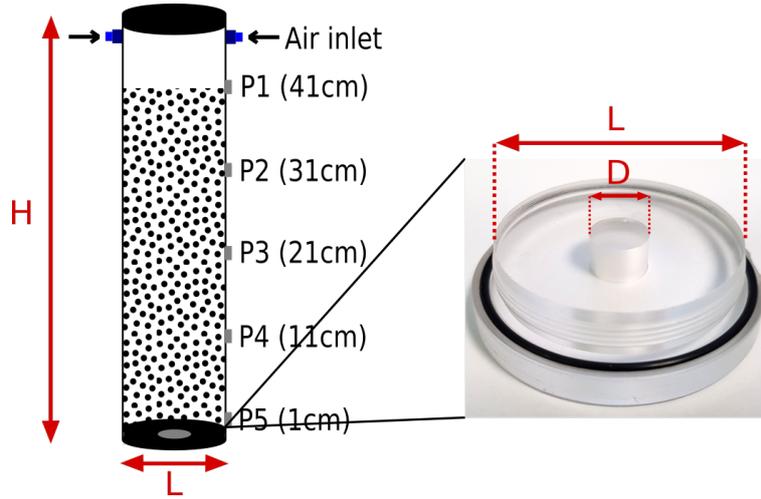
Figure 4.1: Cylindrical silo configuration.

4.1.2 Granular media

Three types of particle are used as the experimental granular media: smooth spherical glass particles of mass density ρ_p = 2500 kg.m^{-3} (provided by $Potter\&Ballotini$), smooth spherical ceramic particles of mass density ρ_p = 6000 kg.m^{-3} (provided by $SiLibeads$), the sand particles having a more angular shape of mass density ρ_p = 2500 kg.m^{-3} (provided by $Sibelco$). All the particles are sieved and the mean size value is given in Table 4.1 with a dispersion of $\pm10\%$. The images displayed in Figures 4.2a and 4.2c, obtained by a Digital Microscope of brand $HIROX\ RH-2000$, illustrated a sample of ceramic particles (see Figures 4.2a) and sand particles (Figures 4.2c), and the corresponding size distributions are illustrated in Figure 4.2b and 4.2d, adjusted by a gaussian distribution law.

Table 4.1: Characteristic of granular media.

	Glass particles	Ceramic particles	Sand particles
d_p (μm)	190; 375; 538; 762; 1129; 1347	180; 550; 1165	864

We carried out also the discharge of silo for a bidisperse granular media, blending the same mass of two particle size (d_p = 180μm and d_p = 1165μm) for the ceramic particles. This bidisperse granular column is filled layer by layer, where each layer is premixed in a container and then slowly poured into the silo.
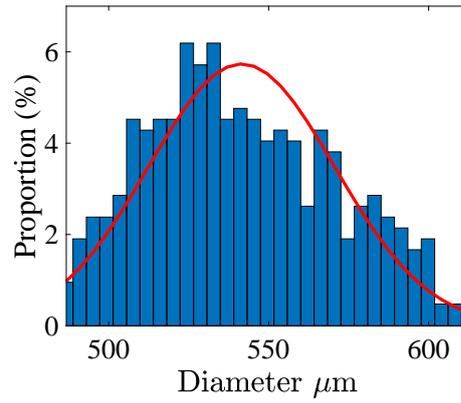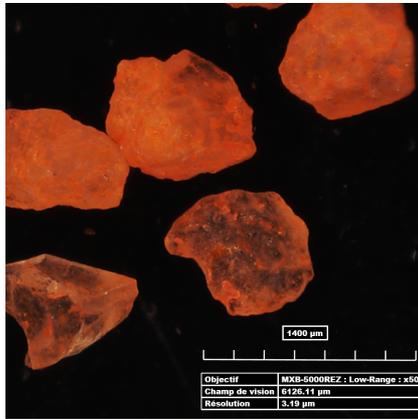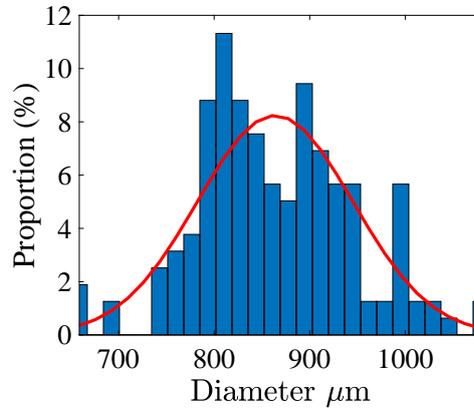
Figure 4.2: Images of two samples of particles (a, c) and their size distributions (b, d): (a, b) for the ceramic particles (≈ 400 particles) and (c, d) for the hydrophobic sand particles (≈ 200 particles). The red lines represent a gaussian distribution law adjusted with (b) $< d_p >= 550\mu m$, $\sigma = 29\mu m$ and (d) $< d_p >= 864\mu m$, $\sigma = 81\mu m$.

4.1.3 Gas injection system

In order to maintain a constant pressure of gas over the granular media during the discharge of the silo, we use 5 latex balloons as a large reservoir of gas providing a large air flow. The latex balloons have a maximum diameter of approximately 50 cm. Once inflated with pressurized air, the air inside the balloon have an overpressure (≈ 3000Pa) which saturates when the balloons are inflated around their maximum size.

Figure 4.3 illustrates the system of gas injection of constant pressure. In order to inflate the balloons, we use the pressurized air system of the laboratory connected to the balloons through the valve 4, which allows the regulation of the inflation speed. There are two air inlets at the top of silo, linked with two groups of balloon. Both air inlets are connected firstly with an $Aalgorg$ gas flow
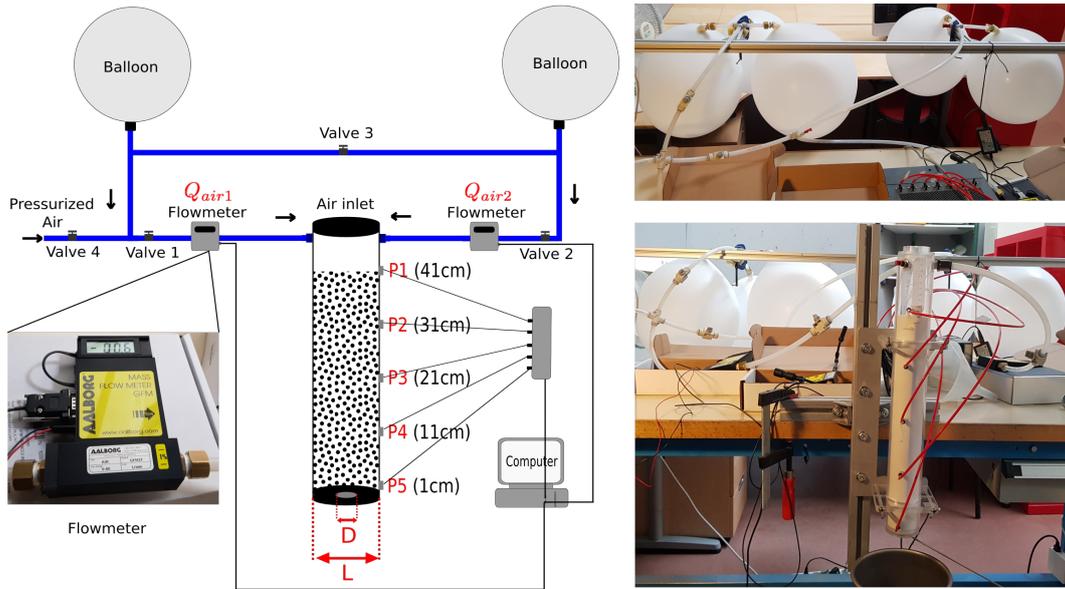
Figure 4.3: System for gas injection of constant pressure.

Table 4.2: Valve states

	Valve 1	Valve 2	Valve 3	Valve 4
Inflation of balloons	Closed	Closed	Open	Open
Discharge of silo	Open	Open	Open	Closed

meter (with various flow ranges of $0-5\,l/min$, $0-20\,l/min$ and $0-50\,l/min$), and then connected to the balloons through the valves 1 and 2. We put also a parallel connection between these two groups of balloon, controlled by the valve 3. The opening of valve 3 ensures the homogeneity of the pressure in all the balloons for both inflation and discharge periods. The states of the valves for the experimental preparation (inflation of balloons) and for the discharge of the silo are shown in the Table 4.2. To inflate the balloons, we open the valves 3 and 4, and close the valves 1 and 2. The pressurized air is then injected into the balloons until they reach approximately their maximum size. During this preparation phase, the silo outlet is closed with a plug. Then, we close the valve 4, we open the valves 1, 2 and 3 and the outlet is quickly opened manually. During the silo discharge, the pressurized air inside the balloons flows through the granular media. The total air flow rate is measured by the flow meters, determined by $Q_{air} = Q_{air1} + Q_{air2}$. Simultaneously, the pressure evolution along the silo are captured by the five pressure sensors $P_1 - P_5$.

4.1.4 Measurements

Several quantities were measured during the discharge of silo: the initial bulk particle volume fraction, the mass flow rate of particles, the volumetric flow rate of gas and the gas pressure along the silo.
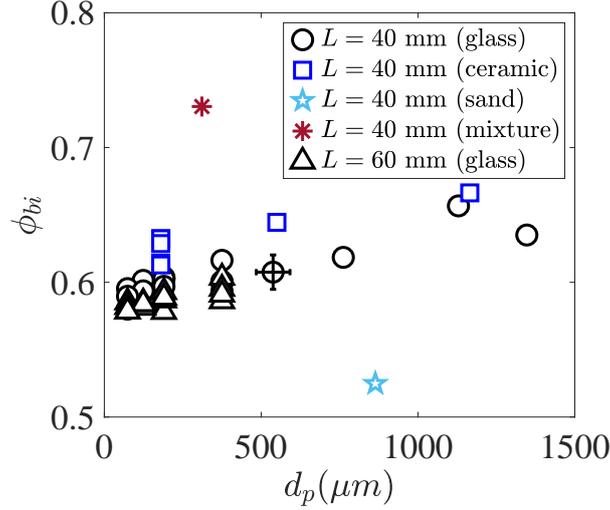
Figure 4.4: Initial bulk particle volume fraction ϕ_{bi} as a function of the mean particle size d_p.

a. Initial bulk particle volume fraction ϕ_{bi}

The silo of diameter L is initially filled by a column of particles of height h_p and of mass m_p, we can determine the initial bulk particle volume fraction by:

$$\phi_{bi} = \frac{4m_p}{\rho_p h_p \pi L^2} \tag{4.1}$$

Figure 4.4 illustrates the initial bulk particle volume fraction ϕ_{bi} as a function of the mean particle size d_p for cylindrical silos with various diameters ($L = 40$ mm and $L = 60$ mm). We observe a slight increase of the initial volume fraction with the mean particle size for the monodisperse spherical glass or ceramic particles. Moreover smaller silo leads to slight increase of the granular packing, comparing the $L = 40$ mm case with the $L = 60$ mm case. For the same silo size and comparing different granular materials (see the black circles for the glass particles and blue squares for the ceramic particles), we observe that the ceramic particle having a larger mass density forms a denser granular media than the glass particles. Furthermore, for the sand particles having a more angular shape, the volume fraction is smaller than that of spherical particles, meaning that the granular media is less compacted. The volume fraction of the bidisperse mixture is illustrated by the the red asterisk symbol, which is much larger than that of the monodisperse particles due to the fact that the gaps between the coarser particles can be filled by the finer ones (Cumberland and Crawford [1987]).

b. Mass flow rate of particles

During the discharge, all the particles are collected by a metal vessel weighted by an electronic balance ($Mettler\ Toledo\ 6002S$) with a precision of 0.1 g at a frequency of 20 Hz. Figure

4.5a shows a typical time evolution of the mass collected. The instantaneous mass flow rate is obtained by processing the local slope of the mass versus time during $\delta t = 1$ s, $Q_i(t) = (m(t + \delta t) - m(t))/\delta t$ (see Figure 4.5b). We observe that the discharge flow rate of the granular media seems to oscillate with a quite regular frequency, and such oscillation of the flow rate is observed for most of the performed experiments during our study.

(a)   (b)
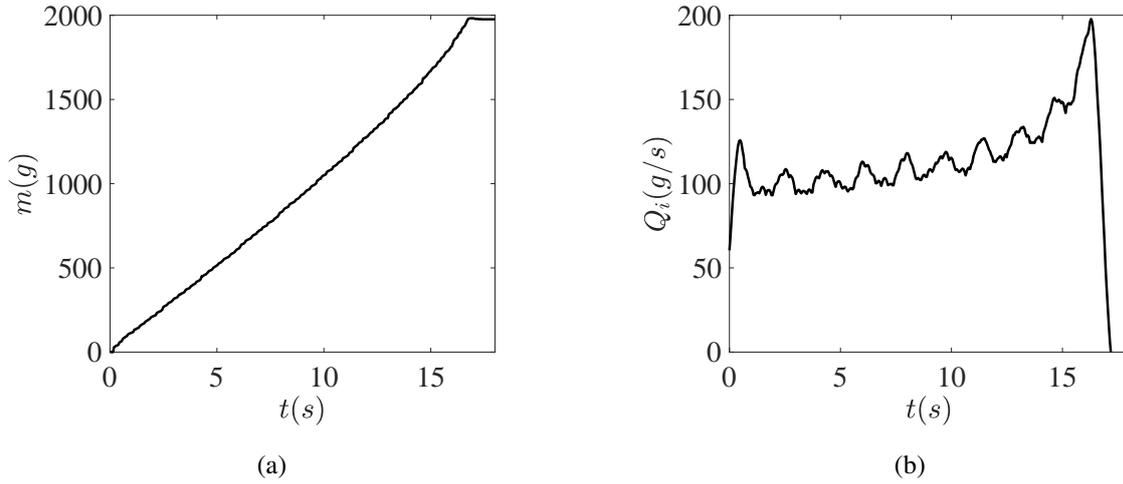
Figure 4.5: Typical result of the discharge of a silo with an imposed pressure of gas at the top of silo for $L = 40$ mm, $d_p = 180\mu m$ (ceramic) and $D = 10$ mm. (a) Temporal evolution of the mass of particles given by the balance. (b) Temporal evolution of the instantaneous mass flow rate Q_i.

In order to explain the origin of this oscillation, we performed a discharge of the silo filled by water and with the outlet immersed in water and a small outlet size $D \approx 5$mm, as shown in Figure 4.6a. Figure 4.6b shows the discharge flow rate of water as a function of time, we observe a decrease of the flow rate, consistent with the classical Torricelli law for liquid filled silo discharge. There is a regular frequency on the mass flow rate, similar to that we observed for the discharge of granular media. We now investigate the relation between the oscillation frequency and the discharge flow rate. As shown in Figure 4.6b, the instantaneous oscillation frequency is determined between two peak values, $f_i = 1/\delta t_i$, where the corresponding discharge flow rate is chosen at the middle time. Then in Figure 4.6c, we plot the frequency of oscillation as a function of the mass flow rate for both the discharge of the water and the granular media. For both cases, the data are superimposed and we observe that the frequency of oscillation increases as the discharge flow rate increases, and saturates for large flow rate. This suggests that this effect is not due to a physical effect but is linked to the balance. Indeed, the constructor specifies that the electronic balance has a response time about 1.5s for catching up a rapid variation of the mass signal. The saturated frequency value corresponds approximately to this stabilization time (see dashed line in Figure 4.6c). Therefore, the oscillations of the flow rate are due to the balance response and should not be considered in the following study.
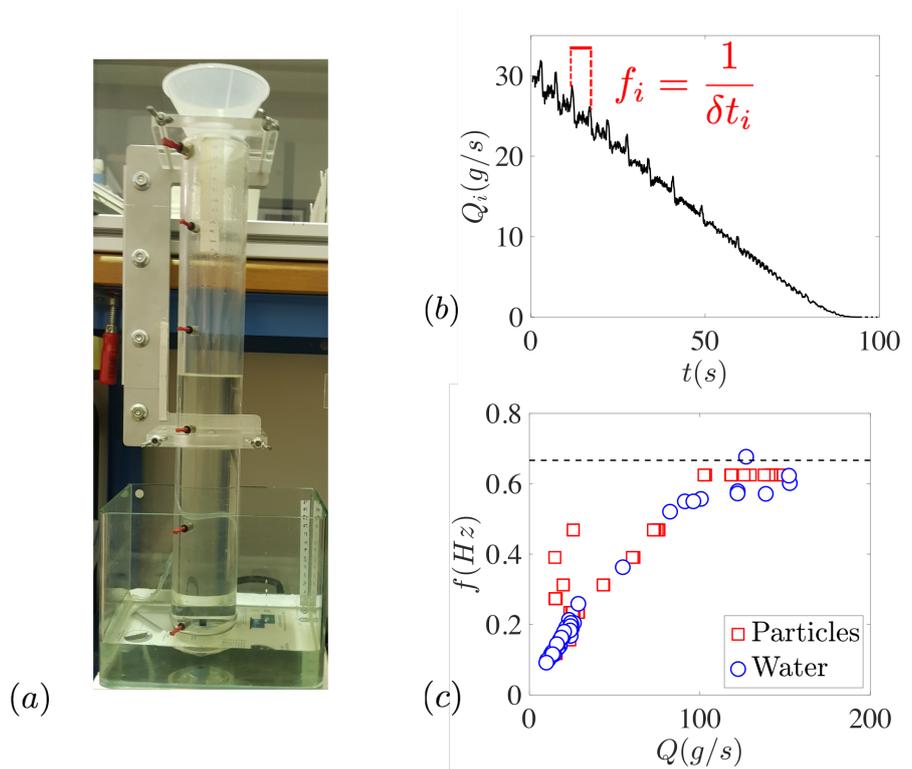
Figure 4.6: (a) Discharge of the silo filled with water. (b) Discharge flow rate of water as a function of time. (c) Frequency of the oscillation of the flow rate as a function of the discharge flow rate, for the granular media and the water. The dashed line represents the stabilization time of the electronic balance.

c. Volumetric flow rate of gas

The volumetric flow rate of gas is an important experimental measurement. Three $Aalgorg$ gas flow meters with various ranges of measurement are used during the experiment: $0 - 5\ l/min$, $0 - 20\ l/min$ and $0 - 50\ l/min$. They all have an accuracy from ± 1.5 to 3%, a maximal response time of 2 s and introduced a negligible pressure drop between the inlet and the outlet. The analog output signals consist of a voltage between 0 to 5 VDC and is acquired at a frequency of 100 Hz. The output signal is linearly proportional to the mass molecular flow rate of gas. A typical result of gas volumetric flow rate measured is shown in Figure 4.7 for ceramic particles of size d_p = $180\ \mu m$, silo diameter L = 40 mm and outlet size D = 10 mm.

d. Gas pressure along the silo

The five pressure sensors come from $Honeywell\ Sensing\ and\ Control$ company. These sensors measure differential pressures related to the atmospheric air pressure with a range of ± 75cm of water with an accuracy of 0.25%. These sensors are supplied with 5.0 VDC and connected with an acquisition device which has an acquisition frequency of 100 Hz. As shown in Figure 4.8a, pressure sensor has two pressure ports: one is connected with the measuring position and the
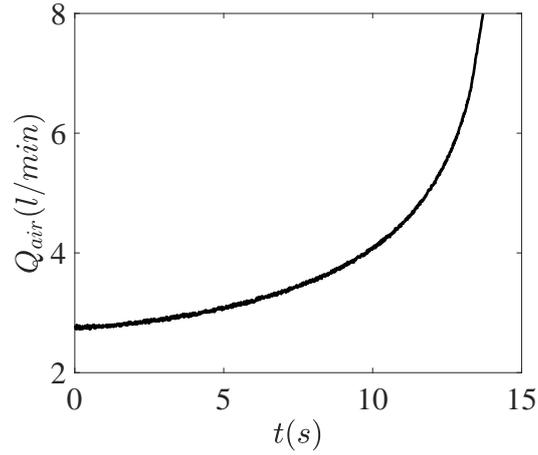
Figure 4.7: Temporal evolution of the volumetric flow rate of air for $L = 40$ mm, $d_p = 180\mu m$ (ceramic) and $D = 10$ mm.

other one is in the ambient environment. We thus measure a differential pressure $p^f = P^f - P_0$, where P^f is the absolute pressure and P_0 is the atmospheric pressure. We calibrated the pressure sensors by measuring the hydrostatic pressure of a tube filled with water (see Figure 4.8b). We observe a linear response for all of them, defining a relation between output voltages and pressure levels. These five pressure sensors are placed along the silo, the pressure sensor 5 located at an elevation of 1 cm from the silo bottom and the others are spaced 10cm apart (see Figure4.3).

(a)

(b)
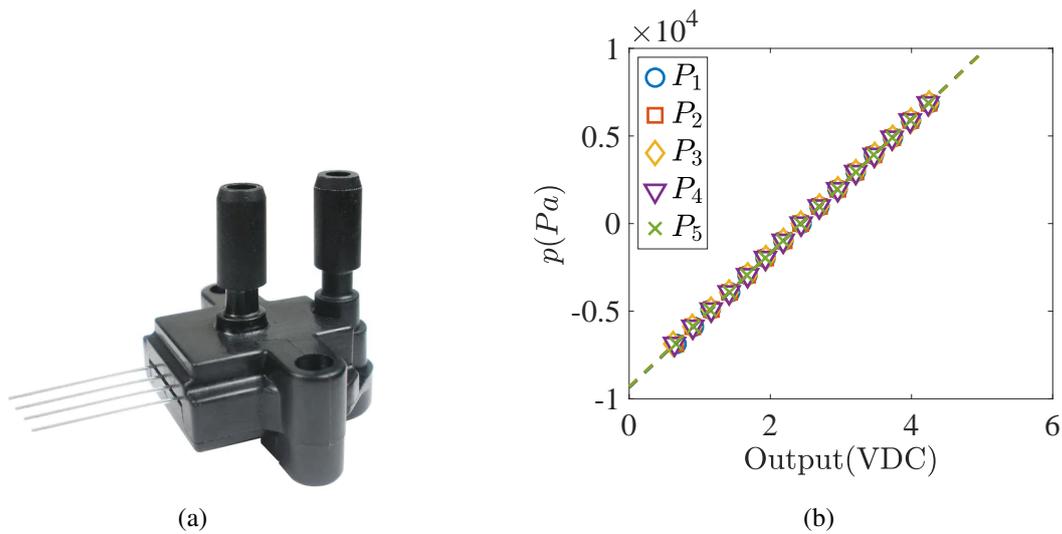
Figure 4.8: (a) Differential pressure sensor. (b) Calibration of the pressure sensors by measuring hydrostatic pressure of water.
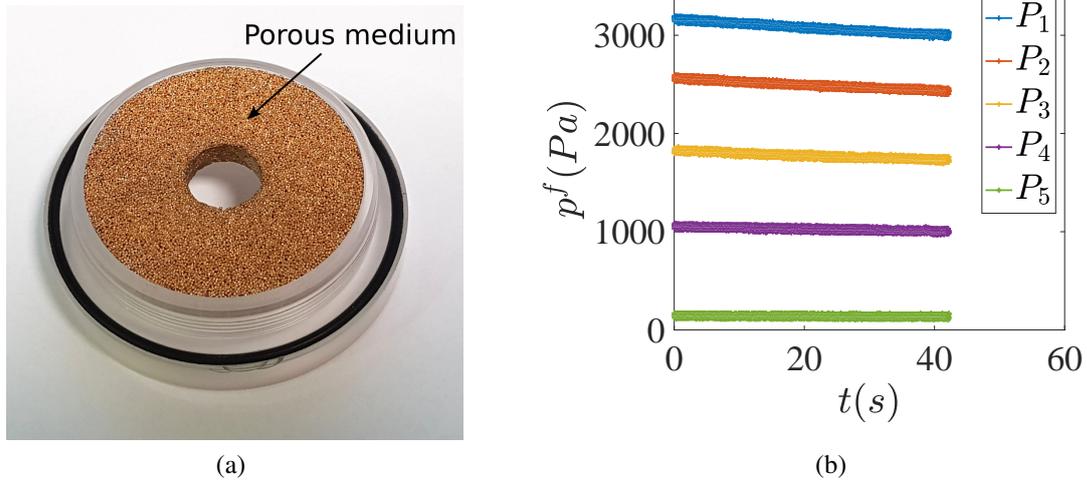
Figure 4.9: (a) Silo bottom with a porous media. (b) Temporal evolution of the pressure along the silo with motionless granular media, for $L = 40$ mm, $D = 10$ mm and $d_p = 180\ \mu m$ (ceramic).

4.1.5   Test of the gas injection system

This experimental setup is designed to maintain a quasi constant pressure at the top of silo during the discharge. This depends on several parameters:

- The gas having difficulty to pass through a low permeable media, it's easier to maintain a constant gas pressure for a granular column composed by fine particles.

- The maximum pressure level provided by the balloons is limited by the balloon material and its dimension. The gas inlet section and the tube diameters should be maximized, in order not to induce additional head loss between the balloon and the top of silo. We use tubes of diameter 12 mm.

- A constant gas pressure is easier to achieve for a smaller silo and a small outlet size.

For testing our gas injection system, we carry out a preliminary experiment using a special bottom plug with a porous medium (see Figure 4.9a). The idea is to examine the deflation behavior of the balloons, discharging through a fixed granular column, namely a static porous media. The bottom plug is composed by a metal porous medium, whose pore size is smaller than the testing particle size, so that the particles can not flow out of the silo, contrarily to the air, the outlet being closed using a solid rubber plug. A silo of diameter $L = 40$ mm is filled by a granular column of height $h_p \approx 40$ cm composed by ceramic particles of size $d_p = 180\ \mu m$. The balloons are inflated approximately to their maximal size with the valve 4 closed and the valves 1, 2 and 3 open. At time $t = 0$, we unlock the valves and the temporal evolution of the pressure profiles along the silo is measured by the pressure sensors, as shown in Figure 4.9b. P_1 represents the pressure

101

measurement at the higher elevation from the bottom of silo, $z_1 = 41$ cm and it is located above the granular media. We observe that the balloons are little deflated after 40 s and their pressure levels have decreased of about 4%. Note that the deflation time of the balloons is much greater than the typical granular discharge ($\approx$ 10 s). Therefore, we manage to maintain a quasi-constant gas pressure during the period of the discharge. For each experiment, we will verify from the air pressure measurement at the top of the silo (given by P_1) that this condition is satisfied. With this system, we can provide a range of overpressure around $[2000 - 4000]\ Pa$ above the atmospheric air pressure.

4.2   Experimental results

Thanks to the experimental setup presented previously, we have carried out a series of experiments for studying the discharge of a granular media out of a cylindrical silo with a constant gas pressure at its top, and an opening outlet in ambient air. Each experiment is repeated at least twice at the same experimental conditions, with a small variation on the imposed gas pressure level which depends slightly on the inflation size of the balloons. The experimental parameters are displayed in Table 4.3. Unless specified, we will present mainly the results acquired for a configuration of silo diameter $L = 40$ mm and of outlet size $D = 10$ mm: for those parameter values, we obtain long discharge period as well as a good performance for maintaining a constant gas pressure, that facilitates the analysis of the experimental results. In the following subsections, we will discuss firstly the mass flow rate of particles and then the gas flow, especially the evolution of the pressure profiles in the silo.

Table 4.3: Experimental parameters.

L	D	d_p
20mm	10mm	Glass particles: $[124;\ 190;\ 375;\ 538;\ 762;\ 1129;\ 1347]\mu m$
$[40;\ 60]$mm	$[10;\ 20]$mm	Ceramic particles: $[180;\ 550;\ 1165]\mu m$ Sand: $864\mu m$ Bidisperse mixture (ceramic particles): 50% mass of $d_p^f = 180\mu m$ and $d_p^f = 1165\mu m$

4.2.1   Mass flow rate of particles

a.   Discharge driven by gravity

As a reference, we have first studied the discharge of a silo driven by gravity (without gas injection). Our silo configurations are similar to that used by Benyamine et al. [2014] and Zhou [2016] who studied experimentally the discharge of a silo driven by gravity, which permits to compare our experimental results.
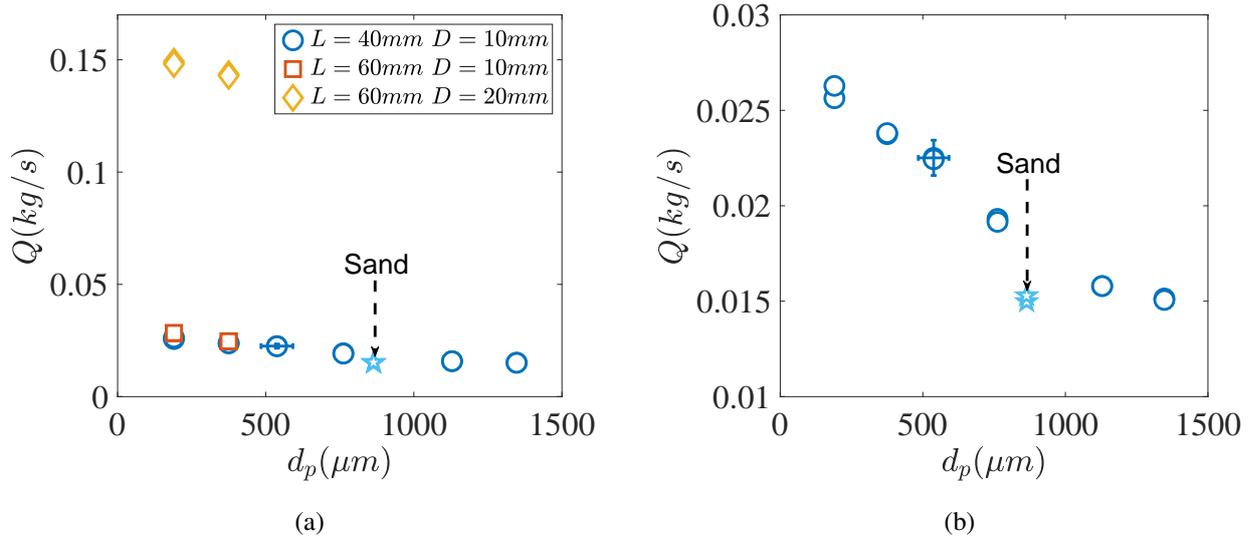
Figure 4.10: Mass flow rate Q as a function of the particle size d_p for glass particle and hydrophobic sand ($\star$). (a) two silo diameters L and two outlet sizes D. (b) $L = 40$ mm and $D = 10$ mm.

During the discharge of the silo, we observe that the mass flow rate reaches rapidly a stationary value. The mean mass flow rate Q is determined by averaging the instantaneous mass flow rate during the stationary state. Figure 4.10a illustrates the mass flow rate of the granular media out of the silo versus the particle size for various silo diameters and outlet sizes. Note that only the results of glass and sand particles ($\star$) are presented here. We observe that the mass flow rate has a strong dependency on the outlet size while being rather insensible to the silo diameter. According to Figure 4.10b for $L = 40$ mm and $D = 10$ mm, the mass flow rate depends moderately on the particle size, it tends to decrease as particle size increasing. For the sand particles with angular shapes, its mass flow rate is slightly lower than that of the spherical particles, a tendency that we assume being related to the initial lower packing fraction.

Following previous authors (Hagen [1852], Beverloo et al. [1961], Janda et al. [2012], Benyamine et al. [2014], Zhou [2016]), we have plotted in Figure 4.11a, the mass flow rate normalized by $\phi_b \rho_p \sqrt{g d_p^5}$ versus D/d_p, for all granular materials studied: glass particles, ceramic particles and sand particles ($\star$). In this representation, the data are superimposed and well adjusted by equation 2.26 (see the dashed line in the figure) with coefficients $c_D = 0.62$, $\alpha = 0.84$ and $\beta = 0.07$, very close to that obtained by Benyamine et al. [2014] ($c_D = 0.75$, $\alpha = 0.96$ and $\beta = 0.09$) and Zhou [2016] ($c_D = 0.54$, $\alpha = 0.81$ and $\beta = 0.08$), which shows that the flow rate obeys mainly the Hagen-Beverloo law $Q \propto D^{5/2}$ with a small dependence with the particle diameter.

To identify more precisely the geometrical function $G\left(\frac{D}{d_p}\right)$, we plot the mass flow rate normalized by $\phi_b \rho_p \sqrt{g D^5}$ versus D/d_p in Figure 4.11b. All the points can be well fitted by the geometrical function $\phi_0/\phi_b \propto G\left(\frac{D}{d_p}\right) = \left[1 - \alpha e^{-\beta \frac{D}{d_p}}\right]$, predicted by equation 2.26. We interpret this effect as being related to a dilation: for a smaller orifice ($D < 50 d_p$), the particles need to
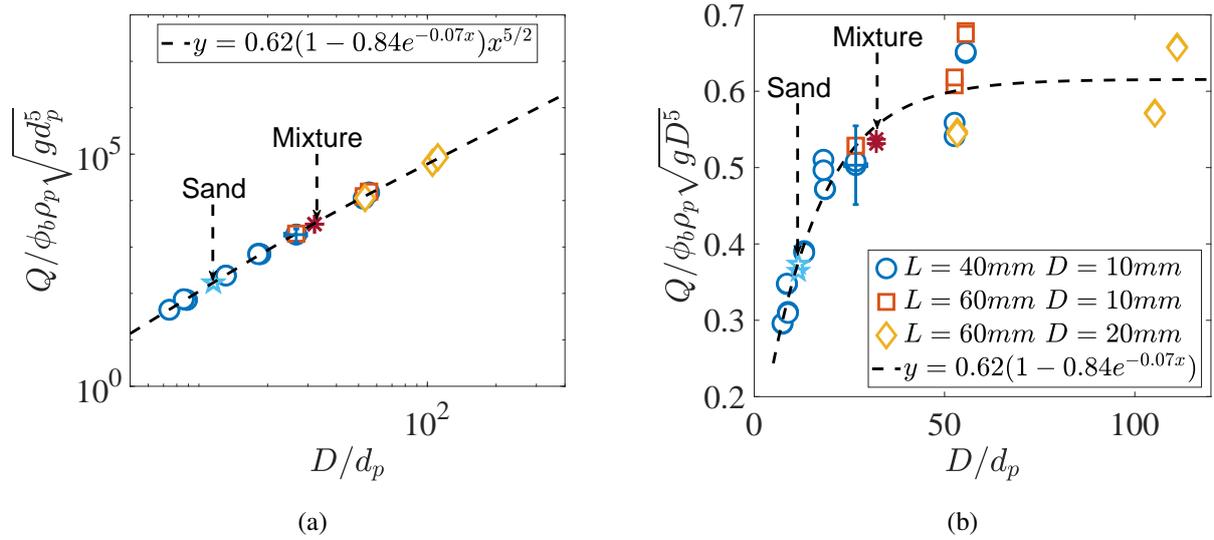
Figure 4.11: Discharge of cylindrical silo driven by gravity: mass flow rate of particles normalized by (a) $\phi_b\rho_p\sqrt{gd_p^5}$ and (b) $\phi_b\rho_p\sqrt{gd_p^5}$, versus aspect ratio D/d_p. The black dotted line represents equation 2.26 with coefficients $c_D = 0.62$, $\alpha = 0.84$ and $\beta = 0.07$.

dilate to cross the outlet. In Figure 4.11, we also plot the data for the sand particles and the bidisperse mixture. We observe that the sand (☆) behaves as the spherical particles. For the bidisperse mixture ∗, we observe that the data lay with the others if we consider the Sauter mean diameter, defined by: $\bar{d}_p = \frac{1}{X_f/d_p^f+(1-X_f)/d_p^c}$, where $X_f = 0.5$ represents the mass fraction of fine particles, d_p^c is the mean diameter of the coarser particles and d_p^f is that of the finer particles.

This study of the discharge of a silo driven by gravity, as well as the study of the discharge of a silo with injection of a constant gas flow carried out by Zhou [2016] will be references for investigating the role of an imposed gas pressure on the granular discharge flow. In the following, we will denote Q_0 the mean mass flow rate of discharge of a silo driven by gravity.

b. Silo discharge coupled with a pressurized gas

Figure 4.12 shows a typical result of the discharge while maintaining an overpressure at the top of the silo. In Figure 4.12a, it is observed that the granular flow rate increases with time and is always larger than that corresponding to the gravity driven case. During the silo discharge, the height of granular column decreased. This diminution of the granular height facilitates the passage of gas, and simultaneously increases the gas pressure gradient through the granular media. As a result, the gas flow at higher velocity. As shown in Figure 4.12b, where we observe that the air flow rate also continuously increases with time, then the gas flow pushes harder on the particles and increases the mass flow rate of discharge.

To investigate more precisely the role of the air flow on the granular flow, different controlling

(a)

(b)
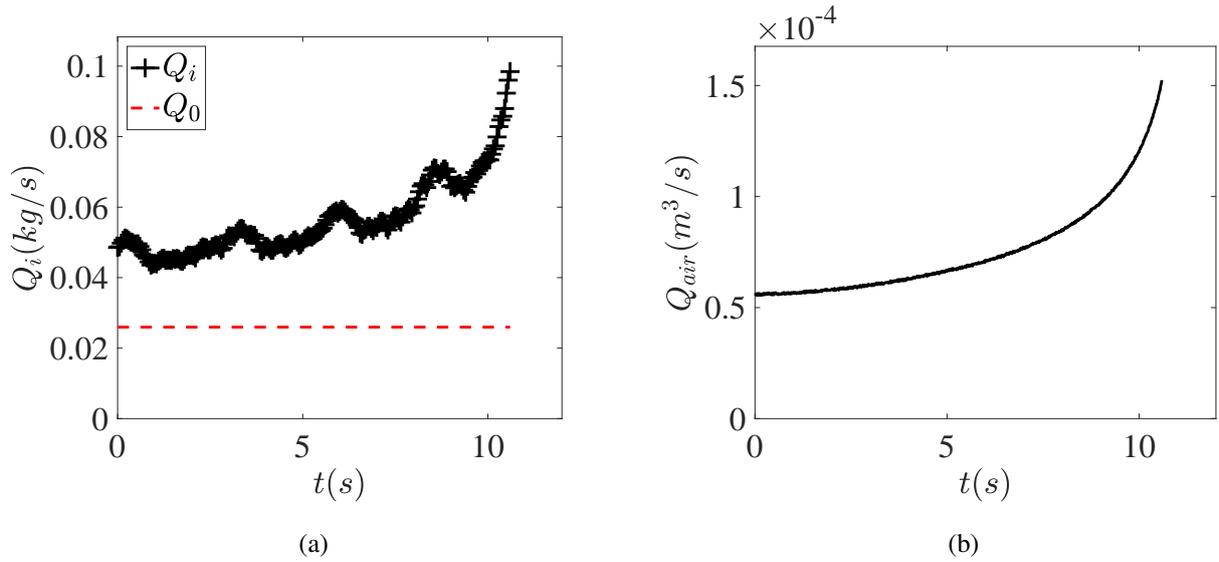
Figure 4.12: Temporal evolutions of (a) the granular mass flow rate and (b) the volumetric flow rate of gas for L = 40mm, D = 10mm and d_p = 190μm (glass particles). The red dashed line represents the mean mass flow rate of discharge without gas injection, Q_0.

parameter are varied during the study, including the silo diameter L, the outlet diameter D and also the particle size d_p.

Firstly, we focus on the influence of the silo and the outlet sizes on the mass flow rate of particles. Figure 4.13a illustrates the mass flow rate of particles as a function of the volumetric

(a)

(b)
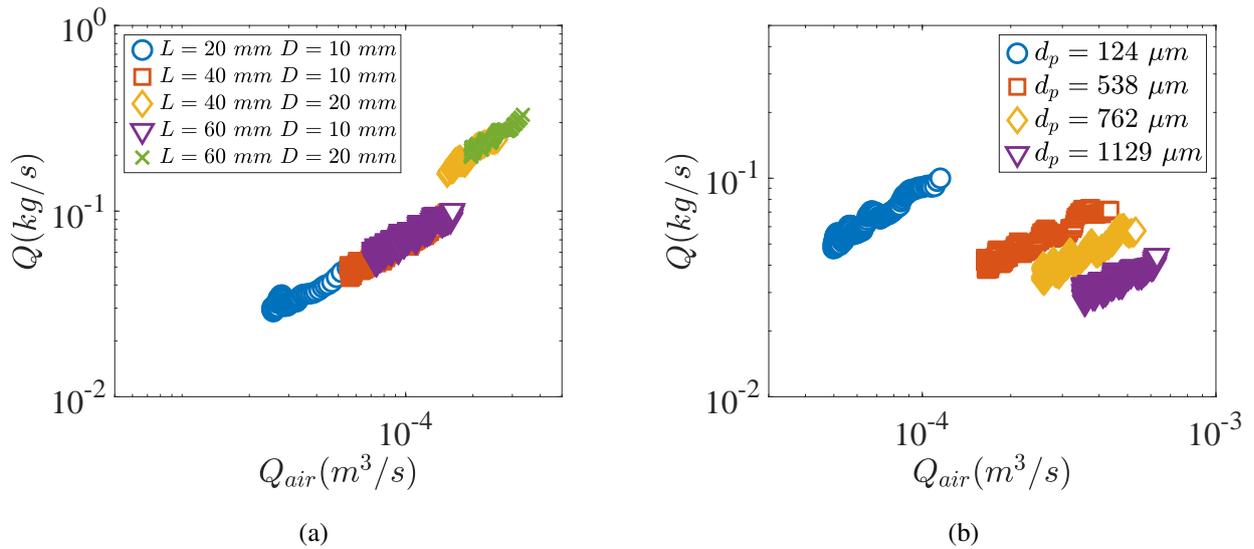
Figure 4.13: Mass flow rate of the granular media as a function of the volumetric air flow rate for (a) various silo sizes and outlet diameters with glass particles of size d_p = 190 μm (b) different glass particle sizes with L = 40 mm and D = 10 mm.

flow rate of air injected for various L and D. First of all, we observe that the discharge rate of granular media Q increases with the volumetric flow rate of gas Q_{air}. Note that the range of volumetric air flow rate that can be investigated with our device varies with the silo and the outlet dimension. For a given particle size, the discharge flow rate of granular media is more important for a larger outlet size, whereas for each (either 10mm or 20mm) outlet size, the relation between Q_{air} and Q is independent from the other geometrical parameters.

Secondly, we focus on the influence of the particle size on the mass flow rate of particles. Figure 4.13b illustrates the mass flow rate of particles as a function of the volumetric air flow rate for various particle sizes with the same silo diameter $L = 40$mm and outlet size $D = 10$mm. The other parameters being kept constant, the particle flow rate increases when the particle size decreases. A granular media composed by coarser particles, having a higher permeability, the air flow resistance is lower which corresponds to a lower momentum transfer from the air flow toward the particles and thus a lower driving force applied on the granular flow.
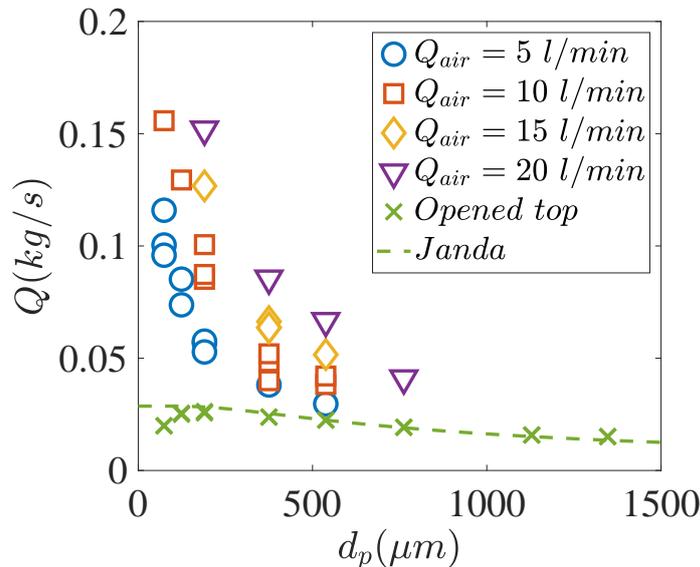
Figure 4.14: Mass flow rate of the granular media as a function of the particle size for various instantaneous air flow rate. The green dashed line represents equation 2.26 with c_D = 0.62, α = 0.84 and β = 0.07.

Additionally, to investigate more precisely the influence of the particle sizes, we plot the instantaneous mass flow rate of particles versus the particle sizes in Figure 4.14 for different given instantaneous air flow rate. The mass flow rate of the discharge driven by gravity without gas injection (×) can be well described by the Janda law (−− see equation 2.26). Four typical air flow rates are chosen in a range of $5 - 20 \; l/min$, and we observe that an injection of air flow increases significantly the mass flow rate of particles, especially for the fine particles, compared to the opened top case. For a given air flow rate, the mass flow rate of particles decreases as the particle size increases and it tends to the opened top cases for the larger particle size.

These observations are similar with the results obtained by Zhou [2016] for the discharge of a silo driven by a constant gas flow rate. It indicates that the air flow plays an important role on the mass flow rate of particles and this phenomenon depends strongly on the permeability of the granular media. Therefore, in the following part, we will investigate in detail the air flow properties during the discharge period.

4.2.2 Air flow

Thanks to the five pressure sensors, we measured the temporal evolutions of the air pressure during the discharge. A typical evolution is represented in Figure 4.15a. We observe that in this case, the total time of the discharge is around fourteen seconds. The evolution of P_1 (+) corresponding to the pressure sensor connected to the position z_1 = 41cm, indicates a quasi-constant pressure level at the top of the silo during the discharge. The pressures at the others elevations increase with time due to the diminution of the granular column height, then they match with P_1 when the surface of the granular media goes by the pressure sensor position.
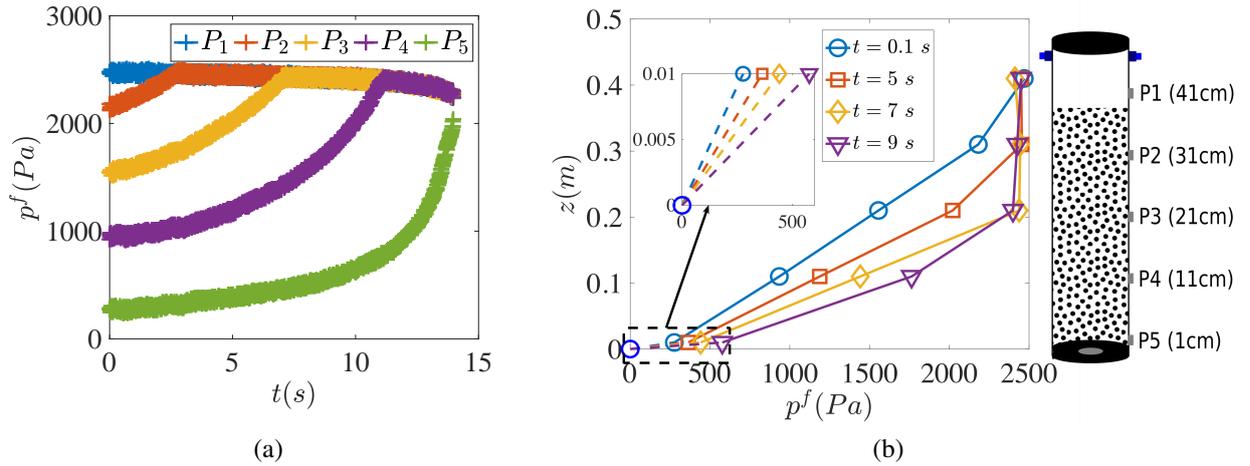
Figure 4.15: Discharge of the silo with an imposed air pressure at the top of the silo, with L = 40mm, D = 10mm and d_p = 180μm (ceramic particles). (a) temporal evolution of the gas pressure $P_1 - P_5$. (b) profiles of the gas pressure along the silo at various instants.

To investigate the spatial and temporal evolution of the pressure profiles along the silo, we plot in Figure 4.15b the instantaneous pressure at different moments ($0.1s$, $5s$, $7s$, $9s$) as a function of their elevations above the silo bottom. The origin, z = 0cm corresponds to the outlet which is at the atmospheric air pressure, namely p^f = 0Pa (○). At the very beginning of discharge t = 0.1s (○), a linear relation is observed for the zone far from the outlet position (from P_2 at z_2 = 31cm to P_5 at z_5 = 1cm). The change of slope between P_1 at z_1 = 41cm and P_2 at z_2 = 31cm is due to the partial filling by granular media between these two pressure taps. Another change of slope is observed at the zone nearby the outlet position between P_5 corresponding to z_5 = 1cm and the
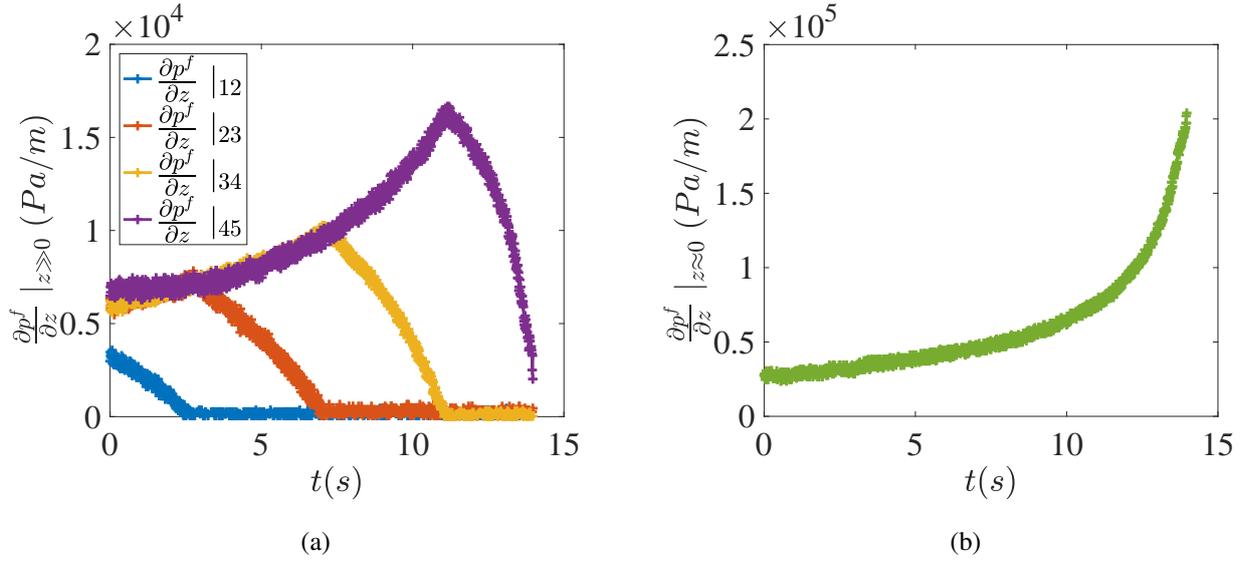
Figure 4.16: Temporal evolution of pressure gradient for (a) the zone far from the outlet $\frac{\partial p^f}{\partial z}\mid_{z\gg0}$ and (b) the zone nearby the outlet $\frac{\partial p^f}{\partial z}\mid_{z\approx0}$, with $L = 40\ mm$, $D = 10\ mm$ and $d_p = 180\ \mu m$ (ceramic particles).

outlet, due to the change of the section of passage of the flow from L to D. The pressure gradient near the outlet increases as a function of time, as shown in the enlarge box in Figure 4.15b.

We can thus distinguish the whole silo in two zones to estimate the vertical pressure gradient along the silo.

- Pressure gradient far from outlet:

  The pressure gradient far from outlet can be estimated by:

$$\frac{\partial p^f}{\partial z}\mid_{z\gg0}(t) = \frac{dp^f}{dz}\mid_{z\geq h_1}(t) \tag{4.2}$$

  where $h_1 \approx D$. If we suppose a linear relation of the pressure in this zone, corresponding to a vertical incompressible flow, we can define:

$$\frac{\partial p^f}{\partial z}\mid_{ij} = \frac{P_i - P_j}{z_i - z_j} \tag{4.3}$$

  Where i and j correspond of index of pressure sensor. Figure 4.16a illustrated the temporal evolution of the pressure gradient at the zone far from the outlet, defined by equation 4.3 using the measurements of $P_1 - P_5$. In this zone, the date are superimposed while the pressure taps are completely immersed in the granular media, which validates the previous hypothesis. The air pressure gradient far from the outlet increases as a function of time.

108

Then the curves rapidly drop toward zero when the pressure taps in the air reservoir are above the granular media.

- Pressure gradient nearby outlet:

We use the P_5 measurement to estimate the pressure gradient in this area as $z_5 \approx 1\text{cm} \approx D$:

$$\frac{\partial p^f}{\partial z} \mid_{z\approx 0} (t) = \frac{P_5}{z_5}(t) \tag{4.4}$$

In this zone, due to the cross section restriction, the air velocity increases and the flow is no longer purely vertical. An example of the temporal evolution of the pressure gradient in the zone nearby the outlet is illustrated in Figure 4.16b.

According to all the previous experimental observations, in the following part, we develop a quasi-steady model based on a two-phase continuum modelling to describe these experimental results.

4.3 Quasi-steady model

4.3.1 Two-phase modelling

Following Zhou [2016], we use the framework of the two-phase continuum modelling developed by Jackson [2000] (equations 2.6 to 2.9 in chapter 2) and we use the same choice of closure relationships for the fluid-grain interaction force as developed below presented in section 4.2 and the stress tensors of each phase.

Then according to the study carried out by Jackson [2000], the interaction forces between two phases can be decomposed into two parts: one part is related to the buoyancy force $\phi \frac{\partial \sigma_{ij}^f}{\partial x_j}$, the other part is due to the drag force between the phases f_{ti}.

$$f_i = \phi \frac{\partial \sigma_{ij}^f}{\partial x_j} + f_{ti} \tag{4.5}$$

The air flow rate for all our experiments fall into a range of $Q_{air} \approx [1 - 40]l/min$ and the particulate Reynolds number of the air given by $Re_p = \rho_f u^f d_p/\eta \sim \rho_f Q_{air} d_p/(\eta S_0)$, varies in a range of $[1 - 800]$. Thus, Darcy-Forchheimer resistance law (see equation 4.6) is applied for determining the drag force between air phase and granular media.

$$f_{ti} = \beta_l(\phi, d_p)\eta(1 - \phi)^2(u_i^f - u_i^p) + \beta_i(\phi, d_p)\rho_f d_p(1 - \phi)^3(u_i^f - u_i^p) \mid (u_i^f - u_i^p) \mid \tag{4.6}$$

where the permeability of the granular media is determined by the Kozeny-Carman equation as the materials are composed by quasi-spherical particles for most cases of study, so we have $\beta_l(\phi, d_p) = \frac{150\phi^2}{(1-\phi)^3 d_p^2}$ and $\beta_i(\phi, d_p) = \frac{1.75\phi}{(1-\phi)^3 d_p^2}$.

Following the study carried out by Jop et al. [2006], the shear-dependent frictional rheology $\mu(I)$ is applied for describing the behavior of granular flow (equations 2.4 and 2.5 in chapter 2).

We also follow the same assumptions than Zhou [2016] to simplify this two-phase continuum modelling:

- We assume that the fluid phase relaxes instantaneously which means that the inertial term is neglected with respect to the drag force in the fluid momentum conservation and we also neglect the gravity term. The assumptions are valid as long as $D \gg d_p$ (Zhou [2016]) and $Fr_p = (u^f - u^p)^2 / g d_p \approx Q_{air}^2 / (g d_p D^2) \gg \beta_i^{-1} d_p^{-2}$, where Fr is the Froude number defined on the particle size.

- The viscous stresses in the fluid phase are negligible with respect to the drag viscous term, as long as $D^2 \gg \beta_l^{-1}$. Therefore, the fluid stress tensor simply reduces to an isotropic pressure term, as $\sigma_{ij}^f = -p^f \delta_{ij}$.

For convenience we introduce a volume average velocity of mixture, $U_i = \phi u_i^p + (1 - \phi) u_i^f$. Under all the previous assumptions, the two-phase continuum modelling equations can be written under a simplified form as follows:

$$\frac{\partial U_i}{\partial x_i} = 0 \tag{4.7}$$

$$\frac{\partial \phi}{\partial t} + \frac{\partial (\phi u_i^p)}{\partial x_i} = 0 \tag{4.8}$$

$$-\frac{\partial p^f}{\partial x_i} = \beta_l \eta_f (U_i - u_i^p) + \beta_i \rho_f d_p (U_i - u_i^p) \mid U_i - u_i^p \mid \tag{4.9}$$

$$\rho_p \phi \left[\frac{\partial u_i^p}{\partial t} + u_j^p \frac{\partial u_i^p}{\partial x_j} \right] = \frac{\partial \sigma_{ij}^p}{\partial x_j} - \frac{\partial p^f}{\partial x_i} + \phi \rho_p g_i \tag{4.10}$$

In such conditions, the fluid pressure gradient reduces to the drag force. In the next part, we will use the pressure gradient to evaluate the drag force and compare it with the Darcy-Forchheimer resistance law given by equation 4.6.

4.3.2 Drag force measurement

a. Zone far from the outlet

Far from the outlet, the flow can be considered as purely vertical, thus, the instantaneous pressure gradient reads:

$$\frac{\partial p^f}{\partial z} \mid_{z \gg 0}^{t_i} \approx -\eta \beta_l (\phi_b, d_p) \left(U_z \mid_{z \gg 0}^{t_i} - u_z^p \mid_{z \gg 0}^{t_i} \right) - \rho_f d_p \beta_i (\phi_b, d_p) \left(U_z \mid_{z \gg 0}^{t_i} - u_z^p \mid_{z \gg 0}^{t_i} \right)^2 \tag{4.11}$$

where $U_z \mid_{z \gg 0}^{t_i} = \phi_b u_z^p \mid_{z \gg 0}^{t_i} + (1 - \phi_b) u_z^f \mid_{z \gg 0}^{t_i}$ is the volume average instantaneous vertical velocity of mixture, $u_z^p \mid_{z \gg 0}^{t_i}$ is the instantaneous particle vertical velocity.

110

The volume average velocity of mixture is deduced from the measurement of the volumetric air flow rate injected into the silo $Q_{air}(t)$, considering the mixture as an incompressible medium.

$$U_z \mid_{z \gg 0}^{t_i} = \frac{-Q_{air}(t_i)}{S_b} \tag{4.12}$$

where $S_b = \pi L^2/4$ is the cross section of the silo.

In the same way, the instantaneous velocity of particles far from the outlet $u_z^p \mid_{z \gg 0}^{t_i}$ is deduced from the mass flow rate of particles $Q(t)$, considering the granular phase incompressible. Let us also note that this velocity is simply the variation of the granular column height h_p with time.

$$u_z^p \mid_{z \gg 0}^{t_i} = \frac{-Q(t_i)}{\phi_b \rho_p S_b} = \frac{dh_p(t_i)}{dt} \tag{4.13}$$

where ρ_p is the density of particles.

Thus, equation 4.11 can be expressed as follows:

$$\frac{\partial p^f}{\partial z} \mid_{z \gg 0}^{t_i} \approx \eta \beta_l(\phi_b, d_p) \frac{Q_{air}(t_i) - Q(t_i)/(\phi_b \rho_p)}{S_b} + \rho_f d_p \beta_i(\phi_b, d_p) \left(\frac{Q_{air}(t_i) - Q(t_i)/(\phi_b \rho_p)}{S_b} \right)^2 \tag{4.14}$$

Let us consider the pressure gradient estimated from P_4 and P_5 measurement. Figure 4.17a illustrates the pressure gradient at the zone far from the outlet as a function of the relative velocity between the air flow and the granular flow $\left[Q_{air} - Q/\rho_p \phi_{bi} \right]/S_b$. Note that the particle velocity far from the orifice is determined using the initial bulk volume fraction ϕ_{bi}. Indeed, we assume that the volume fraction varies slightly compared to its initial value during the discharge. Moreover, the volume flow rate of particles $Q/\phi_{bi}\rho_p$ is much lower compared to that of the air flow Q_{air}, leading to negligible error. Each curve represents a different particles sizes for $L = 40\ mm$ and outlet size $D = 10\ mm$. Each curve is well represented by equation 4.14 (see the dashed lines), adjusting the coefficient ϕ_b in the permeability terms, using the least squares method. As predicted by equation 4.14, the slope of each curve depends strongly on the particle size through the permeability, thus, the smaller the particle, the larger the slope. Interestingly, the bidisperse mixture ($*$ for ceramic particles $d_p = 180\ \mu m$ and $d_p = 1165\ \mu m$) exhibits a larger slope than its finer component ($d_p = 180\mu m$), due to higher volume fraction, the finer particles filling the pores among the coarser particles.

Figure 4.17b displays the ratio between ϕ_b obtained previously and the initial bulk volume fraction ϕ_{bi} as a function of the particle sizes d_p for various silo diameters L and outlet sizes D, where we use the Sauter diameter $\bar{d}_p = \frac{1}{X_f/d_p^f + (1-X_f)/d_p^c}$ for the mixture. The black dashed line represents the equation $\phi_b = \phi_{bi}$. Globally, the ratio ϕ_b/ϕ_{bi} falls in a range $[0.9 - 1.1]$, the mean value $< \phi_b > = 0.95\phi_{bi}$ indicates that the spherical particles tend to dilate very slightly during the discharge, contrary to the sand which tends to compact with $\phi_b = 1.15\phi_{bi}$, however, this effect stays negligible.

The previous observations validate using the Darcy-Forchheimer resistance law with the Kozeny-
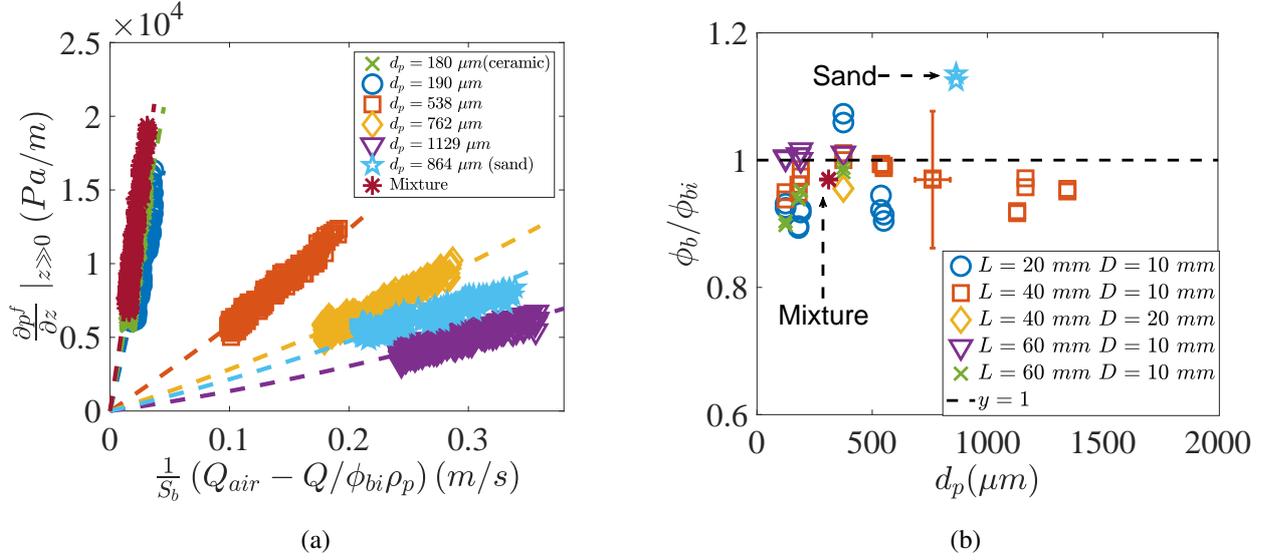
Figure 4.17: (a) Pressure gradient measured by the pressure sensors at the zone far from the outlet $\frac{\partial p^f}{\partial z} \mid_{z \gg 0}$ as a function of $\left[Q_{air} - Q/\rho_p \phi_{bi} \right] / S_b$ with $L = 40\ mm$ and $D = 10\ mm$ for various particle sizes d_p. The dashed lines correspond to equation 4.14 adjusting ϕ_b which is plotted in (b) normalized by the initial bulk volume fraction ϕ_{bi} as a function of particle size d_p for various silo diameters L and outlet sizes D. The horizontal line represents $\phi_b = \phi_{bi}$.

Carman equation to describe the drag force between the air flow and the granular media far from the outlet.

b.   Zone nearby the outlet

Following Zhou [2016], we assumed that the flow is unidirectional at the zone nearby the outlet. Therefore, the drag force between the two phases at the center of the outlet can be also determined by the Darcy-Forchheimer resistance law, as follows:

$$\frac{\partial p^f}{\partial z} \mid_{z \approx 0}^{t_i} \approx -\eta \beta_l(\phi_0, d_p) \left(U_z \mid_{z \approx 0}^{t_i} - u_z^p \mid_{z \approx 0}^{t_i} \right) - \rho_f d_p \beta_i(\phi_0, d_p) \left(U_z \mid_{z \approx 0}^{t_i} - u_z^p \mid_{z \approx 0}^{t_i} \right)^2 \qquad (4.15)$$

Where ϕ_0 represents a local volume fraction of particles nearby the outlet. Again assuming incompressibility of the different phases, we evaluate the relative velocity:

$$U_z \mid_{z \approx 0}^{t_i} - u_z^p \mid_{z \approx 0}^{t_i} = -\left(\frac{Q_{air}(t_i)}{S_0} - \frac{Q(t_i)}{\phi_{bi} \rho_p S_0} \right) \qquad (4.16)$$

where $S_0 = \pi D^2 / 4$ represents the cross section of outlet and we thus obtain:

$$\frac{\partial p^f}{\partial z} \mid_{z \approx 0}^{t_i} \approx \eta \beta_l(\phi_0, d_p) \frac{Q_{air}(t_i) - Q(t_i)/(\phi_{bi} \rho_p)}{S_0} + \rho_f d_p \beta_i(\phi_0, d_p) \left(\frac{Q_{air}(t_i) - Q(t_i)/(\phi_{bi} \rho_p)}{S_0} \right)^2 \qquad (4.17)$$

Here, the pressure gradient of fluid at the outlet is determined by equation 4.4 thanks to the pressure sensor P_5 located at the position $z_5 = 1cm$ above the silo bottom. Figure 4.18a illustrates
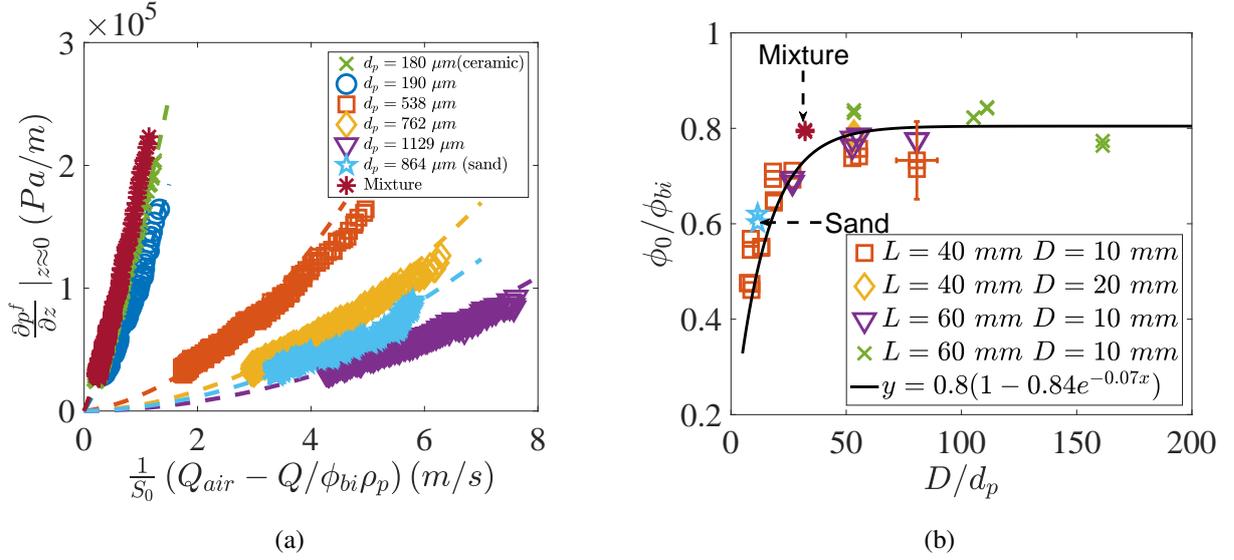
Figure 4.18: (a) Pressure gradient measured by pressure sensor P_5 at the zone nearby the outlet $\frac{\partial p^f}{\partial z}\mid_{z\approx0}$ as a function of $\left[Q_{air} - Q/\rho_p\phi_{bi}\right]/S_0$ with $L = 40\ mm$ and $D = 10\ mm$ for various particle sizes d_p. The dashed lines represent equation 4.17 with the fitting parameter ϕ_0 plotted in (b) normalized by the initial bulk volume fraction ϕ_{bi} as a function of aspect ratio D/d_p for various silo diameters L and outlet sizes D. The black solid line represents the equation 4.18 with the coefficients $\xi_\phi = 0.80$, $\alpha = 0.84$ and $\beta = 0.07$.

the pressure gradient at the outlet as a function of the relative velocity between the air flow and the granular flow at the outlet $\left[Q_{air} - Q/\rho_p\phi_{bi}\right]/S_0$ for various particle sizes and materials with $L = 40mm$ and $D = 10mm$. The dashed lines represent equation 4.17, ϕ_0 being fitted using the least squares method. We observe that equation 4.17 represents fairly well the experimental datas for all granular material types, including the glass, ceramic (×) and sand (☆) particles, as well as the bidisperse mixture (∗).

In Figure 4.18b, we plot ϕ_0 obtained previously normalized by the initial volume fraction ϕ_{bi} as a function of the aspect ratio D/d_p for various silo diameters L and outlet sizes D. This value can be interpreted as a dilation of the particles at the outlet of silo. Indeed the variation of the ratio ϕ_0/ϕ_{bi} with respect to D/d_p can be represented by the geometrical function 4.18 with coefficients $\xi_\phi = 0.80$ and the same coefficients ($\alpha = 0.84$, $\beta = 0.07$) than for the gravity driven experiment.

$$\frac{\phi_0}{\phi_{bi}} = \xi_\phi G(D/d_p) = \xi_\phi\left[1 - \alpha e^{-\beta D/d_p}\right] \qquad (4.18)$$

According to all the previous observations, we can conclude that the pressure gradients along the silo can be well described by the Darcy-Forchheimer resistance law, with the permeabilities of the granular media given by the Kozeny-Carman equation, taking into account the dilation of the particles nearby the outlet. This validates some of the assumptions in section 4.3.1 to obtain the simplified two-phase continuum modelling equation 4.7 - 4.10. In the next section, we propose an

analytical model based on these equations.

4.3.3 Quasi-steady analytical model

In this part, we will propose a quasi-steady analytical model based on the work of Zhou [2016] who proposed a steady analytical model for predicting the discharge granular flow rate out of a silo with a constant air flow rate imposed at its top.

a. Simple analytical model

Based on the studied of Crewdson et al. [1977] and Zhou [2016], and on the momentum equation of the granular phase (see equation 4.10), we suppose that the air flow just acts as an additional driving force. The discharge flow being controlled by the outlet, we thus suppose that the discharge flow rate of particles driven by gravity Q_0 is modified by the pressure gradient of the fluid at the zone around the outlet:

$$Q(t) = Q_0 \left(1 + \frac{1}{\phi_0 g \rho_p} \frac{\partial p^f}{\partial z} \mid_{z \approx 0} (t) \right)^{1/2} \tag{4.19}$$

To verify this approximation, we compare in Figure 4.19 the experimental particle flow rate (given by the balance) for a silo diameter $L = 40$mm, outlet size $D = 10$mm and glass particle mean size $d_p = 190\mu m$ with equation 4.19 using the experimental pressure gradient given by P_5 (equation 4.4) and the experimental Q_0. We suppose that the volume fraction at the outlet is approximate by the initial bulk value, $\phi_0 \approx \phi_{bi}$, as there is a negligible dilation of particles for the
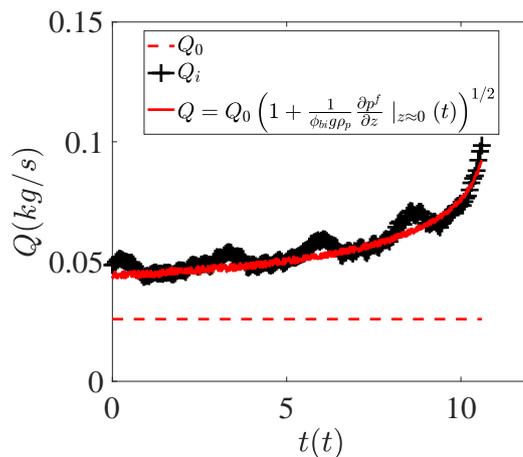

Figure 4.19: Temporal evolution of the discharge flow rate of the granular media from a silo with $L = 40$mm, $D = 10$mm and $d_p = 190\mu m$ (glass particles). The red dashed line represents the experimental mass flow rate of particles driven by gravity, whereas the red line represents equation 4.19 using the experimental pressure measurements.

fine particles ($D \geq 50d_p$). We can observe a very good agreement which validates using equation 4.19 for the pressure imposed configuration where the discharge flow varies with time.

Following Zhou [2016], we introduce the following notations:

$$\bar{Q} = \frac{Q}{Q_0} \quad \text{and} \quad \tilde{Q} = \frac{\phi_0 \rho_p Q_{air}}{Q_0} \tag{4.20}$$

$$\mathcal{N}_{l0,b} = \frac{\eta_f \beta_l(\phi_{0,b}, d_p) Q_0}{\phi_{0,b}^2 \rho_p^2 g S_{0,b}} \quad \text{and} \quad \mathcal{N}_{i0,b} = \frac{\rho_f d_p \beta_i(\phi_{0,b}, d_p) Q_0^2}{\phi_{0,b}^3 \rho_p^3 g S_{0,b}^2} \tag{4.21}$$

where $\bar{Q}$ and $\tilde{Q}$ represent respectively the particles and fluid flow rates made non-dimensional using the gravity driven particle flow rate. Note that the subscript 0 and b of $\mathcal{N}_{l0,b}$ and $\mathcal{N}_{i0,b}$ represent respectively the formula evaluated close to the outlet (using ϕ_0, S_0) or far from the outlet (using ϕ_b, S_b). We also note

$$\pm = \frac{\tilde{Q} - 1}{|\tilde{Q} - 1|} \tag{4.22}$$

whose value is $+1$ for the co-current particle and fluid flows and -1 for the counter-current flows. The singular value corresponds to an injected air volume flow rate equal to the ejected volumetric granular flux through the outlet, leading to the same discharge flow rate than those driven by gravity, $Q = Q_0$.

Notice that the variables $\bar{Q}(t)$, $\tilde{Q}(t)$ and $h_p(t)$ vary with time, however for convenience, all the following discussion will be carried out for a given moment t_i and we will simply denote $\bar{Q}$, $\tilde{Q}$ and h_p. During the discharge of the silo, the air pressure at the top of the silo is maintained at a quasi-constant level, namely p_{air}. The total pressure drop of the air across the silo is $\Delta p^f = p_{air}$. To evaluate analytically the pressure gradient at the outlet, we separate the silo into two zones with different pressure gradients: $\frac{\partial p^f}{\partial z}\big|_{z \gg 0}$ for the zone far from the outlet (see equation 4.14) and $\frac{\partial p^f}{\partial z}\big|_{z \approx 0}$ for the zone nearby the outlet (see equation 4.17). We assume that the vertical pressure gradient is uniform within each zone, so that the total pressure drop of the fluid can be given by the following expression:

$$\Delta p^f = (h_p - h_1) \frac{\partial p^f}{\partial z}\big|_{z \gg 0} + h_1 \frac{\partial p^f}{\partial z}\big|_{z \approx 0} \tag{4.23}$$

where $h_1 \approx D$ represents the vertical position where the jump of the pressure gradient occurs, and h_p represents the granular column height.

We normalize the pressure with $\tilde{p}^f = p^f / \rho_p g D$ and we use the outlet size D as a length scale and $\sqrt{D/g}$ as a time scale. We note $\tilde{\ }$ the dimensionless parameters. According to equation 4.19, the pressure gradient of the fluid at the outlet can be written:

$$\frac{\partial \tilde{p}^f}{\partial \tilde{z}}\big|_{\tilde{z} \approx 0} = \phi_0 \left(\bar{Q}^2 - 1 \right) \tag{4.24}$$

whereas the pressure gradient far from the outlet is given by equation 4.14.

Combining equations 4.14, 4.23 and 4.24, we thus obtain the first expression linking $\bar{Q}$, $\tilde{Q}$ and $\tilde{h}_p$:

$$\Delta\tilde{p}^f = \left(\tilde{h}_p - \tilde{h}_1\right)\left(\mathcal{N}_{lb}\phi_b\left(\frac{\phi_b}{\phi_0}\tilde{Q} - \bar{Q}\right) + \mathcal{N}_{ib}\phi_b\left(\frac{\phi_b}{\phi_0}\tilde{Q} - \bar{Q}\right)^2\right) + \tilde{h}_1\phi_0\left(\bar{Q}^2 - 1\right) \tag{4.25}$$

For all the performed experiments, the air volumetric flow rate is larger than the volumetric granular flux ejected through the outlet, indicating a co-current flow ($\tilde{Q} > 1$ and $\bar{Q} > 1$). The second expression is obtained by introducing equations 4.17 into 4.19, giving a quadratic equation for a given $\tilde{Q}$:

$$-\mathcal{N}_{i0}\tilde{Q}^2 + \left(2\mathcal{N}_{i0}\bar{Q} - \mathcal{N}_{l0}\right)\tilde{Q} + \left(1 - \mathcal{N}_{i0}\right)\bar{Q}^2 + \mathcal{N}_{l0}\bar{Q} - 1 = 0 \tag{4.26}$$

Only the positive root corresponds to a downward air flow:

$$\tilde{Q} = \bar{Q}(t) + \frac{\sqrt{\Delta} - \mathcal{N}_{l0}}{2\mathcal{N}_{i0}} \quad \text{with} \quad \Delta = 4\mathcal{N}_{i0}\bar{Q}^2 - 4\mathcal{N}_{i0} + \mathcal{N}_{l0}^2 \tag{4.27}$$

where the discriminant Δ is strictly positive due to the fact that the value of $\bar{Q}$ is larger than 1. Introducing this solution into the equation 4.25, we can obtain an expression linking directly $\tilde{h}_p$ with $\bar{Q}$, as below:

$$\tilde{h}_p = f(\bar{Q}) = \frac{\Delta\tilde{p}^f - \tilde{h}_1\phi_0\left(\bar{Q}^2 - 1\right)}{\mathcal{N}_{lb}\phi_b\left(\frac{\phi_b}{\phi_0}\frac{\sqrt{\Delta} - \mathcal{N}_{l0}}{2\mathcal{N}_{i0}} - \bar{Q}\right) + \mathcal{N}_{ib}\phi_b\left(\frac{\phi_b}{\phi_0}\frac{\sqrt{\Delta} - \mathcal{N}_{l0}}{2\mathcal{N}_{i0}} - \bar{Q}\right)^2} + \tilde{h}_1 \tag{4.28}$$

Finally the variation of the granular height $\tilde{h}_p$ with time is simply the particle velocity far from the outlet, given by equation 4.13. This gives a non-linear differential equation for $\bar{Q}$:

$$\frac{d\tilde{h}_p}{d\tilde{t}} = \frac{-\bar{Q}Q_0}{\phi_b\rho_p S_b\sqrt{gD}} \quad \text{with the initial condition} \quad \tilde{h}_p(t = 0) = \tilde{h}_p^0 \tag{4.29}$$

where $\tilde{h}_p^0$ represents the dimensionless initial granular column height that we have measured for each experiment. To solve this problem and according to the experimental observation, we suppose that the particle volume fraction far from the outlet keeps its initial value, $\phi_b = \phi_{bi}$, and that $h_1 = D$ as the jump of the pressure gradient appears at the scale of the outlet size. Therefore, the only adjustable parameter in equation 4.29 is the volume fraction at the outlet ϕ_0. This non-linear differential equation is then solved numerically thanks to a dedicated $Matlab$ script that will be described in the next section.

b.   Numerical solver

The discharge is discretized using an Euler explicit method with a small time step $\delta t = 0.05$s, which corresponds to the frequency of acquisition of the balance. A flow chart diagram of the

116

numerical solver for our problem is displayed in Figure 4.20. The entrance variables at the initial time step t_0 contain the experimental parameters (L, D, d_p, η_f, ρ_p), the experimental conditions (h_p^0, ϕ_b), the pressure level at the silo top p_{air} and the experimental discharge flow rate driven by the gravity Q_0. The numerical solver is mainly based on the least squares method minimizing the error on Q with the adjustable parameter ϕ_0. We impose a first value for $\phi_0 = 0.3$.
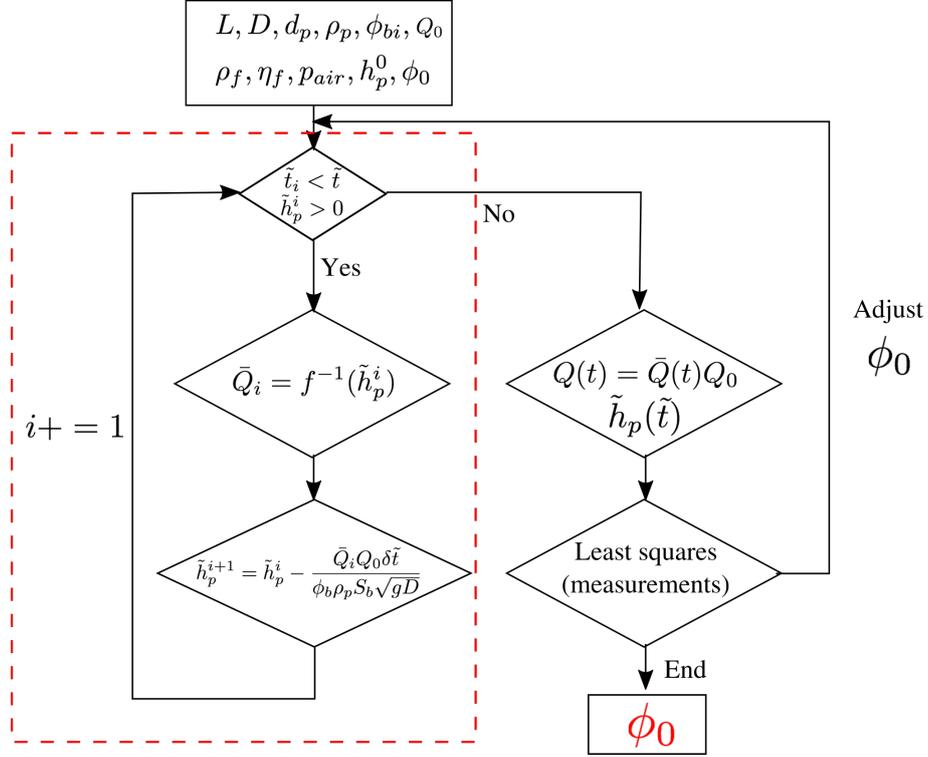
Figure 4.20: Flow chart diagram of numerical solver.

As shown in the part framed by the red dashed lines on this flow chart diagram, called internal loop, for each discrete time step $\tilde{t}_i$, the non-dimensional discharge flow rate of particles $\bar{Q}_i$ is calculated according to the inverse function of equation 4.28 with a known instantaneous granular column height $\tilde{h}_p^i$. Afterwards, the next iteration granular column height $\tilde{h}_p^{i+1}$ can be determined by equation 4.29, linking the non-dimensional discharge flow rate of particles $\bar{Q}_i$ with the variation of granular column height during a short period $\delta \tilde{t}$. This computing loop is run while $\tilde{h}_p$ stays positive. Therefore, the internal loop provides a prediction of the discharge flow rate $Q(t)$ as a function of time linked to a prescribed value of ϕ_0. We then obtain the fitting value of ϕ_0 by comparing the obtained discharge flow rate of particles $Q(t)$ with that measured experimentally and using the least squares method.

c.   Confrontation of the model with the experimental measurements

Following the previous quasi-steady model, we can predict the discharge flow rate of the granular media $Q(t)$ from the silo as well as the air volumetric flow rate $Q_{air}(t)$, adjusting the only
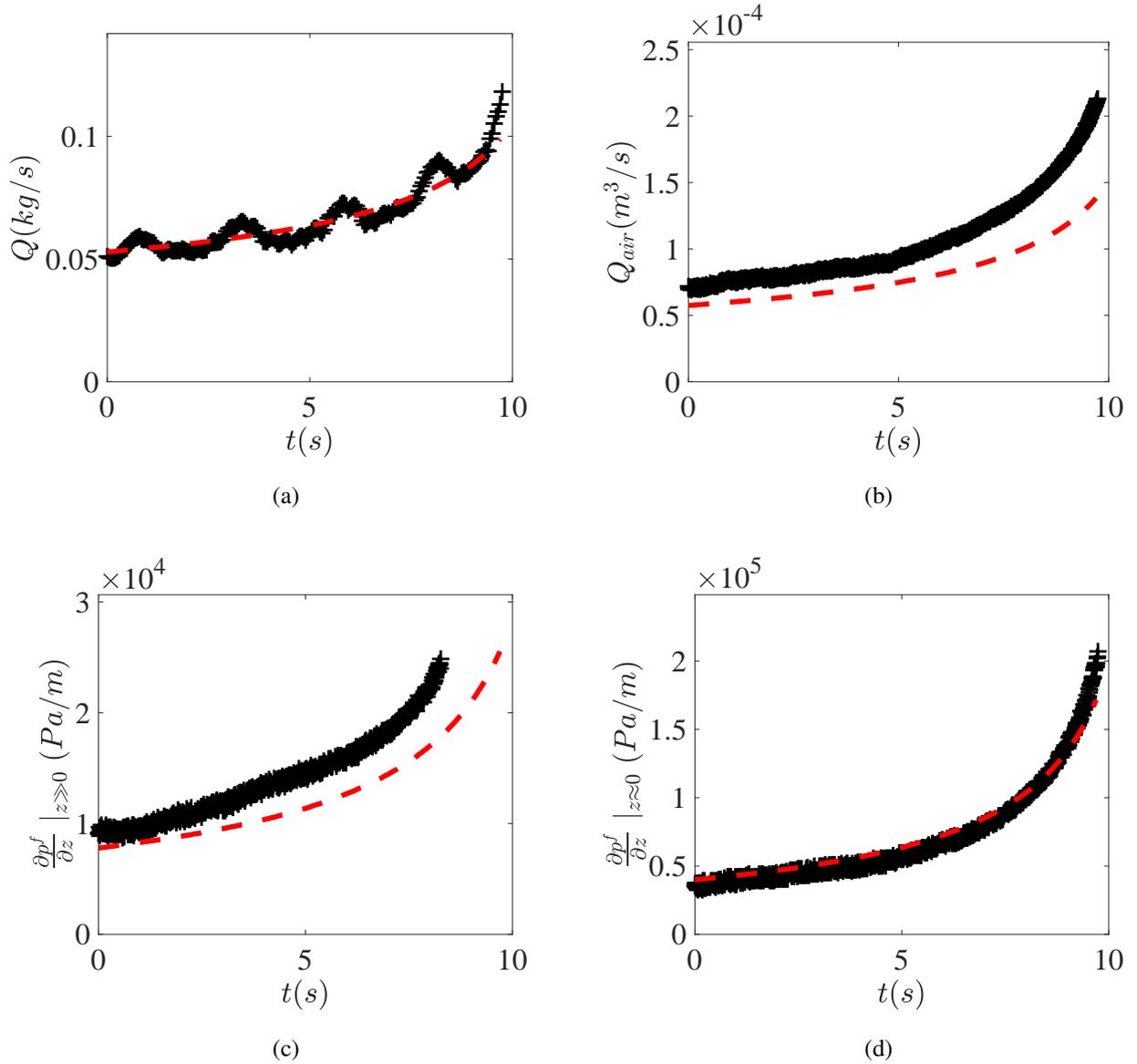
Figure 4.21: Confrontation of the experimental measurements (+) with the results predicted by the quasi-steady model (red dashed line) with $L = 40$mm, $D = 10$mm and $d_p = 190\mu m$ (glass particles) for (a) the discharge flow rate of particles $Q(t)$ (b) the volumetric air flow rate $Q_{air}(t)$ (c) the gas pressure gradient far from the outlet $\frac{\partial p^f}{\partial z}\mid_{z \gg 0} (t)$ and (d) the gas pressure gradient nearby the outlet $\frac{\partial p^f}{\partial z}\mid_{z \approx 0} (t)$.

parameter of the volume fraction at the outlet ϕ_0.

A typical result of comparison between the experimental measurements and the prediction by the model is illustrated in Figure 4.21, for (a) the discharge flow rate of granular media from the silo, (b) the volumetric air flow rate entering into the silo during the discharge, (c) the pressure gradient of the air flow far from the outlet and (d) that nearby the outlet. For glass particles, we observe the model predicts fairly well the experimental results for the particle flow rate, on which the least squares method is based, but also on the volumetric air flow rate and the pressure

gradients.
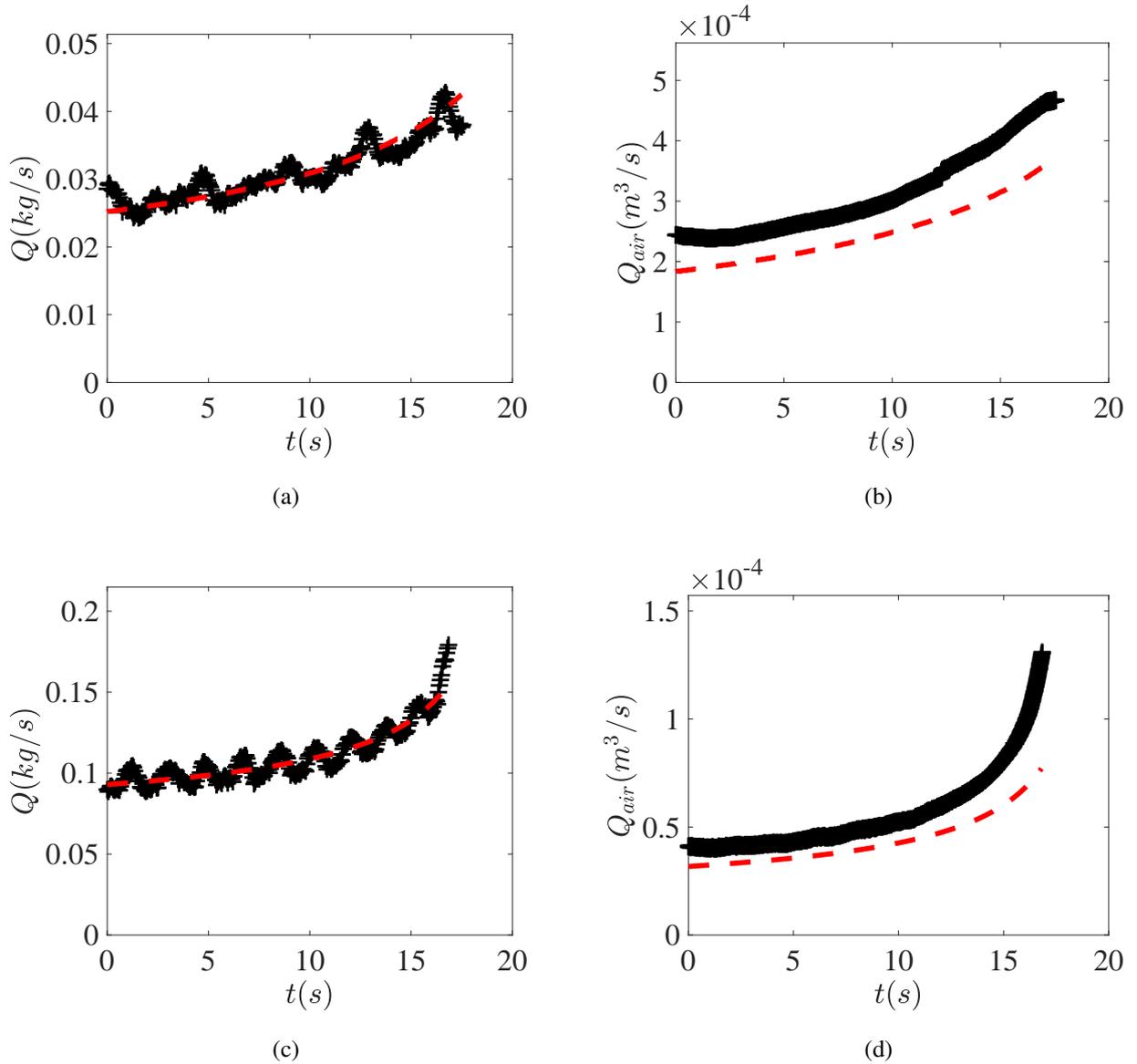
Figure 4.22: Confrontation of the experimental measurements (+) with the results predicted by the quasi-steady model (red dashed line) with $L = 40$mm, $D = 10$mm for (a, b) the sand particle ($d_p = 864\mu m$) and (c, d) the bidisperse mixture (ceramic particles with 50% mass of $d_p = 1165\mu m$ and $d_p = 180\mu m$). (a, c) Discharge flow rate of particles $Q(t)$, (b, d) Volumetric air flow rate $Q_{air}(t)$.

In Figure 4.22, we compare the experimental results with the prediction by the model for (a, b) the sand particle ($d_p = 864\mu m$) and (c, d) for the bidisperse mixture (ceramic particles with 50% mass of $d_p = 1165\mu m$ and $d_p = 180\mu m$). Figure 4.22(a, c) show the comparison of the discharge flow rate of the granular media, and (b, d) for the volumetric air flow rate. We observe that the model predicts also fairly well the experimental results for the sand particle and the bidisperse mixture, which shows that the permeability is the big parameter in this experiment.
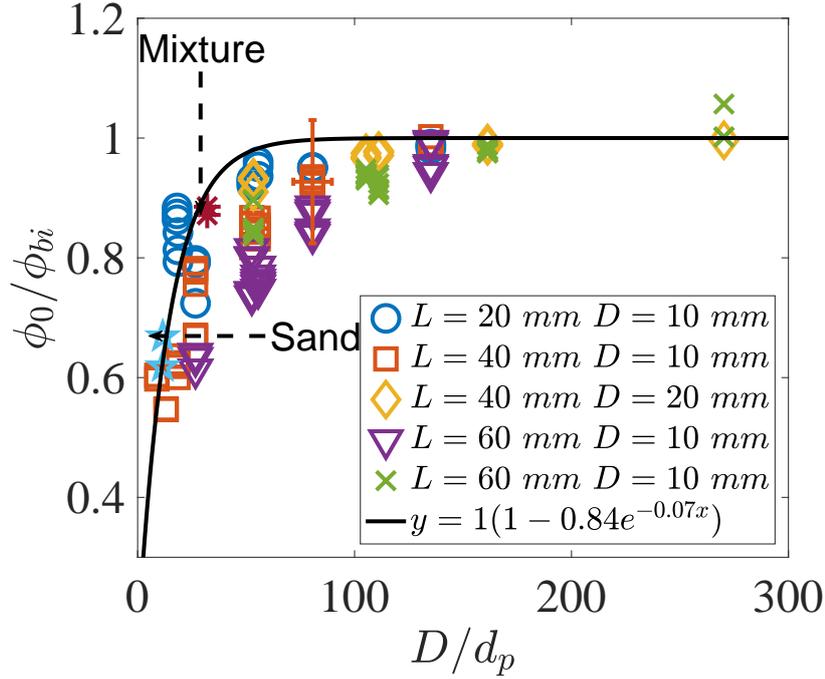
Figure 4.23: Ratio between ϕ_0 adjusted by the model and the initial bulk volume fraction ϕ_{bi} as a function of aspect ratio D/d_p for various silo diameters L and outlet sizes D. The black solid line represents the equation 4.18 with coefficients $\xi_\phi = 1$, $\alpha = 0.84$ and $\beta = 0.07$.

Figure 4.23 illustrates the ratio between ϕ_0 given by the model and the initial bulk volume fraction ϕ_{bi} as a function of the aspect ratio D/d_p for various silo diameters L and outlet sizes D. We observe that the data can be reasonably fitted by equation 4.18 with the same coefficients (α, β) than for the gravity driven experiment. Using a gravity driven experiment to calibrate α and β, we can thus fully predict the temporal evolution of the discharge flow of a granular media from a silo with an imposed air pressure at its top.

To validate the various hypothesis of the model and investigate in more detail the intern properties of the flow, a continuum simulation will be introduced in the following section.

4.4 Continuum simulation

In this section, we test the ability of the two-phase continuum model with the $\mu(I)$ frictional rheology for the granular phase to predict the discharge flow from a silo with an imposed pressure at its top in a cylindrical geometry. We use the open software *Basilisk*. We present the simulation parameters, afterwards, we validate the code by simulating a simple case of the discharge of a silo driven by the gravity and finally we carry out the numerical study of the discharge of the silo with a pressurized gas ejected at the top corresponding to the experimental conditions.

4.4.1 Two-phase continuum modelling

To simulate the role of a pressurized gas on the discharge of silo, we consider the two-phase continuum modelling developed in section 4.3.1. The drag force between granular phase and gas phase is modeled by the Darcy-Forchheimer resistance law which takes into account both the viscous and inertial contributions. Moreover, the experimental study of discharge of a cylindrical silo with a pressurized gas flow can be considered as an axisymmetric flow where the flow movement in the rotational direction (all the components with θ) can be neglected. Therefore, we have implemented the two-phase modelling in the cylindrical coordinate system in *Basilisk*[1], which permits to solve the problem in a 2D plane, representing a 3D cylindrical domain.

$$\frac{\partial(r u_r^f)}{\partial r} + \frac{\partial(r u_z^f)}{\partial z} = 0 \tag{4.30}$$

$$\frac{\partial(r u_r^p)}{\partial r} + \frac{\partial(r u_z^p)}{\partial z} = 0 \tag{4.31}$$

$$-R_f \frac{\partial u_r^f}{\partial t} - \frac{\partial p^f}{\partial r} - B_l(u_r^f - u_r^p) - B_i(u_r^f - u_r^p) \mid u_r^f - u_r^p \mid = 0 \tag{4.32}$$

$$-R_f \frac{\partial u_z^f}{\partial t} - \frac{\partial p^f}{\partial z} - B_l(u_z^f - u_z^p) - B_i(u_z^f - u_z^p) \mid u_z^f - u_z^p \mid = 0 \tag{4.33}$$

$$-\rho \left[\frac{\partial u_r^p}{\partial t} + u_r^p \frac{\partial u_r^p}{\partial r} + u_z^p \frac{\partial u_r^p}{\partial z} \right] + \frac{1}{r} \frac{\partial(r \sigma_{rr}^p)}{\partial r} + \frac{\partial \sigma_{zr}}{\partial z} - \frac{\partial p^f}{\partial r} = 0 \tag{4.34}$$

$$-\rho \left[\frac{\partial u_z^p}{\partial t} + u_r^p \frac{\partial u_z^p}{\partial r} + u_z^p \frac{\partial u_z^p}{\partial z} \right] + \frac{\partial \sigma_{zz}^p}{\partial z} + \frac{1}{r} \frac{\partial(r \sigma_{rz}^p)}{\partial r} - \frac{\partial p^f}{\partial z} - \rho g = 0 \tag{4.35}$$

Where the coordinates are drawn in Figure 4.24. Note that these equations are dimensionless using the silo diameter L as a length scale, $\rho g L$ as a pressure scale and $\sqrt{L/g}$ as a time scale. Note also that $B_l = \beta_l \eta (1 - \phi)$ represents the viscous term and $B_i = \beta_i \rho^f d(1 - \phi)^2$ the inertial term of the Darcy-Forchheimer resistance law. Additionally, $R_f = \rho^f \left(1 + C_{vm} \frac{\phi}{1-\phi}\right)$ represents a virtual mass approach taking unsteady effects into account in the fluid phase (Gu and Wang [1991], Hall et al. [1995], Rajagopal [2007], Zhu et al. [2014]), where $C_{vm} = 2$ is an empirical coefficient (in the range of $0.5 \leq C_{vm} \leq 2.0$ Lowe et al. [2008]) and $\phi = 0.6$ is the volume fraction of granular

---

[1] http://basilisk.fr/src/axi.h

media. In *Basilisk*, the gas phase is a passive scalar. Then we do not solve the two phases coupled equations. Instead at a given time, we write equations 4.32 and 4.33 as:

$$R_f \frac{\overrightarrow{u}_{n+1}^f - \overrightarrow{u}_n^f}{\Delta t} = -\overrightarrow{\nabla} p^f - B_l(\overrightarrow{u}_{n+1}^f - \overrightarrow{u}^p) - B_i \mid \overrightarrow{u}_n^f - \overrightarrow{u}^p \mid (\overrightarrow{u}_{n+1}^f - \overrightarrow{u}^p) \qquad (4.36)$$

According to the continuity equations 4.30 and 4.31, equation 4.36 can be written in the following form:

$$\overrightarrow{\nabla} \cdot \left(\frac{r\Delta t \overrightarrow{\nabla} p^f}{R_f + \Delta t(B_l + B_i |\overrightarrow{u}_n^f - \overrightarrow{u}^p|)} \right) = \overrightarrow{\nabla} \cdot \left(r \frac{R_f \overrightarrow{u}_n^f + \Delta t(B_l \overrightarrow{u}^p + B_i \overrightarrow{u}^p |\overrightarrow{u}_n^f - \overrightarrow{u}^p|)}{R_f + \Delta t(B_l + B_i |\overrightarrow{u}_n^f - \overrightarrow{u}^p|)} \right) \qquad (4.37)$$

Equation 4.37 is in the form of a Poisson-Helmholtz equation that we solve in *Basilisk*, using a specific solver [2]. Thus we obtain the pressure field of the fluid phase as well as the corresponding pressure gradients which corresponds to the drag forces that we impose on the granular media, in equations 4.34 and 4.35.

4.4.2 Silo configuration and boundary conditions
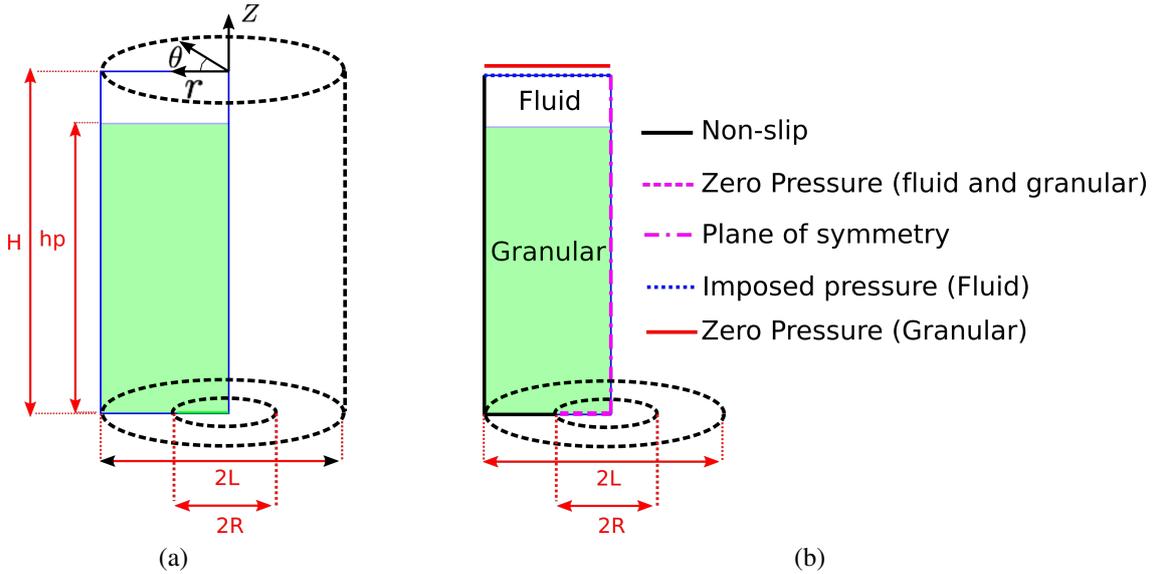
Figure 4.24: (a) Configuration and (b) boundary conditions of the continuum simulation for the discharge of a silo with a pressurized gas in a cylindrical geometry.

The silo configuration for studying the discharge of a silo with an imposed gas pressure at the top is displayed in Figure 4.24a. In the cylindrical coordinate, the calculation domain consists of a two-dimensional plane of height H and width L. The granular media is considered as a continuum media and has a initial height h_p. An outlet of radius $R = D/2$ is placed at the right bottom of the calculation domain.

---

[2] http://basilisk.fr/src/poisson.h

Different boundary conditions are applied to the borders of the calculation domain, illustrated in Figure 4.24b.

On the side walls (see the black lines in Figure 4.24b), a Neumann boundary condition is applied both for the granular pressure ($\overrightarrow{\nabla} p^p \cdot \vec{n} = \vec{0}$) and the fluid pressure ($\overrightarrow{\nabla} p^f \cdot \vec{n} = \vec{0}$) together with a no-penetration condition ($\vec{u}^p \cdot \vec{n} = \vec{0}$ and $\vec{u}^f \cdot \vec{n} = \vec{0}$) as well as a non-slip condition ($\vec{u}^p \cdot \vec{t} = \vec{0}$ and $\vec{u}^f \cdot \vec{t} = \vec{0}$).

At the outlet, a Dirichlet boundary condition is applied (see the purple dashed line in Figure 4.24b) for the pressure of the two phases ($p^p = 0$ and $p^f = 0$) together with a Neumann boundary condition for the normal and tangential components of velocity of both phases ($\overrightarrow{\nabla} (\vec{u}^p \cdot \vec{n}) = \vec{0}$, $\overrightarrow{\nabla} (\vec{u}^p \cdot \vec{t}) \cdot \vec{n} = \vec{0}$), $\overrightarrow{\nabla} (\vec{u}^f \cdot \vec{n}) = \vec{0}$, $\overrightarrow{\nabla} (\vec{u}^f \cdot \vec{t}) \cdot \vec{n} = \vec{0}$).

For the plane of symmetry (see the purple dashed dotted line in Figure 4.24b), a no-penetration condition is applied for the normal velocity component for both phases ($\vec{u}^p \cdot \vec{n} = \vec{0}$ and $\vec{u}^f \cdot \vec{n} = \vec{0}$). And a free-slip boundary condition is applied for the tangential velocity component, along the vertical direction ($\overrightarrow{\nabla} (\vec{u}^p \cdot \vec{t}) \cdot \vec{n} = \vec{0}$ and $\overrightarrow{\nabla} (\vec{u}^f \cdot \vec{t}) \cdot \vec{n} = \vec{0}$).

Finally, for the top border of the calculation domain, a Dirichlet boundary condition is chosen for the pressure of two phases, but with different values. For the fluid phase $p^f = p_{air}$ where p_{air} represents the value of the fluid pressure imposed and for the granular phase $p^p = 0$. Additionally, the normal and tangential components of the velocity for both phases possess a Neumann boundary condition ($\overrightarrow{\nabla} (\vec{u}^p \cdot \vec{n}) = \vec{0}$, $\overrightarrow{\nabla} (\vec{u}^p \cdot \vec{t}) \cdot \vec{n} = \vec{0}$, $\overrightarrow{\nabla} (\vec{u}^f \cdot \vec{n}) = \vec{0}$ and $\overrightarrow{\nabla} (\vec{u}^f \cdot \vec{t}) \cdot \vec{n} = \vec{0}$).

4.4.3 Post-processings

During the simulation, the velocity fields of both phases are calculated for every $\Delta t = 0.1/\sqrt{L/g}$. Therefore, the instantaneous mass flow rate of the granular phase and the volumetric flow rate of the fluid phase can be determined from the velocity fields by integrating the vertical velocity component at the outlet, $Q_i = \rho \int_0^R 2\pi r u_z^p \mid_{z=0} dr$ and $Q_{air} = \int_0^R 2\pi r u_z^f \mid_{z=0} dr$. Additionally, different fields (pressure, ...) are also saved during the simulation for every $\delta t = 1/\sqrt{L/g}$.

4.4.4 Choice of the parameters of the simulations

A series of simulations were performed to choose the relevant parameters, such as the initial granular column height h_p, the radius of silo L, the time step δt and the mesh size L/N, where N is the number of mesh on L. For this parametric study, we consider the discharge of a cylindrical silo driven by gravity. The mass flow rate of the granular media reaches quickly a stationary state, which is expected to be independent on h_p, L, δt and N.

Firstly, we focus on the influence of the initial granular height on the mass flow rate. We vary h_p from L to $3.5L$, where L is the silo width with $L = 100d$, for an outlet radius $R = 25d$. Figure 4.25a illustrates the instantaneous mass flow rate of the granular media $Q_i/\rho\sqrt{gL^5}$ as a function of time $t/\sqrt{L/g}$ for different granular heights. We observe that the curves superimpose for $h_p \geq 2L$.
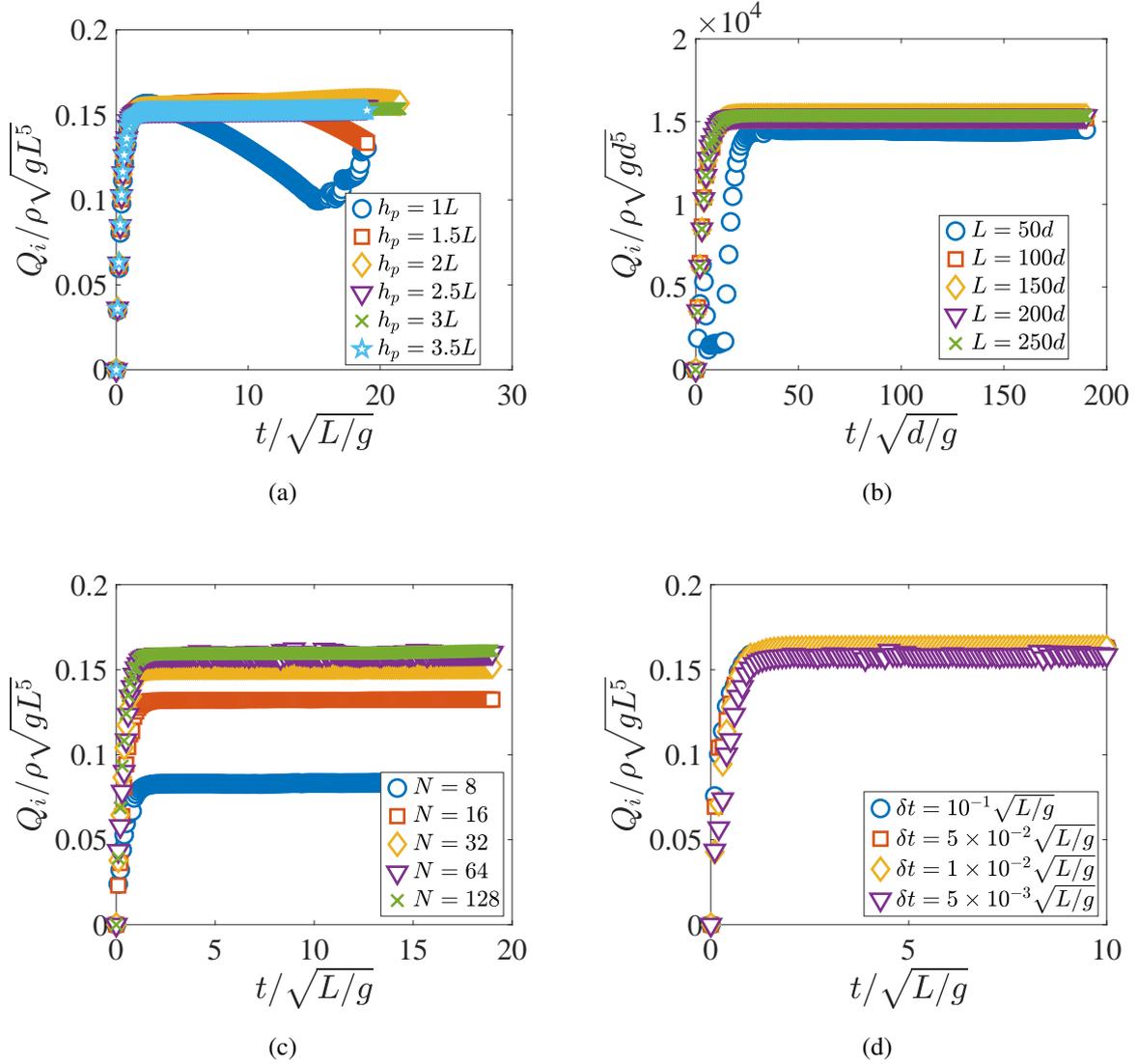
Figure 4.25: Parametric study for the continuum simulation for $R = 25d$. Temporal evolution of the mass flow rate for (a) various initial granular heights h_p, (b) various silo widths L for $h_p = 380d$, (c) various numbers of mesh on L, (d) various time steps.

It shows that the initial granular height does not play a role on the mass flow rate when the silo is filled enough. Thus, we chose an initial granular height $h_p = 3.8L$ to obtain a sufficiently long period where the discharge does not depend on this variable.

Secondly, a parametric study on the influence of the silo width L is displayed in Figure 4.25b, for $R = 25d$, $h_p = 380d$. There is no influence of the silo width on the granular flow for $L \geq 100d$, meaning that the lateral border of silo should locate far enough from the outlet ($L > 4R$) so that the granular flow can well develop and be not disrupted. For all of our following studies, we keep this criterion, fixing the silo width $L = 100d$ and limiting the outlet size range.

The mesh size is an important parameter in our numerical simulation, which can play a role on the accuracy of the results. Figure 4.25c illustrates the temporal evolution of the mass flow rate,

varying the number of mesh N along the fixed silo width $L = 100d$, for $R = 25d$ and $h_p = 380d$. We observe that the results converge when $N \geq 64$. Thus the number of mesh on the silo width $N = 64$ will be used for the following studies to obtain a good accuracy of the numerical results together with saving computing time.

Figure 4.25d illustrates the influence of the time step on the numerical results for $L = 100d$, $R = 25d$, $h_p = 380d$ and $N = 64$. We observe that the tested time step has no influence on the discharge flow when $\delta t > 5 \times 10^{-3}\sqrt{L/g}$. Thus, we chose a time step $\delta t = 0.01\sqrt{L/g}$ for the simulation.

4.4.5 Discharge driven by gravity

We first carried out a study on the discharge flow rate of a granular media driven by gravity in a cylindrical silo varying the outlet radius R in a range of $[0.1 - 0.5]L$.
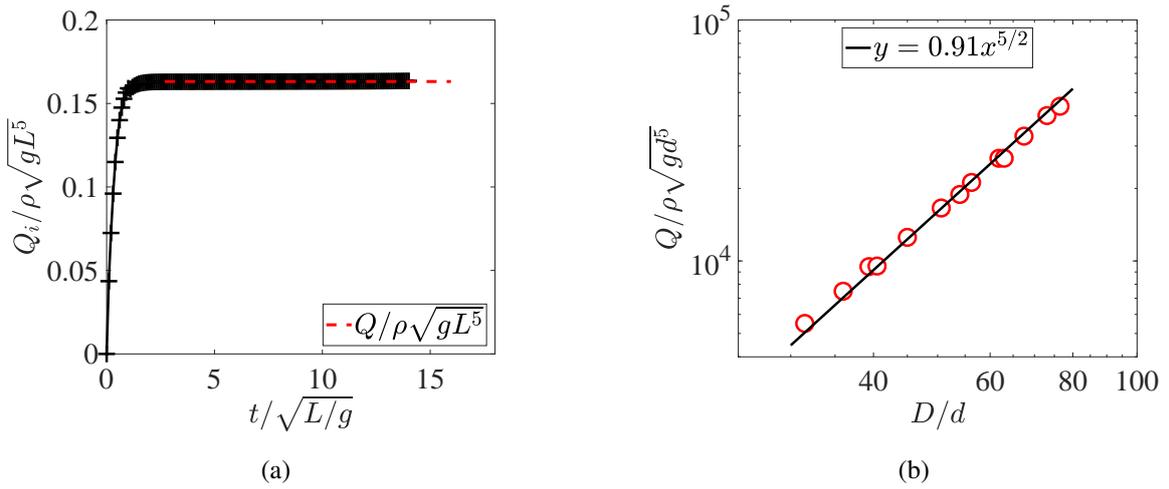
Figure 4.26: (a) Temporal evolution of the non-dimensional discharge flow of the granular media $Q_i/\rho\sqrt{gL^5}$ for $R = 0.25\ L$. The red dashed line represents the mean flow rate $Q/\rho\sqrt{gL^5}$ during the stationary state. (b) Normalized mass flow rate $Q/\rho\sqrt{gd^5}$ as a function of the dimensionless outlet size D/d. The black solid line represents equation 4.38 with coefficient $C = 0.91$.

The temporal evolution of the non-dimensional flow rate $Q_i/\rho\sqrt{gL^5}$ for $R = 0.25L$ is illustrated in Figure 4.26a. We observe that the flow rate reaches quickly a steady value, Q given by the average value of Q_i during the stationary state of discharge. In Figure 4.26b, we plot the normalized mass flow rate $Q/\rho\sqrt{gd^5}$ as a function of D/d. As expected, we observe that all the data can be well fitted by the Hagen-Beverloo law, shown by the black line in Figure 4.26b corresponding to equation 4.38 with a coefficient $C = 0.91$.

$$Q = C\rho\sqrt{gD^5} \tag{4.38}$$

125

Therefore, the continuum modelling with a granular rheology together with the numerical parameters chosen, is successful to describe the gravity driven discharge of a granular media from a cylindrical silo. Then in the following part, we will add the coupling with a gas flow.

4.4.6 Discharge coupled with a pressurized gas

The two-phase continuum model presented in section 4.3.1 is resolved numerically, where we carried out a series of continuum simulations, varying the value of the imposed constant gas pressure p_{air} at the top of the silo and the outlet radius R. The dimensionless coefficients in the drag force between two phases are taken $B_l = \beta_l \eta_f (1 - \phi) = 25$ for the viscous term and $B_i = \beta_i \rho^f d (1 - \phi)^2 = 6.3$ for the inertial term corresponding to the experimental conditions for a particle size about of $500 \mu m$. Additionally, the coefficient $R_f = \rho^f (1 + C \frac{\phi}{1-\phi})$ representing a virtual mass approach taking unsteady effects of the fluid phase into account is set to a value of 0.002ρ.
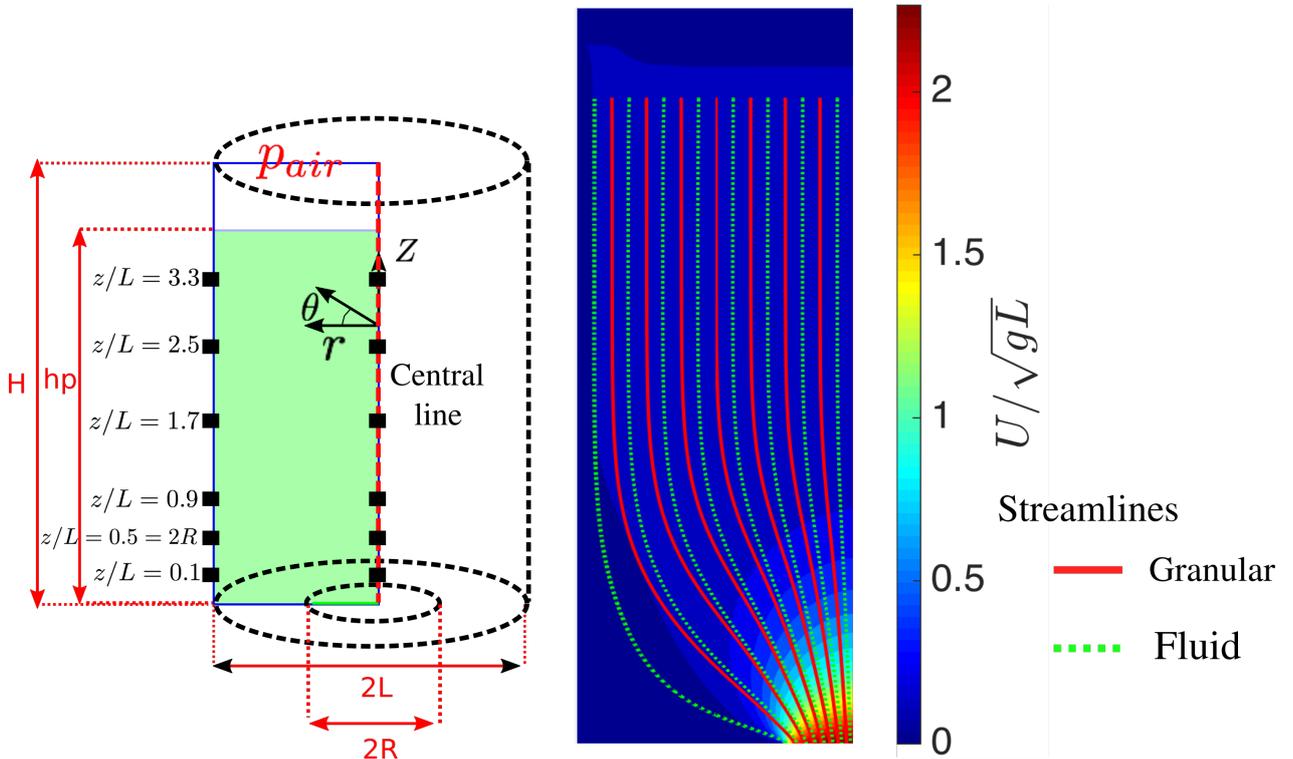
Figure 4.27: Configuration of the numerical simulation, and field of the magnitude of the velocity for the granular phase with the streamlines for the two phase flows, respectively, the red lines for the granular flow and the green dotted lines for the gas flow.

In Figure 4.27, the streamlines for both phases are displayed at the right part of figure, with red lines for the granular phase and green dotted lines for the fluid phase. We observe that both streamlines are vertical far from the outlet. As approaching the outlet due to the restricted cross section, the streamlines converge towards the outlet. The flow at the outlet can be reasonably taken

as vertical, as supposed in the analytical model. In the following part, we will discuss a typical example of numerical simulation, with an outlet radius $R = 0.25L$ and an imposed air pressure $p_{air} = 5\rho gL$.

(a)

(b)
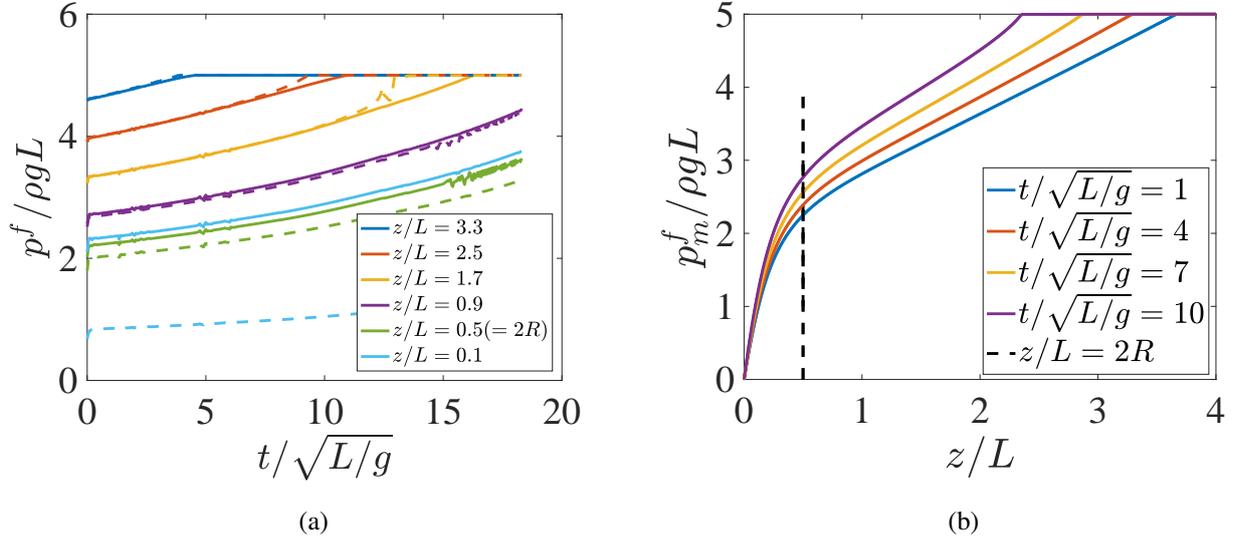
Figure 4.28: Continuum simulation with $R = 0.25L$ and $p_{air} = 5\rho gL$. (a) Temporal evolution of pressure of the fluid phase at different vertical position on the side of the silo, illustrated on the left part of Figure 4.27, taken at the side wall (full line) and at the central line (dashed line). (b) Pressure profiles of the fluid phase at different moments on the central line of the silo. The black dashed line represents the vertical position at which $z/L = 2R$.

The temporal evolution of the pressure profiles of the fluid phase $p^f/\rho gL$ for different positions along the silo, is shown in Figure 4.28a, in full line at the side wall and in dashed line at the center. We observe a similar trend than that observed in the experiment (see Figure 4.15a): the pressure at a given position increases during the discharge period due to the decrease of the granular column height and it finally reaches the imposed pressure level p_{air} when the tap is above the granular media. Moreover, we observe that the measurements at the side wall of the silo (see the full lines in Figure 4.28a) give the same values than at the central line of the silo (dashed lines) as long as $z > 2R$, which confirms the representativity of the experimental pressure measurements at the side wall of the silo. The spatial and temporal evolution of the pressure profiles along the central line of the silo is presented in Figure 4.28b. We observe a similar behavior than in the experiments (see Figure 4.15b): a linear relation is observed far from the outlet and a change of slope occurs near the outlet around $z/L = 2R$. We plot in Figure 4.29a the pressure of the fluid on the central line of the silo at $t = \sqrt{L/g}$ for various outlet sizes with $p_{air} = 5\rho gL$. To estimate the position at which the change of the pressure gradient of the fluid occurs, a linear function is defined for fitting the pressure far from the outlet. This position h^*/L is determined where the pressure reaches 95% of the linear function value. In Figure 4.29b, we observe a linear increase of h^*/L with the outlet size R/L. This observation confirms the choice of $h_1 = 2R$ in the quasi-steady model to

127
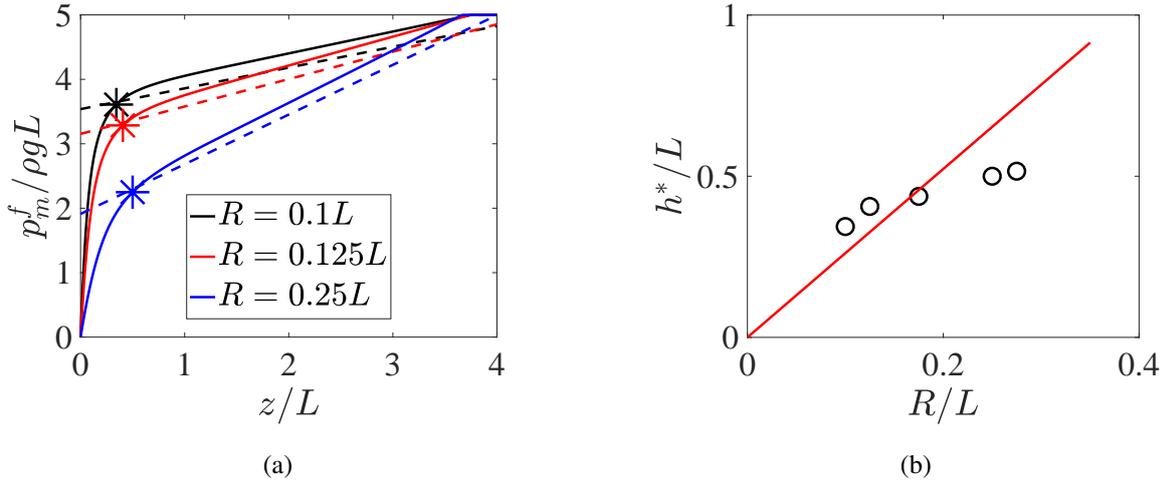
Figure 4.29: (a) Pressure profiles on the central line of the silo at $t = \sqrt{L/g}$ for various outlet sizes with $p_{air} = 5\rho g L$. The dashed lines represent 95% of the linear function value which fits the pressure of the fluid far from the outlet. The horizontal axe of the cross point is considered as the position at which the change of the slope occurs h^*/L, and it is plotted in (b) as a function of the outlet radius R/L. The full line represent $h^* = 2.6R$.

distinguish the whole silo into two zones with different pressure gradients for the fluid phase (see equation 4.23).

We modeled the effect of gas flow on the discharge rate by considering that the discharge law obtained in the case of an open silo remains valid considering that the fluid flow simply generates a supplementary force on the particles to be added to gravity (see equation 4.19). We have evaluated the pressure gradient of the fluid phase at the outlet using equation 4.17, under several assumptions. Following Zhou [2016], we are going to test the validity of equation 4.17 and 4.19 thanks to the numerical simulations. Note that in the simulation, the granular media is incompressible and $\phi_0 = \phi_{bi}$.

In the simulation notations, equation 4.17 writes:

$$\frac{\partial p^f}{\partial z}\bigg|_{z=0} = B_l \frac{Q_{air} - Q/\rho}{S_0} + B_i \left(\frac{Q_{air} - Q/\rho}{S_0}\right)^2 \tag{4.39}$$

This equation, obtained considering the mass conservation of both phases, corresponds to the mean pressure gradient of the fluid phase averaged on the outlet section:

$$\frac{\partial p^f}{\partial z}\bigg|_{(r<R)(z=0)} = \frac{2\int_0^R \frac{\partial p^f}{\partial z}\big|_{z=0} \, r dr}{R^2} \tag{4.40}$$

In Figure 4.30a, we have plotted this mean pressure gradient versus $B_l \frac{Q_{air}-Q/\rho}{S_0} + B_i \left(\frac{Q_{air}-Q/\rho}{S_0}\right)^2$ and the data are well adjusted by a linear trend of slope 1. However, in the case of the stationary discharge of a rectangular silo assisted by the injection of a constant flow rate of air, Zhou [2016]

128
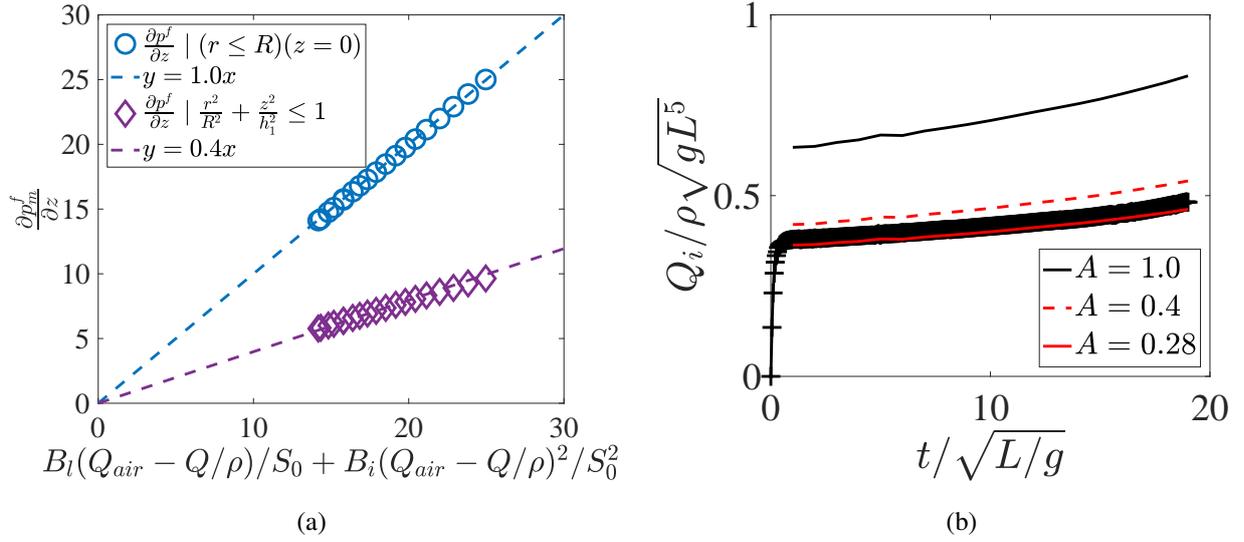
Figure 4.30: (a) Average pressure gradients of the fluid phase by equation 4.40 (○), and equation 4.41 (◇) as a function of $B_l \frac{Q_{air}-Q/\rho}{S_0} + B_i \left(\frac{Q_{air}-Q/\rho}{S_0}\right)^2$. (b) Discharge flow rate predicted by the model with different coefficient values A.

have shown using a continuum simulation with a Darcy resistance law that the zone of influence of the air pressure gradient is not restricted to the outlet but coupled to the zone of acceleration of the particles, above the outlet.

We thus define a volumetric average of the pressure gradient of the fluid phase on an ellipsoidal zone above the outlet with $\frac{r^2}{R^2} + \frac{z^2}{h_1^2} \leq 1$ (◇), obtained by:

$$\frac{\partial p^f}{\partial z} \big|_{\left(\frac{r^2}{R^2}+\frac{z^2}{h_1^2}\leq 1\right)} = \frac{3 \int_0^{h_1} \left(\int_0^R \frac{\partial p^f}{\partial z} \big|_{r,z} r dr\right) dz}{R^2 h_1} \tag{4.41}$$

We observe in Figure 4.30a that this averaged pressure gradient is still proportional to $B_l \frac{Q_{air}-Q/\rho}{S_0} + B_i \left(\frac{Q_{air}-Q/\rho}{S_0}\right)^2$ with a coefficient $A = 0.4$. This suggests that the volume average force exerted by the fluid phase on the granular phase can be determined by $A \frac{\partial p^f}{\partial z} \big|_{z=0}$ with a coefficient A smaller than 1, and that equation 4.19 can be written:

$$Q = Q_0 \left(1 + A\frac{1}{\rho g}\frac{\partial p^f}{\partial z}\big|_{z=0}\right)^{1/2} \tag{4.42}$$

Then equations 4.28 and 4.29 of the analytical model remains still valid replacing $\mathcal{N}_{l0}$ by $A\mathcal{N}_{l0}$ and $\mathcal{N}_{i0}$ by $A\mathcal{N}_{i0}$:

$$\tilde{Q} = \bar{Q}(t) + \frac{\sqrt{\Delta'}-\mathcal{N}_{l0}}{2\mathcal{N}_{i0}} \quad \text{with} \quad \Delta' = \frac{4\mathcal{N}_{i0}}{A}\bar{Q}^2 - \frac{4\mathcal{N}_{i0}}{A} + \mathcal{N}_{l0}^2 \tag{4.43}$$

129

We can then solve numerically equation 4.29 to obtain the temporal evolutions of h_p, Q and Q_{air}. In Figure 4.30b, we have plotted the temporal evolution of the discharge flow rate of the granular media, and compare it with the analytical model for $A = 1$ (black full line) and $A = 0.4$ (red line), corresponding to the volumetric average of the pressure gradient at the outlet. We observe a better agreement taking into account this parameter, the best fit being for $A = 0.28$.
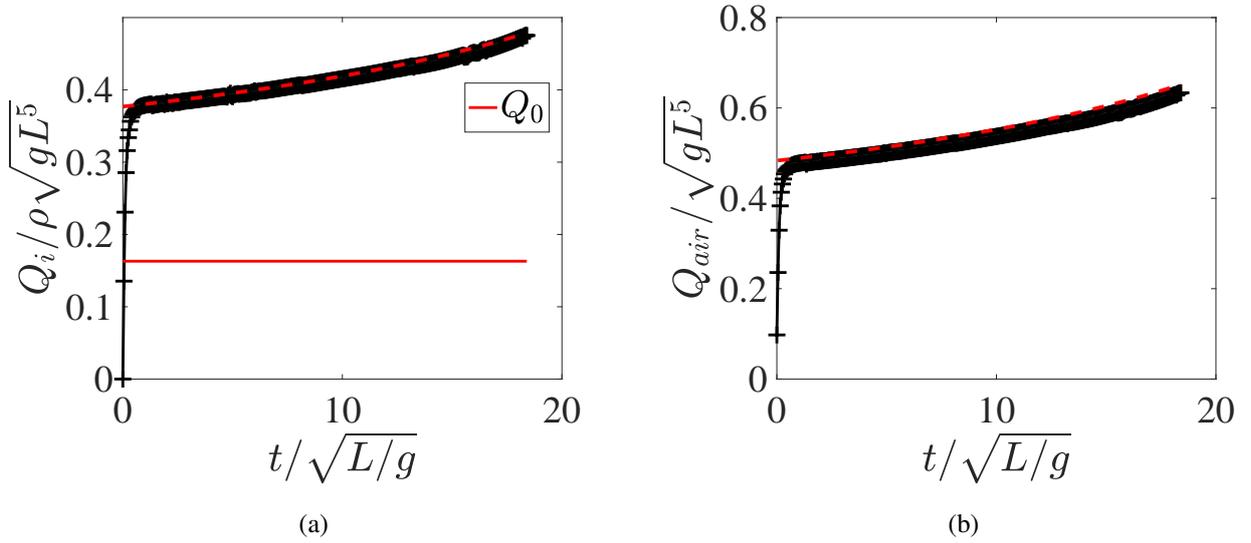
Figure 4.31: Continuum simulation with $R = 0.25L$ and $p_{air} = 5\rho gL$. (a) Temporal evolution of the non-dimensional discharge flow rate of the granular media $Q/\rho\sqrt{gL^5}$. The red solid line represents discharge flow rate driven by gravity and the red dashed line represents the discharge flow rate predicted by the model (see equation 4.28 and 4.29), with $A = 0.28$. (b) Temporal evolution of the non-dimensional discharge flow rate of the fluid $Q_{air}/\sqrt{gL^5}$. The red dashed line represents the prediction of the model.

Finally, Figure 4.31a and 4.31b illustrate respectively the discharge flow rate of the granular media and the air flow rate as a function of time, for $R = 0.25L$ and $p_{air} = 5\rho gL$. The red dashed lines in both figures represent the results predicted by the model, with the adjustable parameter $A = 0.28$. We observe a very good agreement between the numerical results and the analytical model. This parameter A smaller than 1, suggests that the fluid pressure gradient play a role on the whole area near the outlet where the flow is not uniform. In the experiments, the role of the parameter A is taken into account in the parameter ϕ_0.

4.5   Conclusions

In this chapter, we have investigated experimentally the discharge of a silo coupled with an imposed air pressure at the top of the silo. In this case we observe that the particle flow rate increases with time together with the air flow rate, as the height of the granular column decreases. To describe this behavior, we have proposed a continuum two-phase modelling with a granular frictional rheology and a Darcy-Forchheimer resistance law between the phases. In the hypothesis of a quasi-steady flow, we have proposed an analytical model which accounts quite well for the experimental data. We have fully solved the continuum modelling using numerical simulations in a 3D axisymmetric configuration and we have validated most of the assumptions of the analytical model.

We can wonder if these conditions hold for lager pressure gradients. Moreover in the industrial case of interest, the pressurized gas and the granular medium are suddenly (following the clad failure) into contact with a surrounding lower pressure domain, that adds an unsteady process to the flows. In the next chapter, we will study a more violent and transient discharge thanks to an experimental system leading to an instantaneous rupture of the orifice.

Chapter 5

Discharge of a silo with a rupture of the outlet induced by a pressurized gas

In this chapter, we focus on the effect of the pressurized gas on the discharge flow rate of the granular media, under an even more unsteady condition: an instantaneous rupture of the silo outlet. An aluminum foil is chosen to assure the initial closure of the silo, providing a critical rupture pressure level around 3bar, which is much larger than that we have imposed in the previous study. Moreover, the pressure is not maintained constant anymore. The experimental setup and the performed measurements as well as the post-processing techniques are presented in the first section. Then we investigate experimentally the temporal evolution of the discharge flow rate of the granular media and of the gas pressure along the silo for various parameters. An analytical model taking into account the pressure dependent density of the gas is then developed to describe the discharge flow. We also carry out a two-phase continuum simulation to fully model the experimental results. Finally, we will discuss the shape of the granular jet at the outlet.

5.1 Experimental setup, procedure and measurements

The experimental system for the silo discharge with an instantaneous rupture of the outlet was designed in collaboration with the $Compressible\ Flow$, $Shockwave\ and\ Interfaces$ team of the Laboratory IUSTI.

5.1.1 Experimental apparatus

For studying the discharge of a silo with a sudden opening of the outlet, we chose a cylindrical silo with an internal diameter of $L = 40$mm and a height of $H = 0.5$m, and we change the bottom plug compared to the previous section (see Figure 5.1a) with two outlet sizes $D = 10$mm and $D = 20$mm. The new bottom plug is composed of two parts: a metal part at the top and a plexiglas part at the bottom. Both parts are equipped with a lid seal to ensure the silo tightness.
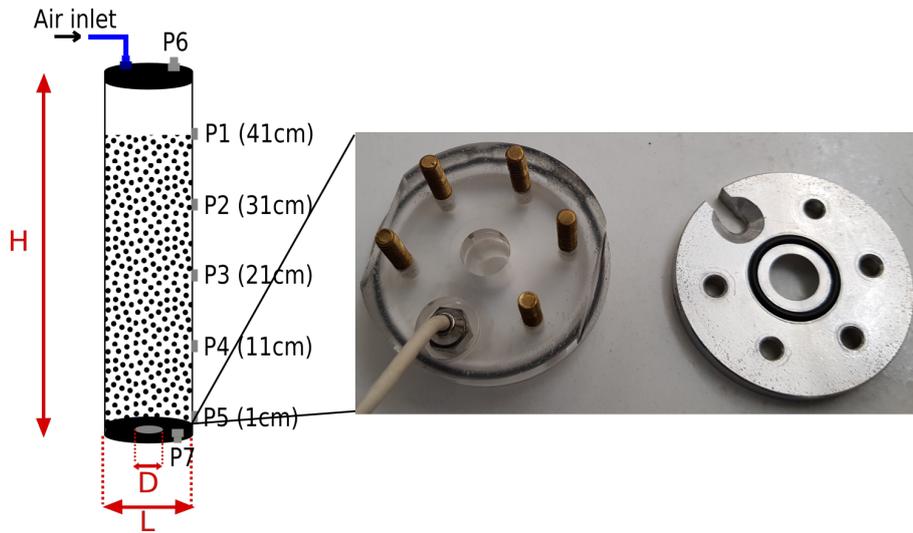
(a) Silo configuration and bottom plug for an instantaneous rupture of the outlet

(b) Installation of bottom plug

(c) Membrane of aluminum foil after rupture

Figure 5.1: Design of the bottom plug for the discharge of a silo with an instantaneous rupture of the outlet with D = 10 mm, L = 40mm and H = 50cm.

Six groups of screw and screw hole are machined on both parts in order to ensure the seamless closure of silo. An aluminum foil is placed in between these two parts for the initial closure of the silo as shown in Figure 5.1b. The metal part has a bevel on the outside to avoid interaction with the outgoing jet. The foil has to be fragile to be broken completely, so that its fragments after the rupture does not disrupt the granular flow at the outlet. We chose a relative thin aluminum foil of thickness ($\approx$ 0.01 mm). Figure 5.1c shows a photo of the aluminum foil after the rupture. We observe that it is completely broken with a circular opening corresponding to the outlet size. Furthermore, the fragments of the aluminum foil stay perpendicular to the outlet and will not influence the granular flow.

After some preliminary tests, we found that it is more difficult to break properly the aluminum foil for a larger outlet size, of diameter D = 20mm. Due to its larger outlet size, the critical pressure of the rupture is lower than that of D = 10mm and the rupture is not complete. In order to break properly the aluminum foil, a higher pressure of crack is required. We use several layers

(a) Pre-cracked preparation

(b) Membrane of aluminum foil after rupture

Figure 5.2: Design of the bottom plug for the discharge of a silo with an instantaneous rupture of the outlet with $D = 20$mm and with four layers of aluminum foil.

of aluminum foil overlaid together to increase the critical rupture pressure level. Moreover, to insure a neat rupture, we weaken the foils by drawing some crosses and a circle with a pencil on the inside of the aluminum foil (see in Figure 5.2a). Figure 5.2b shows a photo of the aluminum foils after the rupture. We observe that the aluminum foils were successfully broken. However, this method is less reproducible than with a simple foil and we will mainly focus on the results obtained with the smaller outlet $D = 10$mm.

The gas injection system is connected to the pressurized air system of the laboratory, as shown in Figure 5.3a. A pressure regulator installed upstream of the air inlet of the silo, allows to impose the maximum pressure level injected to the silo. The entering air flow rate at the top plug of the silo is controlled by a first valve (valve 1). A second valve (so-called safety valve) connects the silo with the atmospheric air.

5.1.2 Instrumentations

The cylindrical silo is instrumented with seven pressure taps (see Figure 5.3a). Fives pressure taps are situated at the lateral positions of the silo like for the previous study. The pressure sensors $P_1 - P_5$ connected with the five taps are differential sensors of model $MPX4250$ provided by NXP and their pressure range is $[0 - 2.5]$bar with an accuracy of $\pm 1.4\%$ and a frequency of acquisition of 100Hz. Moreover, a dynamic pressure sensor P_6 is located at the bottom plug and replaces one of the screws. The top plug has two taps: one for the compressed air inlet and the second one for the second dynamic pressure sensor P_7. The two dynamic pressure sensors $Endevco$, with an absolute pressure range of $[0 - 13.8]$bar and an accuracy of $\pm 1.5\%$ are connected to a digital oscilloscope $TEKTRONIX\ DPO4054$ with an acquisition frequency of 10kHz. All the

pressure sensors are calibrated using the regulator of pressure. In a closed silo configuration, the inlet gas pressure is controlled by the regulator, and the corresponding output signals of all the pressure sensors are recorded. In Figure 5.3b, we have plotted an example of the gas pressure set by the regulator as a function of the output signals for P_1. We obtain a linear function (red line) allowing to define a relation between the output voltages and the pressure levels.
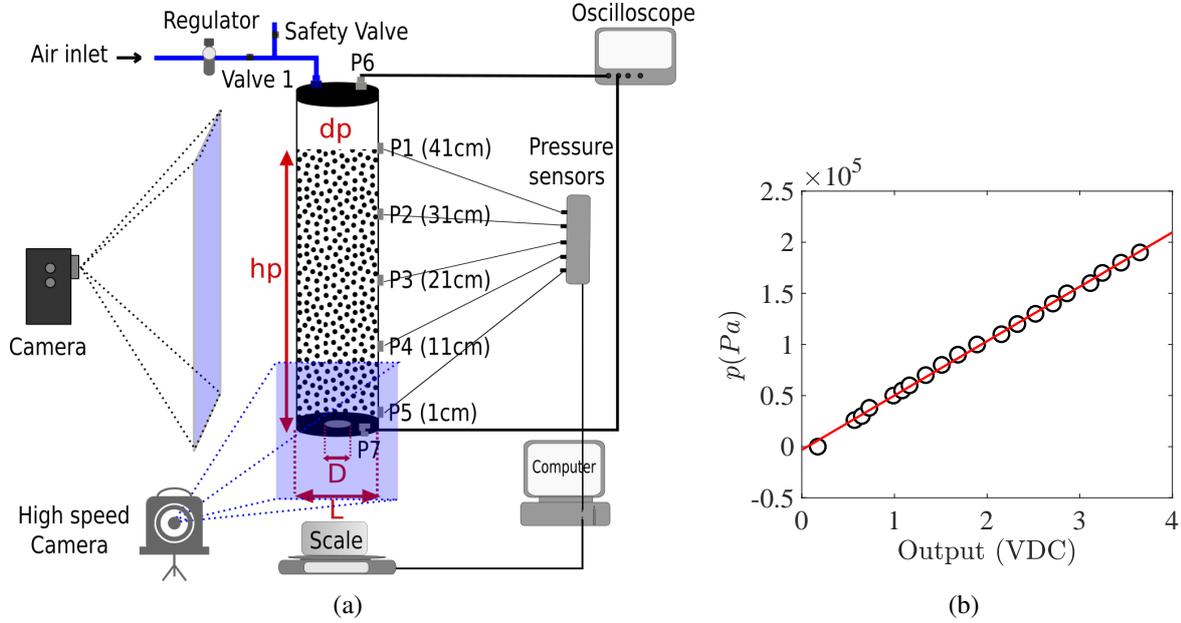
Figure 5.3: (a) Schematic view of the experimental setup for the discharge of silo with an instantaneous rupture of the outlet. (b) Example of the calibration of P_1 using a regulator of pressure.

To study the granular jet at the outlet, a high speed camera ($Phantom\,V711$) is placed in front of the silo, permitting a local view nearby the outlet. The acquisition frequency is set at 3000 or 6000 frames per second with a resolution of $512 \times 512\ pixel^2$, corresponding to a square zone of size approximate $10 \times 10\ cm^2$. To follow the height of the granular column inside the silo, another camera ($GoPro$) is placed around 4m from the silo, permitting a global view of the silo at an acquisition frequency of 240 frames per second and a resolution of $480 \times 848\ pixel^2$, corresponding to a zone of size approximate $60 \times 30\ cm^2$. A rectangular light panel is placed behind the silo, covering the whole silo zone, which provides a homogenous white light source for both cameras. An electronic balance ($Mettler\ Toledo\ 6002S$) is placed below the silo and weights the granular media ejected out of the silo, with frequency of acquisition of 20Hz

5.1.3 Procedure

Initially, the silo is filled by a granular column of height h_p^0, composed by the particles with a mean size d_p. The particles used are shown in Table 5.1. Then the top plug is tightened, connecting with the air injection system with both the valve 1 and the safety valve closed. The high speed camera is set to an auto-trigger mode (triggering the record when it detects a change of the image

contrast). The second camera is activated manually. Then the valve 1 is opened, permitting the entrance of pressurized air into the silo with a small flow rate.

Table 5.1: Particles

	$d_p(\mu m)$
Glass particles	[124; 190; 375; 538; 762; 1129; 1347]
Ceramic particles	[180; 550; 1165]
Bidisperse mixture (ceramic)	180 and 1165
Sand	800 (non-hydrophobic) and 864 (hydrophobic)
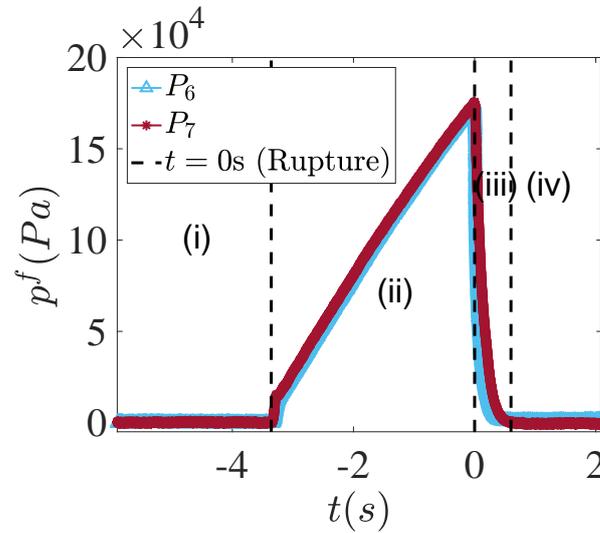
Figure 5.4: A typical result of the gas pressure temporal evolution for the discharge of silo with an instantaneous rupture of the outlet with L = 40mm, D = 10mm and d_p = 762μm (glass). P_6 and P_7 are respectively placed at the top and the bottom of the silo. The left black dashed line represents the rupture moment of the outlet, t = 0s.

Figure 5.4 displays the typical time evolution of the gas pressure P_6 and P_7 (differential pressure compared to the atmospheric air pressure) during the experiment for L = 40mm, D = 10mm and d_p = 762μm (glass particles). The temporal evolution of the gas pressure can be distinguished in four periods: (i) Before the experiment, the silo is initially closed at the atmospheric air pressure, so that we observe 0 differential pressure at the beginning. (ii) As the pressurized gas is injected into the silo, the internal gas pressure increases. This increasing period of the gas pressure lasts approximately 5 s and all of the sensors measure the uniform increase of the gas pressure level. (iii) When the internal gas pressure reaches a critical pressure level, the aluminum foil breaks. We observe that the critical rupture pressure level is ≈ 1.8bar in this case. Notice that the rupture of the outlet is the sign of the beginning of the discharge for both the gas and the granular media, giving the origin of time t = 0s (black dashed line). Then the valve 1 is closed manually as quickly as possible in order to avoid the re-injection of gas. Following the rupture of

the outlet, the pressurized gas as well as the granular media are ejected rapidly through the outlet. The pressure level of the silo decreases quickly during $\approx 0.4s$ in this case. (iv) The pressure level keeps a quasi constant value, sightly below the atmospheric pressure and corresponding to a steady flow.

5.1.4   Measurement of the mass flow rate

The discharge phenomena are very rapid, particularly at the very beginning of the discharge. The 20 Hz acquisition frequency of the electronic balance is not sufficiently high to catch the fast mass variation. Additionally, there is a strong impulse force initiated by the high velocity of the particles as well as that of the pressurized gas, impacting at the vessel over the balance then over-estimating the initial particle mass. Therefore, another technique is used to determine the particle mass flow rate thanks to image processing.
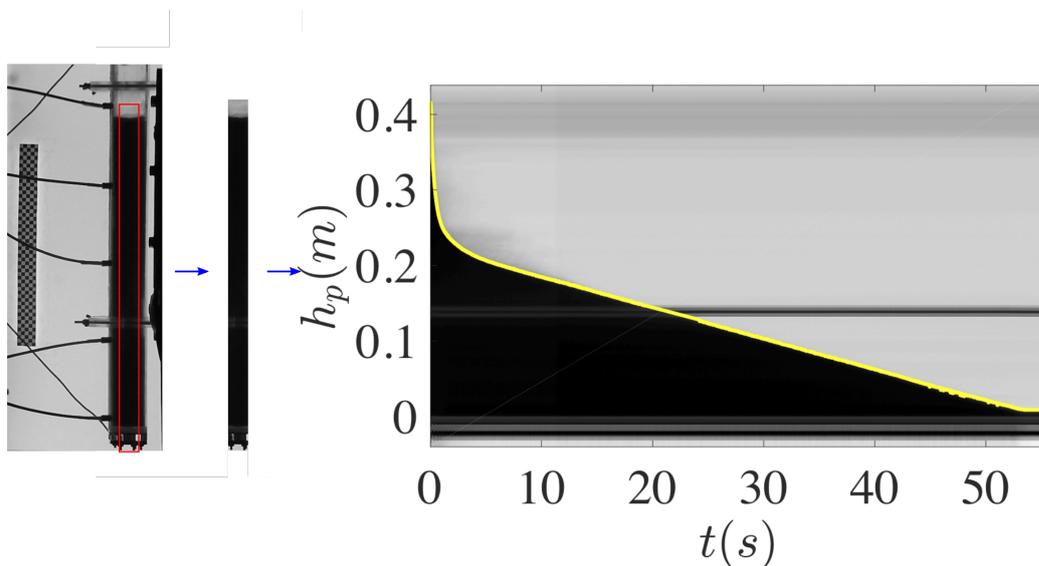
Figure 5.5: An example of the image processing for constructing the spatiotemporal diagram.

An example of the image acquired by the camera giving the global view of the silo, is illustrated on the left part of Figure 5.5 for $D = 10$mm and $d_p = 190\mu m$ (glass particles). A calibration scale is placed on the light panel. We develop a $Matlab$ script to obtain the time evolution of the total height of granular media within the silo. A rectangular area is selected, removing the silo lateral borders as shown by the red framed zone in Figure 5.5. This selected zone is converted to grayscale and averaged along the horizontal direction. We obtain a vector, representing the gray level contrast along the silo. This process is applied for all the frames of the experimental movie and a spatiotemporal diagram is constructed (calibrated using the camera frequency), as shown on the right part of Figure 5.5. The horizontal axis corresponds to the time scale, increasing from left to right, and the vertical axis corresponds to the averaged gray level contrast. Another image

processing script is developed to detect the granular column surface from this spatiotemporal diagram based on a grayscale threshold as shown by the yellow line on the right part of Figure 5.5. We obtain a temporal evolution of the granular column height $h_p(t)$. Assuming that the dynamic bulk particle volume fraction is close to its initial value, $\phi_b \approx \phi_{bi}$. The temporal evolution of the particle mass ejected through the outlet can be determined by the following expression:

$$m = \left(h_p^0 - h_p \right) \rho_p \phi_b S_b \tag{5.1}$$

where S_b represents the cross section of the silo, $S_b = \pi L^2 / 4$.
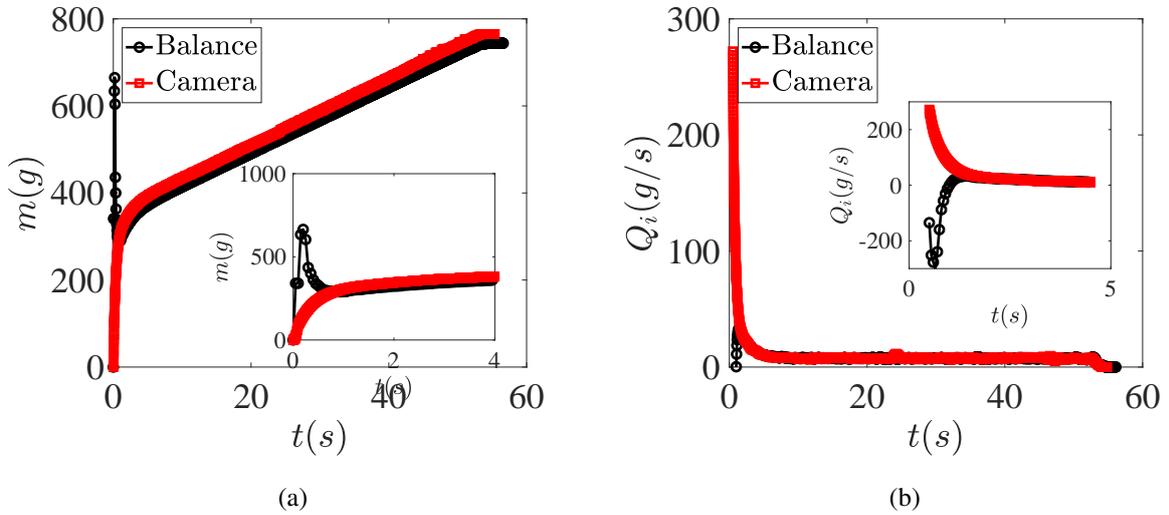
Figure 5.6: Comparison of (a) the particle mass and (b) the mass flow rate, obtained by the balance and by the camera for the discharge of silo with an instantaneous rupture of the outlet with $D = 10$mm and $d_p = 190\mu m$ (glass particles).

Figure 5.6a illustrates a comparison of the temporal evolution of the particle mass out of the silo obtained by the balance (black line) and by the camera (red line) determined by equation 5.1 for $D = 10$mm and $d_p = 190\mu m$ (glass particles). At the very beginning of the discharge, when the aluminum foil is broken, an important over-estimation of the particle mass is observed according to the signal given by the balance. This over-estimation is initiated by the impulse force of the pressurized gas and the particle jet and has an important influence on the determination of the particle mass flow rate, which is therefore negative (see Figure 5.6b). At longer time, the curves are quasi superimposed and the gap between them is attributed by the deviation of the particle volume fraction. The instantaneous particle mass flow rate can be determined by: $Q_i = (m(t + \delta t) - m(t)) / \delta t$, with $\delta t = 1$ s for the balance and $\delta t = 0.08$ s for the camera. Figure 5.6b displays a comparison of the temporal evolution of the particle mass flow rate determined by balance (black line) and by camera (red line). We observe that the balance is not reliable at the beginning of the discharge then both curves overlay after a few seconds when the discharge flow

reaches a quasi-steady state. Therefore, in the following studies, this spatiotemporal method will be used to determine the particle mass flow rate.

5.2   Experimental results

In the following subsections, we will investigate firstly the mass flow rate of the granular media and then the gas flow, especially at the first times of the silo discharge.

5.2.1   Mass flow rate of the granular media
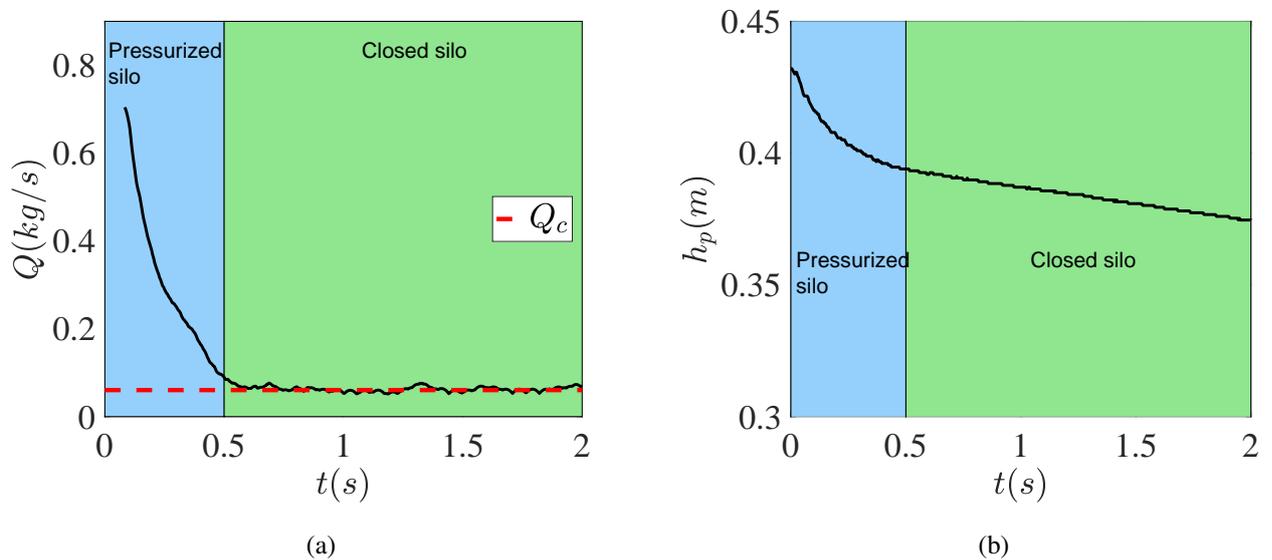
Figure 5.7: Temporal evolution of (a) the discharge flow rate of the granular media $Q(t)$ and (b) the granular column height $h_p(t)$, for L = 40mm, D = 10mm and d_p = 550μm (ceramic particles). The red dashed line represents the mean discharge flow rate during the steady flow corresponding to a closed silo, Q_c.

A typical result of the discharge flow rate with an instantaneous rupture of the outlet by an initial overpressure of the gas is illustrated in Figure 5.7a. For convenience, we set the origin of time when the rupture occurs. At this time, the gas is highly compressed within the silo. The pressurized gas rapidly flows out of the silo and therefore generates a large drag force on the granular media. Thus, we observe a large flow rate of particles through the outlet (black line on the figure) at the very beginning of the discharge. In Figure 5.7b, we plot the temporal evolution of the granular column height $h_p(t)$ and we observe that the granular ejection causes a rapid diminution of the granular column height. As time increases, the internal gas pressure tends to the atmospherical air pressure and the flow rate decreases strongly. The whole discharge period can be distinguished in two parts: the first one when the gas within the silo is pressurized (see the light

blue part in Figure 5.7), for $0 \lesssim t \lesssim 0.5$s in this case, we observe a large variation of the discharge flow rate of the granular media; the second one where the discharge flow reaches a steady state (see the light green part in Figure 5.7), corresponds to the discharge of a silo with a closed top. In this case, the gas pressure is slightly lower than the atmospheric air (see Figure 5.4) and there is a counter-current flow of air. We will investigate separately these two discharge periods.

At the moment of the outlet rupture, the granular flow is strongly coupled to the air flow. To investigate the effect of the particle size, Figure 5.8a illustrates the volumetric flow rates of the granular media Q/ρ_p at the beginning of the discharge for various particle sizes and for several granular materials, with a similar rupture pressure level $p^c \approx 2\ bar$ and an initial granular column height $h_p^0 \approx 0.4\ m$. We observe that for the finer particles, the initial discharge flow rate is higher, and the duration of the pressurized period is longer than for the coarser ones. It seems that the density of the granular material has no influence on the volumetric flow rate (see glass particles of $d_p = 190\mu m$ with $\rho_p = 2500kg/m^3$ and ceramic particles of $d_p = 180\mu m$ with $\rho_p = 6000kg/m^3$). We also test the behavior of sand particles and bidisperse mixture: The sand particles with more angular shape has a very similar behavior than that of spherical particles with the same mean particle size, whereas the bidisperse mixture (composed by an equal mass of ceramic particles of diameter $d_p^c = 1165\mu m$ and $d_p^f = 180\mu m$) has a similar behavior than that composed by the fine particles. These behaviors seem to confirm that the important parameter in the air-grain coupling is the granular media permeability, which justify using a Sauter diameter for the bidisperse mixture.
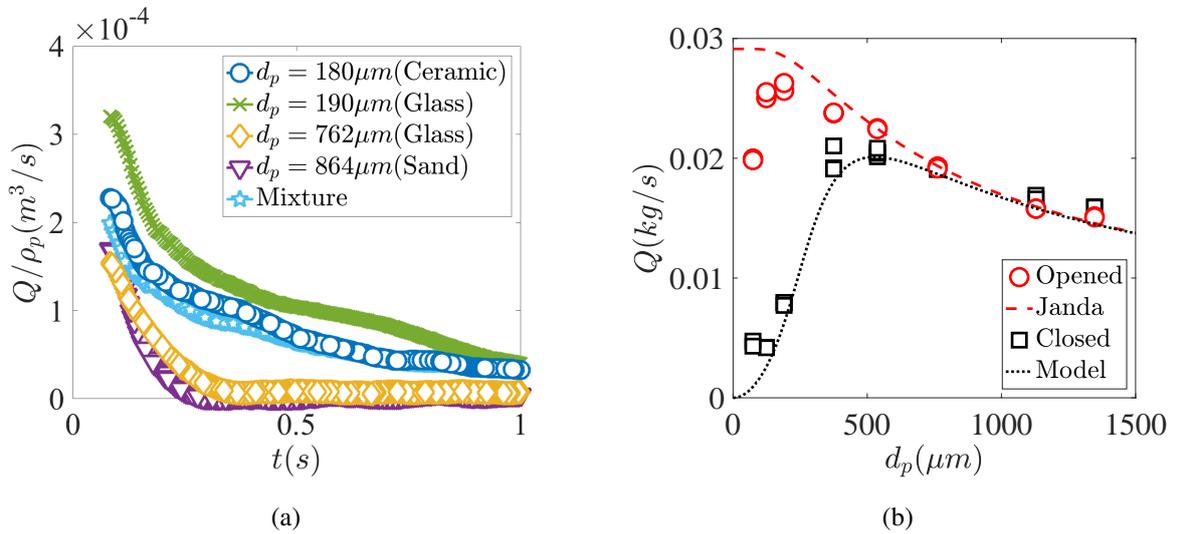
Figure 5.8: (a) Volumetric flow rate at the first times of the discharge, for various granular materials and sizes. (b) Discharge flow rate of the granular media Q versus the particle size d_p for the cases with an opened top (red circles) and for the closed silo flow (black squares). The red dashed line represents equation 2.26 and the red dotted line represents the model of Zhou [2016] (equation 2.37).

Concerning the final discharge period, the red dashed line in Figure 5.7a represents the mean

mass flow rate of particles during this steady state of discharge, noted as Q_c. In Figure 5.8b, we plot the mean discharge flow rate of the granular media as a function of the particle diameter, d_p, for the glass particles, for this regime of flow (red circles) and we compare the discharge of a silo with an opened top (black squares). We observe the same behavior as illustrated by Zhou [2016] when studying the discharge flow of a silo with an imposed air flow rate, Q_{air}, at the top of the silo: the discharge flow rate for the closed silo (Q_{air} = 0), is smaller compared to the opened case, particularly for the fine particles. This decrease of the discharge flow rate can be explained by a counter-current of air flow, which applies an opposite drag force to the granular flow at the outlet. The finer particles have a lower permeability, so the air flow has more difficulty to cross through the granular media leading to a higher drag force, whereas we observe that the discharge flow rate of the granular media of both cases tends to overlay for the coarser particles, the air flowing easily between the particles. The data are well adjusted by the model developed by Zhou [2016] (equation 2.37).

In the following section, we will investigate in detail the air flow during the silo discharge.

5.2.2 Air flow

Thanks to the pressure sensors, we are able to follow temporally and spatially the differential gas pressure along the silo.
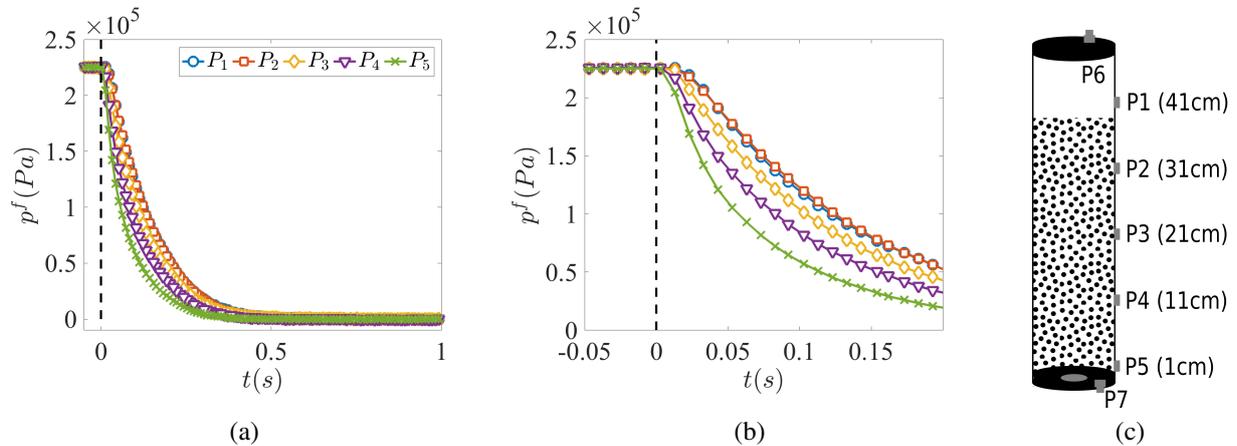
Figure 5.9: (a) Temporal evolution of the differential gas pressure along the silo for L = 40mm, D = 10mm and d_p = $550\mu m$ (ceramic particles). (b) close-up for the first 0.2 s of the discharge. (c) pressure sensors positions.

Figure 5.9 illustrates a typical result of the temporal evolution of differential gas pressure along the silo during the beginning of the discharge. The black dashed line represents the rupture of the outlet, set at t = 0 s. A rapid decrease of the gas pressure is observed as time increasing, beginning from the bottom (P_5), with a slight delay between the sensors from bottom to top. Giving the vertical positions of the pressure sensors (see Figure 5.9c), a first estimation of the gas pressure

gradient can be done by the following expression, using the experimental measurements:

$$\frac{\partial p^f}{\partial z}\Big|_{ij} \approx \frac{P_i - P_j}{z_i - z_j} \tag{5.2}$$

where z_i represents the elevation of the pressure sensor.

Figure 5.10 represents the temporal evolution of the gas pressure gradients along the silo for the first second of the silo discharge, the total gas discharge lasts $\simeq 0.5$ s for this case. At $t = 0$ s, all the gradients are equal to zero corresponding to a homogeneous gas pressure within the silo before the outlet rupture. Afterwards, during ≈ 0.05 s, the gas pressure gradient increases quickly (see the gray zone in figure), which indicates a rapid establishment of the gas pressure gradients. The characteristic time of the establishment of the gas pressure gradient is noted as τ. At the end of this period, we observe that the estimated pressure gradients are no longer homogeneous along the silo. Indeed the pressure gradients increase from the top to the bottom of the granular column. Note that $\frac{\partial p^f}{\partial z}\Big|_{12} \approx 0$ corresponds to $h_p < z_2$.

Afterwards, we observe a decrease of gas pressure gradients due to the ejection of the pressurized air (light blue zone of the figure). Finally, for $t > 0.5$ s, the gas pressure gradients reach a small negative value, corresponding to the steady closed silo with a counter-current gas flow, as shown by the green zone of the figure.
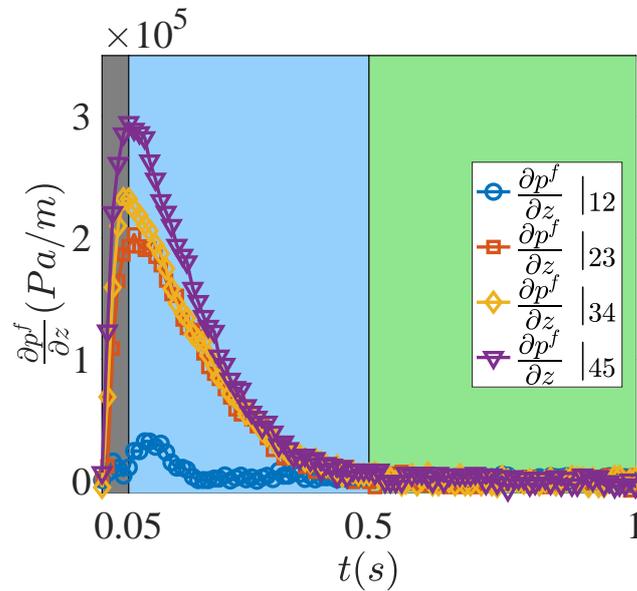

Figure 5.10: Temporal evolution of the gas pressure gradient, estimated by equation 5.2 for $L = 40$mm, $D = 10$mm and $d_p = 550 \mu m$ (ceramic particles).

We will now discuss the 3 periods observed.

a. Establishment of the gas pressure gradient

For each experiment, the characteristic time τ of establishment of the gas pressure gradient is deduced from the position of the peak value of the pressure gradient $\frac{\partial p^f}{\partial z}\big|_{67}$ during the discharge. We use the gas pressure measurement given by the dynamic pressure sensors, P_6 and P_7 for determining this characteristic time, which provide a higher acquisition frequency.
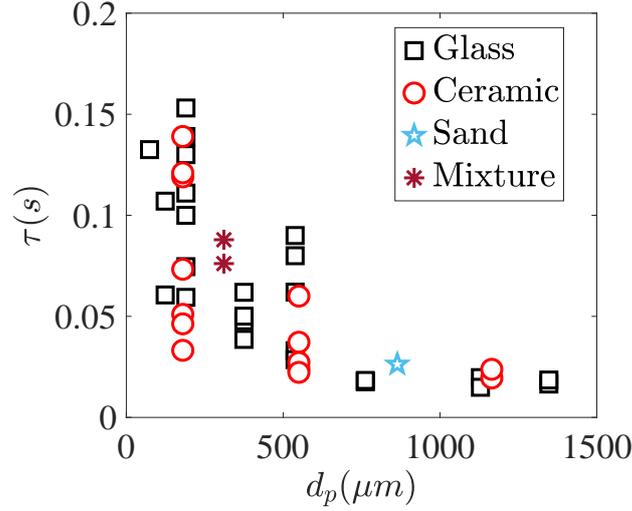
Figure 5.11: Characteristic time of the establishment of the gas pressure gradient τ versus the particle size d_p for various granular materials.

In Figure 5.11, we plot the characteristic time of the establishment of the gas pressure gradient τ as a function of the particle diameter d_p, for various granular materials. We observe that the data are quite scattered but decrease when increasing d_p, in a range between 0.15 s and 0.01 s. As a comparison, the characteristic time of propagation of the acoustic wave within the silo, given by $\tau_s \approx H/c_0 \approx 10^{-3}s$ is much lower, where $H = 0.5m$ represents the silo length and $c_0 \approx 340m/s$ represents the sound speed in the ambient air. It seems that this characteristic time of establishment of the gas pressure gradient depends mainly on the particle size, and not on the density of the particles. We also measure τ for the sand particles and the bidisperse mixture (ceramic particles of $d_p = 1165\mu m$ and $180\mu m$), using the Sauter diameter, deduced by $\bar{d}_p = 1/(X_f/d_p^f + X_c/d_p^c)$, where $X_f = X_c = 0.5$ represent respectively the mass fraction of the fine and the coarse particles. The date seems to lay in the same curve suggesting that the permeability of the granular media plays a role in the establishment of the pressure gradient when the outlet suddenly opens.

We will discuss this characteristic time in the modelling section. We now turn to the discharge period.

b. Pressure profiles during the discharge

We investigate the pressure profiles on the discharge period after the establishment of gas pressure gradient, for ceramic particles with L = 40mm, D = 10mm and d_p = $180\mu m$. In this case, the characteristic time of establishment of the gas pressure is close to 0.1s. We distinguish the two periods of flows: the pressurized period ($0.1s \lesssim t \lesssim 2s$) and the steady counter-current period ($t \gtrsim 2s$).
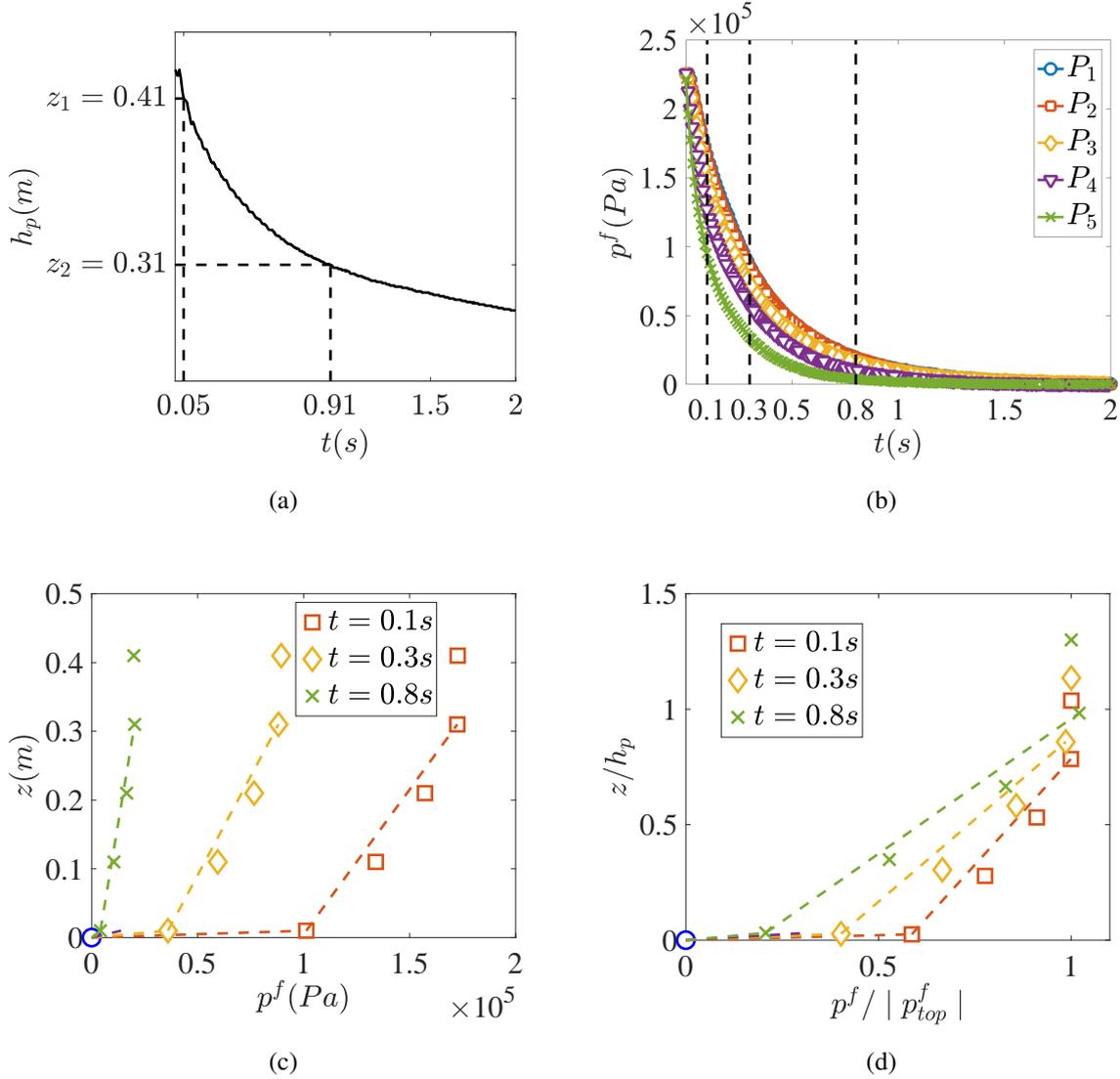
Figure 5.12: Discharge of the silo with an instantaneous rupture of the outlet for L = 40mm, D = 10mm and d_p = $180\mu m$ (ceramic particles) during the pressurized period ($0.1s \lesssim t \lesssim 2s$). (a) temporal evolution of the granular column height. (b) temporal evolution of the pressure along the silo. (c) pressure profiles along the silo at various moments. (d) pressure profiles normalized by the pressure at the top of the silo, $p^f / \mid p^f_{top} \mid$.

For the pressurized period (during the first two seconds of the discharge), we plot the temporal evolution of the granular column height in Figure 5.12a deduced by the camera (see Figure 5.5)

where the dashed lines represents the crossing point at which the granular surface passes by the pressure taps. Figure 5.12b shows the temporal evolution of the gas pressures along the silo. A rapid decrease of the gas pressure is observed with an overpressure going from 2.5bar to 0. For investigating in more detail the pressure evolution along the silo, the instantaneous pressure profiles p^f at various instants ($t = 0.1s$, $0.3s$ and $0.8s$) are illustrated in Figure 5.12c. In Figure 5.12d, we plot the vertical position normalized by the granular column height z/h_p versus the pressure profiles normalized by the pressure at the top of the silo $p^f / \mid p^f_{top} \mid$, with p^f_{top} being given by P_1 at the elevation of $z_1 = 41$cm and assuming a zero differential gas pressure at the outlet ($z = 0$). Similarly to the previous study in chapter 4 with an imposed pressure at the top of the silo, we observe three zones (see for example $t = 0.1$s): close to the outlet, we observe a high pressure gradient due to the reduction of the gas passage section; far from the outlet, we observe a quasi linear pressure gradient, but with a very slight curvature as illustrated by the dashed line which simply links P_2 and P_5. This suggests that the compressibility of air flow mass play a role on the time and space evolution of pressure within the silo during the discharge at such level of pressure.

For the steady discharge flow, the temporal evolution of the granular column height is illustrated in Figure 5.13a and the temporal evolution of the gas pressure along the silo is illustrated in Figure 5.13b. Notice that during the counter-current period, the gas pressure measurement has a lower accuracy due to its low values. A negative differential pressure is observed within the silo corresponding to a counter-current air flow. We recover the same tendency that observed by Zhou [2016] for an imposed air flow rate $Q_{air} = 0$ (closed top silo). The air velocity u^f being constant, the pressure gradient and thus the pressure is constant at a given position inside the granular media whereas the pressure at the top becomes less negative as h_p decreases. In Figure 5.13c we plot the instantaneous pressure profile p^f at various instants ($t = 5s$, $t = 10s$ and $t = 20s$), which is normalized by the pressure at the silo top $p^f / \mid p^f_{top} \mid$ in Figure 5.13d. A linear relation is observed for the zone far from the outlet, indicating a spatially uniform axial pressure gradient, and we recover the change of slope around the outlet, due mainly to the reduction of the passage section. We observe that both pressure gradients remain quasi constant as time increasing.

c.   Correlation between the silo discharge and the air pressure

Following the work carried out by Crewdson et al. [1977], Zhou [2016] and in chapter 4, we can suppose that the discharge flow rate of particles coupled with a gas flow can be described by the modified Hagen-Beverloo law, adding a term of the gas pressure gradient at the outlet on the driving term of the gravity:

$$Q = Q_0 \left(1 + \frac{1}{\phi_0 g \rho_p} \frac{\partial p^f}{\partial z} \mid_{z \approx 0} (t) \right)^{1/2} \qquad (5.3)$$
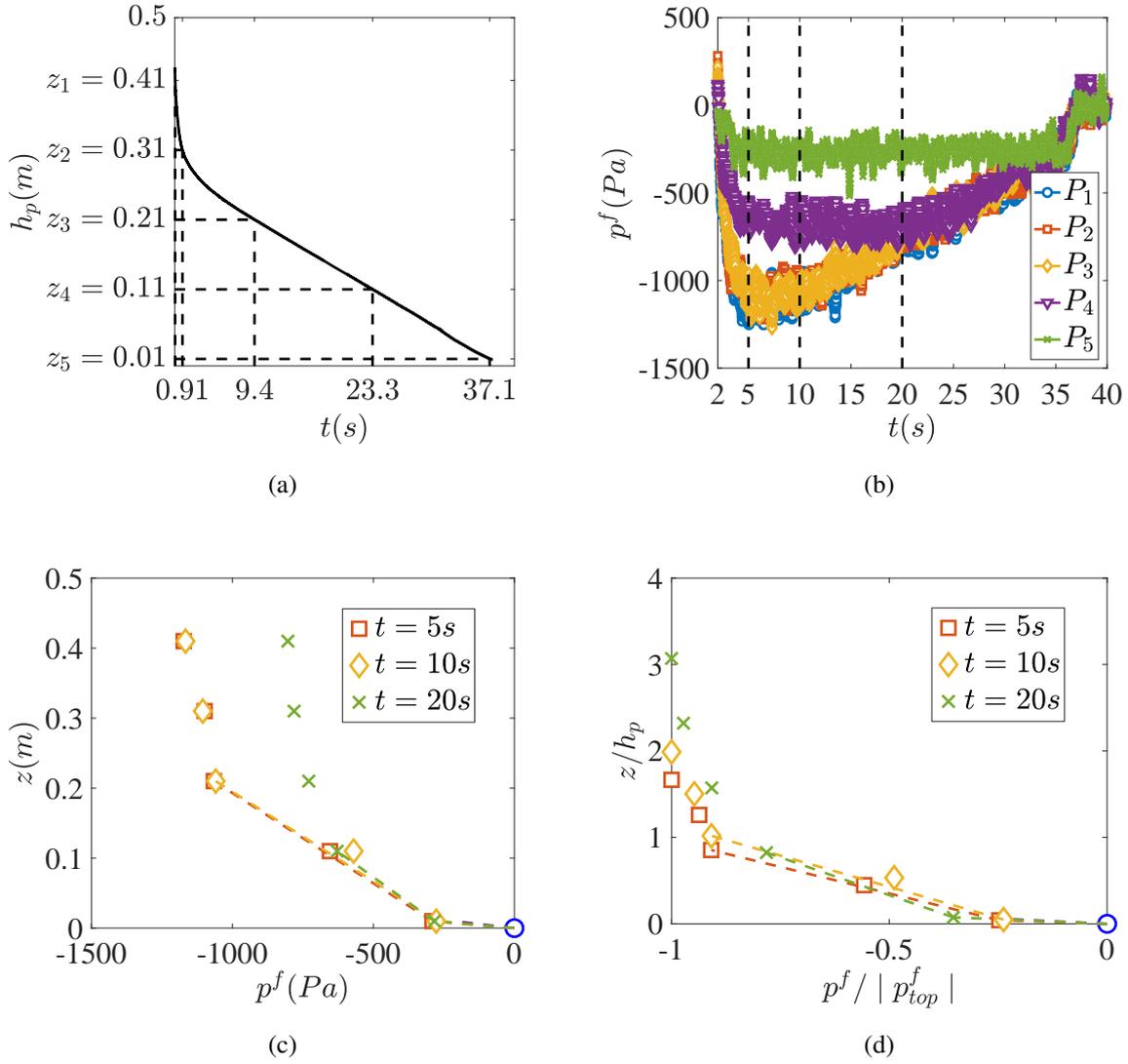
Figure 5.13: Discharge of the silo with an instantaneous rupture of the outlet for $L = 40$mm, $D = 10$mm and $d_p = 180\mu m$ (ceramic particles) during the counter-current period with a closed top ($t \gtrsim 2s$). (a) temporal evolution of the granular column height. (b) temporal evolution of the pressure along the silo. (c) pressure profiles along the silo at various moments. (d) pressure profiles normalized by the pressure at the top of the silo, $p^f / \mid p^f_{top} \mid$.

where Q_0 represents the discharge flow rate of particles without the gas injection and ϕ_0 is the volume fraction of the particle at the outlet. To verify this approximation, let us assume that the gas pressure gradient at outlet can be approximately determined by the equation 5.2, using the experimental measurement of pressure given by P_5 at the elevation of $z_5 = 1\ cm$, giving $\partial p^f / \partial z \mid_{z\approx 0} (t) = P_5(t)/z_5$. Additionally, we use the initial bulk volume fraction of the particle to evaluate $\phi_{bi} \approx \phi_0$, valid for $D/d_p \geq 50$.

Figure 5.14 illustrates the comparison of the discharge flow rate with equation 5.3 (see the red solid lines), using the experimental measurements for Q_0, and taking $\phi_0 \approx \phi_{bi}$. Figure 5.14a concerns for the pressurized period, for the first two seconds, and Figure 5.14b is the steady counter-
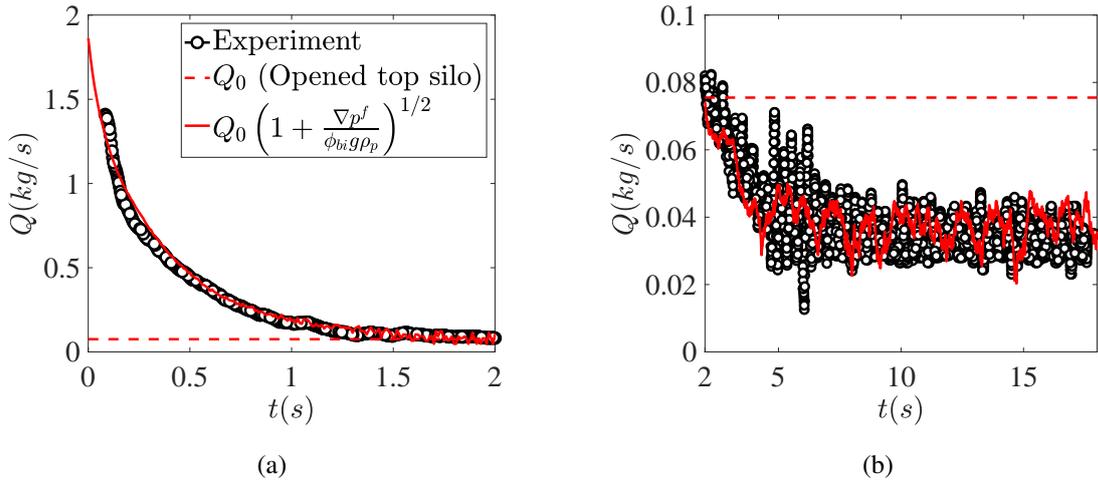
Figure 5.14: Comparison of the mass flow rate of the granular media for $L = 40$mm, $D = 10$mm and $d_p = 180 \mu m$ (ceramic particles) with equation 5.3 for (a) the pressurized period and (b) the steady counter-current period. The black lines represent the experimental measurements, the red solid lines represent the mass flow rate predicted by equation 5.3, taking $\phi_0 \approx \phi_{bi}$, and the red dashed lines represent the steady discharge flow rate with an opened silo top driven by gravity.

current period ($t \gtrsim 2s$) where we smoothen the gas pressure data by averaging 60 acquisition points, for the same experimental condition than Figure 5.13. We observe that equation 5.3 has a fairly good agreement with the experimental result for both periods. It suggests that the granular flow instantaneously (without inertia) follows the gas flow variations. Therefore, a quasi steady model of the air-granular flows coupling is sufficient for describing this very unsteady discharge flow with an instantaneous rupture of the outlet.

From these observations, we propose in the following section an analytical model based on the two-phase continuum modelling. We will first discuss the establishment of the gas pressure gradient within the silo. Then a quasi-steady analytical model will be developed, taking into account the compressibility of the gas flow with two degrees of sophistication, for describing the discharge flow rate during both the pressurized and the steady counter-current flow periods.

5.3   Modelling

5.3.1   Establishment of the gas pressure gradient

The characteristic time of establishment of the gas pressure gradient, after the rupture of the orifice, is quite short ($\tau < 0.15s$ see Figure 5.11). Moreover, the air flow speed is very large with respect to the granular particles speed. Therefore, for the modelling of the air flow, it is reasonable to consider the granular height to be constant and the granular media to be motionless. The granular media is then modeled as a porous media. Let us consider the fluid phase mass and

momentum balance equations. In the gas phase momentum balance, we neglect the convective term and the gravity term, as well as the viscous stresses component, with respect to the drag force (see Nield and Bejan [2006]). The mass and the momentum conservation equations of the gas flow can then be simplified as follows:

$$\frac{\partial \rho_f}{\partial t} + \frac{\partial (\rho_f u_i^f)}{\partial x_i} = 0 \tag{5.4}$$

$$\frac{\partial (\rho_f u_i^f)}{\partial t} = -\frac{\partial p^f}{\partial x_i} - f_{ti} \tag{5.5}$$

where the term f_{ti} represent the drag forces between two phases and can be determined by the Darcy-Forchheimer resistance law (equation 2.13 in chapter 2):

$$f_{ti} \approx -\eta \beta_l (1 - \phi) u_i^f - \rho_f d_p \beta_i (1 - \phi)^2 \left(u_i^f\right)^2 \tag{5.6}$$

According to the Kozeny-Carman equations with: $\beta_l = \frac{150\phi^2}{(1-\phi)^3 d_p^2}$ and $\beta_i = \frac{1.75\phi}{(1-\phi)^3 d_p^2}$.

Then, we derive the mass conservation equation of air flow with time:

$$\frac{\partial^2 \rho_f}{\partial t^2} - \frac{\partial}{\partial x_i} \left(\frac{\partial \rho^f u_i^f}{\partial t}\right) = 0 \tag{5.7}$$

Introducing the momentum conservation equation we thus obtain:

$$\frac{\partial^2 \rho_f}{\partial t^2} - \frac{\partial^2 p^f}{\partial x_i^2} - \eta \beta_l (1 - \phi)\left[1 + \frac{Re_p(1 - \phi)}{43\phi}\right]\frac{\partial u_i^f}{\partial x_i} = 0 \tag{5.8}$$

with $Re_p = \rho_f d_p u_i^f / \eta$.

We suppose that before the rupture of the outlet, the silo is pressurized at $p^f = p_c^f$ a constant pressure, corresponding to a density $\rho_f = \rho_{fc}$. We suppose that when opening the outlet, we can write $p^f = p_c^f + p_1^f$ and $\rho_f = \rho_{fc} + \rho_{f1}$, with $p_1^f \ll p_c^f$ and $\rho_{f1} \ll \rho_{fc}$. Moreover we introduce the speed of sound $c_0 = \sqrt{(\partial p^f / \partial \rho_f)_s}$, where the derivative is taken isentropically, supposing that the heat transfer between the gas and the granular media can be neglected. Therefore, using equation 5.4, equation 5.8 can be splitted between terms of first order (0) that corresponds to static balance equation and terms of first order that leads to the following equation:

$$\frac{1}{c_0^2}\frac{\partial^2 p_1^f}{\partial t^2} - \frac{\partial^2 p_1^f}{\partial x_i^2} + \frac{\eta \beta_l (1 - \phi)}{\rho_{f0} c_0^2}\left[1 + \frac{Re_p(1 - \phi)}{43\phi}\right]\frac{\partial p_1^f}{\partial t} = 0 \tag{5.9}$$

At the very beginning after the rupture of the outlet, we can suppose that the velocity of fluid is negligible, thus we can neglect the term $(1 - \phi)Re_p/43\phi \ll 1$. In addition, we suppose that the term of secondary derivative of time, $\frac{1}{c_0^2}\frac{\partial^2 p_1^f}{\partial t^2}$, can be neglected compared to the first derivative of time as long as $\tau > \rho_{fc}/(\eta \beta (1 - \phi)) \approx 10^{-4} s$, where τ represents the time scale for establishment

149

of pressure gradient. We valid this assumption (see Figure 5.11), using the experimental measurements, since τ order of magnitude is at least 10^{-2} s. Therefore, we obtain a typical diffusion equation for the evolution of the gas pressure:

$$\frac{\partial p^f}{\partial t} = \mathcal{D}\frac{\partial^2 p^f}{\partial x_i^2} \tag{5.10}$$

with the diffusion coefficient $\mathcal{D} = \frac{\rho_{fc}c_0^2}{\eta\beta_l(1-\phi)} = \frac{\rho_{fc}c_0^2 d_p^2(1-\phi)^2}{150\eta\phi^2}$.
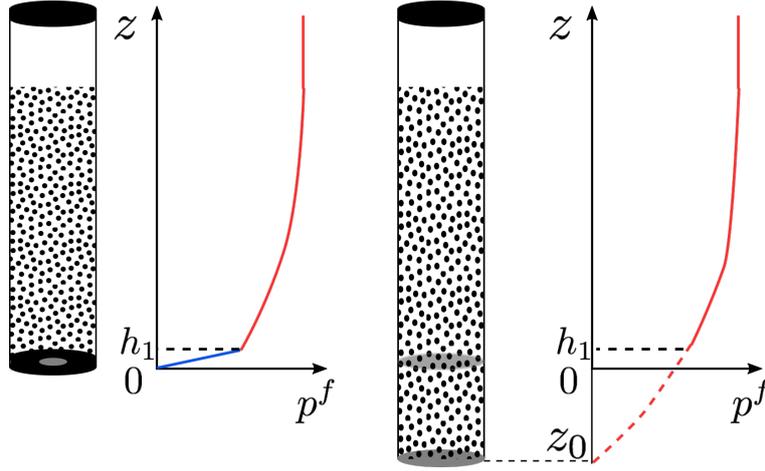

Figure 5.15: Schematic view of the gas pressure profile for the experimental silo (left part) and for a virtual elongated silo with uniform cross section (right part).

We suppose that the gas pressure within the silo is initially homogeneous and equal to the value leading to the outlet rupture, $p^f(t = 0, z) = p_c^f$. At the rupture, the gas pressure at the outlet drops to zero. For resolving this diffusion equation of the gas pressure, the initial condition is then given by the Heaviside step function. Following the experimental observation, the pressure profile along the silo is schematized on the left part of Figure 5.15: a jump of pressure gradient appears nearby the outlet, mainly initiated by the reduction of the gas passage section. For taking into account this pressure drop, a virtual elongated silo with an uniform cross section is considered with an outlet situated at $z = z_0$, shown on the right part of the figure, where we can set the boundary initial condition $p^f(t = 0, z = z_0) = 0$. We will consider z_0 as an adjustable parameter. The solution of equation 5.10 along the vertical position of the silo z can thus be expressed as:

$$p^f(z, t) = p_c^f \operatorname{erf}\left(\frac{z - z_0}{2\sqrt{\mathcal{D}t}}\right) \tag{5.11}$$

with the error function $\operatorname{erf}(x) = \frac{1}{\pi}\int_{-x}^{x} e^{-t^2}$.

In Figure 5.16, we plot the temporal and spatial evolution of the gas pressure profiles along the silo right after the rupture of the outlet, for the glass particles of $d_p = 375\mu m$ (see Figure 5.16a) and for the ceramic particles of $d_p = 180\mu m$ (see Figure 5.16b). The dashed lines represent the gas pressure profile obtained by the analytical solution given by equation 5.11 with a fitting parameter

150
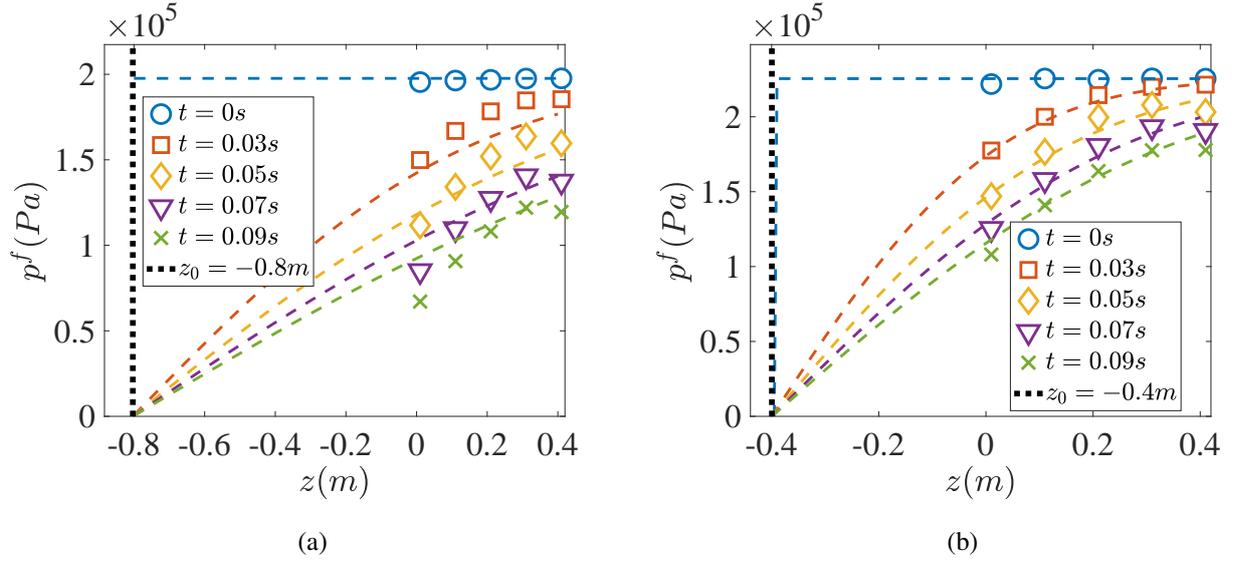
Figure 5.16: Gas pressure profile $p^f(z)$ along the silo at various instants, for (a) $L = 40$mm, $D = 10$mm and $d_p = 375\mu m$ (glass particles) and (b) $L = 40$mm, $D = 10$mm and $d_p = 180\mu m$ (ceramic particles). The individual points are given by the experimental measurements and the dashed lines correspond to equation 5.11. The black dotted lines represent the fitting parameter position, z_0.

z_0, taking the viscosity of air $\eta = 1.8 \times 10^{-5} Pa \cdot s$, the speed of sound $c_0 \approx 340 m/s$ and the initial volume fraction of particles ϕ_{bi}. We suppose that the injection process of the pressurized air before the rupture (see Figure 5.4) is isothermal, the initial density of air can be estimated by $\rho_{fc} = \rho_{f0}(P_c^f/P_0^f) \approx 3.5 kg/m^3$, where ρ_{f0} and P_0^f represent the density and the pressure of atmospheric air and $P_c^f \approx 3$bar is the absolute pressure of the rupture of outlet. We observe a fairly good agreement with the experimental measurements.

Figure 5.17a illustrates the virtual elongated length of the silo z_0, as a function of the particle sizes, d_p. The data, including the sand particles and the bidisperse mixture, seems to superimpose in this representation which suggests that z_0 is linked to the particle permeability. We observe that z_0 is longer for the coarser particles. In this case, large permeability results to a large diffusion coefficient, thus, a longer virtual granular media is needed to balance the pressure drop nearby the outlet.

A typical filling height of the granular column for our experiments is $h_p^0 \approx 0.4\ m$, therefore, the characteristic time of establishment of the gas pressure gradient can be estimated as:

$$\tau \approx \frac{\left(h_p^0\right)^2}{\mathcal{D}} = \frac{150(h_p^0)^2\eta\phi_{bi}^2}{\rho_{fc}c_0^2 d_p^2(1-\phi_{bi})^2} \tag{5.12}$$

Figure 5.17b illustrates the comparison of the characteristic time of establishment of the gas pressure as a function of the particle size, d_p, for various granular materials, with equation 5.12 (blue dashed line), using the initial bulk particle volume fraction ϕ_{bi}, a typical granular column

151
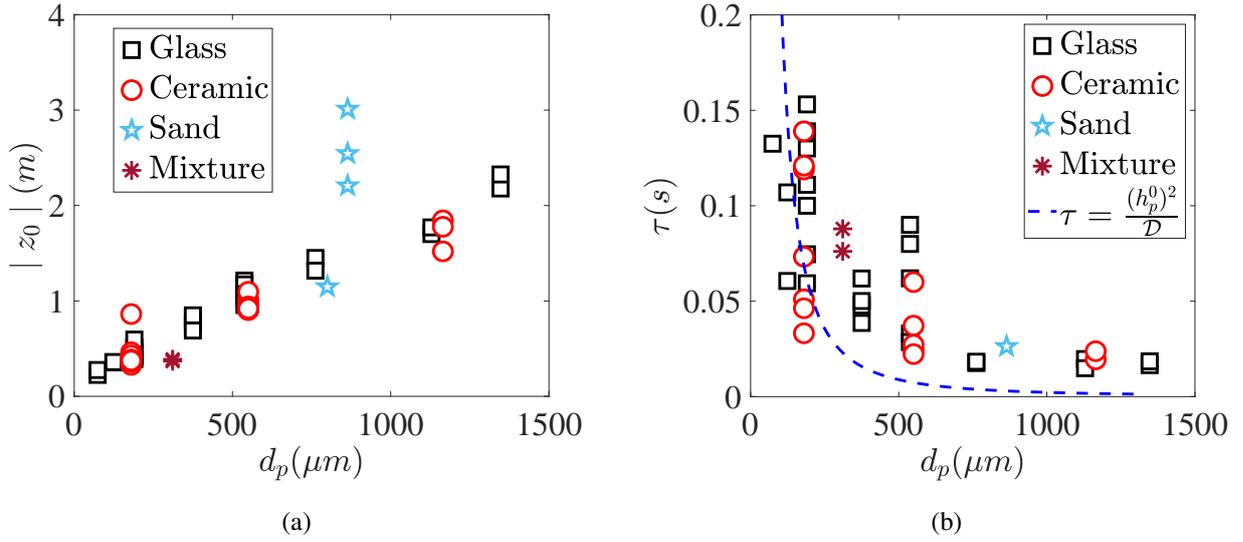
Figure 5.17: (a) Virtual elongated length of the silo $\mid z_0 \mid$ as a function of the particle size. (b) Characteristic time of the establishment of the gas pressure gradient τ versus the particle size d_p. The blue dashed line represents the equation 5.12.

height, $h_p^0 = 0.4$m, $\eta = 1.8 \times 10^{-5} Pa \cdot s$, $c_0 \approx 340 m/s$ and $\rho_{fc} \approx 3.5 kg/m^3$. We observe a fairly good agreement between the model and the experimental measurements, for all used granular materials including the glass particles, the ceramic particles, the sand particles as well as the granular media composed by the bidisperse mixture. We observe that this characteristic time depends particularly on the particle size, through the permeability of the granular media. For the coarser particles, the establishment of the gas pressure gradient is more rapid than for the finer ones, the gas flow can cross more easily the granular media. Additional experiments, varying for example h_p^0 could be viewed as perspectives to further validate the scaling of τ.

Once the gas pressure gradient within the silo establishes, we will now focus on the prediction of the flow rate.

5.3.2 Quasi-steady compressible unidimensional analytical model

Once the gas pressure gradient established in the silo, according to the previous experimental observations, we can suppose that our system relaxes instantaneously during both the pressurized and the steady counter-current periods, meaning that the granular flow adapts instantly with the gas flow. Agin we assume that the fluid phase has no inertia and we neglect the viscous stress in the fluid phase together with the gravity term. We also assume a quasi-steady value for the gas density. Thus, we can follow the previous study on the discharge of silo with an imposed gas pressure (see chapter 4), using a two-phase continuum modelling. A Darcy-Forchheimer resistance law (see equation 2.13) is used to model the drag force and the shear-dependent rheology $\mu(I)$ is applied to describe the behavior of the granular flow (see equation 2.5). The main difference is that the

pressure at the top of the silo evolves with time due to the ejection of air. Moreover, considering the highly pressurized air within the silo at the beginning of the discharge ($\approx$ 2bar above the atmospheric air pressure), the compressibility of air flow should be taken into account in our model.

Under these assumptions, the two-phase continuum modelling equations for the compressible gas flow and the granular flow can be simplified as follows:

$$\frac{\partial(\rho_f(1-\phi)u_i^f)}{\partial x_i} = 0 \tag{5.13}$$

$$\frac{\partial \phi}{\partial t} + \frac{\partial(\phi u_i^p)}{\partial x_i} = 0 \tag{5.14}$$

$$-\frac{\partial p^f}{\partial x_i} = \beta_l \eta_f (1-\phi)(u_i^f - u_i^p) + \beta_i \rho_f d_p (1-\phi)^2 (u_i^f - u_i^p) \mid (u_i^f - u_i^p) \mid \tag{5.15}$$

$$\rho_p \phi \left[\frac{\partial u_i^p}{\partial t} + u_j^p \frac{\partial u_i^p}{\partial x_j} \right] = \frac{\partial \sigma_{ij}^p}{\partial x_j} - \frac{\partial p^f}{\partial x_i} + \phi \rho_p g_i \tag{5.16}$$

Two other closures are then necessary: First, we choose the ideal gas law to take into account the compressibility of air within the silo.

$$P^f = \frac{n_f RT}{V_f} = \rho_f \frac{R}{M} T \tag{5.17}$$

where P^f is the absolute pressure, V_f is the volume of gas, n_f is the number of moles of gas, $R = 8.314 J \cdot mol^{-1} \cdot K^{-1}$ is the gas constant, T is the gas temperature, ρ_f is the gas density and M is the molar mass of gas, for air $M = 29g/mol$. Then we can test two assumptions to describe the heat exchange in the silo:

- Adiabatic process: we suppose that no heat transfer occurs between the air and its environment (silo walls and particles). Air temperature varies due to pressure variation.

- Isothermal process: we suppose that the temperature of the silo adjusts to the temperature of the external environment through heat exchange, the air system remains at the constant ambient temperature T_0. It means that the air cooling due to its pressure decrease is fully compensated by heat transfer with particles that remains at T_0.

Just after the rupture, we suppose that the air within the silo has a initial pressure $P_c^f \approx 3 \times 10^5 Pa$, and a temperature equal to that of the external environment, $T_0 = 298K$. The initial gas density can be given by: $\rho_{fc} = (P_c^f M)/(RT_0) \approx 3.5kg/m^3$. Firstly, if we suppose an adiabatic system during the silo discharge, we can write:

$$T^\gamma (P^f)^{1-\gamma} = T_0^\gamma (P_c^f)^{1-\gamma} \tag{5.18}$$

where $\gamma = 1.4$ is defined as the heat capacity ratio.

During the discharge of the silo, the gas pressure tends to the atmospheric air pressure, $P_0^f = 1 \times 10^5 Pa$. Thus, the temperature of the gas within the silo after the pressurized period can be given by: $T_1 = T_0(P_0^f/P_c^f)^{(\gamma-1)/\gamma} \approx 218K$ ($\approx -55°C$). Thus, under the adiabatic process assumption, we should have observed a strong cooling of the air that does not correspond to our experimental observations. On the other hand, if air cools down while its pressure goes down, an intense heat transfer between the gas phase and the granular phase should occur. If we suppose that the heat is transferred by convection between the two phases, we can write:

$$(1-\phi)\rho_f c_p \frac{dT^f}{dt} = ah\left(T^p - T^f\right) \tag{5.19}$$

where $c_p \approx 1 \times 10^3 J \cdot kg^{-1} \cdot K^{-1}$ represents the specific heat capacity, $a = 6\phi\pi d_p^2/\pi d_p^3$ represents the specific surface for the heat transfer between two phases, T^f and T^p represent respectively the temperature of the gas and the granular phases, h is the heat transfer coefficient between the two phases, $\lambda \approx 2 \times 10^{-2} W \cdot m^{-1} \cdot K^{-1}$ is the thermal conductivity of the gas and the d_p is the particle diameter. The Nusselt number can be introduced to describe the heat transfer between a spherical particle and the gas, $Nu = h\frac{d_p}{\lambda}$. Following Aissa et al. [2015], we can take $Nu \approx 2$, that is the lower value for this convective case, giving $h \approx 400W \cdot m^{-2} \cdot K^{-1}$ for $d_p = 100\mu m$. From equation 5.19, we can estimate the characteristic time of the heat transfer between the two phases by:

$$\tau_h \approx \frac{(1-\phi)\rho_f c_p}{ah} \tag{5.20}$$

Therefore, we obtain a typical characteristic time of the heat transfer between the gas and the granular phases, $\tau_h \approx 8 \times 10^{-5}s$ for the particle diameter $d_p = 100\mu m$. This characteristic time is much lower than that of the establishment of the gas pressure gradient, which indicates a rapid heat transfer between the two phases. Moreover, the granular media having a specific heat capacity much higher than the air, we can suppose that the granular media keeps roughly its initial temperature and impose it to the air phase.

The previous result leads us to take the assumption of an isothermal process during the silo discharge, rather than an adiabatic process assumption, for describing the behavior of the gas flow. Under this isothermal assumption, the temperature of the whole silo stays constant during the discharge and is equal to that of ambient environment, $T = 293K$. Therefore, considering air as an ideal gas we get:

$$\frac{P^f V_f}{n_f} = RT = constant \quad \text{or} \quad \frac{P^f}{\rho_f} = \frac{RT}{M} = constant \tag{5.21}$$

As time increasing, the granular media and air flow are ejected through the outlet, which initiates an extension of the gas volume V_f, as well as a decrease of the gas mole number, n_f.

To investigate the discharge flow at a given time t, we distinguish three zones within the silo, as shown in Figure 5.18. We note the silo height as H and the granular column height as $h_p(t)$.
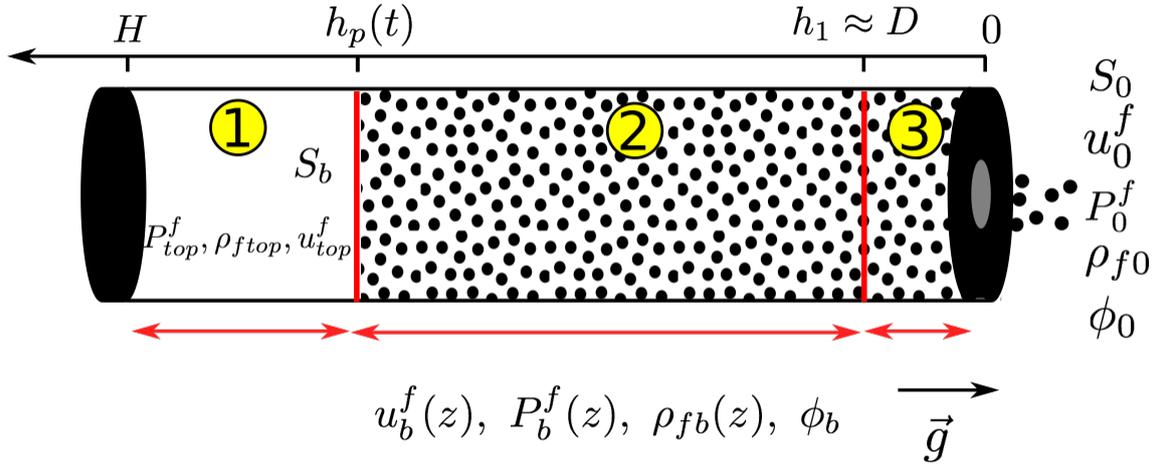
Figure 5.18: A schematic view of the whole silo and the notations of the variables.

The first zone is above the granular column ($h_p \leq z \leq H$), where there is only the fluid phase. The second zone corresponds to the bulk granular column far from the outlet ($h_1 \leq z \leq h_p$). And the third zone is the zone nearby the outlet ($0 \leq z \leq h_1$). For convenience, we use respectively the subscripts top, b and 0 for representing the variables of these different zones.

The mass conservation of the granular flow reads:

$$\rho_p \phi S u^p = constant \qquad (5.22)$$

Concerning the fluid phase, since we assume a quasi-steady value for the gas density, the continuity equation reads:

$$\rho_f (1 - \phi) S u^f = constant \qquad (5.23)$$

In the following subsections, we will investigate the behaviors of the gas flow and the granular flow within the zones far and near the outlet.

a. Zone far from the outlet

In the zone far from the outlet (zone 2 in Figure 5.18), corresponding to a constant cross section S_b, the flow of both phases can be considered unidimensional with a constant volume fraction ϕ_{bi}. Thus at a given time, the mass conservation of the granular flow (equation 5.22) gives:

$$u_b^p(z) = u_b^p = constant \qquad (5.24)$$

The mass conservation of the fluid phase (see equation 5.23), introducing the ideal gas law (equation 5.21) gives:

$$P_b^f(z) u_b^f(z) = P_{top}^f u_{top}^f = constant \qquad (5.25)$$

Where P_{top}^f and u_{top}^f represent respectively the absolute pressure and the velocity of the air flow

155

above the granular column. As previously, we introduce a definition of sign which distinguishes the co-current air flow and the counter-current air flow:

$$\pm = \frac{u^f - u^p}{\mid u^f - u^p \mid}$$

(5.26)

whose value is $+1$ for the case of a co-current air flow and -1 for the case of a counter-current air flow.

According to the Forchheimer resistance law (equation 2.13), the ideal gas law (equation 5.21) and equation 5.25, the momentum conservation of air flow (equation 5.15) for the zone far from the outlet can be written as the following expression:

$$\frac{\partial P^f}{\partial z}\mid_{z \gg 0} = -\beta_{lb}\eta_f(1 - \phi_b)(\frac{P_{top}^f u_{top}^f}{P_b^f(z)} - u_b^p) \mp \beta_{ib}\frac{P_b^f(z)M}{RT}d_p(1 - \phi_b)^2(\frac{P_{top}^f u_{top}^f}{P_b^f(z)} - u_b^p)^2$$

(5.27)

with $\beta_{lb}(\phi_b, d_p) = \frac{150\phi_b^2}{(1-\phi_b)^3 d_p^2}$ and $\beta_{ib}(\phi_b, d_p) = \frac{1.75\phi_b}{(1-\phi_b)^3 d_p^2}$. Notice that under the isothermal assumption, we suppose that the viscosity of the air stays constant.

To find the analytical solution of this differential equation, we normalize it using $\rho_p g D$ as a pressure scale, $\sqrt{gD}$ as a velocity scale and D as a length scale. We note $\tilde{\cdot}$ the dimensionless parameter, thus we write:

$$\frac{\partial \tilde{P}_b^f}{\partial \tilde{z}} = \frac{a\left(\tilde{P}_b^f(\tilde{z})\right)^2 + b\tilde{P}_b^f(\tilde{z}) + c}{\tilde{P}_b^f(\tilde{z})}$$

$$a = \mp \frac{2M}{RT}d_p g D^2 \beta_{ib}(1 - \phi_b)^2 (\tilde{u}_b^p)^2$$

$$b = \frac{\beta_{lb}\eta_f}{\rho_p}\sqrt{\frac{g}{D}}(1 - \phi_b)\tilde{u}_b^p \pm \frac{2M}{RT}d_p g D^2 \beta_{ib}(1 - \phi_b)^2 \tilde{u}_b^p \tilde{u}_{top}^f \tilde{P}_{top}^f$$

$$c = -\frac{\beta_{lb}\eta_f}{\rho_p}\sqrt{\frac{g}{D}}(1 - \phi_b)\tilde{P}_{top}^f \tilde{u}_{top}^f \mp \frac{M}{RT}d_p g D^2 \beta_{ib}(1 - \phi_b)^2 (\tilde{P}_{top}^f \tilde{u}_{top}^f)^2$$

(5.28)

with the notations: $\mathcal{R} = a(\tilde{P}_b^f(z))^2 + b\tilde{P}_b^f(z) + c$ and $\Delta = b^2 - 4ac$, we checked that $\Delta > 0$ in our cases. Therefore the analytical solution of the equation 5.28 can be written:

$$\tilde{h}_p - \tilde{z} = \int_{\tilde{z}}^{\tilde{h}_p} d\tilde{z} = \int_{\tilde{P}_b^f(z)}^{\tilde{P}_{top}^f} \frac{\tilde{P}_b^f(z)}{\mathcal{R}}d\tilde{P}^f = \frac{1}{2a}\ln\mathcal{R} - \frac{b}{2a}\int_{\tilde{P}_b^f(z)}^{\tilde{P}_{top}^f} \frac{d\tilde{P}^f}{\mathcal{R}}$$

$$\text{with} \int_{\tilde{P}_b^f(z)}^{\tilde{P}_{top}^f} \frac{d\tilde{P}^f}{\mathcal{R}} = \frac{-2}{\Delta}\operatorname{arctanh}\frac{b + 2a\tilde{P}_b^f(z)}{\sqrt{\Delta}} \quad \text{for} \quad \Delta > 0$$

(5.29)

According to the mass conservation equations 5.22 and 5.23 respectively for the granular phase and the fluid phase, we can obtain:

$$\tilde{u}_{top}^f = \frac{(1 - \phi_0)\rho_{f0}S_0\tilde{u}_0^f}{(1 - \phi_b)\rho_{ftop}S_b} \quad \text{and} \quad \tilde{u}_{top}^p = \tilde{u}_b^p = \frac{\tilde{u}_0^p\phi_0 S_0}{\phi_b S_b}$$

(5.30)

Finally, we obtain an instantaneous gas pressure profile for the zone far from the outlet $\tilde{P}_b^f$, as follows:

$$\tilde{P}_b^f = \mathcal{F}_1\left(\tilde{z}, \tilde{P}_{top}^f, \tilde{h}_p, \rho_{ftop}, \tilde{u}_0^p, \phi_0\right) \tag{5.31}$$

where $\mathcal{F}_1$ is given by solving numerically equation 5.29.

b. Matching with the zone nearby the outlet

Nearby the outlet (zone 3 in Figure 5.18), the experimental observations denotes that there is a jump of the gas pressure gradient, which is due to the diminution of the passage section for the air flow, from $S_b(1 - \phi_b)$ to $S_0(1 - \phi_0)$. Following the work carried out by Zhou [2016] and in chapter 4, we assumed that the jump of the gas pressure gradient occurs at the scale of the outlet size, with $h_1 = D$ and that the pressure gradient is constant within this zone. Following the Forchheimer resistance law (equation 2.13), the dimensionless gas pressure gradient can be determined by the following expression:

$$\frac{\partial \tilde{P}^f}{\partial \tilde{z}}\Big|_{\tilde{z}\approx 0}^{t_i} = -\frac{\beta_{l0}\eta_f}{\rho_p}\sqrt{\frac{g}{D}}(1 - \phi_0)(\tilde{u}_0^f - \tilde{u}_0^p) \mp \frac{\beta_{i0}\rho_{f0}d_p D}{\rho_p}(1 - \phi_0)^2(\tilde{u}_0^f - \tilde{u}_0^p)^2 \tag{5.32}$$

with: $\beta_{l0}(\phi_0, d_p) = \frac{150\phi_0^2}{(1-\phi_0)^3 d_p^2}$, $\beta_{i0}(\phi_0, d_p) = \frac{1.75\phi_0}{(1-\phi_0)^3 d_p^2}$ and ρ_{f0} represents the density of ambient air.

Combining equations 5.3 and 5.32, the mass flow rate of granular media can be modelled as:

$$Q(t) = \rho_p\phi_0 S_0 u_0^p = Q_0\left(1 + \frac{-\frac{\beta_{l0}\eta_f}{\rho_p}\sqrt{\frac{g}{D}}(1 - \phi_0)(\tilde{u}_0^f - \tilde{u}_0^p) \mp \frac{\beta_{i0}\rho_{f0}d_p D}{\rho_p}(1 - \phi_0)^2(\tilde{u}_0^f - \tilde{u}_0^p)^2}{\phi_0}\right)^{1/2} \tag{5.33}$$

We obtain a relationship linking the dimensionless velocity of air flow $\tilde{u}_0^f$ and granular flow $\tilde{u}_0^p$ at the outlet, noted as $\mathcal{F}_2$:

$$\tilde{u}_0^f = \mathcal{F}_2\left(\tilde{u}_0^p, \phi_0\right) \tag{5.34}$$

Following the previous study in chapter 4, we suppose that the pressure gradient of the gas nearby the outlet is uniform, thus, combining equations 5.32 and 5.34, we obtain the gas pressure at the position h_1:

$$\tilde{P}^f(\tilde{h}_1) = \tilde{h}_1 \frac{\partial \tilde{P}^f}{\partial \tilde{z}}\Big|_{\tilde{z}\approx 0}^{t_i} + \tilde{P}_{atm} = \mathcal{F}_3(\tilde{u}_0^p, \phi_0) \tag{5.35}$$

Finally by matching the air pressure at the interface between the zones 2 and 3, we obtain:

$$\tilde{P}^f(\tilde{h}_1) = \mathcal{F}_1\left(\tilde{h}_1, \tilde{P}_{top}^f, \tilde{h}_p, \rho_{ftop}, \tilde{u}_0^p, \phi_0\right) = \mathcal{F}_3\left(\tilde{u}_0^p, \phi_0\right) \tag{5.36}$$

This relationship allows to predict the instantaneous velocity of particles at the outlet, and thus the instantaneous discharge flow rate $Q = \rho_p\phi_0 S_0 u_0^p$, for a granular flow coupled with a highly pressurized gas, considering the variation of the gas density along the silo.

c. Numerical solver

The whole discharge duration t is discretized by a small time step $\delta t = 0.01s$, corresponding to the acquisition frequency of the pressure sensors $P_1 - P_5$. The problem can be resolved step by step, taking the volume fraction of the particles at the outlet ϕ_0 as the only adjustable parameter.
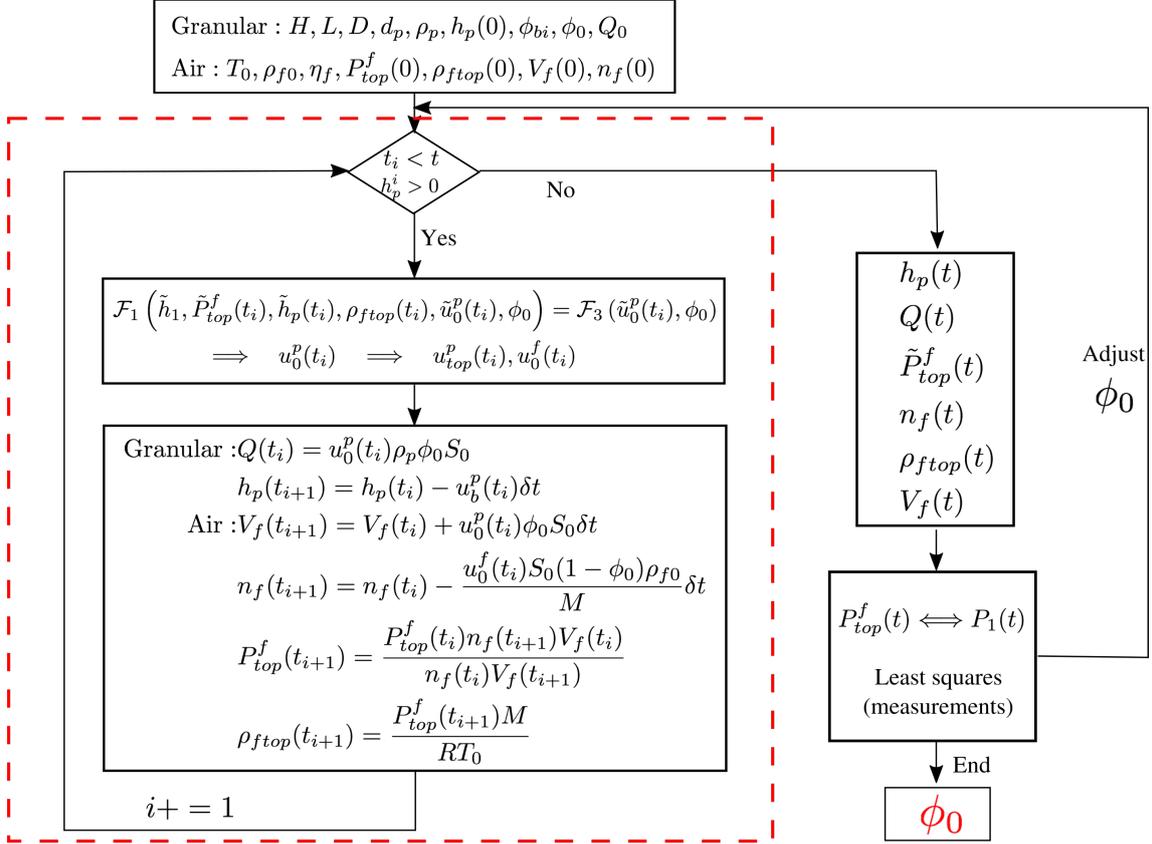

Figure 5.19: Flow chart diagram of numerical solver.

The input variables correspond to the experimental conditions: the silo geometry (L, D), the granular material (d_p, ρ_p, ϕ_{bi}), the pressurized air property (M, R, T_0) and the initial granular column height h_p^0. We suppose that the volume fraction of particles far from the outlet is given by its initial value, $\phi_b \approx \phi_{bi}$. As in the previous study (see chapter 4), the discharge flow rate of the granular media driven by gravity, without gas injection is considered as an input variable, Q_0, given by the experimental measurements. At $t = 0$, the rupture of the outlet occurs. Therefore the variable $P_{top}^f(0)$ represents the critical cracking pressure level of the aluminum foil, $P_{top}^f(0) = P_c^f$. The initial gas volume within the silo is given by: $V_f(0) = HS_b - \frac{m_p}{\rho_p}$. According to the ideal gas law (equation 5.17), we can then determine the initial gas density $\rho_{ftop}(0) = \frac{P_{top}^f(0)M}{RT}$ and its quantity $n_f(0) = \frac{P_{top}^f(0)V_f(0)}{RT}$.

For each time step t_i, the velocity of particles at the outlet $u_0^p(t_i)$ can be determined by equation 5.36, for a given volume fraction at the outlet ϕ_0, whereas equation 5.34 allows to determine the velocity of air flow at the outlet, $u_0^f(t_i)$. The instantaneous discharge flow rate of granular media

158

is calculated by: $Q(t_i) = u_0^p(t_i)\rho_p\phi_0 S_0$. Afterwards, the velocity of particles far from the outlet $u_b^p(t_i)$ can be calculated using the mass conservation equation 5.22. Sequentially, for the next time step t_{i+1}, all the linked variables can be determined by the following equations, respectively for the granular flow and air flow.

$$\text{Granular}: h_p(t_{i+1}) = h_p(t_i) - u_b^p(t_i)\delta t \tag{5.37}$$

$$\text{Air}: \quad V_f(t_{i+1}) = V_f(t_i) + u_0^p(t_i)\phi_0 S_0\delta t \tag{5.38}$$

$$n_f(t_{i+1}) = n_f(t_i) - \frac{u_0^f(t_i)S_0(1-\phi_0)\rho_{f0}}{M}\delta t \tag{5.39}$$

Even though the gas pressure within the silo is not uniform inducing a variation of the gas density along the silo, the experimental observation shows that the main pressure drop of the gas flow occurs at the zone near the outlet (see Figure 5.12). We suppose that the evolution of the gas pressure at the top of the silo follows the ideal gas law by taking into account the variation of the total gas volume within the silo and its quantity. We can write:

$$P_{top}^f(t_{i+1}) = \frac{P_{top}^f(t_i)n_f(t_{i+1})V_f(t_i)}{n_f(t_i)V_f(t_{i+1})} \quad \text{and} \quad \rho_{ftop}(t_{i+1}) = \frac{P_{top}^f(t_{i+1})M}{RT_0} \tag{5.40}$$

The discharge period ends when the granular column height falls to zero. During the discharge, for a given ϕ_0, this internal loop provides a prediction of the granular column height $h_p(t)$, the discharge mass flow rate of the granular media $Q(t)$ and the temporal evolution of gas pressure at silo top $P_{top}^f(t)$ which we measured experimentally. Thanks to the pressure sensors and to the camera giving a global view of silo. The measurement of the gas pressure being more precise, we decide to use the measurement of the gas pressure given by P_1 which is located above the granular media at the position $z_1 = 41$cm and compare it with the prediction of the analytical model, $P_{top}^f(t)$, for carrying out the least squares method to adjust the value of ϕ_0. Figure 5.19 illustrates the flow chart diagram of numerical solver.

d.   Confrontation of the model with experimental measurements

In Figure 5.20, we confront between the experimental measurements and the results predicted by the model for $L = 40$mm, $D = 10$mm and $d_p = 375\mu m$ (glass particles).

We observe a fairly good agreement between the experiments and the quasi-steady compressible model for the differential gas pressure at the top of the silo, for the pressurized period (see Figure 5.20a) and the steady counter-current period (see Figure 5.20b), comparing the experimental measurement given by P_1 at position $z_1 = 41$cm (black lines) and that predicted by the model (red dashed dotted lines) with a fitting parameter $\phi_0 = 0.42$. The model allows to predict the rapid relaxation of the gas during the pressurized period, in addition, a negative pressure is observed at the top of the silo during the steady period, due to the counter-current gas flow at the outlet.
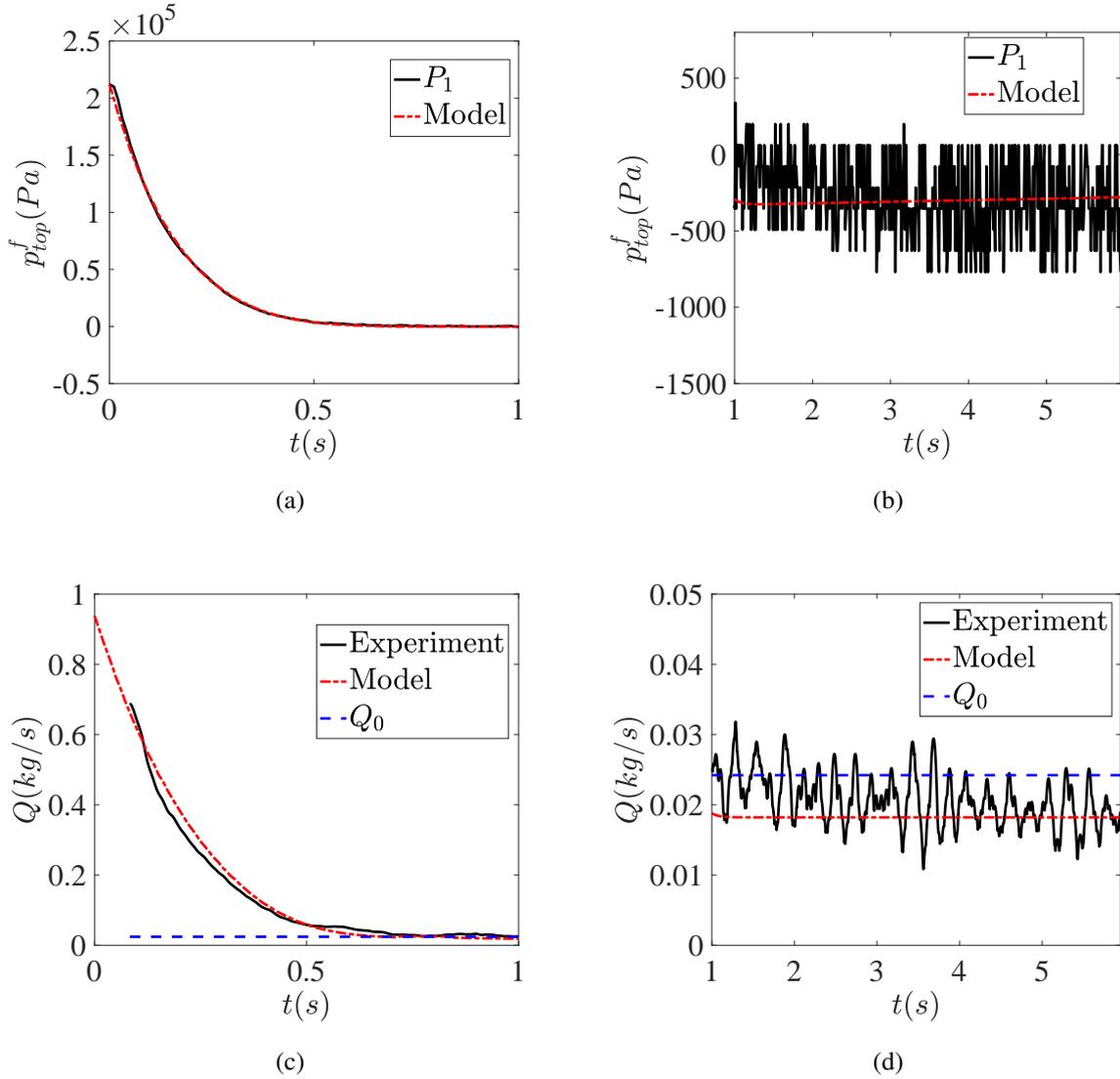
Figure 5.20: Confrontation of the experimental measurements (black lines) with the results predicted by the analytical model (red dashed dotted lines), with the fitting parameter $\phi_0 = 0.42$, for $L = 40$mm, $D = 10$mm, $d_p = 375\mu m$ (glass particles), for (a, b) the differential gas pressure at the top of the silo and (c, d) the discharge flow rate of the granular media. (a, c) during the pressurized period and (b, d) during the steady counter-current period.

The comparison of the mass flow rate of the granular media is illustrated in Figure 5.20c for the pressurized period and 5.20d for the steady counter-current period, where the black line represents the experimental discharge flow rate, $Q(t)$, the red dashed dotted line represents the prediction by the model and the blue dashed line represents the mass flow rate for an opened silo Q_0. We observe that the result of the analytical model adjusts quite well the experimental results. During the pressurized period, the decrease of experimental flow rate is reasonably described by the model. During the steady flow, we recover that the mass flow rate predicted by the model is very slightly smaller than the opened top silo Q_0, due to the counter-current air flow at the outlet.

In Figure 5.21, we plot the volumetric gas flow rate predicted by the analytical model for (a) the
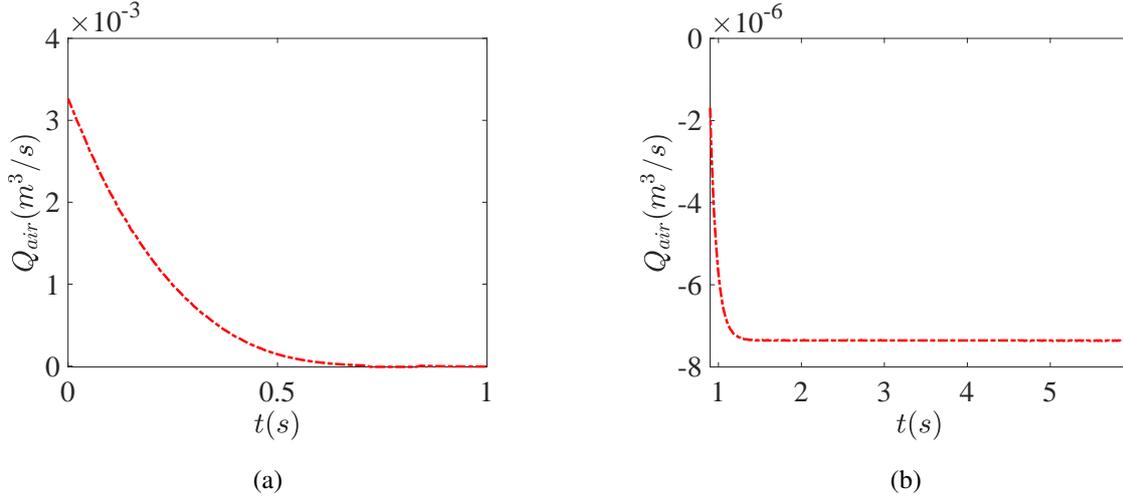
Figure 5.21: Volumetric gas flow rate predicted by the analytical model, with the fitting parameter $\phi_0 = 0.42$, for L = 40mm, D = 10mm, $d_p = 375\mu m$ (glass particles), during (a) the pressurized period and (b) the steady counter-current period.
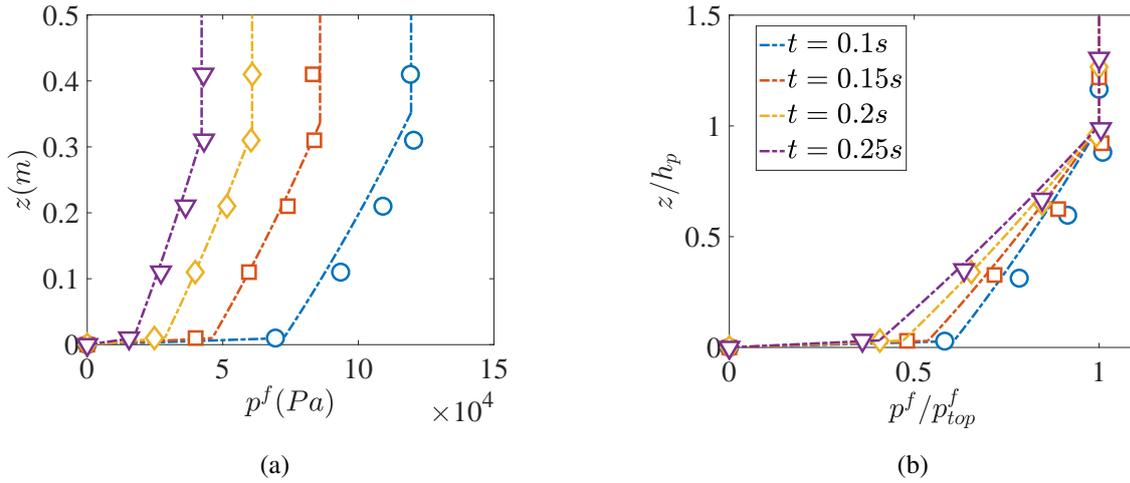

Figure 5.22: Gas pressure profiles along the silo at various instants for L = 40mm, D = 10mm, $d_p = 375\mu m$ (glass particles) for (a) the vertical position versus p^f and (b) the vertical position normalized by the granular column height z/h_p as a function of the gas pressure normalized by the pressure at the top of the silo p^f/p^f_{top}. The symbols correspond to the experimental measurements and the dashed dotted lines correspond to the analytical model, with the fitting parameter $\phi_0 = 0.42$.

pressurized period and (b) the steady counter-current period. We observe a similar evolution than for the gas pressure. Due to the high density of gas within the silo at the rupture, an intense gas flow is ejected simultaneously with the granular flow through the outlet, leading to a rapid relaxation of the gas pressure level within the silo as well as the gas flow rate. Finally, the volumetric gas flow rate tends to a negative constant value corresponding to a counter-current gas flow at the outlet

161

(see Figure 5.21b).

Figure 5.22 shows a comparison of the gas pressure profiles along the silo for different instants $t = 0.1s$, $0.15s$, $0.2s$ and $0.25s$, between the experimental measurements (symbols) and the prediction of model (dashed dotted lines). In Figure 5.22a, we plot the vertical position z as a function of the differential gas pressure p^f. In Figure 5.22b, we plot the vertical position normalized by the granular column height z/h_p as a function of the gas pressure normalized by the pressure at the top of the silo p^f/p^f_{top}. We observe a good agreement on the gas pressure profile at zone 2, with a very tiny curvature due to the inhomogeneity of the gas density within the granular media.
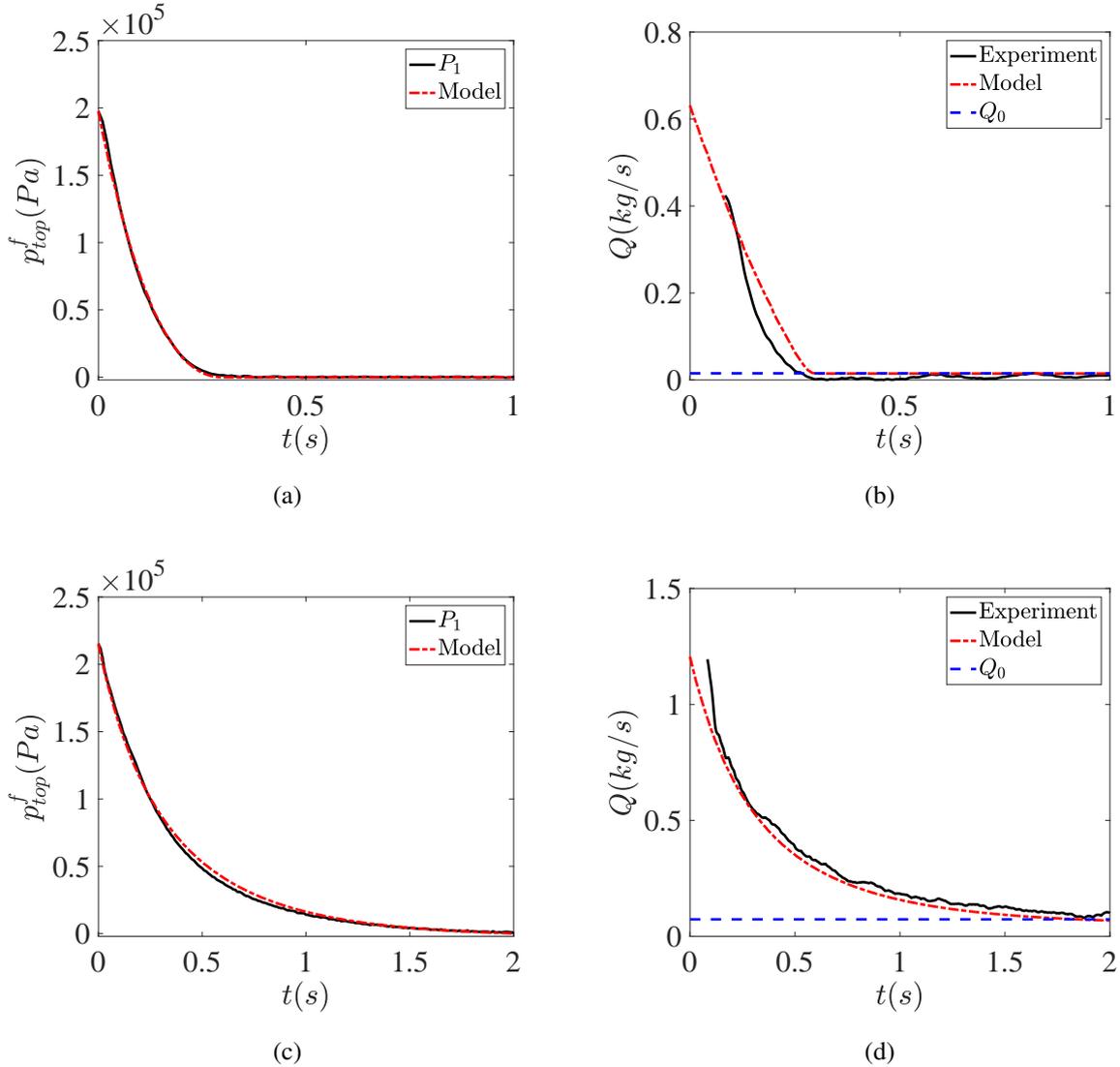
Figure 5.23: Confrontation of the experimental measurements (black lines) with the results predicted by the model (dashed dotted lines), with $L = 40$mm, $D = 10$mm for (a, b) $d_p = 864\mu m$ (sand particles) and (c, d) the bidisperse mixture. (a, c) temporal evolution of the differential gas pressure at the top of the silo and (b, d) discharge flow rate of the granular media during the pressurized period, with the fitting parameter $\phi_0 = 0.41$ for the sand particles, and $\phi_0 = 0.54$ for the bidisperse mixture.

In Figure 5.23, we compare the experimental results with the model for (a, b) the sand particles of $d_p = 864\mu m$ and (c, d) the bidisperse mixture (ceramic particles of $d_p = 1165\mu m$ and $180\mu m$), using the Sauter diameter, for (a, c) the temporal evolution of the gas pressure at the top of the silo and (b, d) the discharge flow rate of the granular media during the pressurized period. We observe that the model gives a good prediction for the gas pressure evolution at the top of the silo, however a small deviation of the discharge flow rate of the granular media is observed for the sand particles, which may be due to the variation of the volume fraction of particles during the discharge (see Figure 4.17b in chapter 4). Again, it shows that the main parameter of the gas induced discharge is the permeability of the granular media.
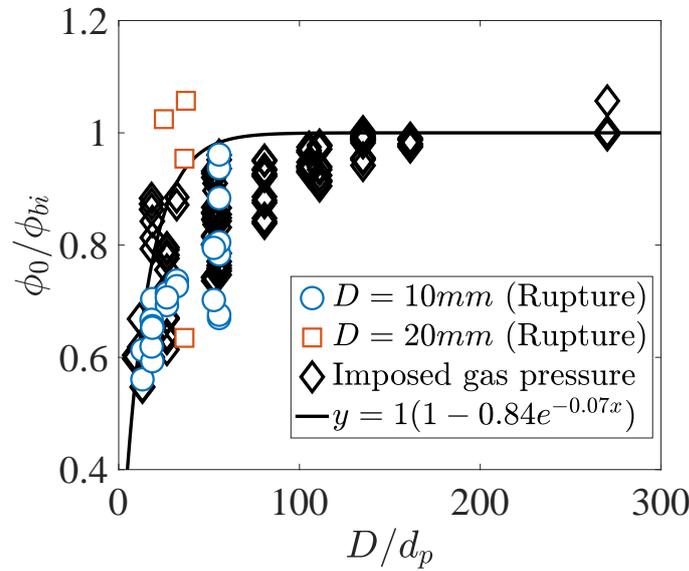

Figure 5.24: Ratio between ϕ_0 obtained by the analytical model and the initial bulk volume fraction of particles ϕ_{bi} as function of the ratio D/d_p for the discharge of a silo with an instantaneous rupture of the outlet for $D = 10$mm (○) and for $D = 20$mm (□) and with an imposed gas pressure at the top of the silo (black diamonds) extracted from the chapter 4. The black line represents $\frac{\phi_0}{\phi_b} = \xi_\phi G(D/d_p) = \xi_\phi \left[1 - \alpha e^{-\beta D/d_p}\right]$ with coefficients $\xi_\phi = 1$, and α, β corresponding to an opened top silo.

The volume fraction ϕ_0 at the outlet is the only fitting parameter of the model developed, similarly to the quasi-steady analytical model in chapter 4. In Figure 5.24, we plot the results ϕ_0/ϕ_{bi} obtained for the discharge of silo with an instantaneous rupture of the outlet for two outlet sizes $D = 10$mm and $D = 20$mm, together with the results for the discharge of silo with an imposed gas pressure extracted from the chapter 4. We observe that the data are a little bit scattered, however the results of both cases can be well described by the geometrical function $\frac{\phi_0}{\phi_b} = \xi_\phi G(D/d_p) = \xi_\phi \left[1 - \alpha e^{-\beta D/d_p}\right]$ with $\xi_\phi = 1$, and the same coefficients ($\alpha = 0.84$ and $\beta = 0.07$) than for the gravity driven experiments.

Then with the model developed, we are able to predict without any adjustable parameter the

violent discharge consecutive to the rupture of an orifice due to an initially pressurized gas. This model takes into account the compressibility of the gas and the variation of its density with the vertical position which induces a curvature in the gas pressure gradient profiles. However, we observe that this curvature is really tiny, so in the next subsection, we present a simplified model where we suppose the gas density constant in the zone 2, far from the orifice.

5.3.3   Simplified model

Let us now propose a simplified model for the gas flow considering a constant gas density in the calculation of inertial term coefficient in the Darcy-Forchheimer resistance law far from the orifice for investigating the influence of the gas density in the drag force. The gas pressure gradient at zone 2 at a given instant can now be expressed as:

$$
\frac{\partial P^f}{\partial z}\mid_{z\gg0} = -\beta_{lb}\eta_f(1-\phi_b)\left(\frac{P_{top}^f u_{top}^f}{P_b^f(z)} - u_b^p\right) \mp \beta_{ib}\rho_{ftop}d_p(1-\phi_b)^2\left(\frac{P_{top}^f u_{top}^f}{P_b^f(z)} - u_b^p\right)^2 \tag{5.41}
$$

Note that we keep the variation of the gas density in the velocity term. This differential equation can be written dimensionless as:

$$
\frac{\partial \tilde{P}^f}{\partial \tilde{z}} = \frac{a'\left(\tilde{P}_b^f(\tilde{z})\right)^2 + b'\tilde{P}_b^f(\tilde{z}) + c'}{\left(\tilde{P}_b^f(\tilde{z})\right)^2} \tag{5.42}
$$

$$
\text{with}\quad a' = \frac{\beta_{lb}\eta_f}{\rho_p}\sqrt{\frac{g}{D}}\left(1-\phi_b\right)\tilde{u}_b^p \mp \frac{\beta_{ib}\rho_{ftop}d_pD}{\rho_p}\left(1-\phi_b\right)^2\left(\tilde{u}_b^p\right)^2
$$

$$
b' = -\frac{\beta_{lb}\eta_f}{\rho_p}\sqrt{\frac{g}{D}}\left(1-\phi_b\right)\tilde{P}_{top}^f\tilde{u}_{top}^f \pm 2\frac{\beta_{ib}\rho_{ftop}d_pD}{\rho_p}\left(1-\phi_b\right)^2\tilde{P}_{top}^f\tilde{u}_{top}^f\tilde{u}_b^p
$$

$$
c' = \mp\frac{\beta_{ib}\rho_{ftop}d_pD}{\rho_p}\left(1-\phi_b\right)^2\left(\tilde{P}_{top}^f\tilde{u}_{top}^f\right)^2
$$

We note $\mathcal{R}' = a'\left(\tilde{P}_b^f(\tilde{z})\right)^2 + b'\tilde{P}_b^f(\tilde{z}) + c'$ and $\Delta' = b'^2 - 4a'c' > 0$ in our configurations. The analytical solution of equation 5.42 can be written as follows:

$$
\tilde{h}_p - \tilde{z} = \int_{\tilde{z}}^{\tilde{h}_p} d\tilde{z} = \int_{\tilde{P}_b^f(\tilde{z})}^{\tilde{P}_{top}^f}\frac{\left(\tilde{P}_b^f(\tilde{z})\right)^2}{\mathcal{R}}d\tilde{P}^f = \frac{\tilde{P}_b^f(\tilde{z})}{a'} - \frac{b'}{2a'^2}\ln\mathcal{R}' + \frac{b'^2 - 2a'c'}{2a'^2}\int_{\tilde{P}_b^f(\tilde{z})}^{\tilde{P}_{top}^f}\frac{d\tilde{P}^f}{\mathcal{R}'} \tag{5.43}
$$

$$
\text{with}\quad \int_{\tilde{P}_b^f(\tilde{z})}^{\tilde{P}_{top}^f}\frac{d\tilde{P}^f}{\mathcal{R}'} = \frac{-2}{\Delta'}\text{arctanh}\frac{b' + 2a'\tilde{P}_b^f(\tilde{z})}{\sqrt{\Delta'}}\quad\text{for}\quad\Delta' > 0
$$

Using equation 5.30, we obtain a relationship for describing the gas pressure profile at each instant for the zone far from the outlet $\tilde{P}_b^f$, with a supplementary input variable ρ_{ftop}:

$$
\tilde{P}_b^f = \mathcal{F}_{s1}\left(\tilde{z}, \tilde{P}_{top}^f, \tilde{u}_{top}^f, \tilde{u}_b^p, \tilde{h}_p, \rho_{ftop}\right) \tag{5.44}
$$

Following the same steps as previously, we can resolve numerically the whole system by discretizing the discharge period.
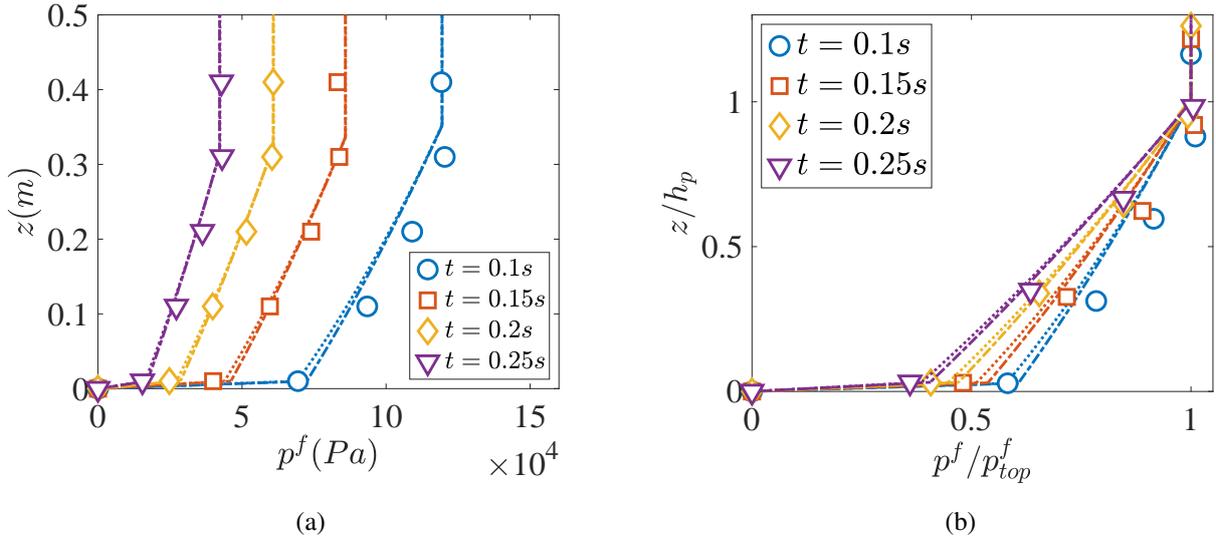
Figure 5.25: (a) Gas pressure profiles and (b) dimensionless gas pressure profiles along the silo at various instants for L = 40mm, D = 10mm, d_p = 375μm (glass particles). The dashed dotted lines are representative for the model and the dotted lines represent the simplified model with ϕ_0 = 0.42 for both models.

Figure 5.25 illustrates the gas pressure profiles (a) and the dimensionless gas pressure profiles (b) along the silo at various instants t = 0.1s, 0.15s, 0.2s and 0.25s for L = 40mm, D = 10mm, d_p = 375μm (glass particles), with a comparison between the experimental measurements and those predicted by the two models. The difference between the two models is quite small and located at the bottom part of the silo (z < 0.1m) for the first instant (t < 0.2s). Therefore, both models give a good prediction of the experimental phenomena.

In Figure 5.26, we compare the experimental results (black lines) to the model (red dashed dotted lines) and the simplified model (blue dotted lines), for (a, b) the temporal evolution of the differential gas pressure at the top of the silo p_{top}^f and (c, d) the discharge flow rate of the granular media Q, for (a, c) the pressurized period and (b, d) the steady counter-current period. We observe that both models have a quite similar prediction for the gas pressure and the discharge flow rate with very close fitting parameter (ϕ_0 = 0.42 for the model and ϕ_0 = 0.43 for the simplified model) and a fairly good agreement is observed with the experiments.
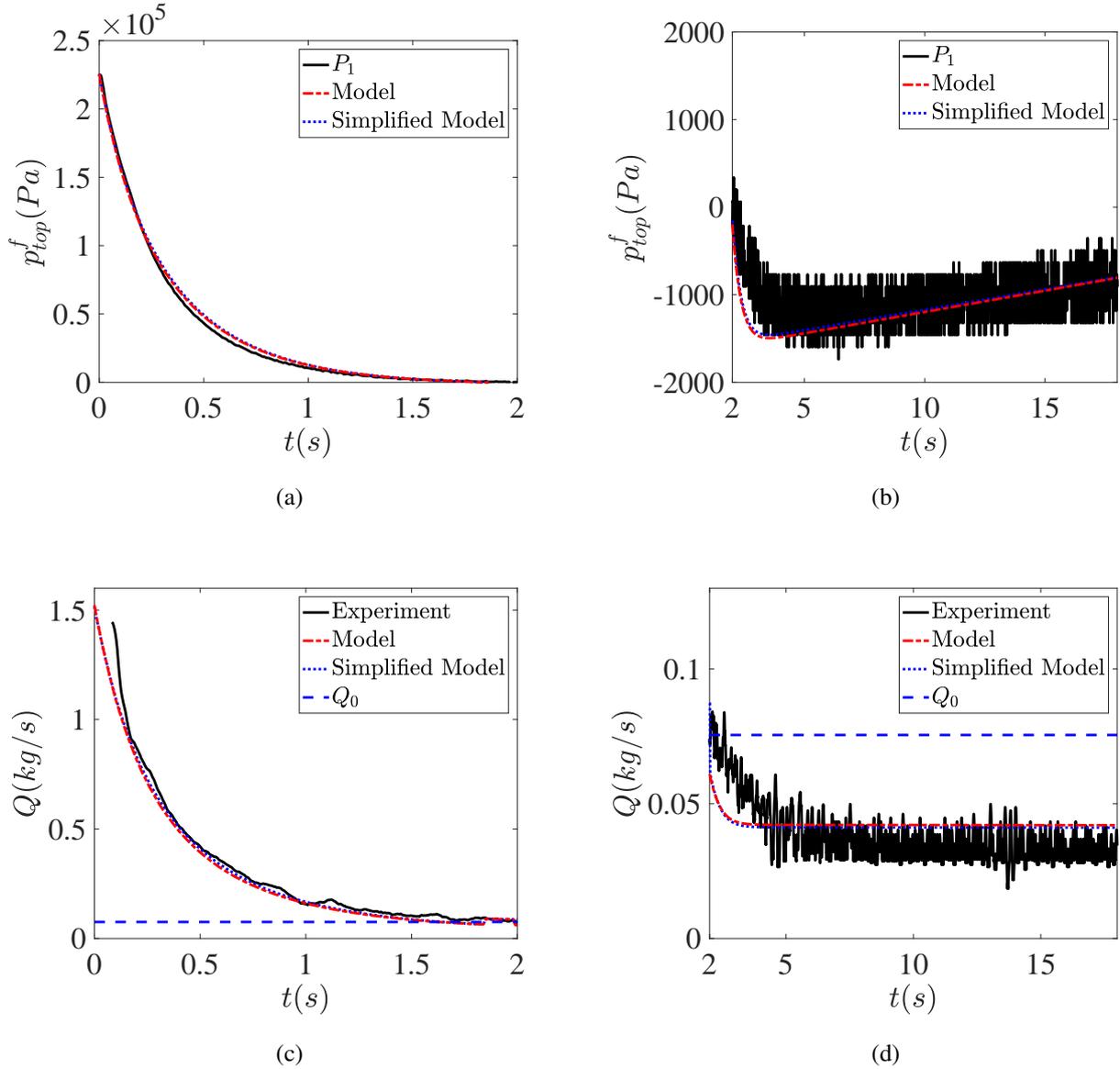
Figure 5.26: Confrontation of the experimental measurements (black lines) with the results predicted by the model (dashed dotted lines) with the fitting parameter $\phi_0 = 0.42$ and the simplified model (blue dotted lines) with the fitting parameter $\phi_0 = 0.43$, for $L = 40$mm, $D = 10$mm, $d_p = 180\mu m$ (ceramic particles), for (a, b) the differential gas pressure at the top of the silo and (c, d) the discharge flow rate of the granular media. (a, c) during the pressurized period and (b, d) during the steady counter-current period.

In Figure 5.27, we plot the ratio ϕ_0/ϕ_{bi} as a function of D/d_p, where ϕ_0 is the fitting parameter of the simplified model. As previously, the black diamonds represent the results obtained for the discharge of silo with an imposed constant gas pressure at silo top (see chapter 4). All the results can be well adjusted by the dilation function of the particles at outlet $\frac{\phi_0}{\phi_b} = \xi_\phi G(D/d_p) = \xi_\phi \left[1 - \alpha e^{-\beta D/d_p} \right]$ with coefficients $\xi_\phi = 1$, and α and β obtained for an opened top silo, similarly to the previous model. It indicates that both of the two models permit to predict well the discharge phenomena for the granular flow and the gas flow with an instantaneous rupture of the outlet, and
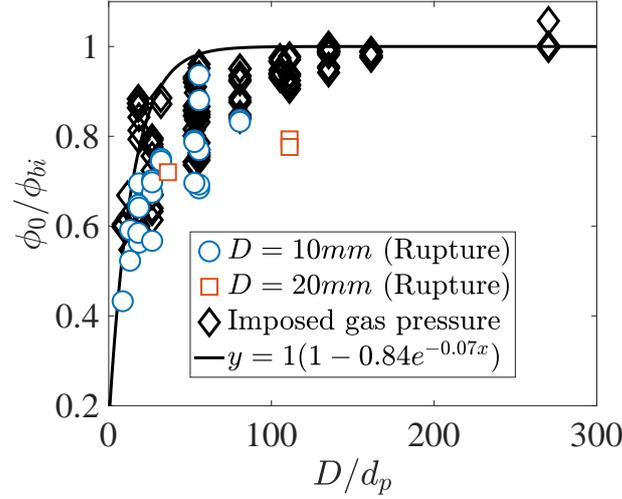
Figure 5.27: Ratio between ϕ_0 obtained by the simplified analytical model and the initial bulk volume fraction of particles ϕ_{bi} as a function of the ratio D/d_p for the discharge of a silo with an instantaneous rupture of the outlet with various outlet diameters and with an imposed gas pressure at the top of the silo (black diamonds) extracted from the chapter 4. The black line represents the the geometrical function $\frac{\phi_0}{\phi_b} = \xi_\phi G(D/d_p) = \xi_\phi \left[1 - \alpha e^{-\beta D/d_p}\right]$ with coefficients $\xi_\phi = 1$, and α, β corresponding to an opened top silo.

we can neglect the role of the variation of the gas density inside the granular media in the inertial term coefficient of the Darcy-Forchheimer law far from the orifice.

The compressible, unidimensional, analytical model is based on several hypothesis, the main of them being to consider (i) a simple modification of the gravity driving force by the gas pressure at the outlet and (ii) a quasi steady variation of the granular flow. In the next section, we will test the ability of the numerical simulation of a two-phase continuum modelling with a granular rheology to reproduce the experimental results and we will use these simulations to discuss the hypothesis of the unidimensional model.

5.4 Continuum two-phase compressible modelling

In this study, we use the framework presented in chapter 4. The continuum simulation is carried out with the software *Basilisk*, using a cylindrical coordinates system. In this section, we will first introduce the configuration and the boundary conditions of the simulation, then we will discuss the characteristic times for both the granular flow and the gas flow relaxation towards quasi-steady flow, and eventually we will confront the numerical results with the experiments within the unidimensional model.

5.4.1 Configuration and boundary conditions

As shown in Figure 5.28, similarly to chapter 4, the calculation domain consists of a three-dimensional cylindrical silo of height H and radius L, using an axisymmetric plane at silo center. The outlet of radius R is placed at the center of the bottom of the silo. The silo is filled initially by the granular media, which is considered as a continuous medium with a height $h_p^0 = 3.8L$.


Figure 5.28: Schematic view of configuration and boundary conditions of continuous simulation.

Concerning the boundary conditions of simulation, the differences appear on the fluid phase, compared to the case with an imposed fluid pressure. First, a Dirichlet boundary condition is applied to the outlet border for the fluid phase (red dotted line in Figure 5.28), with $P^f = P_0^f = 20\rho gL$, to reproduce the atmospherical air pressure.

The temporal variation of the fluid pressure, $P_{top}^f(t)$, is chosen for the Dirichlet boundary condition at silo top (blue dotted line in Figure 5.28), following the ideal gas law for taking into account the compressibility of gas flow. The calculation domain filled by the fluid phase is considered as a gas reservoir, located at silo top. As the granular media is discharging out of the silo, the fluid phase volume increases over time, leading to a decrease of fluid density. As previously we suppose that the system is isothermal during the discharge, thus according to the ideal gas law, the fluid phase obeys:

$$\frac{P^f}{\rho_f} = \frac{P_0^f}{\rho_{f0}} = constant \tag{5.45}$$

where ρ_{f0} represents the fluid density corresponding to the atmospherical gas pressure P_0^f, with $\rho_{f0} = 1 \times 10^{-4} \rho$ (where $\rho \equiv \phi \rho_p$ is the density of granular media). Thus, a decrease of fluid density leads to a relaxation of fluid pressure level at silo top. We set an initial gas pressure at silo top, $P_{top}^f(0) = 60 \rho g L$, therefore, the initial gas density in the reservoir is $\rho_{ftop}(0) = 3 \times 10^{-4} \rho$, with a volume $V_{top}^f(0) = \pi L^2 (H - h_p^0)$ and a mass $m_{top}^f(0) = V_{top}^f(0)\rho_{ftop}(0)$. For each time step of simulation, the volumetric flow rate of the granular media can be determined by $\mathcal{V}_i = \int_0^R 2\pi r u_z^p \mid_{z=0} dr$. The mass flow rate of the fluid phase is calculated by $\dot{m}_{top,i}^f = \int_0^R 2\pi \rho_{f0} r u_z^f \mid_{z=0} dr$, supposing that the fluid density at the outlet is equal to ρ_{f0}. The explicit method is applied for determining the gas pressure at next time step:

$$P_{top}^f(i+1) = \frac{P_0^f}{\rho_{f0}}\rho_{ftop}(i+1) = \frac{P_0^f}{\rho_{f0}} \frac{m_{top}^f(i) - \dot{m}_{top}^f(i)dt}{V_{top}^f(i) + \mathcal{V}_i dt} \tag{5.46}$$

Following the previous study, the momentum equation of the fluid phase, using the Darcy-Forchheimer resistance law, can be written as follows:

$$R_f \frac{\partial u_z^f}{\partial t} = -\frac{\partial p^f}{\partial z} - B_l \left(u_z^f - u_z^p \right) - B_i \mid u_z^f - u_z^p \mid \left(u_z^f - u_z^p \right) \tag{5.47}$$

$$R_f \frac{\partial u_r^f}{\partial t} = -\frac{\partial p^f}{\partial r} - B_l \left(u_r^f - u_r^p \right) - B_i \mid u_r^f - u_r^p \mid \left(u_r^f - u_r^p \right) \tag{5.48}$$

with $B_l = \beta_l \eta_f (1 - \phi)$ and $B_i = \beta_i \rho_{ftop} d (1 - \phi)^2$. Again, we use a virtual mass approach to take into account the unsteady effects of the fluid phase, with $R_f = \rho_{ftop}\left(1 + C\frac{\phi}{1+\phi}\right)$. Note that the coefficients $B_i = B_{i0}\frac{\rho_{ftop}}{\rho_{f0}}$ and $R_f = R_{f0}\frac{\rho_{ftop}}{\rho_{f0}}$ vary as the density of the fluid phase at the top of the silo, ρ_{ftop}. Then we consider that the density is spatially uniform in the whole silo except at the outlet.

5.4.2 Numerical results

a. Effect of the granular media permeability

We focus firstly on the effect of the permeability of the granular media, varying the coefficient B_l and B_{i0} in equation 5.48 with $R_{f0} = 0.002\rho$. Two continuum simulations are carried out with $R = 0.25L$, $h_p^0 = 3.8L$, corresponding to the finer particles ($B_l = 25\rho\sqrt{g/L}$, $B_{i0} = 6.3\rho/L$ and $R_{f0} = 0.002\rho$), represented by the solid black line in Figure 5.29 and the coarser particles ($B_l = 2.5\rho\sqrt{g/L}$, $B_{i0} = 0.63\rho/L$ and $R_{f0} = 0.002\rho$), represented by the dashed black line in Figure 5.29.

Figure 5.29a illustrates the temporal evolution of the differential gas pressure at silo top, $p_{top}^f = P_{top}^f - P_0^f$. We observe a rapid relaxation of gas pressure at the very beginning of discharge,

169
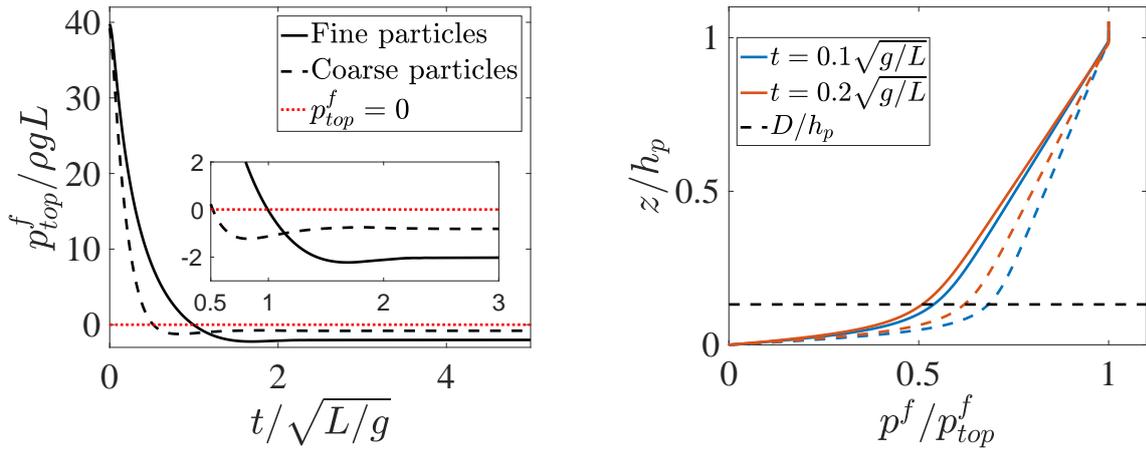
(a) Temporal evolution of the differential fluid pressure at the top of the silo, $p_{top}^f/\rho g L$.

(b) Pressure profile at the center of the silo for various instants.
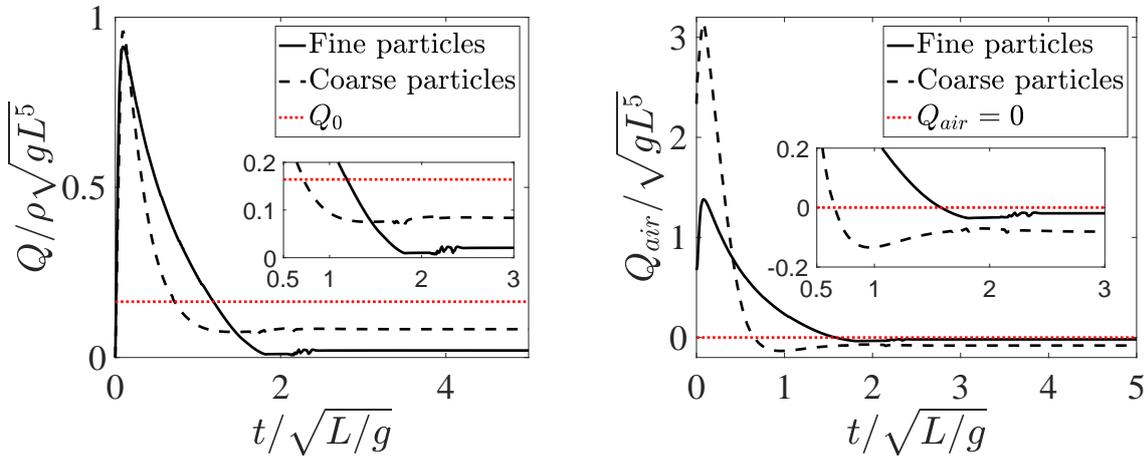
(c) Temporal evolution of the discharge flow rate of the granular media $Q/\rho\sqrt{gL^5}$.

(d) Temporal evolution of the discharge volumetric flow rate of gas flow, $Q_{air}/\sqrt{gL^5}$.

Figure 5.29: Effect of the granular media permeability: the solid line corresponds to the finer particles with $B_l = 25\rho\sqrt{g/L}$, $B_{i0} = 6.3\rho/L$ and $R_{f0} = 0.002\rho$, and the dashed line to the coarser particles with $B_l = 2.5\rho\sqrt{g/L}$, $B_{i0} = 0.63\rho/L$ and $R_{f0} = 0.002\rho$.

corresponding to the pressurized discharge period, then, the differential gas pressure becomes slightly negative, which corresponds to the steady period of the discharge with a counter-current flow (see enlarged zone in figure) as in the experiments (see Figure 5.20b). The relaxation period is shorter for the granular media corresponding to the coarser particles (black dashed line), due to its higher permeability facilitating the gas flow through the granular media. Note that we observe an overshoot of the pressure that is not seen experimentally. Moreover, contrary to the experiments, the air pressure at the top of the silo seems to tend to a constant due to the very small discharge flow rate of the granular media during the steady period, the granular column height remaining quasi constant, as shown in Figure 5.30.
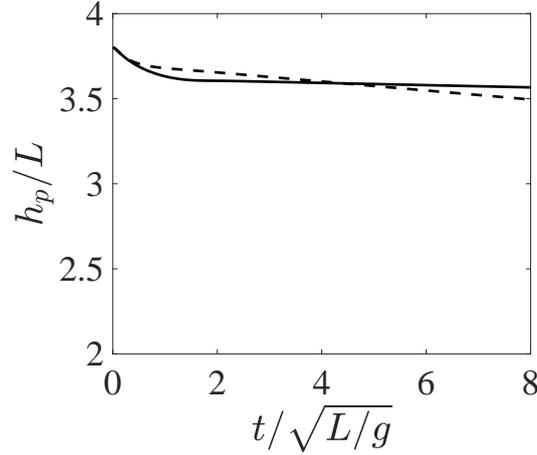
Figure 5.30: Temporal evolution of the granular column height h_p/L. The solid line corresponds to the finer particles with $B_l = 25\rho\sqrt{g/L}$, $B_{i0} = 6.3\rho/L$ and $R_{f0} = 0.002\rho$, and the dashed line to the coarser particles with $B_l = 2.5\rho\sqrt{g/L}$, $B_{i0} = 0.63\rho/L$ and $R_{f0} = 0.002\rho$.

In Figure 5.29b, we plot the pressure profiles of the fluid phase normalized by the pressure at the top of the silo p^f/p^f_{top} at the center of the silo for various instants. The solid lines correspond to the finer particles and the dashed lines correspond to the coarser particles. We observe a more rapid decrease of the pressure for the granular media corresponding to the finer particles. Moreover, we observe that the pressure profile of the fluid phase is similar to the experiments (see Figure 5.29b), where a jump of the pressure gradient occurs at the scale of the outlet size D/h_p (see the black dashed line).

Figure 5.29c illustrates the dimensionless discharge flow rate of the granular phase as a function of time $t/\sqrt{L/g}$. The red dotted line in Figure 5.29c represents the mean discharge flow rate of the granular phase for the case with an opened silo top, without gas injection, Q_0. First, we observe a rapid increase of the flow rate, the granular media being initially motionless. The maximum flow rate is reached after $\approx 0.1\sqrt{L/g}$ and is seemingly the same for both fine and coarser cases. Then we observe the rapid decreases of the flow rate corresponding to the discharge of the pressurized gas (till $\sqrt{L/g}$). This discharge is faster for the coarser particle case. Finally the flow rate reaches the steady value lower than the gravity driving case Q_0, similarly to the experiments (see Figure 5.20). Note that the transition with the steady flow is not very well resolved with an overshoot which generates numerical oscillations.

In Figure 5.29d, we finally plot the temporal evolution of the dimensionless discharge volumetric flow rate of the fluid phase, $Q_{air}/\sqrt{gL^5}$. We observe the same characteristic than the granular flow rate, an acceleration phase, leading to a higher Q_{air} for the coarser particles, then the pressurized gas discharges, faster for the coarser particles, finally the steady flow is reached with a negative value corresponding to a counter-current flow. We observe a more important effect of the counter-current gas flow on the discharge flow rate of the granular media for the finer particles.

171

In the following section, we will investigate the dependency of characteristic time of the acceleration for both phases.

b.   Characteristic time of the granular flow establishment

We suppose that at the very beginning of discharge, the characteristic time of the granular flow establishment is determined by the equilibrium between the unsteady term, the gas pressure gradient and the gravity, neglecting the convective term and the granular stress terms. The momentum conservation of the granular phase in the z direction reduces to:

$$\rho \frac{\partial u_z^p}{\partial t} \sim -\frac{\partial p^f}{\partial z} - \rho g \tag{5.49}$$

The Hagen-Beverloo law (equation 2.21) indicates that the velocity of granular media is proportional to the square root of the outlet size, $u_0^p \sim \sqrt{gD}$, for the discharge of a silo without gas injection. Following equation 5.3, the velocity of the granular media for a pressurized silo can be written:

$$u_z^p \sim \sqrt{gD} \left(1 + \frac{1}{g\rho} \frac{\partial p^f}{\partial z} \Big|_{z=0} \right)^{1/2} \tag{5.50}$$

Combining equation 5.49 and 5.50, the characteristic time of granular media can be expressed as follows:

$$\tau \approx \sqrt{\frac{D}{g}} \frac{1}{\sqrt{1 + \frac{1}{\rho g} \frac{\partial p^f}{\partial z} \Big|_{z=0}}} \tag{5.51}$$

To test this scaling we first carry out a series of simulations in a simplified configuration where we impose a step of the gas pressure at the top of the silo $p_{top}^f = \rho_0 gL$ during $5 \leq t/\sqrt{L/g} \leq 10$ with $\rho_0 = 1$, while during the beginning ($t/\sqrt{L/g} < 5$) and the ending ($t/\sqrt{L/g} > 10$) periods, the granular media is flowing without gas injection, corresponding to an opened top silo. For all the simulations, we also fix $R = 0.25L$, $h_p^0 = 3.8L$ and we vary the density of the granular media, ρ. Figure 5.31 shows the imposed step pressure and the temporal evolution of the dimensionless discharge flow rate of the granular media, $Q/\rho\sqrt{gL^5}$. We observe for each step, a relaxation toward the steady or quasi steady flow rate. We focus on the acceleration period of discharge, right after the loading of the gas pressure at $t/\sqrt{L/g} = 5$, for determining the characteristic time of the granular flow establishment.

Figure 5.32a illustrates the temporal evolution of discharge flow rate $Q/\rho\sqrt{gL^5}$ for various granular densities, during the imposed pressure period with $p_{top}^f = \rho_0 gL$. In this regime, as shown in chapter 4, the flow rate increases with time and to determine the time of relaxation, we adjust it by a linear fit. The characteristic time of the granular flow establishment is defined as the time necessary for the increase of flow rate from Q_0 to reach 95% of its quasi steady value (see the dotted lines). The characteristic time is illustrated by the asterisk symbols in the figure. In
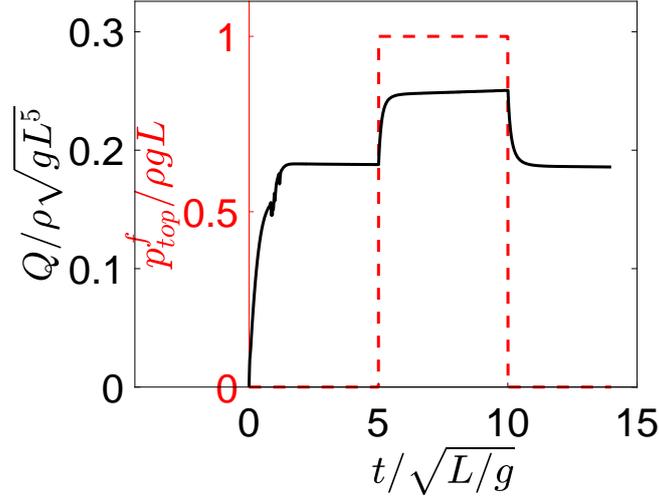
Figure 5.31: Temporal evolution of the flow rate (black line) and imposed pressure step at the top of the silo (red dashed line) for $R = 0.25L$, $h_p^0 = 3.8L$ and $\rho = \rho_0$.

Figure 5.32b, we plot the characteristic time $\tau/\sqrt{L/g}$ as a function of dimensionless granular density ρ/ρ_0. The red dashed line represents equation 5.51, using $\frac{\rho_0 gL}{h_p^0}$ to approximate the pressure gradient at the outlet. The red solid line represent 5.51 using the average pressure gradient at the

| (a) | (b) |
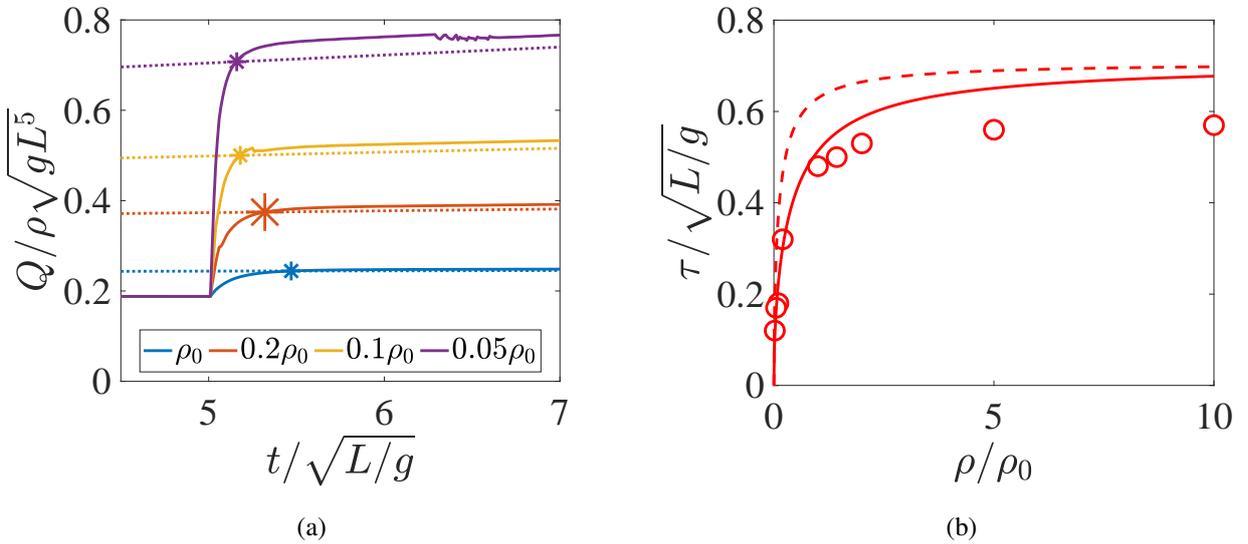
Figure 5.32: Simulation of a step of p_{top}^f from 0 to $\rho_0 gL$ for $h_p^0 = 3.8L$ and $R = 0.25L$. (a) Temporal evolution of the discharge flow rate and determination of the characteristic time for various granular densities. The dotted lines represent the 95% of linear fit of the quasi steady regime. (b) Characteristic time $\tau/\sqrt{L/g}$ as a function of the dimensionless granular density ρ/ρ_0. The red dashed line represents equation 5.51 with $\frac{\partial p^f}{\partial z}\big|_{z=0} \approx \frac{\rho_0 gL}{h_p^0}$. The red solid line represent 5.51 using the average pressure gradient at the outlet, evaluated by the simulation.

outlet, evaluated by the simulation. We observe that equation 5.51 gives a fairly good description of this relaxation time of the granular media.


(a)

(b)
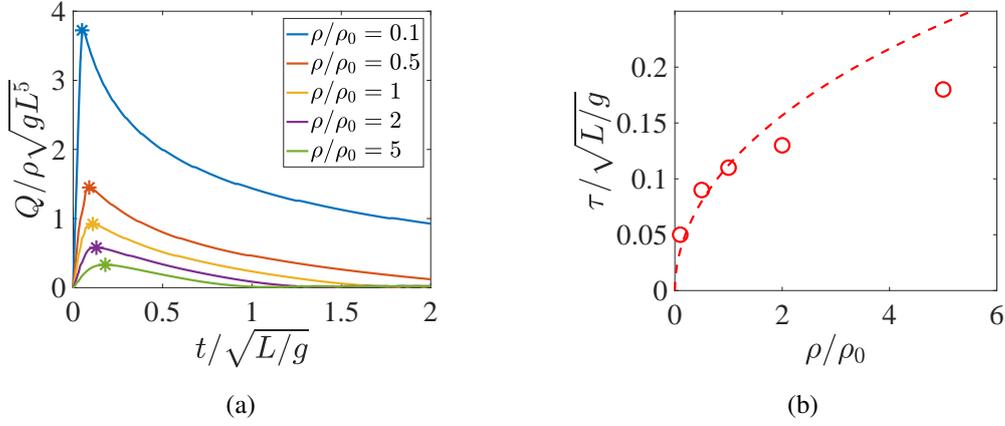
Figure 5.33: (a) Temporal evolution of the discharge flow rate $Q/\rho\sqrt{gL^5}$ and the determination of the characteristic time for various granular densities. (b) Characteristic time $\tau/\sqrt{L/g}$ as a function of the dimensionless granular density ρ/ρ_0. The red dashed line represents the equation 5.51 with $\frac{\partial p^f}{\partial z}\big|_{z=0} \approx \frac{p^f_{top}}{h^0_p}$.

We also evaluate this characteristic time, simulating the discharge of silo with an initial imposed gas pressure, $p^f_{top} = 40\rho_0 gL$, varying the granular density, ρ/ρ_0 and keeping the values $h^0_p = 3.8L$, $R = 0.25L$. The characteristic time is determined at the peak value of the discharge flow rate, displayed in Figure 5.33a. According to the Figure 5.33b, the characteristic time as a function of the dimensionless granular density ρ/ρ_0, is well adjusted by equation 5.51 with $\frac{\partial p^f}{\partial z}\big|_{z=0} \approx \frac{p^f_{top}}{h^0_p}$.

In the experimental study, equation 5.51 estimates characteristic time of the granular flow establishment on the order of magnitude, $\tau \approx 1 \times 10^{-3}s$, due to the extremely strong gas pressure gradient at the outlet at the beginning of discharge. This denotes that the acceleration of the granular media at the first time of the discharge can be neglected, compared to the discharge time scale or to the time for the establishment of the fluid pressure gradient. We can consider that the particle phase reaches instantaneously the quasi steady regime.

c. Characteristic time of the gas flow establishment

To evaluate the characteristic time of the establishment of the fluid phase, we suppose that at the very beginning of the discharge, the pressure gradient drives the acceleration of the fluid phase:

$$\rho_f \frac{\partial u^f_z}{\partial t} \sim -\frac{\partial p^f}{\partial z} \tag{5.52}$$

Where we assume that the pressure gradient establishes instantaneously. Let also assume that the fluid phase respects the Darcy law, neglecting the inertial term, the relaxed gas velocity can be
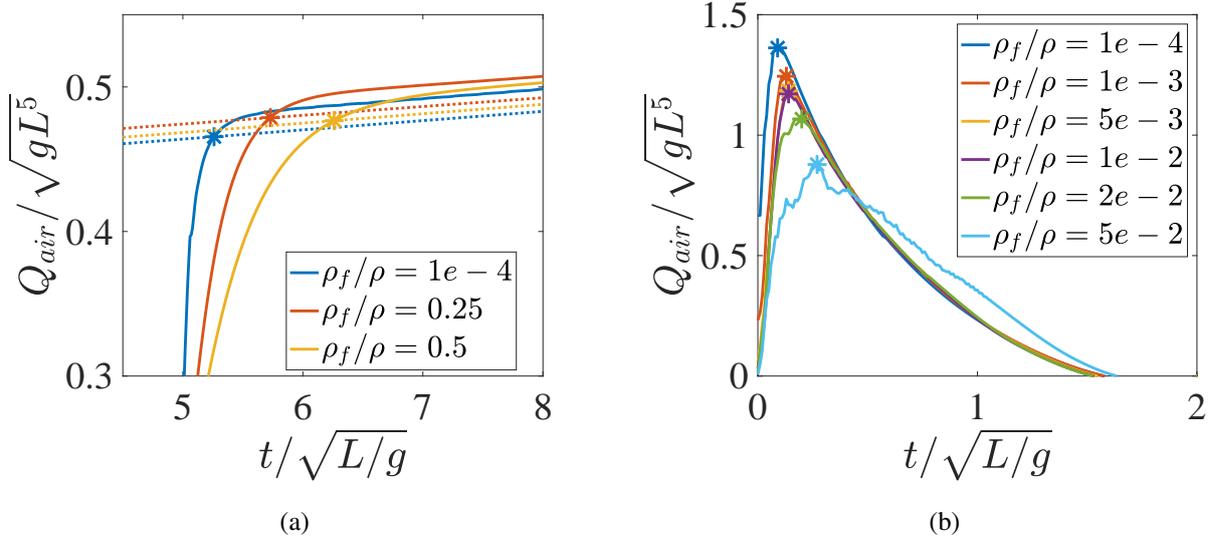
Figure 5.34: Temporal evolution of discharge flow rate of the fluid phase and the determination of characteristic time for various granular densities, for discharge of silo with $h_p^0 = 3.8L$, $R = 0.25L$ and $\rho = 1$ (a) with an imposed gas pressure $p_{top}^f = 5\rho gL$ for $5 \leq t/\sqrt{L/g} \leq 10$ and (b) with an initial imposed gas pressure $p_{top}^f = 40\rho gL$ at $t/\sqrt{L/g} = 0$.

expressed as $u^f \sim -\frac{\partial p^f}{\partial z}\frac{1}{\mathcal{B}_l}$. Thus, the characteristic time of fluid phase can be estimated by:

$$\tau_f \sim \frac{\rho_f}{\mathcal{B}_l} \tag{5.53}$$

This time scale is inversely proportional to the permeability of the granular media.

To verify this estimation, we carry out the same simulations than previously, for $h_p^0 = 3.8L$, $R = 0.25L$ and $\rho = 1$. We impose either a constant gas pressure at the top of the silo, $p_{top}^f = 5\rho gL$ for $5 \leq t/\sqrt{L/g} \leq 10$ or we impose an initial gas pressure $p_{top}^f = 40\rho gL$ at $t/\sqrt{L/g} = 0$. Note that we keep the granular density constant for all of the simulations $\rho = 1$, but we vary the fluid density. The determination of characteristic time is illustrated in Figure 5.34, following the same method than the previous study.

Figure 5.35 illustrates the dimensionless characteristic time of the fluid phase, $\tau_f/\sqrt{L/g}$, obtained by the two series of simulations, versus the dimensionless density, ρ_f/ρ. As suggested by equation 5.53, a linear function adjusts well both of the two results, however, with an offset certainly due to the characteristic time of establishment of the granular flow.

In the experimental study, the relaxation of the gas flow can be estimated in the order of magnitude, $\tau_f \approx 1 \times 10^{-5}$, due to the small gas density with respect to the granular density. This indicates that the acceleration of the gas flow at the very beginning of the discharge can be neglected, compared to the discharge time scale, or to the time of establishment of the gas pressure gradient.
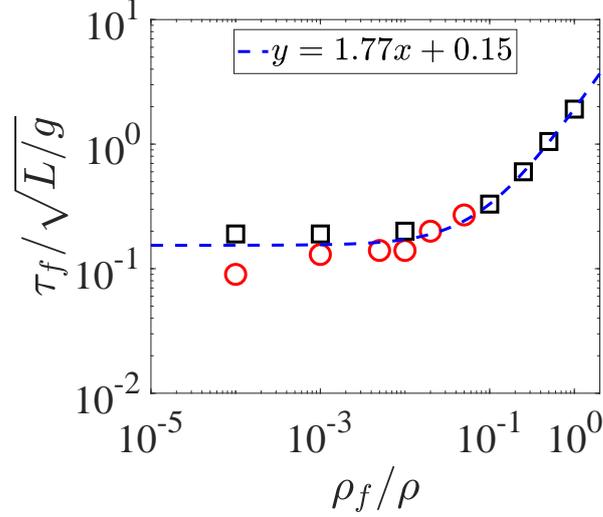
Figure 5.35: Characteristic time $\tau_f/\sqrt{L/g}$ as a function of the dimensionless granular density ρ_f/ρ. The black squares represent the results of simulation with an imposed gas pressure with $p_t^f = 5\rho g L$, and the red circles represent that with an initial imposed gas pressure, $p_t^f = 40\rho g L$. The dashed line represents a linear adjustment.

d.   Confrontation with the quasi-steady compressible unidimensional model

After the acceleration period for both phases, we concentrate on the discharge period, including the pressurized gas period and the steady period with a counter-current of air.

Following the previous study on the discharge flow with an imposed gas pressure at silo top, the discharge flow rate of the granular media can be determined by equation 5.54, considering the fluid pressure gradient driving force at the outlet.

$$Q = Q_0 \left(1 + A \frac{1}{\rho g} \frac{\partial p^f}{\partial z} \Big|_{z=0} \right)^{1/2} \tag{5.54}$$

Where the adjustable coefficient A takes into account the averaged pressure gradient at the outlet. This role is played by the parameter ϕ_0, representing the dilation at the outlet for the experimental study.

With equation 5.54 instead of 5.3, we can perform the quasi steady unidimensional model with a spatially uniform gas density and compare it with the numerical results for the pressurized period as shown in Figure 5.36 for $R = 0.25L$, $h_p^0 = 3.8L$ and $p_{top}^f(0) = 40\rho g L$, with the coefficients $B_l = 25\rho\sqrt{g/L}$, $B_i = B_{i0}\frac{\rho_{ftop}}{\rho_{f0}}$ and $R_f = R_{f0}\frac{\rho_{ftop}}{\rho_{f0}}$ with $B_{i0} = 6.3\rho/L$ and $R_{f0} = 0.002\rho$.

Figure 5.37 shows the confrontation for the steady discharge period with a counter current flow of air, where we observe a negative pressure at the top of the silo, similarly to the experiments (see Figure 5.20b) and a lower discharge flow rate of the granular media than the gravity driving case Q_0 (black dotted line). We observe that the quasi-steady model gives a good prediction of
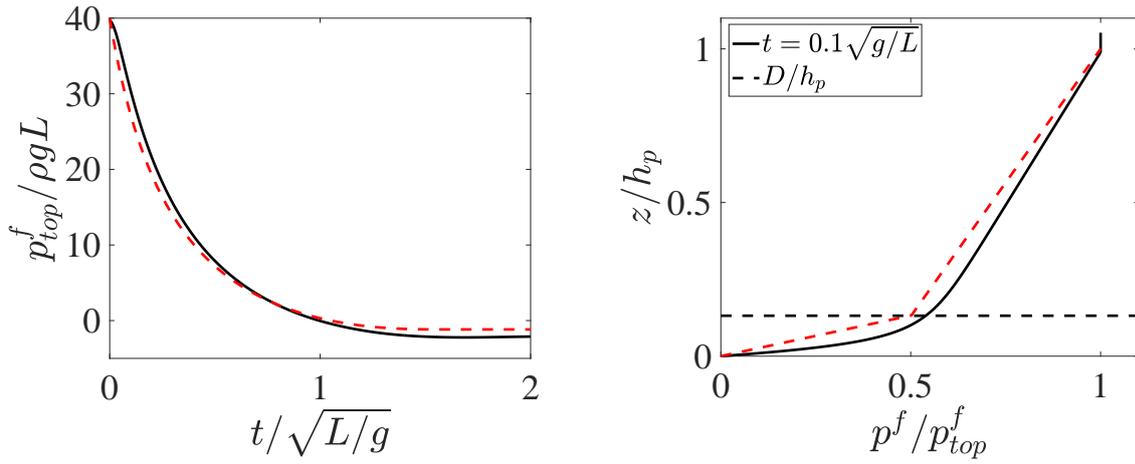
(a) Temporal evolution of the dimensionless differential fluid pressure at silo top, $p_{top}^f/\rho g L$.

(b) Dimensionless pressure profiles at the center of the silo for various instants, p^f/p_{top}^f
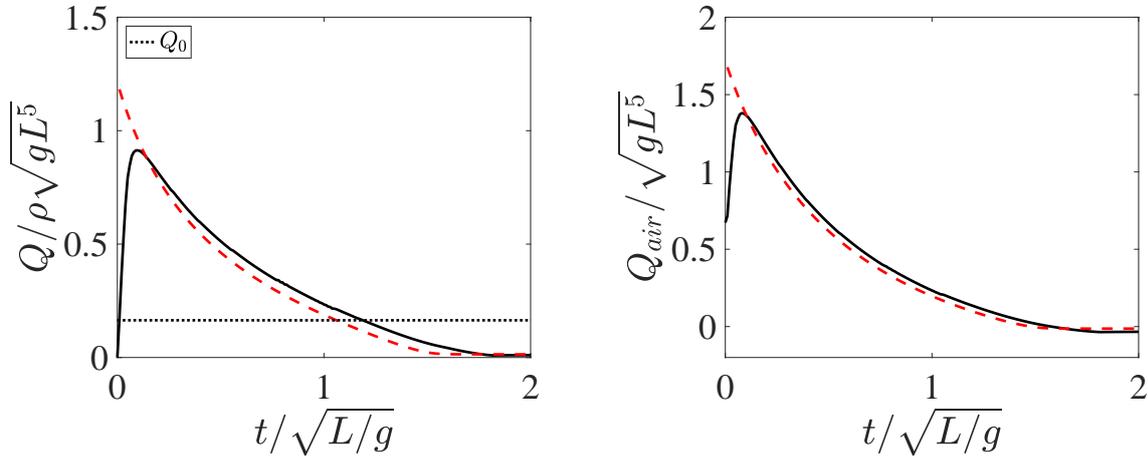
(c) Temporal evolution of the dimensionless discharge flow rate of granular media $Q/\rho\sqrt{gL^5}$.

(d) Temporal evolution of the dimensionless discharge volume flow rate of gas flow, $Q_{air}/\sqrt{gL^5}$.

Figure 5.36: Pressurized period: confrontation between the numerical results (black solid lines) and the quasi-steady model (red dashed lines), with the coefficient $A = 0.28$, for $R = 0.25L$, $h_p^0 = 3.8L$ and $p_{top}^f(0) = 40\rho g L$ with the coefficients $B_l = 25\rho\sqrt{g/L}$, $B_{i0} = 6.3\rho/L$ and $R_{f0} = 0.002\rho$.

the numerical results for the whole discharge period, after the acceleration period with the same adjustable coefficient $A = 0.28$ obtained in the previous study. Otherwise, we verify that this coefficient allows us to take into consideration of an averaged gas pressure gradient around the outlet zone, representing an effective pressure gradient which modifies the discharge driving force in the equation 5.54.
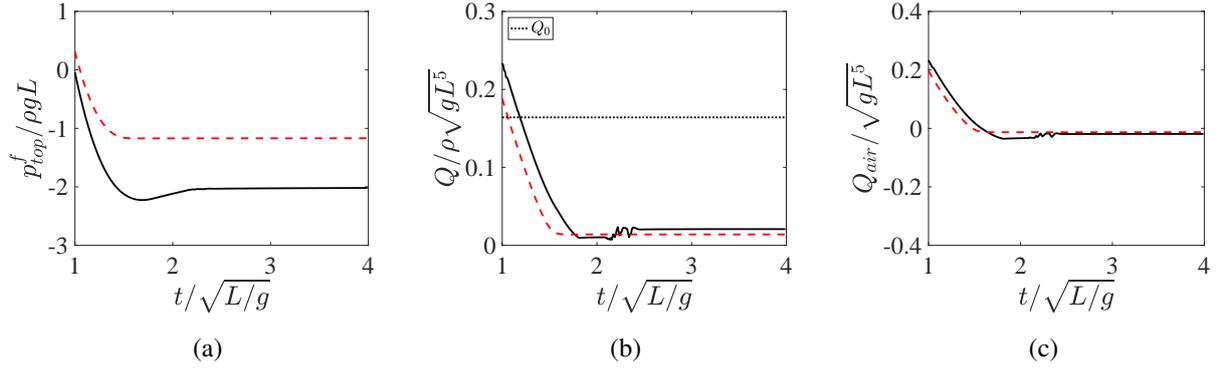
Figure 5.37: Steady period with a counter current flow: Confrontation between the numerical results (black solid lines) and the quasi-steady model (red dashed lines), with the adjustable coefficient $A = 0.28$, for $R = 0.25L$, $h_p^0 = 3.8L$ and $p_{top}^f(0) = 40\rho gL$ with the coefficients $B_l = 25\rho\sqrt{g/L}$, $B_{i0} = 6.3\rho/L$ and $R_{f0} = 0.002\rho$. Temporal evolution of (a) the dimensionless differential fluid pressure at silo top, $p_{top}^f/\rho gL$, (b) the dimensionless discharge flow rate of granular media $Q/\rho\sqrt{gL^5}$ and (c) the dimensionless discharge volume flow rate of gas flow, $Q_{air}/\sqrt{gL^5}$.

5.4.3 Conclusion

Using numerical simulation of the two-phase modelling considering a compressible fluid and a granular rheology, we have successfully reproduced the main features observed in the experiments for a violent discharge flow subsequent to the rupture of the orifice by a pressurized gas. The numerical simulation allows us to validate some of the hypothesis done in the quasi steady unidimensional model. In the following part, we will discuss the feature of the granular jet out of the silo.

5.5 Granular jet shape

5.5.1 Puff jet shape
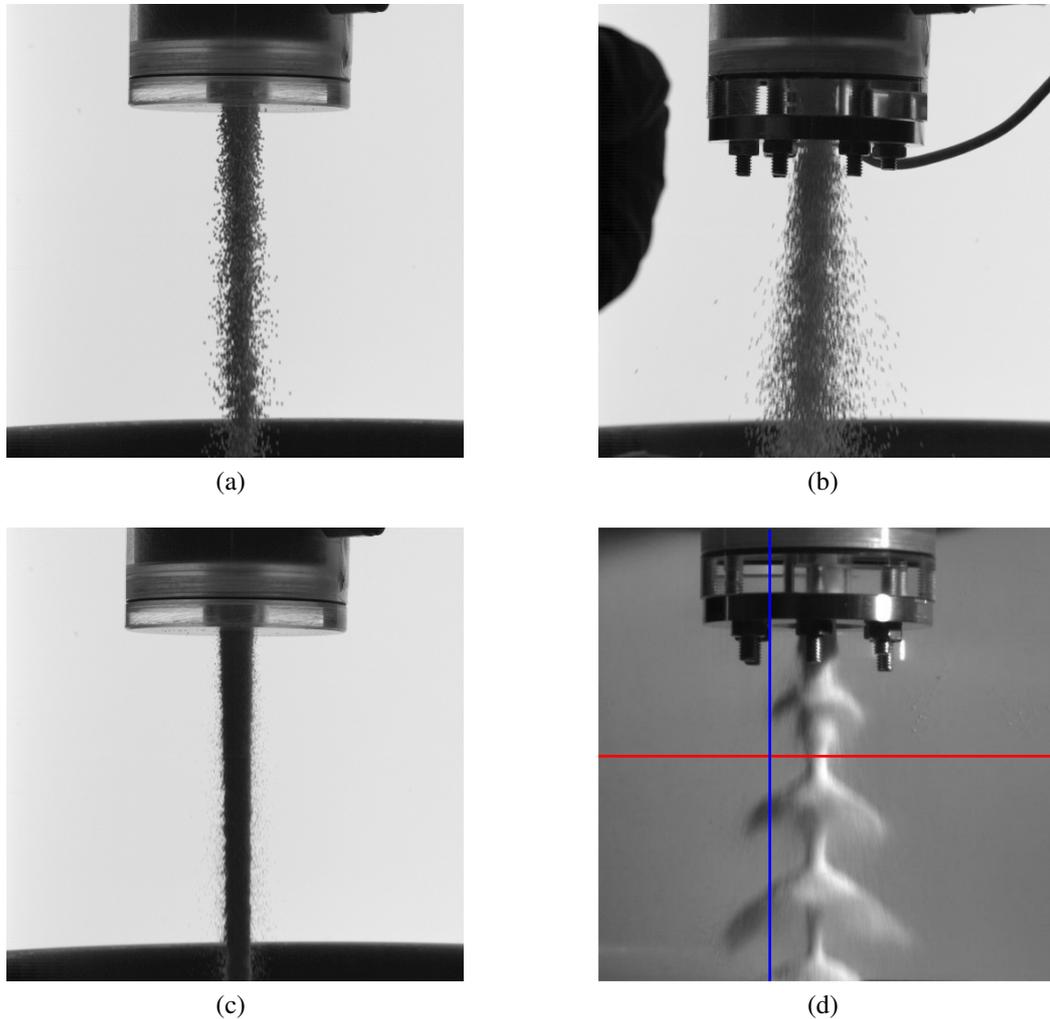
Figure 5.38: Snapshots of the granular jet shapes for different experimental conditions, with $L =$ 40mm, $D = 10$mm and ceramic particles. (a, b) for $d_p = 550\mu m$ and (c, d) for $d_p = 180\mu m$. (a, c) for the discharge flow without gas injection and (b, d) for the discharge flow with an instantaneous rupture of the outlet.

During the discharge, the high speed camera installed in front of the silo, provides a close view of the granular jet shape nearby the outlet with a high frequency of acquisition (3000 or 6000 frames per second with a resolution of $512 \times 512 \ pixel^2$). Initially the aim of the camera was to measure the ejected granular velocity at the first instant but it appears an interesting feature on the jet shape that we decided to study. In Figure 5.38, we present several examples of snapshot of the granular jet shape taken at the very beginning of the discharge ($t \approx 0.1s$) and different experimental conditions for $L = 40$mm, $D = 10$mm and ceramic particles: Figure 5.38 (a, c) illustrate the granular shapes at the outlet for the discharge of the silo without gas injection, for
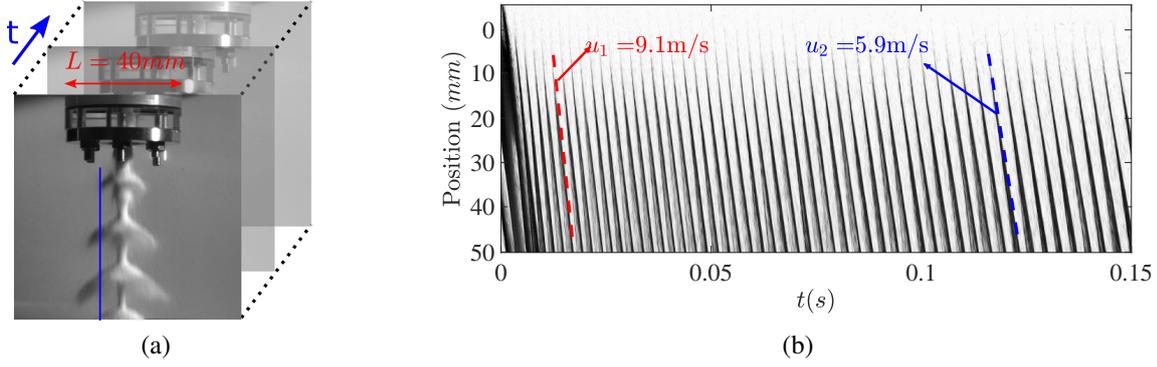
Figure 5.39: Spatiotemporal analysis of the vertical blue line shown in (a) for $L = 40$mm, $D = 10$mm and $d_p = 180\mu m$ (ceramic particles).

(a) $d_p = 550\mu m$ and for (c) $d_p = 180\mu m$. With these two snapshots, we observe that the granular jet has a nearly cylindric shape due to the circular outlet. Figure 5.38 (b, d) show the granular jet for an instantaneous rupture of the outlet, again for (b) $d_p = 550\mu m$ and for (d) $d_p = 180\mu m$. For the bigger particles, comparing Figure 5.38 (a) and (b), we observe that the highly pressurized gas leads to a wider spread of the granular jet at the outlet. Whereas for the smaller particles, we observe a destabilization of the granular jet with an instantaneous rupture of the outlet (Figure 5.38d), that we call the puff jet shape.

To characterize this phenomena, we performed a spatiotemporal analysis. The analysis procedure developed with $Matlab$, is illustrated in Figure 5.39, with a silo diameter of $L = 40$mm, an outlet size of $D = 10$mm and the ceramic particle of size $d_p = 180\mu m$. The Experimental film is recorded under a sequence of grayscale images, as shown in Figure 5.39a. The film is then analyzed along two lines: a vertical one (blue line in Figure 5.38d), parallels to the jet and crosses only the puffs of the granular jet and a horizontal one (red line in Figure 5.38d), that crosses the jet section. The spatiotemporal diagram carried out for the vertical line on the film, as shown by the blue line in Figure 5.39a, is displayed in Figure 5.39b. Each oblique vertical line corresponds to one moving puff whose velocity is given by the slope. The velocity has been illustrated in Figure 5.39b at two different instants during the discharge and is about $9m/s$. The puff velocity is indicative of the particle velocity at the outlet. We observe that the velocity of the granular flow is quite important at the very beginning of the discharge and decreases rapidly over time, reaching $5m/s$ after 0.1s. This behavior corresponds to the observation of the flow rate (see section 5.2.1). For the $L = 40$mm, $D = 10$mm and $d_p = 180\mu m$ (ceramic particles), we obtained a important discharge flow rate of the granular media at the beginning of the discharge $\approx 1.3kg/s$ at $t \approx 0.1$s, corresponding to a particle velocity at the outlet $\approx 4.5m/s$, estimated by $u_0^p \approx Q/(\rho_p \phi b i S_0)$.

A second spatiotemporal diagram of the beginning period of the discharge is constructed and displayed in Figure 5.40b for the horizontal line. On this diagram, the puffs correspond to the vertical peaks that clearly occur at a given frequency. To obtain the temporal evolution of the puff

(a) Experimental film

(b) Spatiotemporal diagram for the horizontal red line in Figure (a)

(c) Temporal evolution of the grayscale along the dashed red line in Figure (b)
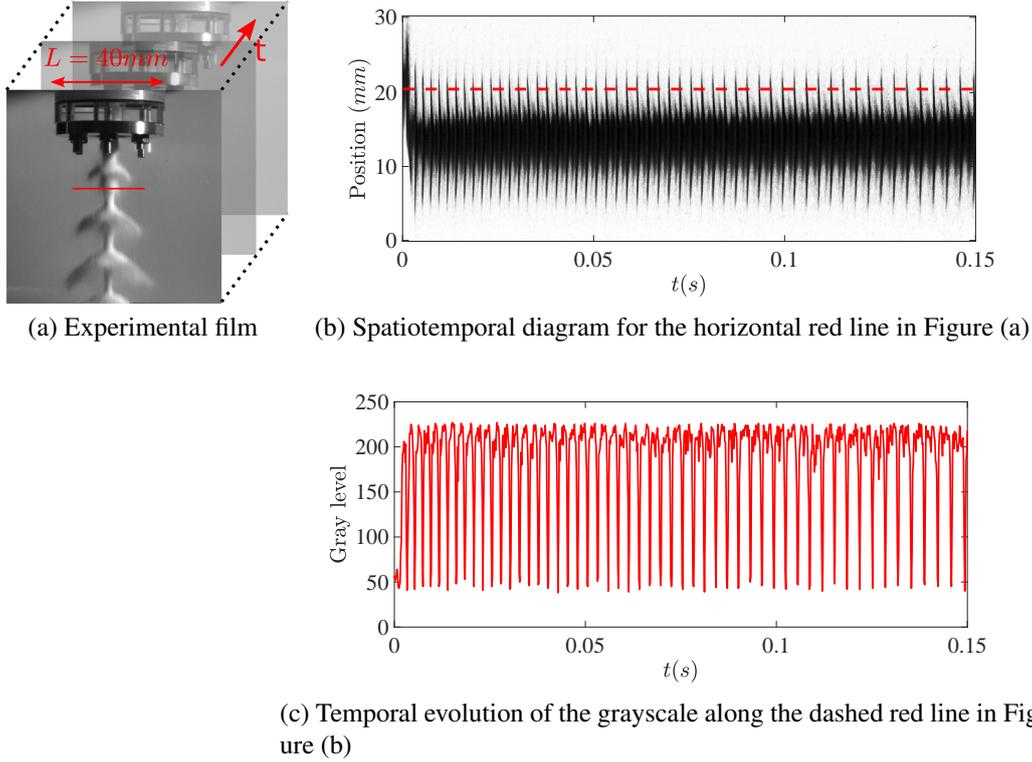
Figure 5.40: Spatiotemporal analysis of the granular jet shape at the outlet for L = 40mm, D = 10mm and d_p = 180μm (ceramic particles).

frequency, we first extract the grayscale level along the red dashed line in Figure 5.40b. Indeed, the passage of an individual puff corresponds to a minimal value of the grayscale level along this line (see Figure 5.40c).

Then we perform a Short-time Fourier Transform (STFT) implemented in the Matlab environment as a complementary ready-to-use functions developed by Zhivomirov [2019]. This algorithms determines the frequency and the phase of a signal which evolves over time. The signal is divided into shorter segments of equal length on which the Fourier transform is computed to produce the local spectrum. The resulting spectrogram is displayed in Figure 5.41a. The vertical axis represents the frequency and the horizontal axis the time evolution whereas the color represents the amplitude of the frequency. The fundamental frequency of the granular jet puff corresponds to the first yellow thread in the figure, the other threads represent its harmonics. This fundamental frequency is plotted in Figure 5.41b as a function of time. We observe that this frequency is quite high around 450Hz at the beginning of the discharge and then decreases to 150Hz on a short time ($\approx$ 0.5 s), corresponding roughly to the pressurized gas period. At long time, this instability of the jet shape disappears.

To investigate on the origin of puff jet shape instability, in the following part, we will study the gas pressure response at the outlet level.
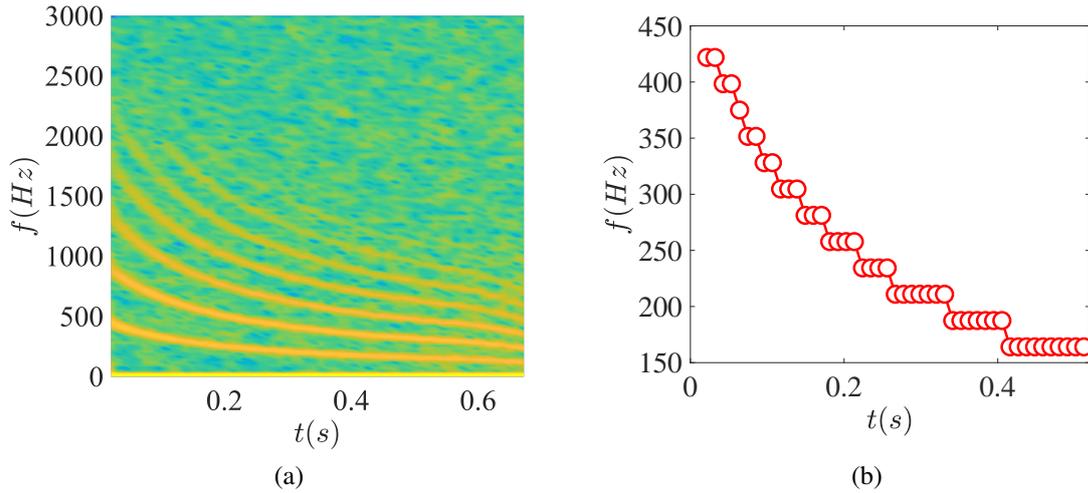
Figure 5.41: Frequency analysis of the granular jet puff for L = 40mm, D = 10mm and d_p = 180μm (ceramic particles). (a) Spectrogram of the grayscale signal. (b) Temporal evolution of the fundamental frequency of the granular jet puff.

5.5.2 Gas pressure oscillations

Thanks to the dynamic pressure sensor at the bottom plug of silo, P_6 with an acquisition frequency of 10000 Hz, we are able to follow the rapid variation of gas pressure, which is inaccessible to the pressure sensors situated at the side of the silo with a lower frequency of 100Hz.
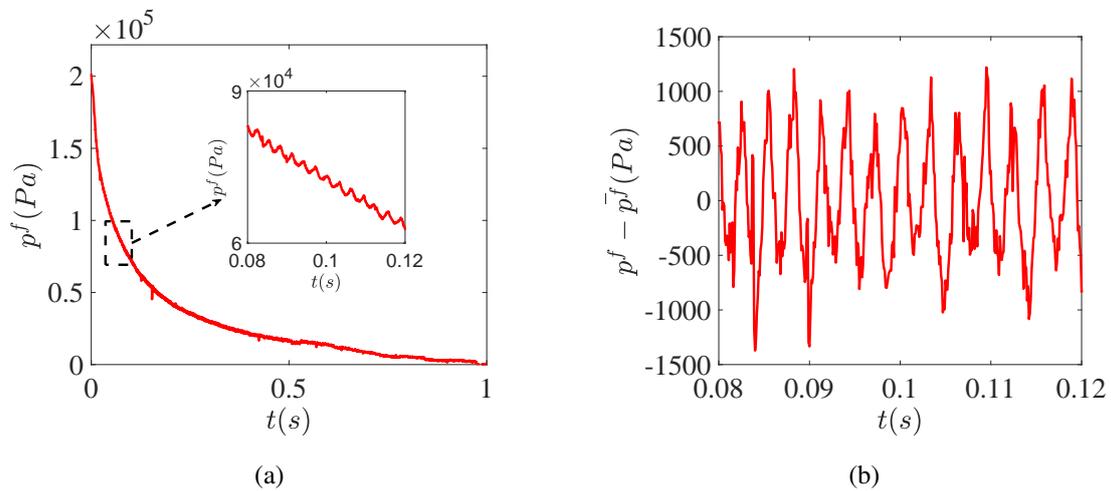
Figure 5.42: Silo discharge for L = 40mm, D = 10mm and d_p = 180μm (ceramic particles). (a) Temporal evolution of the differential gas pressure given by the dynamic pressure sensor at the bottom of silo, P_6. (b) Oscillations part of the gas pressure signal.

The temporal evolution of the differential gas pressure at the bottom of the silo is shown in Figure 5.42 for L = 40 mm, D = 10 mm and d_p = 180 μm (ceramic particles). We recover the typical fast decrease of the air pressure during the pressurized regime. However, if we zoom on a

small period of the signal, we observe oscillations as shown in the inset and in Figure 5.42b where the mean linear tendency of the pressure was subtracted to the signal to observe the oscillating part. We observe that the pressure amplitude is quite weak, about $500Pa$. This pressure oscillations are not observed at the top of the silo, measured by the other dynamic pressure sensor at the top plug P_7, which suggests a local occurrence of the pressure oscillations at the outlet. We decide to carry out a frequency analysis on the pressure oscillations, performing a STFT with a interval of $\approx 0.5s$ at the beginning of the discharge.
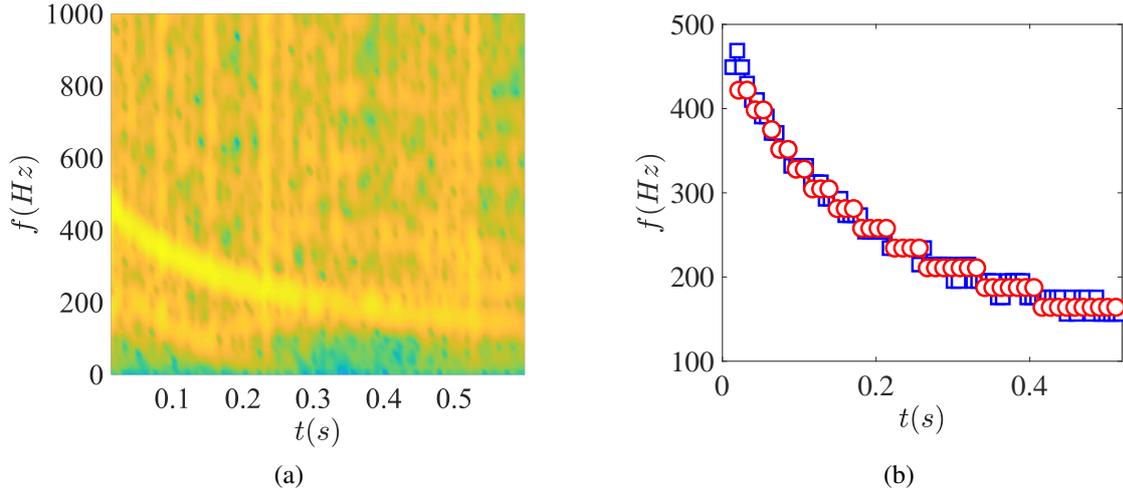
Figure 5.43: Silo discharge for $L = 40$mm, $D = 10$mm and $d_p = 180\mu m$ (ceramic particles). (a) Spectrogram of the pressure oscillation. (b) Comparison between the temporal evolution of the granular puff jet frequency ($\circ$) and the pressure oscillation frequency ($\square$).

The resulting spectrogram of the gas pressure oscillations at the bottom of the silo is shown in Figure 5.43a. The bright yellow thread in the figure gives the fundamental frequency of the pressure oscillation over time. In Figure 5.43b, we compare the temporal evolution of the granular puff jet frequency and the pressure oscillations frequency. We observe a strong correlation between these two frequencies, the data being nearly superimposed. This indicates that the granular puffs are linked to the local oscillation of the gas pressure close to the outlet.

This suggests a mechanism for the puff formation that will be discussed in the following section.

5.5.3   Mechanism of the granular jet instability

To explain the origin of the puff on the granular jet, a schematic view of the assumed mechanism is shown in Figure 5.44a. In this chapter, we have shown that in the presence of a gas flow, the particle flow rate, and thus the particle velocity depends on the gas pressure gradient at the outlet: $u^p = u_0^p \left(1 + \frac{1}{\phi_0 \rho_p g} \frac{\partial p^f}{\partial z} \mid_{z=0} (t) \right)^{1/2}$. Thus, the oscillations of the gas pressure at the outlet can generate an oscillation of the granular jet velocity at the outlet. If we neglect the gravity driving

term, writing $u^p \sim \frac{u_0^p}{(\phi_0 \rho_p g)^{1/2}}(\frac{p^f}{D})^{1/2}$, we obtain $\frac{\Delta u^p}{u^p} \sim \frac{1}{2}\frac{\Delta p^f}{p^f}$. At the beginning of the discharge, with $u^p \approx 9m/s$, $p^f \approx 2 \times 10^5$Pa and $\Delta p^f = 500$Pa, we obtain $\Delta u^p \approx 1cm/s$. This small velocity difference may induce the puff formation. Indeed as shown in Figure 5.44a, if the granular velocity at the upstream position $u^p + \Delta u^p$ is larger than that of the downstream position u^p, the upstream particles may impinge the downstream ones, which can be considered as a granular jet impingement on a fixed target.
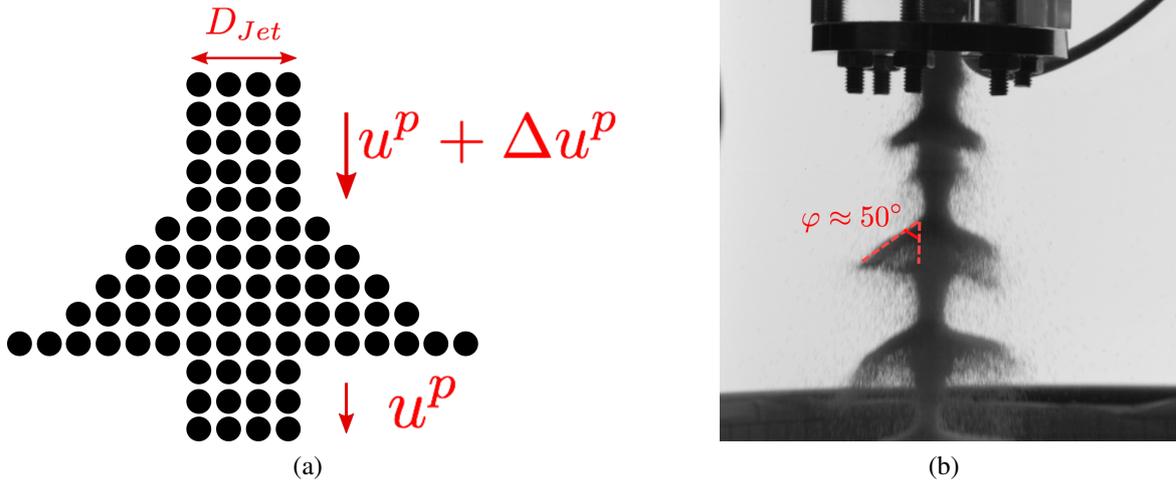

Figure 5.44: (a) Schematic view of the mechanism describing the granular puff jet. (b) Estimation of the opening angle of the granular puff jet for $L = 40$mm, $D = 10$mm and $d_p = 180\mu m$ (ceramic).

Recently, Cheng et al. [2007] have studied a granular jet of diameter D_{jet} and velocity U_0 impingement on a target of diameter D_{Tar}. They found that after the collision, the jet adopts a cone shape similar to water bell and to the puff (see Figure 5.44b). Writing the momentum conservation of the granular jet, they predict a dependency of the opening angle of granular jet, φ on the ratio between the target diameter and that of the granular jet, D_{Tar}/D_{Jet}, when $D_{Tar} \leq D_{Jet}$:

$$\varphi = acos(1 - (A - B)(\frac{D_{Tar}}{D_{Jet}})^2) \tag{5.55}$$

where A is a constant describing the average glancing collision angle for a particle and B depends on the coefficient of restitution of particles hitting the target, where the authors suppose $A - B = 0.3$.

For our case, we suppose that the granular jet impinges itself, thus, $\frac{D_{Tar}}{D_{Jet}} = 1$. Therefore, we obtain a theoretical opening angle of the granular jet at the outlet, $\varphi = 45°$, which is close to the observed value $\varphi \approx 50°$, as shown in Figure 5.44b. We are not in the same order of magnitude of the jet impacting velocity than in this study, however, they show that in the range explored, this angle does not depend on the jet velocity.

Thus the air pressure oscillation may be responsible for the puff formation. A possible origin

of those oscillations may be due to the propagation of acoustic waves. The acoustic waves propagate at a frequency $f \sim \frac{c_0}{l}$, where l is a characteristic length, with $c_0 \approx 300 m/s$ (see equation 5.9 neglecting the dissipating term). Considering the frequency of the puff, $f \approx 300$Hz, the length scale on which the waves propagate should be on the order of 1m. Then we can suppose that this wave develops on the fluid phase at the top of the silo $l \approx H - h_p^0$. To test this hypothesis, we vary the initial filling height of the granular column h_p^0. Figure 5.45a illustrates the first frequency of granular puff just after the rupture of the outlet, f_0, versus h_p^0 for the ceramic particle of density $\rho_p = 6000 kg/m^3$ (black squares) and the glass particles of density $\rho_p = 2500 kg/m^3$ (red circles). We observe that there is no correlation between the frequency of the granular puff and the initial filling height of the granular media, however, the frequency seem to be lower for the lighter particles. This indicates that the gas pressure oscillation at the outlet is not associated with an acoustic waves on the fluid reservoir. This is consistent with the fact that we do not see gas pressure oscillations with the sensor at the top plug. This suggests that the origin of the gas pressure oscillation is located close to the outlet.

(a)

(b)
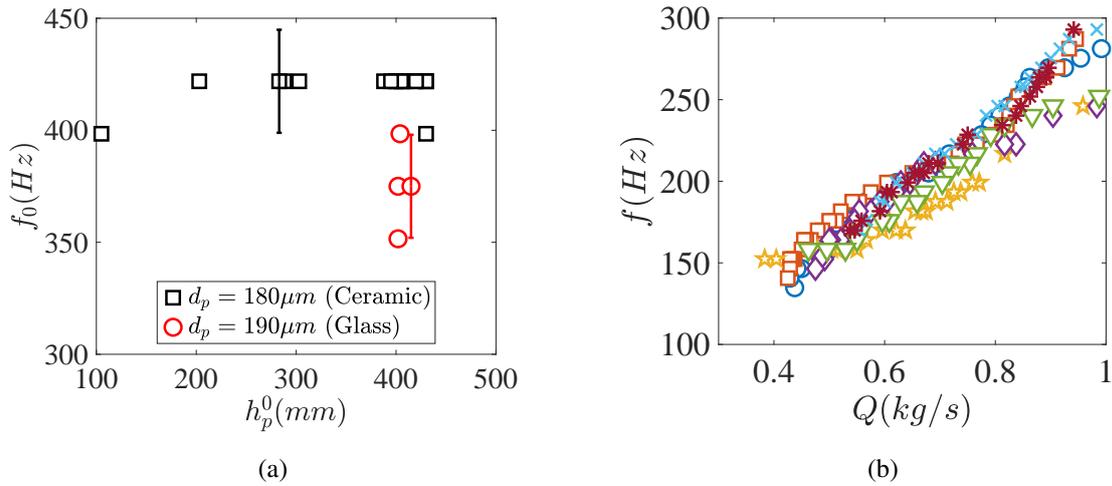
Figure 5.45: (a) Initial frequency of the granular puff versus the filling granular column height, h_p^0. (b) Frequency of the granular puff versus the discharge flow rate of the granular media for several experiments, for $L = 40$mm, $D = 10$mm and $d_p = 180\mu m$ (ceramic particles).

Finally, in Figure 5.45b, we plot the frequency of the granular puff versus the particle flow rate for several experiments, for $L = 40$mm, $D = 10$mm and $d_p = 180\mu m$ (ceramic particles). We observe that the frequency of the granular puff is highly correlated to the particle flow rate. The observed gas pressure oscillation at the outlet which appears only for the smallest particles may be due to the particle volume fraction fluctuation and local compression of the gas. However, more work, experimental and theoretical, need to be done to fully understand this mechanism.

5.6 Conclusion and perspective

In this chapter, we have investigated a transient discharge flow with an instantaneous rupture of the outlet, representing a more realistic configuration with our situation of interest. We designed a bottom plug with a membrane at the outlet which breaks for a silo pressure about 2bar above the atmospheric pressure. Three discharge periods are observed during the silo discharge: the establishment of the gas pressure gradient, the pressurized gas discharge and the steady flow periods. We find that the characteristic time of the establishment of the gas pressure gradient depends particularly on the permeability of the granular flow, being shorter for a more permeable granular media and in the range of parameter explored is between $[0.02, \ 0.2]s$. Then during the pressurized gas discharge, we observe first a very high particle flow rate (about $1kg/s$), corresponding to high particle velocity at the outlet (about $10m/s$). Then the discharge flow rate decreases rapidly together with the gas pressure to reach the steady flow period after roughly $1s$. This steady flow corresponds to a closed top silo with a counter current flow. To describe the whole discharge, we develop an unidimensional model which takes into account the air compressibility. This model gives a fairly good prediction of the experimental observations. Then we resolve numerically a full two-phase continuum modelling considering a compressible fluid and a granular rheology. This model reproduces well the experimental observation and allows to validates some of the hypothesis of the analytical unidimensional model. Finally, an instability of the granular jet is observed for the smallest particles and we have discussed the mechanism which could lead to such phenomena.

In the next chapter, to further approach the situation of interest, we will investigate the effect of a surrounding liquid on the discharge flow rate.

Chapter 6

Effect of the surrounding liquid

In the situation of interest, the fuel rod is immersed in pressurized water, thus in the RIA scenario, hot fuel fragments will discharge in a liquid. Then in this chapter, we focus on the effect of a surrounding liquid on the discharge flow rate of the granular media, by immersing the silo outlet in water. To mimic the effect of the hot temperature of the fragments, which will tend to have a vaporized gas layer around them, we also use hydrophobic particles which tend to entrain gas as a surrounding layer. In section 6.1, we will present the experimental setup and the granular materials used for carrying out this study. In section 6.2, we present the results of the silo discharge for three different conditions: an imposed air flow rate, an imposed constant gas pressure at the top of the silo and the discharge with an instantaneous rupture of the outlet. Finally, in section 6.3, we try to forecast the phenomenon of interest of this thesis, predicting the discharge flow rate of the fuel fragments and the fission gas while the hypothetical scenario occurrs, using the analytical model.

6.1 Experimental apparatus

The schematic view of the experimental setup is illustrated in Figure 6.1, based on the experimental setup presented in chapter 4 and 5. We use 3 types of gas injection at the top of the silo:

- To inject a constant air flow, we use the same system than Zhou [2016] with a valve, a pressure regulator and a tube full of particles of size 1mm to impose an high pressure loss and thus a constant air flow rate.

- To inject a constant pressure, we use the system presented in chapter 4.

- For the rupture of the outlet, we use the system presented in chapter 5.

During the discharge of the silo, the granular media and the gas are ejected simultaneously through the outlet and there is not backward water flow toward the silo (the pressure level within
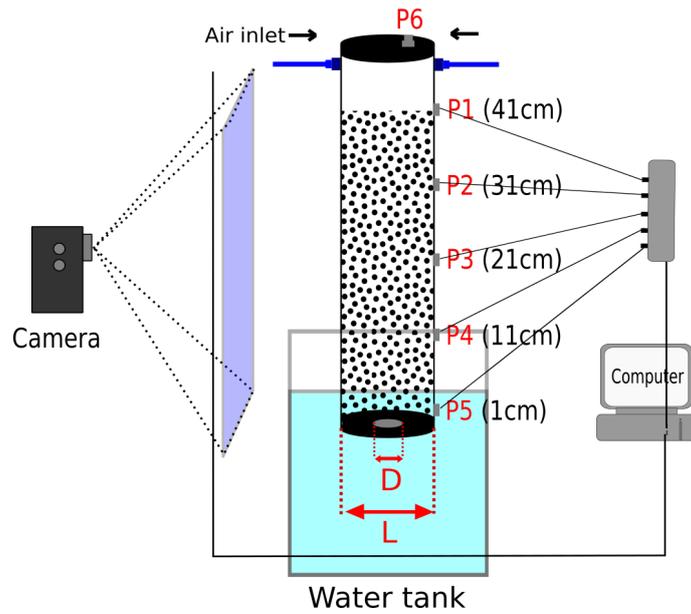
Figure 6.1: Schematic view of the experimental setup for studying the discharge of silo immersed in water with an imposed gas pressure.

the silo is high enough to prevent water intrusion). We can thus keep using the pressure sensors at the lateral position ($P_1 - P_5$) in order to follow the gas pressure evolution within the silo. In the rupture experiment, we keep the pressure at the top plug but not the one at the bottom plug, immersed in water. A rectangular water tank is placed below the silo instead of the electronic balance. A camera is placed in front of the silo to film the whole silo zone at an acquisition frequency of 240 frames per second: the granular mass flow rate is then deduced using the spatiotemporal diagram technique presented in chapter 5.
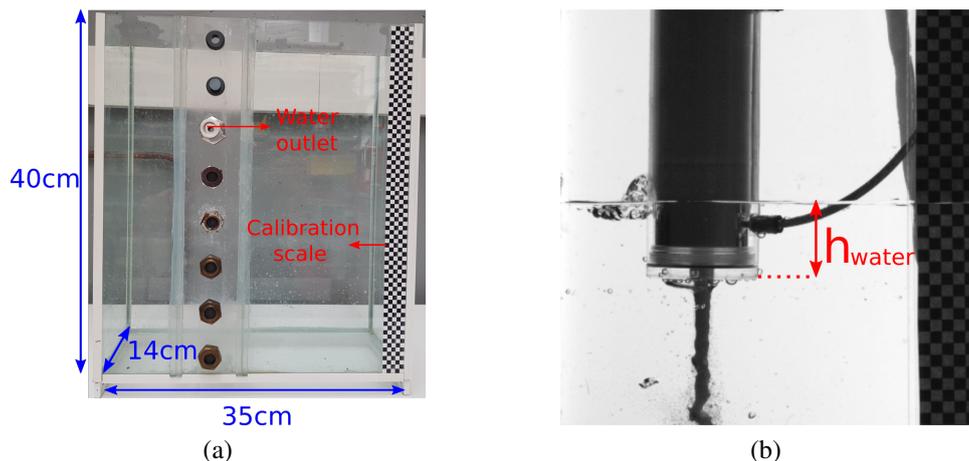
Figure 6.2: (a) Water tank and (b) a local view of the experiment for the discharge of silo immersed in water for a pressure imposed experiment.

The rectangular water tank is made on glass, allowing visualization, with an internal dimension of $14 \times 35 \times 40 \ cm^3$ as shown in Figure 6.2a. A calibration scale composed by black-white squares

of side 5 ± 0.1 mm is placed in front of the water tank. Furthermore, the water tank possesses eight holes in the front side, the first one located at 2.5 cm high from the tank bottom and the others spaced every 5 cm. During the experiment, we open the hold placed at 27.5cm from the tank bottom to maintain the level of water constant when the granular media is ejected from the silo to the water tank. For each experiment, the tank is filled initially with water until the level of the opened hole. Then, the silo already closed by a rubber plug and filled by a granular column of height h_p^0, is immersed in the water tank as shown in Figure 6.2b. During the discharge for the two first types of gas injection, we observe that there is a gas bubble of ≈ 1cm height which is trapped at the outlet. This steady gas bubble keeps the particles dry at the outlet, and they become wet when they pass through the bubble limit and contact with water. We note h_{water} the water depth above the bottom of the silo. This new controlling parameter is varied by moving the silo position.

6.1.1 Granular materials

We use the same particles as previously, a summed up in Table 6.1

Table 6.1: Characteristic of granular media.

	Glass particles	Ceramic particles	Sand particles
untreated	$[190; 538]\mu m$	$[180; 550]\mu m$	$800\mu m$
hydrophobic	$[190; 538]\mu m$	$[180; 550]\mu m$	$864\mu m$

<div align="center">(a)   (b)   (c)   (d)</div>
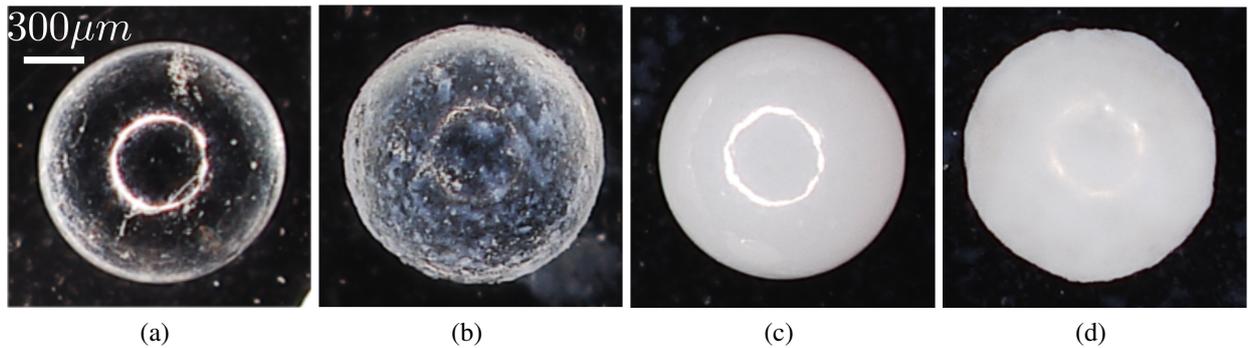
Figure 6.3: Visual aspect of (a, c) the untreated and (b, d) the treated hydrophobic particles for the different materials considered: (a, b) glass particle with $d_p = 1129\mu m$ and (c, d) ceramic particles with $d_p = 1165\mu m$.

The hydrophobic sand particles are provided directly by $Educational Innovations$. The glass and ceramic particles are separated in two batches, one being treated by a chemical product provided by $NeverWet^{TM}$. This product is a commercial superhydrophobic treatment. It normally consists on two coats: the base coat and the top coat. However, we found that the top coat tends to make the particles cohesive and does not increase much the contact angle. Thus, only the base

coat is sprayed homogeneously on the particles about ten rounds, waiting at least 15 minutes for drying between each spray. A comparison of the hydrophobic particles and the untreated particles surfaces is shown in Figure 6.3, using a microscope. For example, comparing the glass particle shown in Figure 6.3a and the hydrophobic glass particle shown in Figure 6.3b, we observe a thin layer of the base coat around the particles, which thickness is assumed negligible with respect to the particle size.

Figure 6.4: Comparison of the macroscopical behavior between (a) untreated and (b) hydrophobic ceramic particles, with $d_p = 180\mu m$, poured in a water tank.

A comparison of the macroscopical behavior between the untreated and the hydrophobic ceramic particles of the same particle size $d_p = 180\mu m$ is shown in Figure 6.4. The particles are poured freely and slowly into a rectangular water tank, and stay at its bottom, due to their larger density than water. For the untreated case shown in Figure 6.4a, we observe that most of the particles are mixed with the water, with some small gas bubble trapped in the granular bed. For the hydrophobic case shown in Figure 6.4b, the granular media forms a hill in which air is trapped.
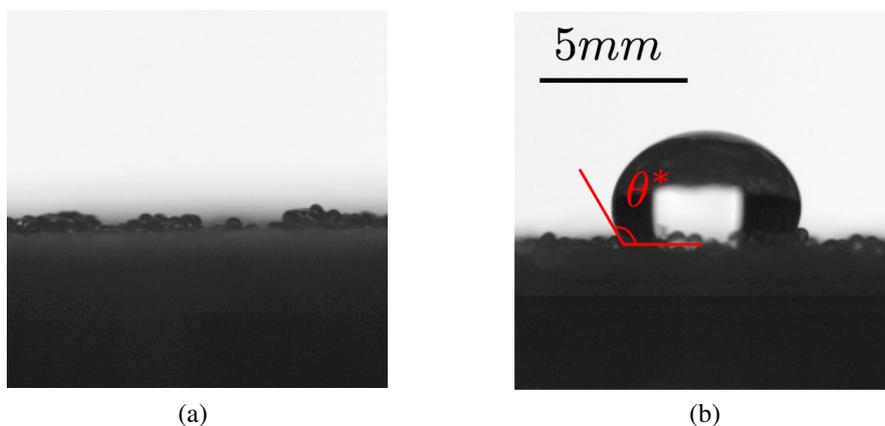

Figure 6.5: Measurement of the apparent contact angle between the liquid and the granular bed composed by (a) untreated and (b) hydrophobic glass particles, with $d_p = 538\mu m$.

To characterize the surface property of the particles, we carry out a study on their apparent contact angle with water. A flat bed composed by several layers of particles is prepared in a small petri dish, then a droplet of water is slowly ejected from a thin syringe on the top of the granular bed. After a few minutes, when the droplet becomes steady above the granular bed, we capture a picture of the drop with a camera. As shown in Figure 6.5, for a granular bed composed by the untreated glass particles (see Figure 6.5a), we observe that the droplet of water was completely absorbed by the bed, whereas it rests on the hydrophobic glass bed (see Figure 6.5b). The apparent contact angle θ^* between the granular bed and the water droplet is measured as shown in Figure 6.5b. When the water is absorbed, we consider a zero apparent contact angle. Each measurement is repeated a dozen times and the average value is considered.
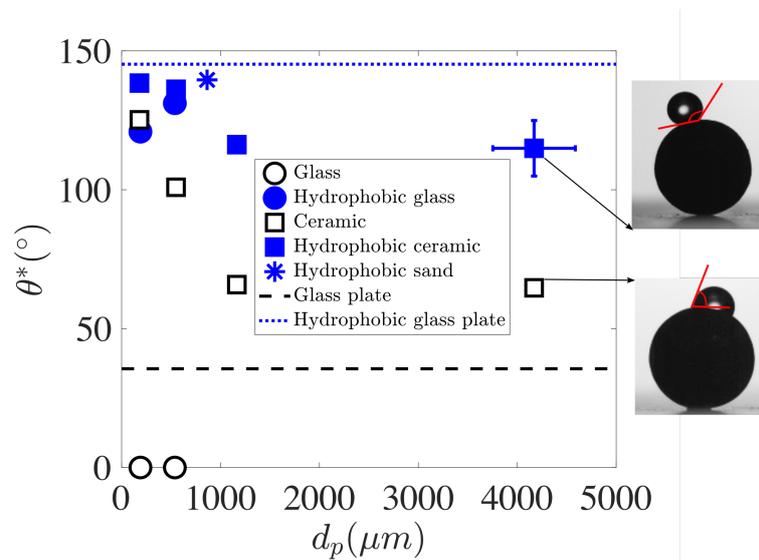

Figure 6.6: Apparent contact angle of the granular bed θ^* versus the composing particle sizes d_p.

Figure 6.6 illustrates the apparent contact angle between the granular media and the liquid, as a function of the particle sizes, for hydrophobic (full blue symbols) and untreated granular beds (empty black symbols). For the glass particles, we observe that the water droplet is absorbed by the granular bed composed by the untreated glass particles ($\theta^* = 0°$), while it does not penetrate the bed for the treated hydrophobic case with $\theta^* \approx 130°$. We also performed experiments with the glass plate to measure the equilibrium contact angle and we obtain $\theta = 35°$ for the untreated plate and $\theta = 145°$ for the hydrophobic plate. For the ceramic particles, we can estimate the angle of contact using the single large particle ($d_p = 4170\mu m$) and deposit a small drop on it. We found that $\theta \approx 70°$ for the untreated case and $\theta \approx 120°$ for the hydrophobic case. Then the apparent angle θ^* increases when decreasing the particle size as expected for rough hydrophobic surfaces (Bico et al. [1999]).

For each experiment, the silo is initially filled by a granular column composed by the dry particles. After the experiment, the particles are removed from the water tank and dried in a oven at a low temperature around $70°C$. Thanks to their waterproof property, the hydrophobic particles

191

become dry again once they are removed from the water, and can be used again rapidly, saving a considerable time for this study.

In the following section, we first present the discharge of the silo with an imposed gas flow rate at the top of the silo and with an outlet immersed in water.

6.2 Discharge of a silo immersed in water

6.2.1 Discharge flow with a constant air flow rate at the top

To investigate the role of the water on the discharge flow rate of the granular media, we begin with a steady experiment injecting a constant volumetric air flow rate from silo top. Indeed following the study carried out by Zhou [2016], the constant volumetric air flow rate induced a constant gas pressure gradient at the outlet, leading to a constant discharge flow rate of the granular media. All the experimental conditions are fixed, including the silo diameter $L = 40$mm, the outlet size $D = 10$mm, the particle diameter $d_p = 180\mu m$ (untreated ceramic particles), the volumetric air flow rate $Q_{air} \approx 6l/min$, except the water depth h_{water}.
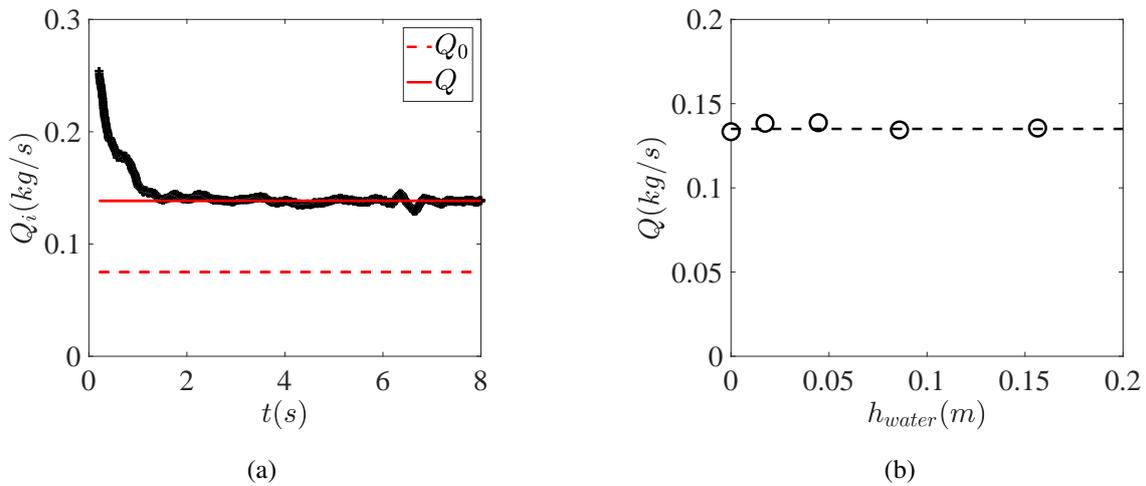
Figure 6.7: (a) Temporal evolution of the discharge flow rate for $L = 40$, $D = 10$mm, $d_p = 180\mu m$ (untreated ceramic particles) and $h_{water} = 44$mm. (b) Discharge flow rate as a function of the water depth h_{water}. The dashed line represents the model of Zhou [2016] (equation 2.37 in chapter 2) for a steady discharge flow with a constant air flow rate at the top of silo.

In Figure 6.7a, we plot the temporal evolution of the particle flow rate for $L = 40$, $D = 10$mm, $d_p = 180\mu m$ (untreated ceramic particles) and $h_{water} = 44$mm and we observe that it decreases at the beginning of the discharge which is linked to the large air flow rate when the rubber plug is removed, then it reaches a steady flow as expected. The presence of water does not change this behavior. The mean flow rate Q is determined during this steady discharge period (red solid line), and the red dashed line represents the flow rate driven by gravity Q_0 in air. In Figure 6.7b, we

192

plot the mean flow rate versus h_{water} and we observe no dependency on this parameter. Indeed as suggested by equation 2.31 of chapter 2, for a constant air and particle flow rate, the pressure gradient at the outlet (the driving force) is constant. The model of Zhou [2016] (equation 2.37 in chapter 2) gives a fairly good prediction of the discharge flow rate (dashed line).
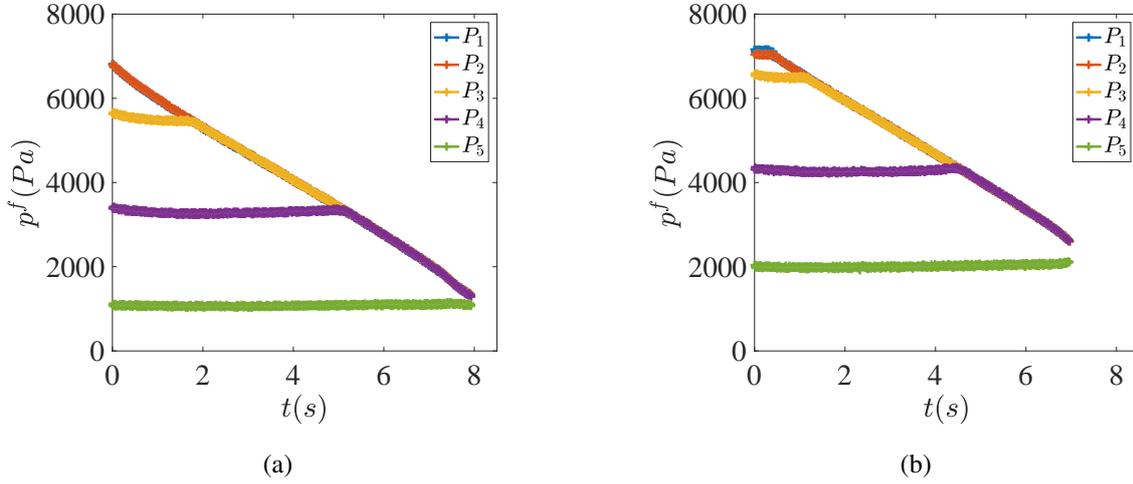
Figure 6.8: Discharge of silo with a constant volumetric air flow $Q_{air} \approx 6l/min$, for $L = 40$, $D = 10mm$ and $d_p = 180\mu m$ (untreated ceramic particles): temporal evolution of pressure profiles within the silo P_1 to P_5 for (a) $h_{water} = 0mm$ (with the outlet in air) and (b) $h_{water} = 85mm$.

Then Figure 6.8 illustrates how the gas pressures within the silo (P_1 to P_5) vary during the silo discharge, for (a) the outlet in open-air ($h_{water} = 0 \ mm$) and (b) $h_{water} = 85mm$. The position of the pressure sensors is illustrated in Figure 6.1. We observe the same behavior for a discharge either in air or water, described by Zhou [2016]: while the pressure sensor is inside the granular column, the pressure is constant. However, we observe a translation of the pressure level between these two cases. To characterize this shift, we focus on the gas pressure level P_5, which is located near the silo outlet ($z_5 = 1cm$).

Figure 6.9 illustrates the mean pressure level of P_5 during the discharge as a function of the water depth h_{water}. We observe a linear increase of the gas pressure near the outlet, corresponding to a slope equal to $\rho_{water}g$ (where ρ_{water} is the density of water), but with a small offset. This suggests that the surrounding liquid adds a hydrostatic overpressure at the outlet, following equation 6.1:

$$P_{outlet}^f = P_0 + \rho_{water}g\left(h_{water} + h_0\right) \tag{6.1}$$

We find that $h_0 \approx 1cm$, which corresponds to the bubble height located at the bottom of the silo. While this hydrostatic overpressure has no influence on the particle flow rate for a constant Q_{air}, we can think that it may play a role for a pressure imposed discharge.
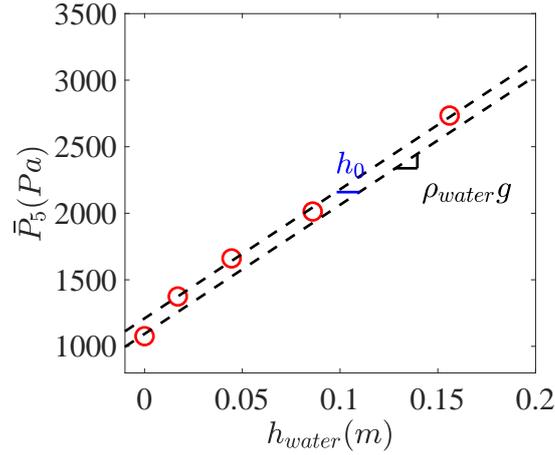
Figure 6.9: Mean value of P_5 as a function of the water depth h_{water}. The dashed line represents equation 6.1.

6.2.2 Discharge with an imposed gas pressure at the top of the silo

In Figure 6.10, we plot the temporal evolution and the profiles of the gas pressure for $L = 40$mm, $D = 10$mm, $D = 180\mu m$ (hydrophobic ceramic particles) and $h_{water} \approx 50$mm. We recover the same behavior than for a discharge in air. However, to obtain the pressure gradient at the outlet, we need to know the gas pressure at the outlet. Following the previous section, we can suppose that this pressure is given by equation 6.1. In the analytical model, we suppose that the

(a)

(b)
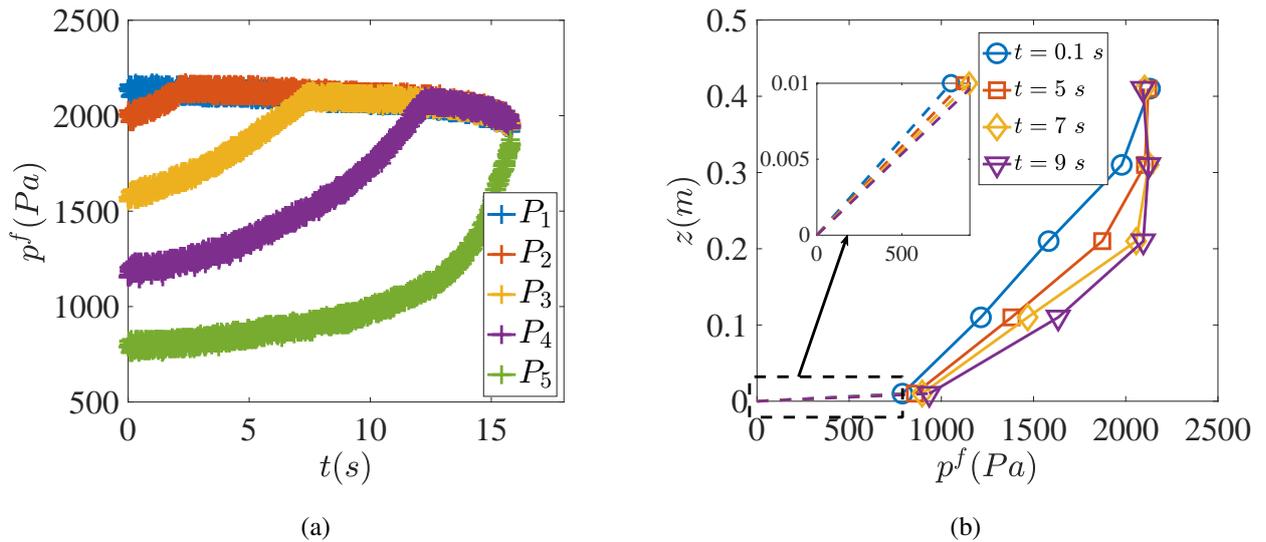
Figure 6.10: Discharge of the silo in water with an imposed air pressure at the top of the silo, for $L = 40$mm, $D = 10$mm, $D = 180\mu m$ (hydrophobic ceramic particles) and $h_{water} \approx 50$mm. (a) temporal evolution of the gas pressure $P_1 - P_5$. (b) profiles of the gas pressure along the silo at various instants.

total pressure drop of the air flow is now given by $\Delta p^f = p^f_{top} - p^f_{outlet}$, where p^f_{top} represents the imposed gas pressure at the top of the silo, with $p^f_{outlet} = \rho_{water} g (h_{water} + h_0)$. Thus, the pressure drop of the gas flow reads:

$$p^f_{top} - p^f_{outlet} = \left(h_p - h_1 \right) \frac{\partial p^f}{\partial z} \mid_{z \gg 0} + h_1 \frac{\partial p^f}{\partial z} \mid_{z \approx 0} \tag{6.2}$$

Following the quasi-steady analytical model of chapter 4, we can predict the discharge flow rate
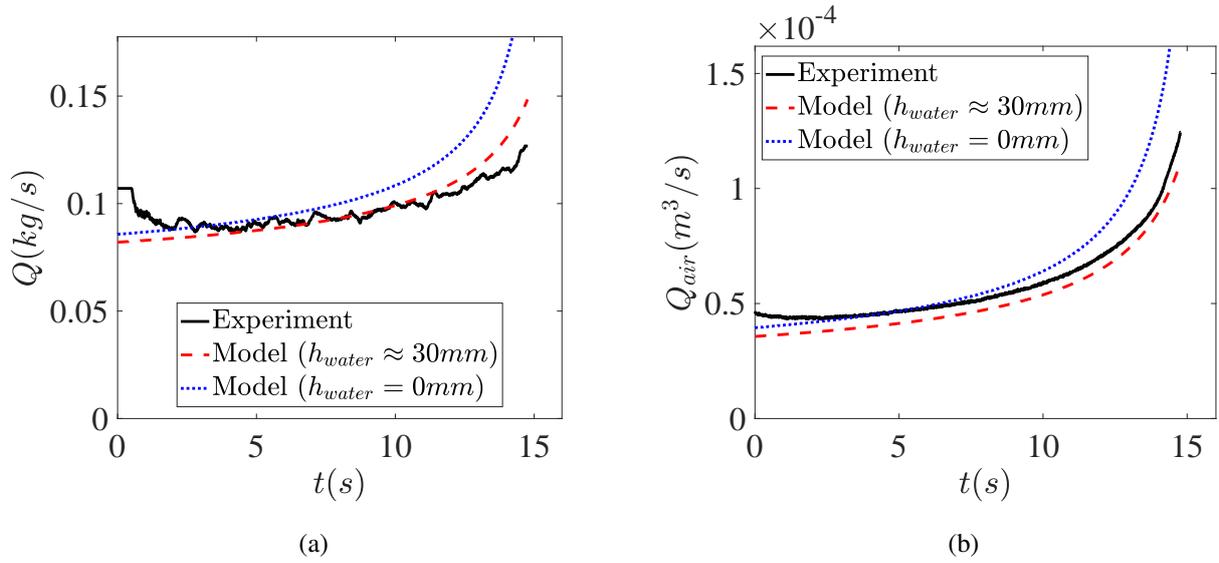
Figure 6.11: Discharge of the silo immersed in water for $L = 40mm$, $D = 10mm$, $d_p = 180\mu m$ (untreated ceramic particles) and $h_{water} \approx 30mm$: confrontation of the experimental measurements (black solid line) with the results predicted by the quasi-steady model with $\phi_0 = 0.44$, taking $h_{water} \approx 30mm$ (red dashed line) and $h_{water} = 0mm$ (blue dotted line), for (a) the temporal evolution of the discharge flow rate $Q(t)$ and (b) the volumetric gas flow rate $Q_{air}(t)$.

of the granular media Q from the silo as well as the volumetric gas flow rate Q_{air}, adjusting the parameter of the volume fraction at the outlet ϕ_0 and introducing the modified equation 6.2. Figure 6.11 illustrates a confrontation between the experimental measurements and the predictions obtained by the analytical model, with $\phi_0 = 0.44$ (see red dashed line) for the discharge flow rate of particles and the volumetric gas flow rate, for $L = 40mm$, $D = 10mm$, $d_p = 180\mu m$ (untreated ceramic particles) and $h_{water} \approx 30mm$. We observe that the model gives a fairly good prediction of the discharge of a silo immersed in water, considering the role of the surrounding liquid as a hydrostatic overpressure with respect to the atmospherical air pressure. Indeed, if we set $p^f_{outlet} = 0Pa$, we obtain an overestimation of the flow rates with the same coefficient $\phi_0 = 0.44$ (see the blue dotted line). Finally, we do not see any difference for the untreated and the hydrophobic particles.

6.2.3 Discharge of silo immersed in water with an instantaneous rupture of the outlet

Figure 6.12 illustrates a snapshot of the view nearby the outlet at the very beginning of the discharge, filmed by the high-speed camera at a frequency of 6000 frames per second, for $L = 40$mm, $D = 10$mm, $d_p = 180\mu m$ (hydrophobic ceramic particles) and $h_{water} \approx 80$mm. We observe that there is a large gas bubble ejected through the outlet, whereas the granular jet is mainly within this gas bubble.
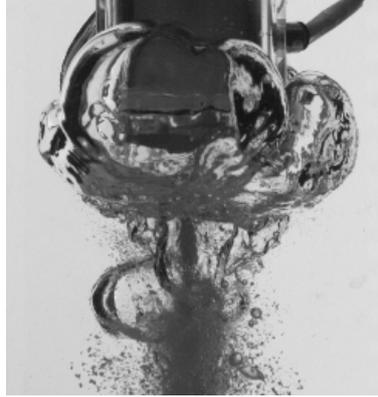
Figure 6.12: Snapshot of the discharge of a silo immersed in water with an instantaneous rupture of the outlet for $L = 40$mm, $D = 10$mm, $d_p = 180\mu m$ (hydrophobic ceramic particles) and $h_{water} \approx 80$mm.

According to the previous result with an imposed gas pressure at top of the silo, we expect that the role of the water will correspond to a hydrostatic overpressure, compared to the discharge on air. However the pressure being in the silo $p_{air} \gg p^f_{outlet}$ for the case of the silo discharge with an instantaneous rupture of the outlet, then we can neglect this hydrostatic overpressure during the pressurized gas period of the discharge. Thus, the quasi-steady model that we have developed in chapter 5 should describe such discharge flow for a silo immersed in the water, using the discharge flow rate for an opened top silo discharging on air, Q_0, as a reference.

Figure 6.13 illustrates a typical result of confrontation between the simplified quasi-steady unidimensional model (see section 5.3.3 of chapter 5), with the experimental measurements, for (a) the differential gas pressure at the top of the silo and (b) the discharge flow rate of the granular media, for $L = 40$mm, $D = 10$mm, $d_p = 190\mu m$ (untreated glass particles) and $h_{water} \approx 75$mm. Due to the agitation of the water in the tank by the gas bubble, we are able to follow the discharge flow rate of the granular media only at the beginning of discharge. The blue dotted line in Figure 6.13b indicates the particle discharge flow rate on air without gas injection. We observe a good agreement suggesting that in this experiment, the surrounding water does not plays a role during the pressurized period. However, the steady flow period, corresponding to a closed top silo is different due to the water imbibition. This leads to interesting behaviors that will be discussed in the perspective part.

(a)

(b)
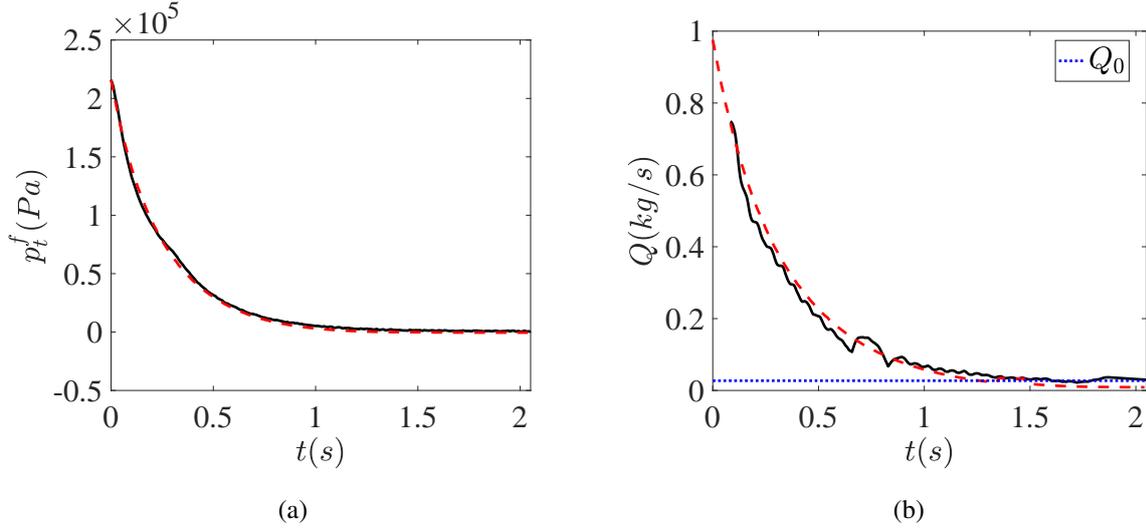
Figure 6.13: Confrontation between the experimental measurements (black lines) and the simplified quasi-steady model (red dashed lines) with $\phi_0 = 0.46$ for the discharge of silo with an instantaneous rupture of the outlet, immersed in water, for $L = 40$mm, $D = 10$mm, $d_p = 190\mu m$ (untreated glass particles) and $h_{water} \approx 75$mm. (a) Temporal evolution of the differential gas pressure at the silo top p_{top}^f. (b) Temporal evolution of the discharge flow rate of the granular media Q. The blue dotted line represents the discharge flow rate for an opened top silo and discharge on air, Q_0.
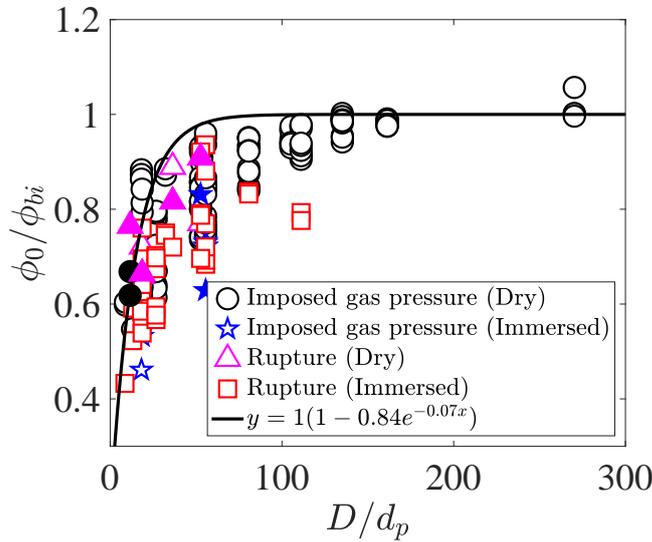
Figure 6.14: (a) Ratio between ϕ_0 obtained by the analytical model and the initial bulk volume fraction of the particles ϕ_{bi} as a function of the ratio D/d_p for different studies. The full symbols represent the results for the hydrophobic particles and the empty symbols for the untreated particles. The black line represent equation 2.24 of chapter 2 with coefficients: $\xi_\phi = 1$, $\alpha = 0.84$ and $\beta = 0.07$.

197

Finally, Figure 6.14 illustrates the ratio between ϕ_0 obtained by the analytical model and the initial bulk volume fraction of particles ϕ_{bi} as a function of the ratio D/d_p for different studies, including the silo discharge with an imposed gas pressure at the silo top and with an instantaneous rupture of the outlet, with the outlet immersed in water or in the open-air, for the hydrophobic particles (full symbol) and the untreated particles (empty symbol). The solid line represents the equation: $\frac{\phi_0}{\phi_b} = \xi_\phi G(D/d_p) = \xi_\phi \left[1 - \alpha e^{-\beta D/d_p}\right]$ with the coefficients obtained for the opened top silo discharging on air ($\alpha = 0.84$ and $\beta = 0.07$), with fitting $\xi_\phi = 1$. We observe a fairly good agreement for all these studies with various experimental conditions, which suggests that the dilation of the particles at the outlet is only due to geometrical effect.

We have finally developed a model which takes into account the transient discharge flow in water out of a silo driven by a compressible pressurized gas flow. In the following section, we will try to apply this model to the industrial case of interest.

6.3   Forecast of the discharge flow rate of the fuel fragments

To simulate the RIA case, several parameters should be taken into consideration, mainly including the breach surface S_0, the differential pressure within the fuel rod compared to the pressure at the outlet $p_{air} = P_{in} - P_{outlet}$ and the fuel fragment size d_p. These parameters could vary depending on the conditions of the accident: $S_0 \approx [10^{-5} - 10^{-4}]m^2$, $p_{air} \approx [1 - 100]MPa$ and $d_p \approx [20 - 1000]\mu m$. We chose the value $d_p \approx 50\mu m$ with $\beta_l \approx 10^{14}m^{-2}$ and $\beta_i \approx 10^{12}m^{-2}$. Note that the fuel rod has a density of $\rho_p \approx 10^4 kg/s$ and is about $H = 4$m long and $L = 1$cm diameter. We will investigate two extreme cases, one is for a small breach with a low internal pressure and the other one is for a large breach with a high internal pressure. First, we estimate the characteristic time of the establishment of the gas pressure gradient in the fuel rod $\tau \approx [1 - 10]s$ given by equation 5.12 in chapter 5. This characteristic time is much longer than that obtained in the experimental study, due to the large initial gas density in the fuel rod. Then the characteristic time of the granular flow establishment can be estimated by equation 5.51, giving $\tau_p \approx [10^{-3} - 10^{-2}]s$ and the characteristic time of the gas flow establishment given by equation 5.53, giving $\tau_f \approx [10^{-7} - 10^{-5}]s$.

Then we focus on the pressurized gas period, particularly at the very beginning of the rupture of the cladding, using the same framework than in section 5.4 of chapter 5 for the continuum simulation. Figure 6.15 illustrates the predictions by the model for a small breach $S_0 \approx 10^{-5}m^2$ and a low initial gas overpressure $p_{air} \approx 1MPa$, for the temporal evolutions of (a) the differential gas pressure at the top of the fuel rod p_{top}^f, (b) the height of fuel h_p, (c) the discharge flow rate of the fuel fragments Q and (d) the volumetric gas flow rate Q_{air}. The dotted line represents the discharge flow rate driven by gravity. Figure 6.16 shows the predictions for a more violent case with a large breach $S_0 \approx 10^{-4}m^2$ and a high initial gas pressure $p_{air} \approx 100MPa$. We suppose that the initial height of the fuel is $h_p^0 = 3.8m$ and the solver is stopped when reaching $h_p = 2.5m$ to
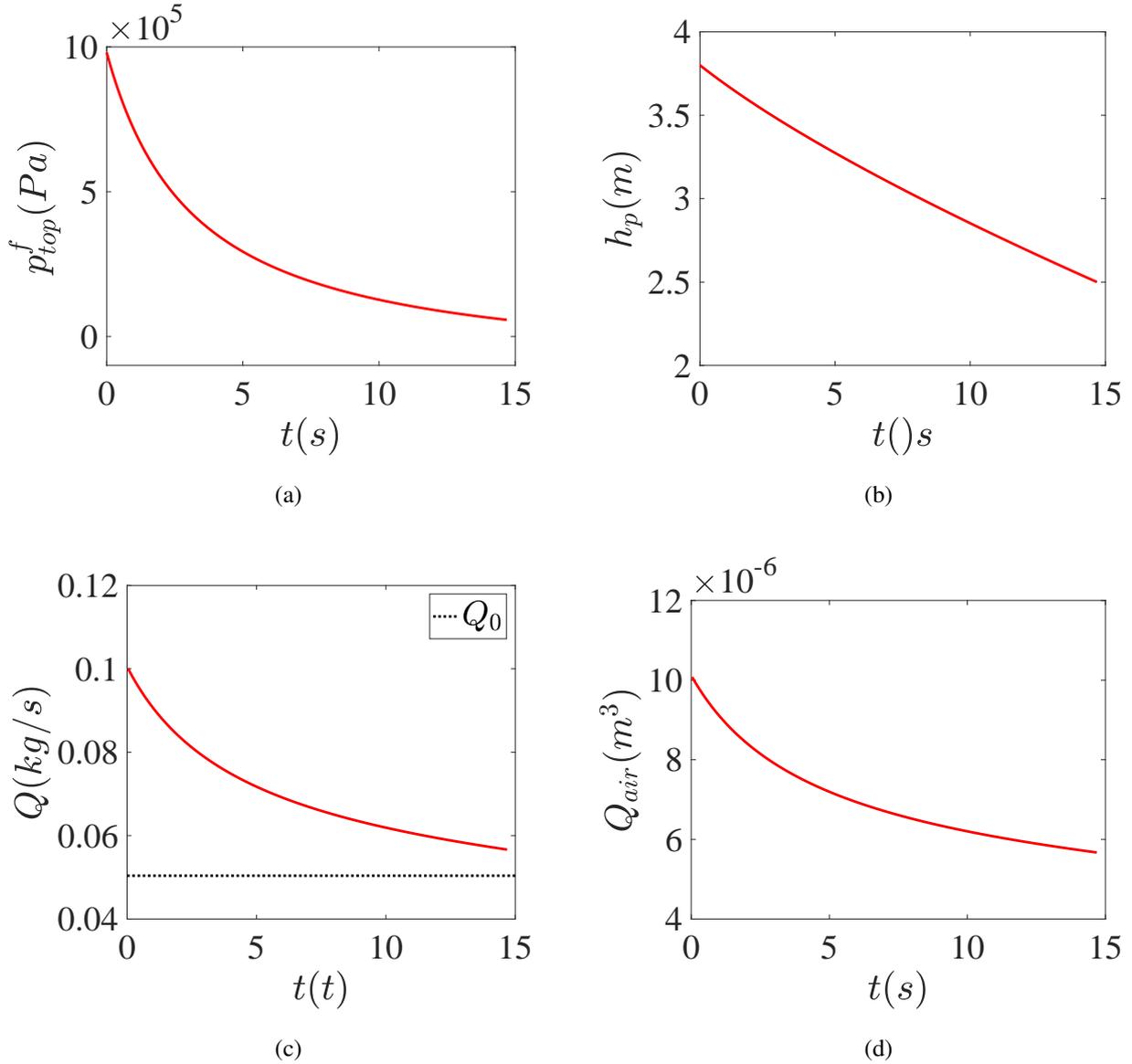
Figure 6.15: Prediction of the phenomena during a RIA scenario, for a small breach $S_0 \approx 10^{-5}m^2$ and a low initial gas pressure $p_{air} \approx 1MPa$. Temporal evolutions of (a) the differential gas pressure at the top of the fuel rod p_{top}^f, (b) the height of fuel h_p, (c) the discharge flow rate of the fuel fragments Q and (d) the volumetric gas flow rate Q_{air}.

compare these two cases. We observe the discharge with a larger breach and a higher initial gas pressure is much faster, around $0.8s$, and $15s$ for the small breach case. The model predicts an initial discharge flow rate of the fuel fragments for the large breach case, around $2kg/s$ which is more important than the small breach case, around $0.1kg/s$. For both cases, we observe that the volumetric discharge flow rate of the fuel rod Q/ρ is approximately to the volumetric gas flow rate Q_{air}, due to the low permeability of the media with $\beta_l \approx 10^{14}m^{-2}$.

For sure, this model is still quite rough, since the fragment material made of fuel particles can not be well represented by a collection of spherical particles of constant diameter. In reality, the
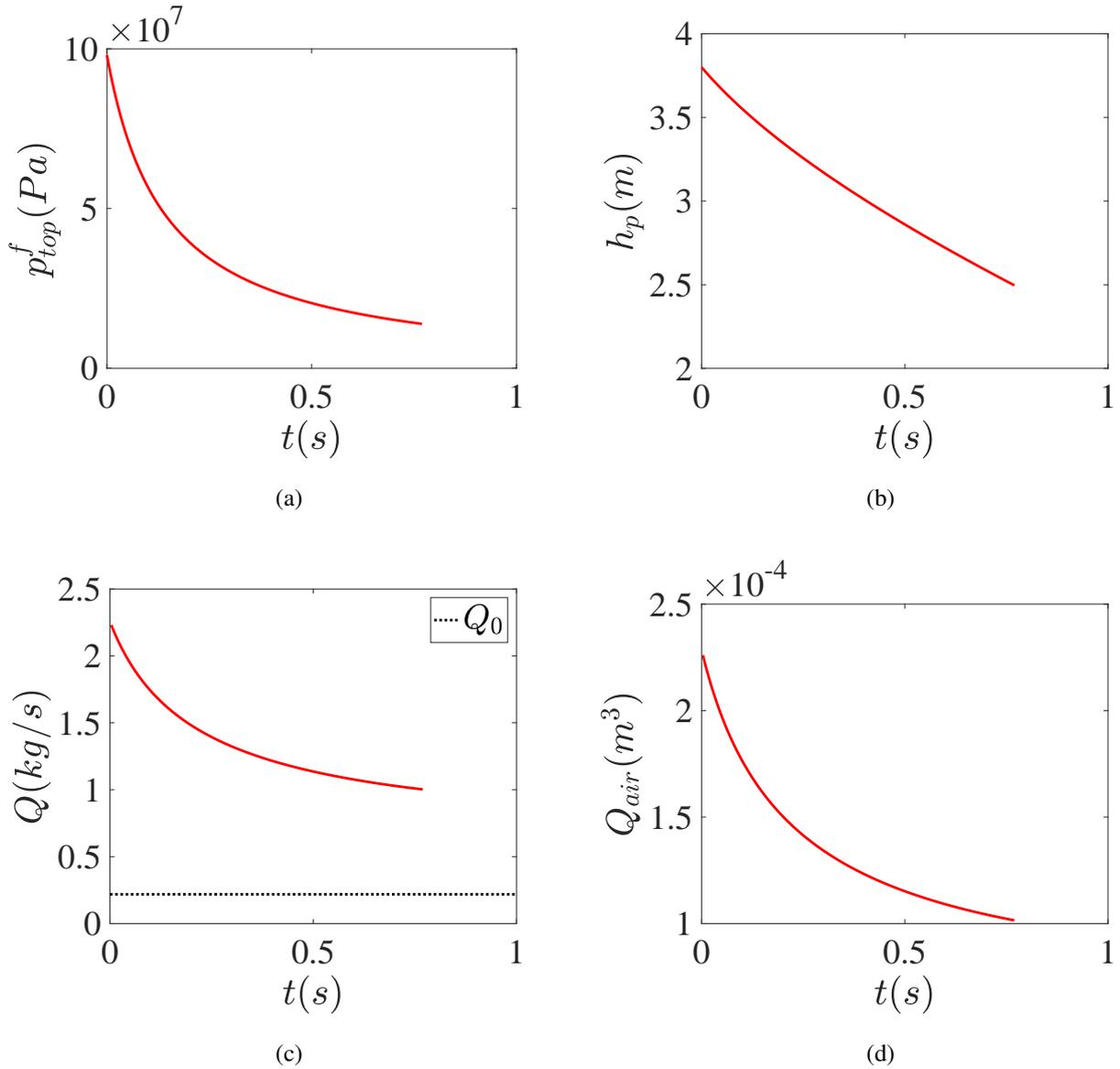
Figure 6.16: Prediction of the phenomena during a RIA scenario, for a large breach $S_0 \approx 10^{-4} m^2$ and a high initial gas pressure $p_{air} \approx 100 MPa$. Temporal evolutions of (a) the differential gas pressure at the top of the fuel rod p_{top}^f, (b) the height of fuel h_p, (c) the discharge flow rate of the fuel fragments Q and (d) the volumetric gas flow rate $Q_{air}/\sqrt{gL^5}$.

volume fraction of fuel within the granular media is very much larger than the one of a collection of spheres and the permeability of the fuel is relatively low. This first application provides nevertheless a first way to apply our understanding of the dynamics of particles and gas in the context of a RIA related fuel ejection out of a rod.

6.4 Conclusion and perspective

In this chapter, we have investigated the effect of a surrounding liquid on the discharge flow rate of a granular media out of a silo coupled with an injection air at its top, beginning with the simplest case of a constant air flow rate. We have shown that the flow rate is not modified by the surrounding liquid, but the liquid applies a hydrostatic overpressure at the outlet. In the case of an imposed gas pressure, we have shown that the unidimensional model developed in chapter 4 stays valid for an immersed silo if we take into account a hydrostatic overpressure. Finally, with a rupture of the outlet, we have shown that this hydrostatic overpressure is negligible compared to the internal pressure of the silo and the model developed in chapter 5 is still valid. Therefore, using this model we propose to give an estimation of the fuel fragments flow rate in case of a RIA.
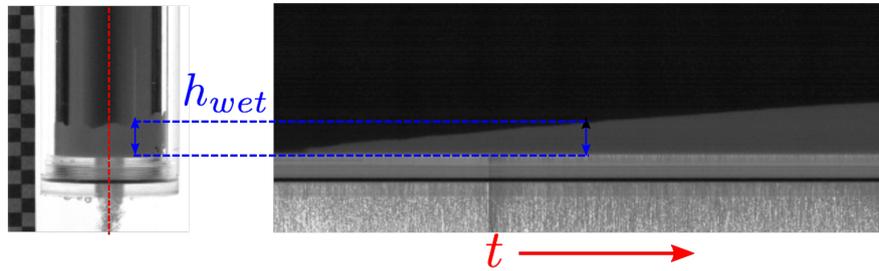

Figure 6.17: Experiment of the discharge of a silo without gas injection for $L = 40$mm, $D = 10$mm, $d_p = 180\mu m$ (untreated ceramic particles) and construction of spatiotemporal diagram.

In this chapter, we focus on the silo discharge with air injection where the water do not enter the silo. However, we performed few preliminary experiments on the discharge flow for an immersed silo without gas injection. The experimental setup was the same as previously, but we removed the gas injection system and we use a small water tank (cross section $12 \times 12 cm^2$) whose water level was not maintained constant during the experiment. Using untreated particles, with contact angle $< 90°$, we observe an imbibition of water in the silo together with the granular discharge. In Figure 6.17, we can see that the granular jet is quite dilute and that the particles are completely immersed in water. Using the high speed camera, we can construct a spatiotemporal diagram (see the right part of Figure 6.17), taking the central vertical line as a referential line, as shown by the dashed red line in the figure. We can thus obtain the temporal evolution of the water depth in the silo $h_{wet}(t)$, following the border between the black and the gray zones. We then deduce the water entrance velocity $u_{wet} = \frac{dh_{wet}}{dt}$.

In Figure 6.18, we plot in (a) the spatiotemporal diagram obtained by the high speed camera, following the temporal evolution of the granular column height h_p and the water depth in the silo h_{wet} for $L = 40$mm, $D = 10$mm, $d_p = 180\mu m$ (untreated ceramic particles) and $h_{water} \approx 150$mm, and in (b) the temporal evolution of the discharge flow rate Q/Q_0 (red solid line) normalized by the discharge flow rate for an opened top silo on air $Q_0 = 75g/s$ and h_{wet} (blue dotted line). During the experiment, the water level in the tank stayed quasi constant due to the small discharge
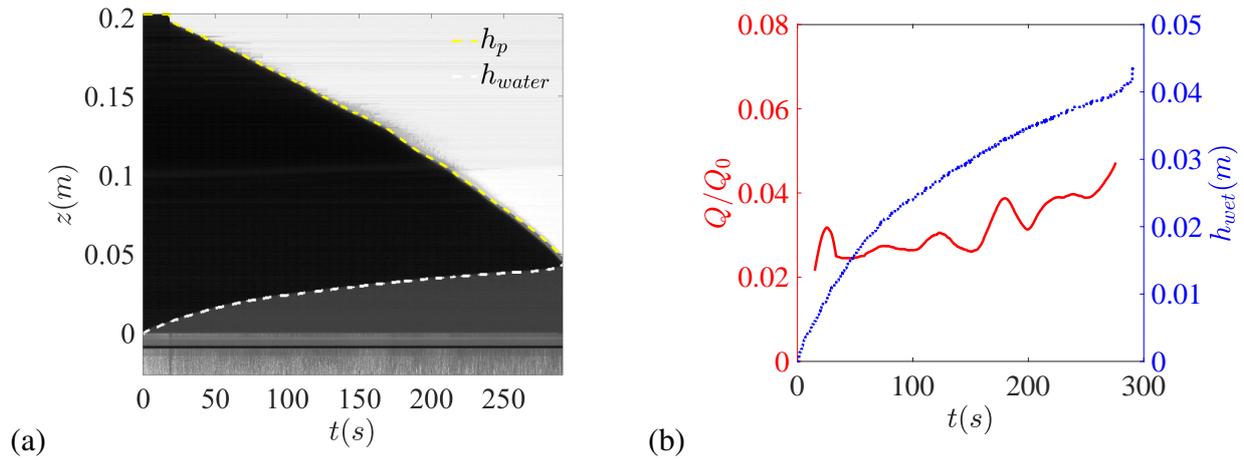
Figure 6.18: Discharge of a silo immersed in water, without gas injection: $L = 40$mm, $D = 10$mm, $d_p = 180\mu m$ (untreated ceramic particles) and $h_{water} \approx 150$mm. (a) Spatiotemporal diagram, following the granular column height, h_p (red dashed line) and the water depth in the silo, h_{wet} (blue dashed line). (b) Temporal evolution for the discharge flow rate of the granular media normalized by the discharge flow rate for an opened top silo on air Q_0 (red line) and the water depth in the silo (blue dotted line).

flow rate of the granular media. We observe that h_{wet} increases with time and tends to saturate as expected for a capillary imbibition. The particle flow rate is quite low (about $2g/s$) compared to the flow rate for an opened top silo on air Q_0 and tends to increase with h_{wet}. Following Saingier [2018], equation 2.40 predicts a velocity around $10mm/s$ and a flow rate around $40g/s$, which is one order of magnitude above the experimental observation. More work need to be done to understand this discharge flow regime.
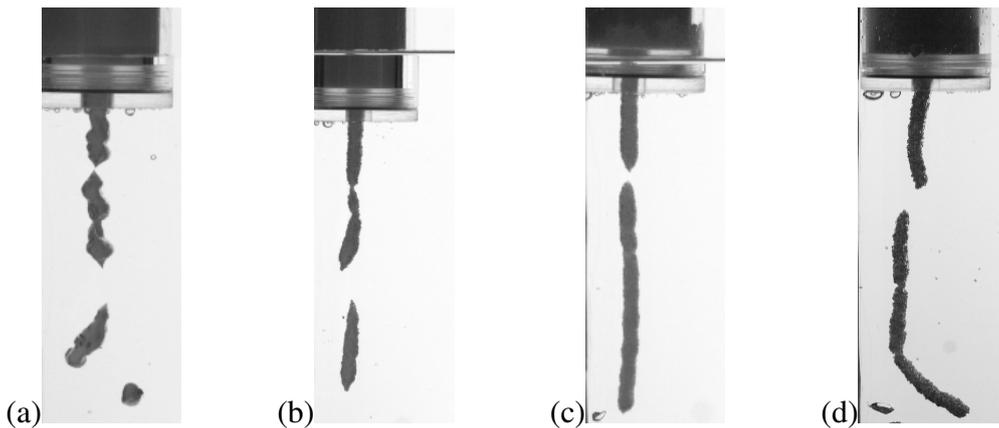

Figure 6.19: Snapshots of the granular jet at the outlet for the discharge of a silo with an outlet immersed in water and without gas injection, and for various hydrophobic granular materials: ceramic particles (a) $d_p = 180\mu m$ (b) $d_p = 550\mu m$ and glass particles (c) $d_p = 538\mu m$ and sand particles (d) $d_p = 864\mu m$.
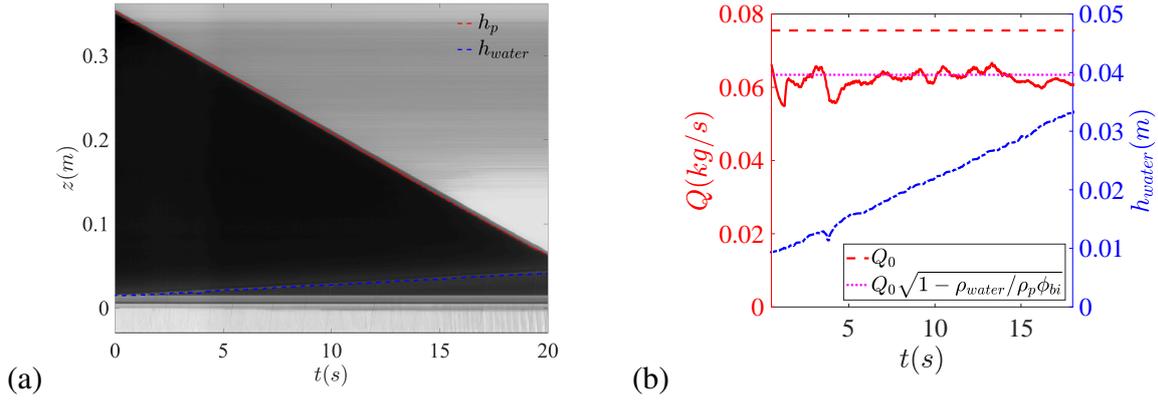
Figure 6.20: Discharge of a silo immersed in water, without gas injection, for $L = 40mm$, $D = 10mm$ and $d_p = 180\mu m$ (hydrophobic ceramic particles). (a) Spatiotemporal diagram, following the granular column height, h_p and the water depth, h_{water}. (b) Temporal evolution of the flow rate of granular media (red line) and water depth (blue line).
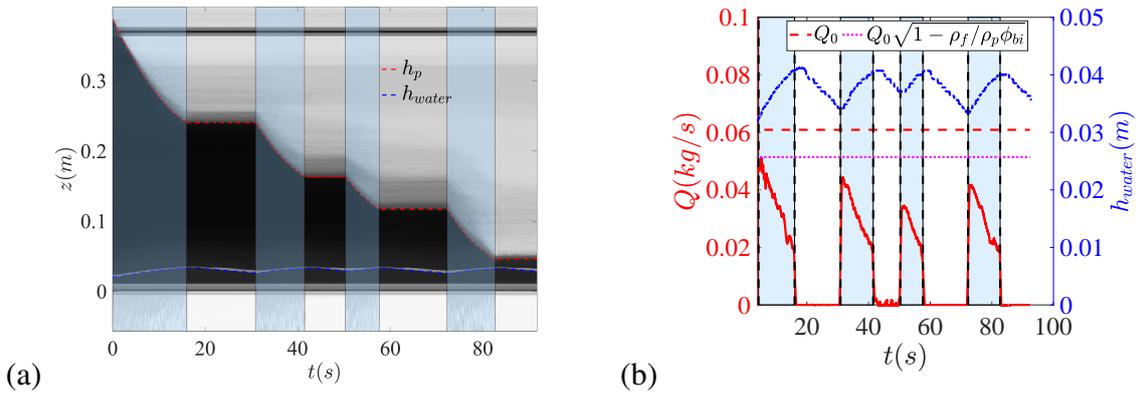
Figure 6.21: Discharge of silo immersed in water, without gas injection: $L = 40mm$, $D = 10mm$ and $d_p = 550\mu m$ (hydrophobic ceramic particles). (a) Spatiotemporal diagram, following the granular column height, h_p and the water depth, h_{water}. The blue marked zones represent the flowing periods. (b) Temporal evolution for the discharge flow rate of granular media (red line) and water depth (blue line).

If we now turn to the hydrophobic particles, we obtain a completely different behavior. In this case, there is no imbibition as long as $h_{water} < p_c/\rho g$. But we also observe that if $h_{water} > h_c$, where h_c is on the order of few centimeters, there is no discharge flow. We can think that the flow rate occurs only if the particle pressure at the outlet overcomes the water overpressure. Then for $h_{water} < h_c$, we observe a fast granular discharge, similar to the one in air. In Figure 6.19, we display some snapshots of the granular jet at the outlet for various granular materials and sizes. We observe a cylindrical granular jet, immersed in water but which remains completely dry. This jet tends to break into small pieces of length that is several times of the jet diameter.

For small particles (see Figure 6.20), we observe a constant flow rate which is well adjusted if we consider the buoyancy force of the liquid on the granular media (see the purple dotted line),

through an effective gravitational acceleration: $g(1 - \rho_{water}/\rho_p \phi_0)$. Therefore, the mass flow rate of the granular media can be written with the following expression, considering the flow rate Q_0 with an opened outlet on air:

$$Q = Q_0 \left(1 - \frac{\rho_{water}}{\rho_p \phi_0} \right)^{1/2} \tag{6.3}$$

For bigger particles (see Figure 6.21), we observe an interesting hysteresis behavior: during the discharge, the water level increases while the particle flow rate decreases, then when reaching a critical value $h_{water} > h_{c2}$, the discharge flow suddenly stops. We can reproduce this behavior by sucking water out of the reservoir. These behaviors are beyond the scope of this PhD thesis but represent interesting perspectives of studies.

Chapter 7

Conclusions and perspectives

Following the work carried out by Zhou [2016], in order to model the dynamics of the gas and particle ejection following the rupture of a nuclear fuel rod, we chose to study a simplified configuration at the laboratory scale, considering the discharge flow of a granular media out of a pressurized silo. The fuel fragments are idealized as a granular media and modeled by a collection of particles of several materials (spherical glass or ceramic beads, sand grains) mostly monodisperse in size, but also a bidisperse mixture.

Concerning the role of the lateral position of the orifice, particular for the case of the opening of the clad of a fuel rod, we have first investigated the role of the acceleration and the friction (internal and lateral) on the discharge flow rate of a granular media from a silo, using a non-conventional geometry: that is relevant for the fuel rod problematic, a rectangular silo with an inclined bottom which ends up at a lateral outlet. Experimentally, different parameters have been varied, including the size of the outlet D, the particle diameter d_p, the thickness of the silo W and the inclination angle of the silo bottom θ_i. A continuum simulation with a $\mu(I)$ frictional rheology has been performed to recover the experimental observations. We have shown that the flow-rate is controlled by two phenomena. For lateral aperture with a horizontal bottom, two regimes of flow exist depending on the aperture aspect ratio D/W and resulting from the competition between wall friction and internal friction. This controls the orientation of the granular flow that leads to deviate toward the outlet. In the geometry of interest when varying the bottom inclination, two flow regimes have also been identified. For small angles of inclination the flow is not perturbed by the bottom and the central streamline orientation is controlled by the outlet aspect ratio D/W. The second regime is observed for large inclined angles where the flow orientation is imposed by the bottom inclination. Then we have shown that the outlet corresponds to an area where the grains are accelerated, the potential energy being transferred to kinetic energy. However this balance and thus the magnitude of the velocity at the center of the outlet was found to be quite sensitive to the silo geometry, the granular rheology and the boundary conditions. Finally, we present a phenomenological model that predicts the discharge flow rate of particles from a rectangular silo with an inclined bottom according to its aperture aspect ratio with a good agreement in the

asymptotic regimes.

Secondly, we have investigated experimentally the discharge of a silo coupled with an imposed air overpressure at the top of a cylindrical silo. We observed that an imposed air overpressure generated an increase of the particle flow rate with time together with the air flow rate, as the height of the granular column decreases during the discharge. Following the work carried out by Zhou [2016], who has studied the steady discharge of a silo with injection of a constant gas flow Q_{air} at the top of the silo, we found that the discharge flow rate of granular media can be described by a modified Hagen-Beverloo law, which considers term the gas pressure gradient near the outlet as an additional driving force to gravity. We validated that the interaction drag force between the two phases can be well described by the Darcy-Forchheimer resistance law. In the range of gas pressure explored, we have shown that the fluid phase relaxes instantaneously which means that the inertial term can be neglected with respect to the drag force between the two phases. Then we have proposed an analytical model based on a continuum two-phase modelling with granular frictional rheology and the modified Hagen-Beverloo law with the Darcy-Forchheimer resistance law between the phases which accounts quite well for the experimental data. Additionally, we have shown the fluid-grain coupling depends mainly on the permeability of the granular media. The model is valid for all particle types, namely the spherical glass or ceramic particles, the sand particles with an angular shape and as well as the bidisperse mixture if we take the Sauter diameter. Finally, we have fully solved the continuum modelling using numerical simulations in a 3D axisymmetric configuration and we have validated most of the assumptions of the analytical model.

In the industrial case, the pressurized gas and the granular media are suddenly (following the clad failure) into contact with a surrounding lower pressure domain, that adds an unsteady process to the flows. To be more realistic with the configuration of interest, we have carried out a study on the effect an instantaneous rupture of the silo outlet. A fast break of an aluminum foil at a critical pressure level around 3bar allowed to simulate this sudden rupture. Three discharge periods were observed during the silo discharge: the establishment of the gas pressure gradient, the pressurized gas discharge and the steady flow periods. We find that the characteristic time of establishment of the gas pressure gradient depends particularly on the permeability of the granular flow, being shorter for a more permeable granular media. Then during the pressurized gas discharge, we observed first a very high particle flow rate, corresponding to high particle velocity at the outlet. Then the discharge flow rate decreases rapidly together with the gas pressure to reach the steady flow period. This steady flow corresponds to a closed top silo with a counter current flow. To describe the whole discharge, we have developed an unidimensional model which takes into account the air compressibility. This model gives a fairly good prediction of the experimental observations. Then we resolved numerically a full two-phase continuum modelling considering a compressible fluid and a granular rheology. This model reproduces well the experimental observation and allows to validates some of the hypothesis of the analytical unidimensional model. Finally, an instability of

the granular jet is observed for the smallest particles and we have discussed the mechanism which could lead to such phenomena.

In the situation of interest, the fuel rod is immersed in pressurized water, thus in the RIA scenario, hot fuel fragments will discharge in a liquid. To understand the effect of the surrounding liquid on the discharge flow rate of the granular media, we have carried out a study of discharge of a silo by immersing the silo outlet in water, with three configurations of gas injection. Additionally, hydrophobic particles have also been used to mimic the effect of the hot temperature of the fragments which tend to have a vaporized gas layer around them. In the case of imposing a constant air flow rate Q_{air} at the top of the silo, we have shown that the flow rate of the granular media is not modified by the surrounding liquid, but the liquid applies a hydrostatic overpressure at the outlet. In the case of an imposed gas pressure at the silo top, we have shown that the unidimensional model developed for the case with the outlet in air is still valid if we take into account hydrostatic overpressure. Finally, with a rupture of the outlet immersed in water, we have shown that this hydrostatic overpressure is negligible with respect to the internal pressure of the silo and the model developed for the open-air outlet case stays valid. In addition, we have propose a forecast of the discharge flow rate of the fuel fragments in the RIA case.

This PhD thesis brings some elements to model the granular discharge with a lateral orifice or coupled with an unsteady gas flow. Nevertheless, many questions remain open during this work.

- During the study of the effect of inclined bottom on the discharge flow, the continuum modelling was shown to be the good framework to describe the discharge flow of a granular media from a silo, and in future work it will allow to perform a full parametric study of the influence of the rheological parameters on the analytically predicted flow rate in various geometry. It may therefore, reduce the empirical parameters in the flow rate scaling law to the geometrical and materials related parameters that could be inferred from more simple experiments (allowing to determine the $\mu(I)$ rheological parameters). In particular these results may have practical interest considering the effect of the hopper angle for an industrial silo. In addition, we observed a different behavior between the 2D mono-layer experiments and the DEM simulations, particularly for the magnitude of the velocity at the center of the outlet. To understand this difference, more DEM simulations should be envisaged for example, a complete 3D simulation which takes into account the friction at the front and rear walls.

- For the discharge of a silo with an instantaneous rupture of the outlet, we have shown that the characteristic time of establishment of the gas pressure gradient τ depends not only on the permeability of the granular media, but also on the initial granular column height h_p^0 and the gas density ρ_f. Therefore additional experiments for example varying h_p^0 or using a denser gas could be viewed as perspective to further validate the scaling of τ. From a point of view of numerical simulation, a complete two-phase simulation considering the fluid phase as a

compressible media could be envisaged to validate the model. To explain more precisely the instability of the granular jet at the outlet at the very beginning after the outlet rupture, more experimental work need to be done, for example varying more largely the silo and the outlet dimensions to verify the occurrence of this instability.

- For the discharge of a silo with outlet immersed in water and without gas injection, we have observed a constant flow rate for small particles independently on the water level in the tank, contrary to bigger particles where we observe a hysteretic behavior with the water level. This behavior is interesting to study experimentally and theoretically, for example controlling more precisely the surface property of the granular media, varying the outlet size and keeping the water level constant in the tank during the discharge.

- On the basis of this PhD work, we have clearly identified the role of gas compressibility, gas pressure gradients near the outlet, permeability of the granular media, geometry of the cylindrical rod, size and position of the outlet, as well as outside environment on the discharge flow rate of granular media out of a pressurized elongated silo. This work provides therefore a solid basis for developing evaluation of fuel fragments ejection in a RIA case. Nevertheless some aspects are still quite rough in the model for the fragmented fuel as a granular media due to its wide size distribution and its high compaction. More experimental and theoretical research need to be done to predict such complex condition.

Appendices

Appendix A

Discrete simulations for the discharge of a silo with a lateral orifice and an inclined bottom for 2D flow

In this appendix, we test the ability of a discrete 2D simulation, corresponding to an infinite thickness configuration (no friction of the front and the rear walls), to reproduce the experimental results obtained with a monolayer.

A.1 Methods

We simulated an infinite thickness configuration using the contact dynamics method implemented in the *LMGC90* software (Dubois et al. [2011]). As shown in Figure A.1a the two-dimensional silo consists of a rectangular silo of width $L = 3D$ bounded by two vertical walls and an inclined bottom with a variable angle $\theta_i \subset [0; 20; 40; 60; 70]$ which ends up at the lateral outlet delimiting the outlet of size D which can be varied $D \subset [40; 45; 50; 55; 60]$ mm. The silo is initially filled using a random deposition with a height $h_p = 18D$ of spherical particles of mean size $d_p = 4.2$ mm $\pm 10\%$ (density $\rho_{ps} = 100$kg.m^{-3}). We considered that the particles are perfectly rigid and inelastic, their contact dissipation is modelled in terms of a friction coefficient that we set to $\mu_p = 0.4$ between the particles and to $\mu_w = 0.5$ between the particles and the walls (Radjai and Dubois [2011]).

For comparison with the laboratory experiments the data are analyzed similarly to a monolayer flow in a silo of thickness $W = d_p$. After the preparation phase the initial bulk particle volume fraction was obtained by considering the surface average, σ, of the particle indicator function (whose value is 1 on the particles and 0 otherwise) over the central zone of the silo, with $\phi = 2\sigma/3$. Then simulations are run with a time step of $\delta t = 0.0005$ s for a number of time steps $N_t = 8000$. The computational domain is periodic in the vertical direction to keep constant the number of particles (see Zhou et al. [2015] for more details). A snapshot of all particle positions

and velocities was recorded every twenty time steps. From these snapshots, the instantaneous flow rate, $Q_i = \rho_p/\rho_{ps}(\sum_{\Delta t} 2S_p d_p)/(3\Delta t)$ was obtained by measuring the surface of particles leaving the silo during $\Delta t = 0.2$ s and calibrating with the experimental particle density (ρ_p). Similarly to the experiments, we observed a steady-state regime of discharge and the steady flow rate Q was obtained by time averaging the instantaneous flow rate during this stationary state.

(a)   (b)
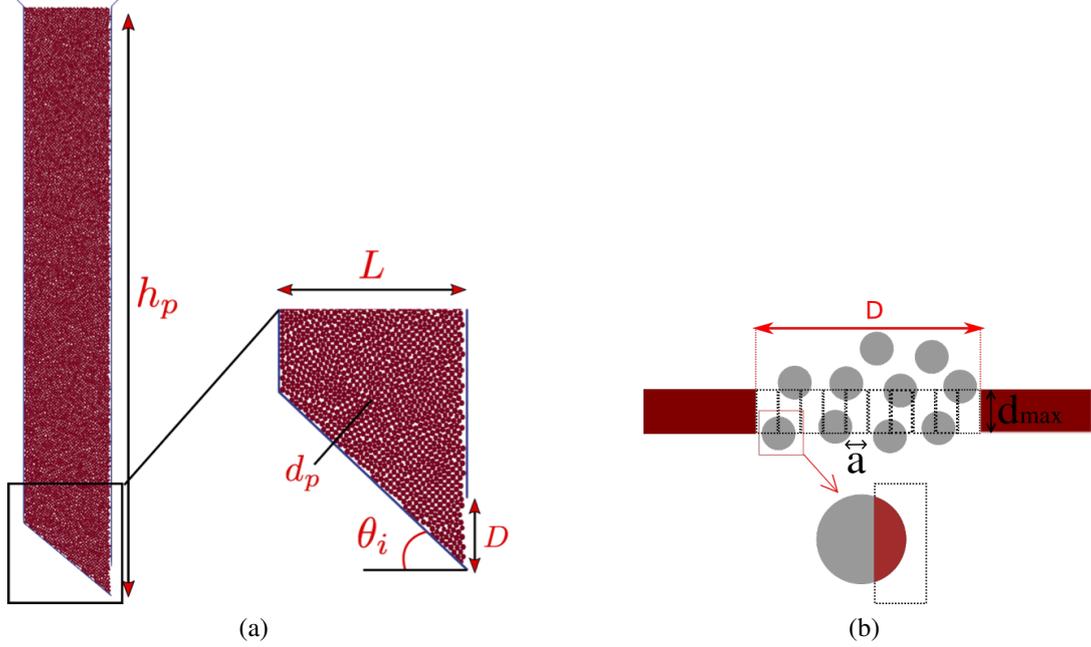
Figure A.1: (a) Simulated silo. (b) Schematic view of the calculation for the volume fraction and the velocity profile at the outlet.

The volume fraction of particle at the outlet is an important measurement in our simulation. Following the ergodic theory, the mean value of volume fraction is the spatial and temporal mean of the particle indicator function. A rectangular area at the outlet of dimension $d_{max} \times D$ is chosen for calculating the mean volume fraction, shown in Figure A.1b, where d_{max} is the maximum diameter of particles. This rectangular area is divided in several smaller rectangular boxes of side $a = 0.2 d_{max}$ and of height $h = d_{max}$. For each time step and for each box area, the intersection surface between particles and boxes is determined, note s_j^i. Afterwards, we calculate the sum of intersection surfaces in time, divided by the sum of the whole box area in time to obtain the mean value of volume fraction, given by: $\phi_k = \sum_{i=1}^{N_t}(\sum_{j=1}^{N_p} s_j^i)/\sum_{i=1}^{N_t} ah$, where N_t represents the number of time step to average, N_p represents the number of particles intersecting with box k at time step i and s_j^i is its intersection surface.

Following the same steps, the mean velocity profile of particle at the outlet is obtained by averaging the individual particle velocity weighted by the intersection surfaces for each time step et for each calculation box area, given by: $v_k = \sum_{i=1}^{N_t}(\sum_{j=1}^{N_p} s_j^i v_j^i)/\sum_{i=1}^{N_t}(\sum_{j=1}^{N_p} s_j^i)$, where v_j^i represents the individual velocity of particle j at time step i.

A.2 Results and discussion

Figure A.2 shows the evolution of the flow rate with the bottom inclination and the outlet size. We observe that similarly to the monolayer experiment, as soon as $\theta_i > 20°$ the flow rate decreases when increasing the angle of inclination of the bottom of the silo. For a given θ_i each curve can be adjust by equation 3.3, with a fitting parameter c_D which depends on θ_i. However we do not recover the slight increase of the flow rate with θ_i for small bottom inclination.
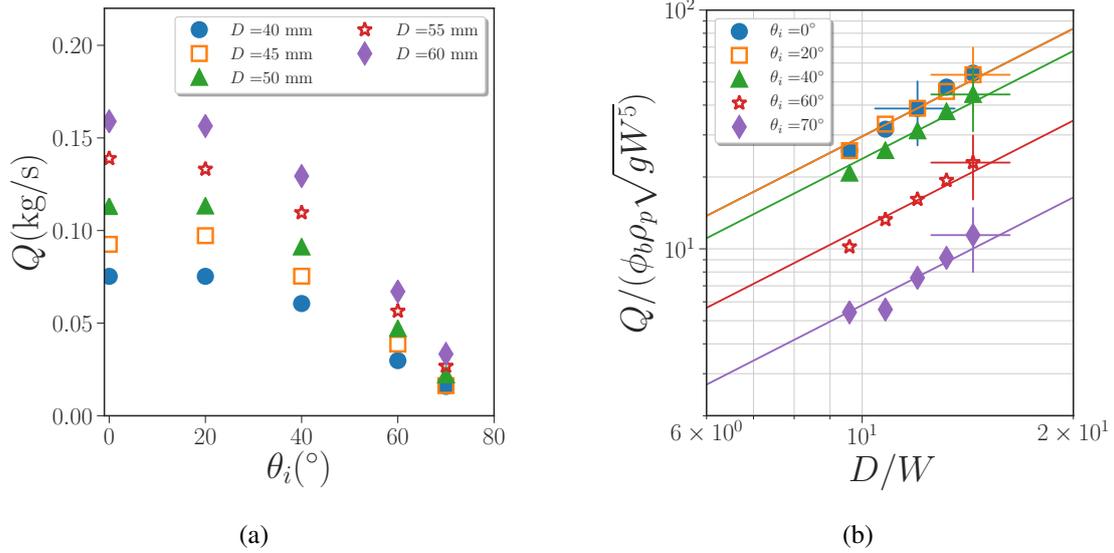

Figure A.2: (a) Mass flow rate of particles as a function of the bottom angle of inclination θ_i for several outlet size D. (b) Mass flow rate of particles made dimensionless by $\phi_b \rho_p \sqrt{gW^5}$ versus the dimensionless outlet size D/W. The full lines represent the Hagen-Beverloo equation 3.3 with the fitting parameters c_D which depends on θ_i.
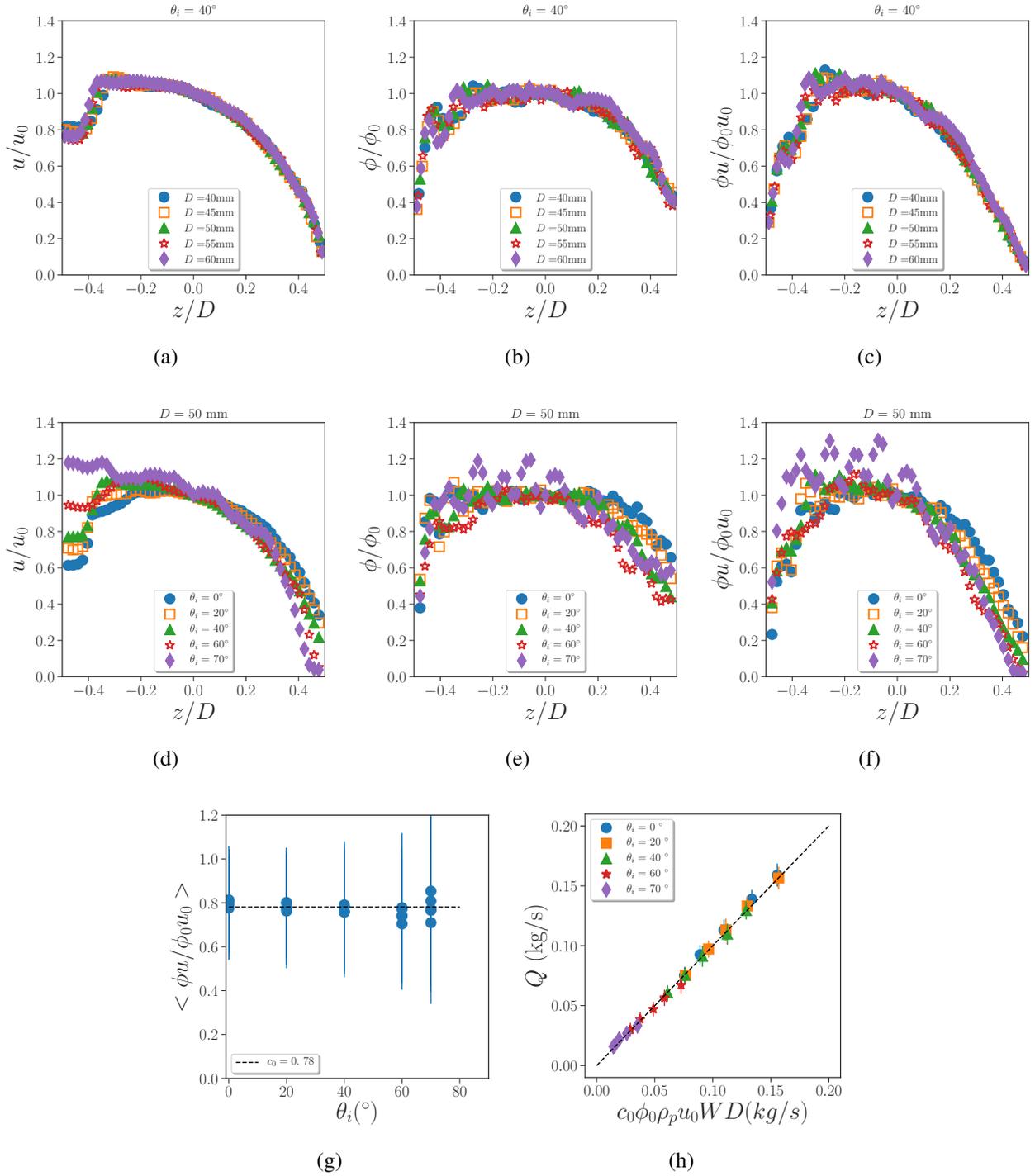
Figure A.3: Normalized profiles at the outlet for (a, d) the horizontal velocity, (b, e) the volume fraction profiles, and (c, f) ϕu, versus the vertical position normalized by the outlet size z/D for (a, b, c) $\theta_i = 40°$ and several outlet sizes D, (d, e, f) $D = 50$ mm and several bottom inclinations θ_i. The vertical position, z, is oriented upward and its origin is taken at the centre of the outlet. (g) Mean value of the normalized profiles of ϕu versus the bottom angle of inclination for all the experiments. The horizontal line represents the mean value $c_0 = 0.78$. (d) Experimental flow rate versus $c_0 \phi_0 \rho_p u_0 W D$ for all the data. The dashed line represents equation 3.5.

In Figure A.3 we have plotted the normalized profile of the horizontal velocity u/u_0, the volume fraction ϕ/ϕ_0 and $u\phi/u_0\phi_0$. We recover the same characteristic than observed in the experiments (see section 3.2.1) with a sliding velocity at the bottom. A slight difference is that in the DEM this sliding velocity increases with the bottom inclination. The profiles are seen to be rather self-similar and the flow rate is well adjusted by equation 3.5 with c_0 = 0.78. The inclination and the magnitude of the velocity profiles, plotted in Figure A.4 are also found to be rather self-similar and comparable to the experimental profiles.
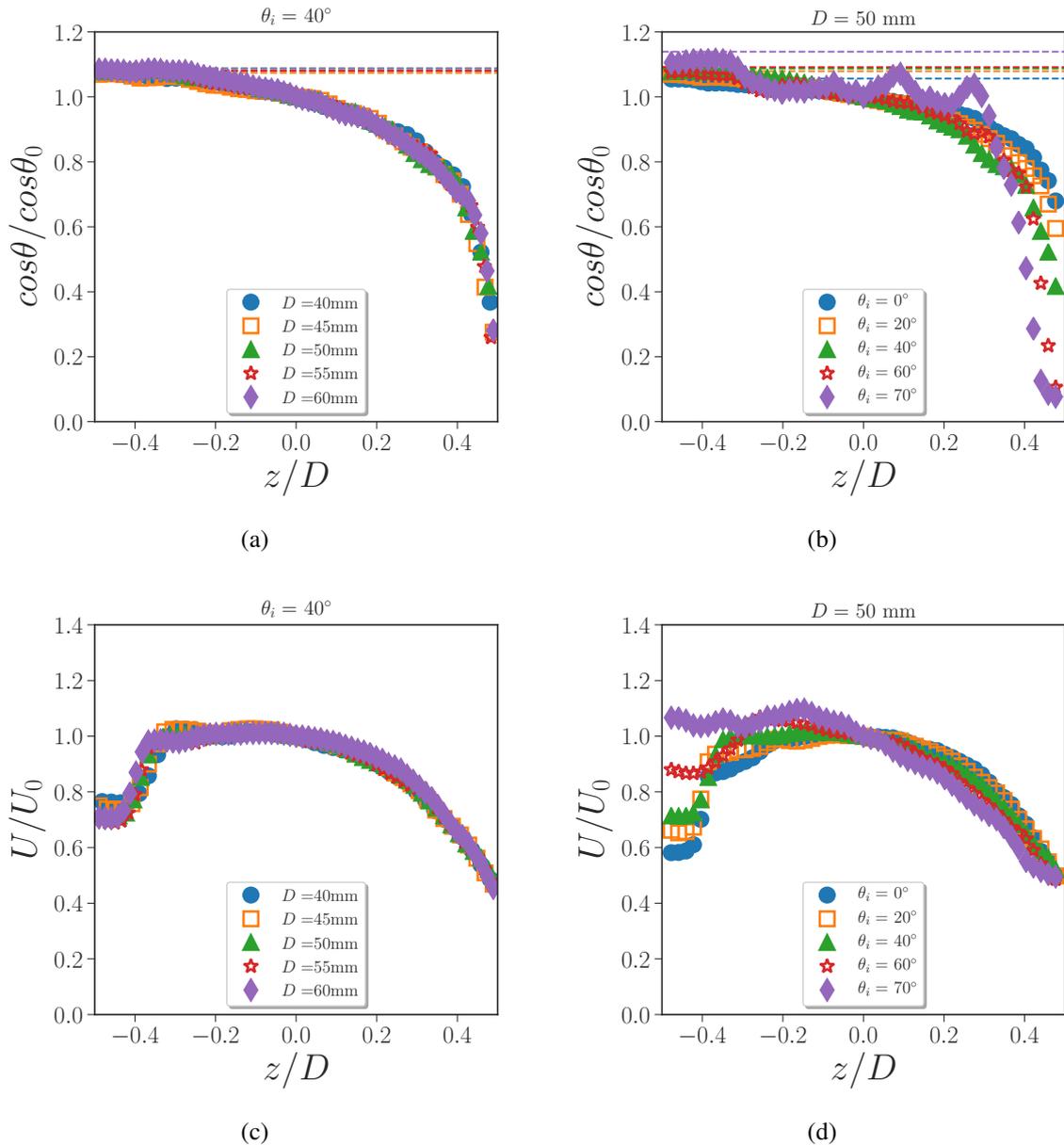
Figure A.4: Normalized profiles at the outlet for (a,b) the cosine of the angle of inclination and (c,d) the magnitude of the velocity, versus the normalized vertical position normalized z/D for (a,c) $\theta_i = 40°$, and several outlet sizes D and (b,d) $D = 50$ mm and several bottom inclinations θ_i. The horizontal dashed lines correspond to the imposed angle of inclination $\cos\theta_i/\cos\theta_0$.
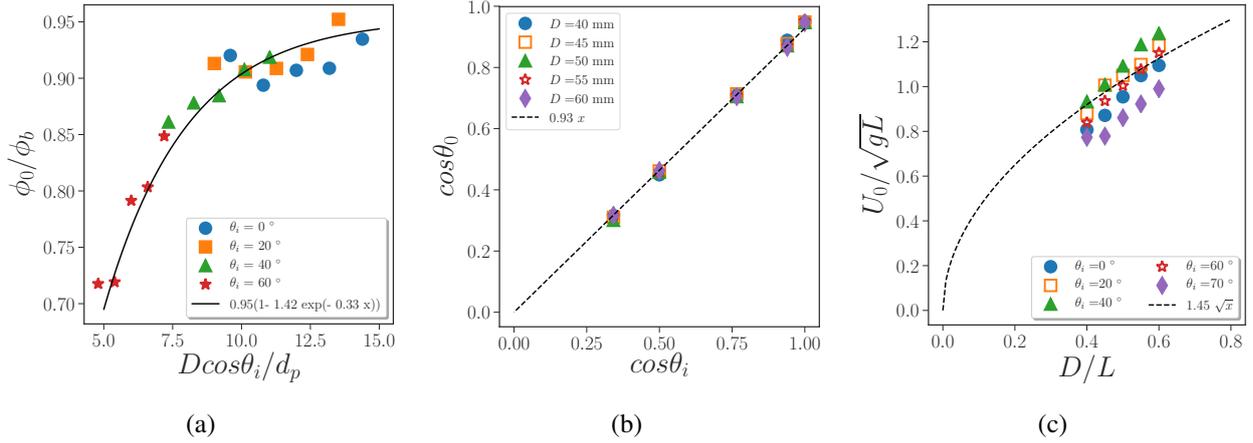
Figure A.5: (a) Volume fraction at the centre of the outlet ϕ_0 normalized by the bulk volume fraction ϕ_b versus the outlet size D normalized by $d_p/\cos\theta_i$, for various bottom inclination. The black line represents equation 3.6. (b) Inclination of the central streamline at the outlet, $\cos\theta_0$ versus $\cos\theta_i$. The dashed black line represents equation 3.8 with $\zeta = 0.93$. (c) Magnitude of the velocity profiles at the centre of the outlet, U_0, normalized by $\sqrt{gL}$ versus the outlet size D normalized by L for several outlet inclination θ_i. The dashed line represents equation 3.11 with $c_E = 1.45$.

Regarding the flow characteristic at the central streamline of the outlet, we first observed in Figure A.5a that there is a dilatation of the granular media at the outlet and the volume fraction ϕ_0 is well adjusted by equation 3.6 with $\xi_\phi = 0.95$, $\alpha = 1.42$ and $\beta = 0.33$ in good agreement with the experimental observations. Concerning the streamline orientation, when the bottom is horizontal, we measure $\theta_0^f = 18.5°$ close to the angle of friction $\delta = \text{atan}(\mu_p) = 21.8°$. Then we can see in Figure A.5b that similarly to the experiment the inclination of the flow is well described by equation 3.8 with $\zeta = 0.93$. The evolution of the inclination of the central streamline at the outlet can then be represented by equation 3.9. However, due to the fact that $\cos\theta_0^f/\zeta > 1$ equation 3.10 is not valid and we can consider that the critical angle at which the transition occurs $\theta_c = 0$ and that there is no plateau regime in this simulation.

The main difference between the DEM simulation and the mono-layer experiments lay in the magnitude of the velocity on the central streamline at the outlet. In the experiment this velocity was varying with the bottom inclination 3.12, whereas in Figure A.5c we can see that U_0 does not sensibly depends on θ_i. The data can be adjusted by equation 3.11 with $c_E = 1.45$. We do not have justification on this change of behavior. It may be linked to the fact that the mono-layer flow is not a true 2D flow but encounter friction at the front and rear wall, or it may be due to boundary condition at the bottom wall. New DEM simulation testing this hypothesis should answer this question.
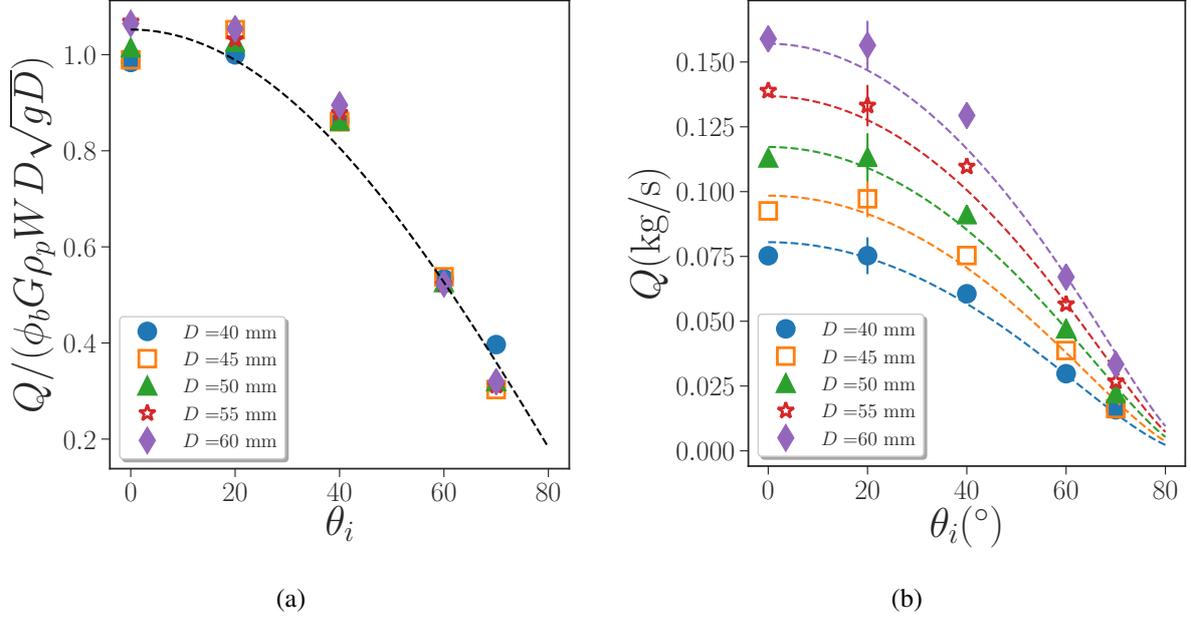
Figure A.6: (a) Mass flow rate normalized by $\rho_p \phi_b G(\frac{D\cos\theta_i}{d_p})DW\sqrt{gD}$ and (b) Mass flow rate, versus the bottom angle of inclination. The dashed lines represent equations 3.13 with $\xi_\phi = 0.95$, $\alpha = 1.42, \beta = 0.33, \zeta = 0.93, c_E = 1.45, c_0 = 0.78$.

We can thus adapt the simple model (equation 3.13) to this DEM simulation to predict the flow rate:

$$\frac{Q}{\rho_p \phi_b G(\frac{D\cos\theta_i}{d_p})DW\sqrt{gD}} = c_\theta \cos\theta_i \tag{A.1}$$

with $G(x) = \xi_\phi(1-\alpha e^{-\beta x})$, $c_\theta = c_0 c_E \zeta$. In Figure A.6 we compare the DEM results with equation A.1 and we obtain a fairly good agreement. The DEM simulation will be a really interesting tool to see the effect of the grain and wall parameters (μ_p and μ_w) on the flow rate, when the reason of the discrepancy of the behavior of the magnitude of the flow rate will be found.

Appendix B

Discharge flow from a lateral orifice with an inclined bottom: Continuum simulation with a free slip condition

The wall not being rough, we expect that the real condition at the wall is not a no-slip condition but a slip condition with a particle-wall friction coefficient. However this condition has still to be implemented in Basilisk. For simplicity and to verify if there is an influence of the boundary condition on the flow rate, we will consider the extreme limit of a free slip condition at the bottom wall which corresponds to a null particle-wall friction coefficient. On the other walls we kept a no slip condition to vary only the condition at the bottom wall. The various profiles at the outlet are still found to be self-similar as can be seen in Figures B.1 and B.2, the main difference with the previous condition is that the velocity at the bottom of the outlet is not zero leading to a strongly asymmetric shape. This velocity profile shape does not correspond to the experimental profiles (Figure 3.22) however in the experiment we do not depart a lot from the free flow with a large stagnant zone corresponding to a no-slip boundary.
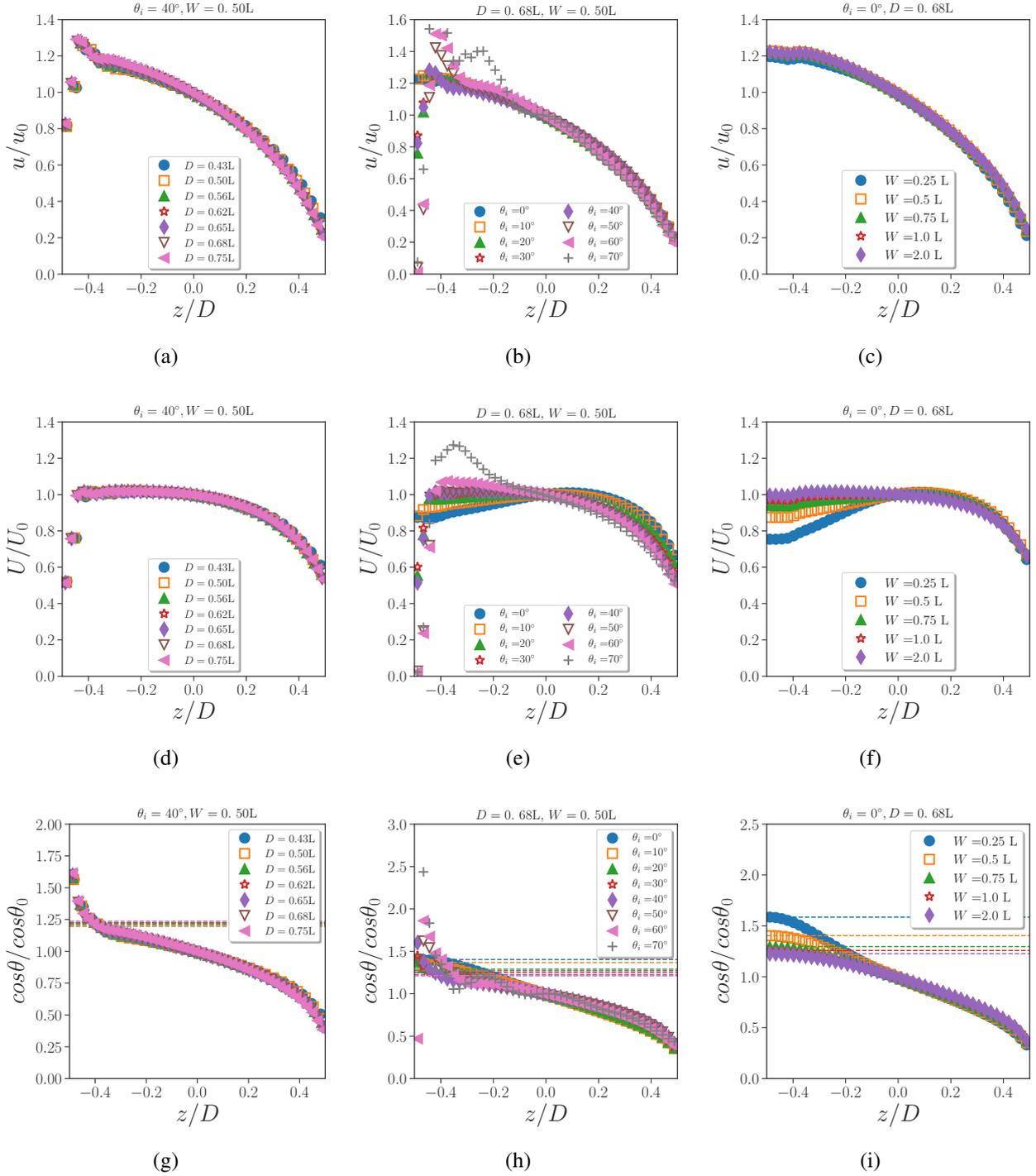
Figure B.1: Continuum simulation with Free slip condition: Profiles of (a,b,c) the horizontal velocity, (d,e,f) the magnitude of the velocity and (g,h,i) the cosine of the angle of inclination, normalized by the value at the centre of the outlet, with (a,d,g) $\theta_i = 40°$, $W = 0.5L$ and several outlet diameters D, (b,e,h) $D = 0.68L$, $W = 0.5L$ and several outlet inclinations θ_i and (c,f,i) $\theta_i = 0°$, $D = 0.68L$ and several silo thicknesses W.
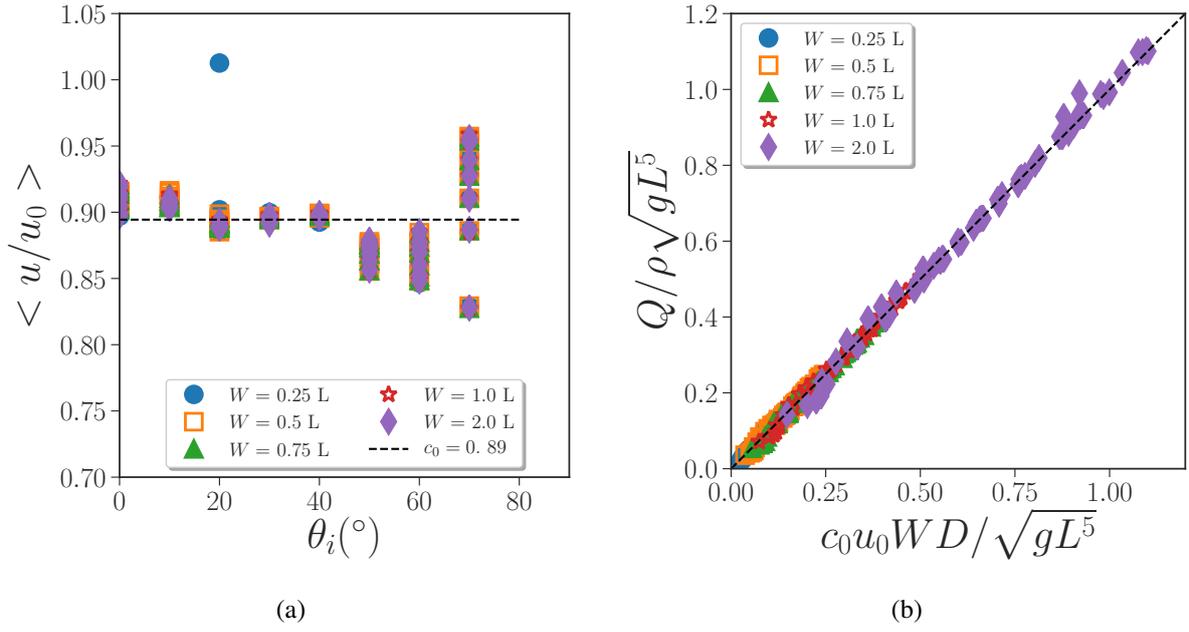
Figure B.2: (a) Mean value of the normalized horizontal velocity profiles versus the bottom angle of inclination. The horizontal line represents the mean value $c_0 = 0.81$. (b) Flow rate versus $c_0 \phi_b \rho_p u_0 W D$. The dashed line represents the equation $y = x$.
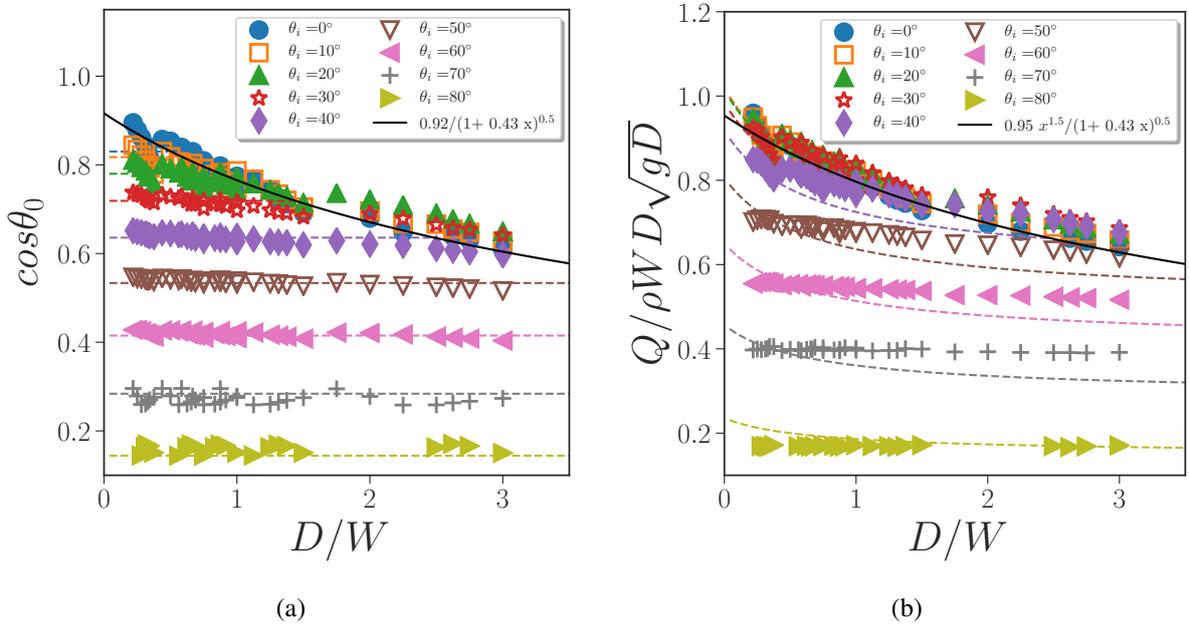
Figure B.3: (a) Inclination of the central streamline at the outlet, $\cos\theta_0$ versus the aspect ratio of the aperture D/W for all the bottom inclinations. The full line represents equation 3.17 with $c_{\theta_0} = 0.81$ and $\gamma = 0.35$. The dashed lines represent equation 3.16 with $\zeta = 0.83$. (b) Mass flow rate normalized by $\rho D W \sqrt{gD}$ for all the bottom inclinations, versus D/W. The full line represents equation 3.20 and the dashed lines represent equation 3.21 with $c_D = 0.95$, $c_{\theta_0} = 0.92$ and $\gamma = 0.43$ and $\zeta = 0.83$

Figure B.3 show the results obtained with this new boundary condition, for the inclination of the central streamline, $\cos\theta_0$ and the dimensionless flow rate $Q/\rho W D\sqrt{gD}$ versus the dimensionless aperture size D/W. Concerning the flow inclination, we can see that the data are again well adjusted by equation 3.18 with $c_{\theta_0} = 0.92$ and $\gamma = 0.43$ and $\zeta = 0.83$ (see Figure B.4a). This shows that this behavior is robust and does not depend on the boundary condition, the streamline inclination is either given by the free flow for low θ_i or impose by the bottom inclination for large θ_i. If we now turn to the flow rate we observe that similarly to the experiment for an intermediate range of bottom inclination the flow rate does not depend on this parameter, contrarily to $\cos\theta_0$ (see the curves corresponding to $\theta_i = 20°$ and $\theta_i = 30°$). The model develop in equations 3.25 and 3.26 is not very good in predicting the flow rate for large θ_i, which can also be seen in Figure B.4b where the mean velocity at the outlet is found to depart from equation 3.24 for large θ_i. This suggests that it may exist a third regime, corresponding to large θ_i where no stagnant zone exists close to the outlet and where U_0 does not depend on W anymore. Finally in the large aspect ratio regime $D/W > 2$, in condition where the central streamline inclination is not controlled by the bottom inclination $\theta_i < 40°$ it is surprising to note that the flow rate seems to depend slightly on this parameter. This can be seen in Figure B.4c where for small W the dimensionless flow rate increases slightly with θ_i in the plateau regime. This effect could be taken into account by a dependency of γ on θ_i.

(a) (b) (c)
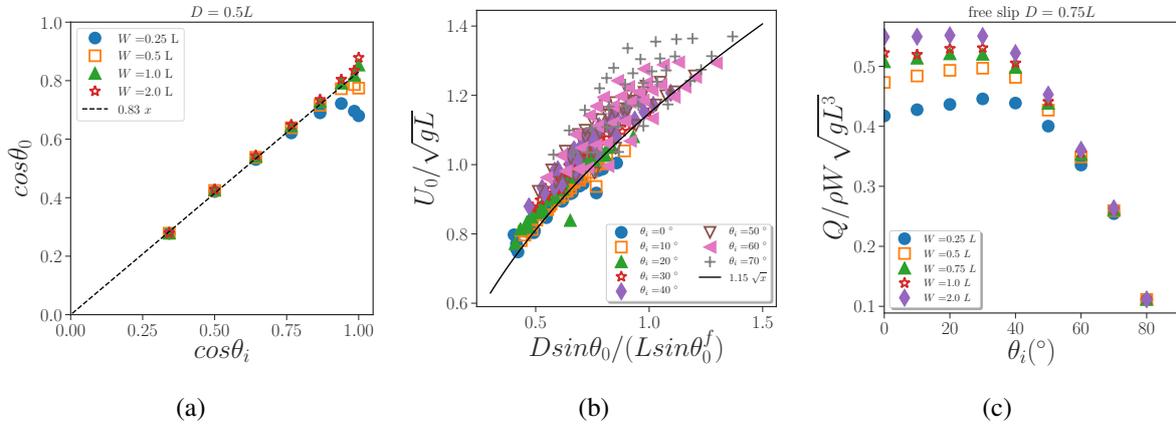
Figure B.4: Continuum simulations with free slip condition: (a) Inclination of the central streamline at the outlet, $\cos\theta_0$ versus the inclination of the bottom of the silo, $\cos\theta$ for $D = 0.75L$ where the dashed line represents equation 3.16 with $\zeta = 0.83$. (b) Magnitude of the velocity profiles at the centre of the outlet, U_0, normalized by $\sqrt{gL}$ versus the normalized outlet size $D\sin\theta_0/(L\sin\theta_0^f)$, where θ_0^f is given by equation 3.17, for several outlet inclination θ_i. The full lines represents equation 3.24 with $c_E = 1.15$. (c) Mass flow rate of particles as a function of the angle of inclination θ_i for $D = 0.75L$.

Bibliography

Aguirre, M. A., Grande, J. G., Calvo, A., Pugnaloni, L. A., and Géminard, J.-C. (2011). Granular flow through an aperture: Pressure and flow rate are independent. *Phys. Rev. E*, 83:061305.

Aissa, A., Abdelouahab, M., Noureddine, A., El Ganaoui, M., and Pateyron, B. (2015). Ranz and Marshall Correlations Limits on Heat Flow Between a Sphere and its Surrounding Gas at High Temperature. *Thermal Science*, 19(5):1521–1528.

Altenkirch, R. A. and Eichhorn, R. (1981). Effect of fluid drag on low Reynolds number discharge of solids from a circular orifice. *AIChE J.*, 27:593.

Amarsid, L. (2015). *Rhéologie des écoulements granulaires immergés dans un fluide visqueux.* PhD thesis, Université de Montpellier.

Andréotti, B., Forterre, Y., and Pouliquen, O. (2011). *Les milieux granulaires : entre fluide et solide.* EDP sciences.

Aussillous, P., Chauchat, J., Pailha, M., Médale, M., and Guazzelli, E. (2013). Investigation of the mobile granular layer in bedload transport by laminar shearing flows. *J. Fluid Mech.*, 736:594–615.

Barker, T., Schaeffer, D. G., Bohorquez, P., and Gray, J. M. N. T. (2015). Well-posed and ill-posed behaviour of the μ(I)-rheology for granular flow. *J. Fluid Mech.*, 779:794–818.

Benyamine, M., Djermane, M., Dalloz-Dubrujeaud, B., and Aussillous, P. (2014). Discharge flow of a bidisperse granular media from a silo. *Phys. Rev. E*, 90:032201.

Bertho, Y., Giorgiutti-Dauphiné, F., and Hulin, J.-P. (2003). Dynamical Janssen effect on granular packing with moving walls. *Phys. Rev. Lett.*, 90:144301.

Beverloo, W. A., Leniger, H. A., and de Velde, J. V. (1961). The flow of granular solids through orifices. *Chem. Eng. Sci.*, 15:260–269.

Bico, J., Marzolin, C., and Quéré, D. (1999). Pearl drops. *Europhysics Letters (EPL)*, 47(2):220–226.

Börzsönyi, T. and Ecke, R. E. (2006). Rapid granular flows on a rough incline: Phase diagram, gas transition, and effects of air drag. *Phys. Rev. E*, 74:061301.

Bouchut, F., Fernández-Nieto, E. D., Mangeney, A., and Narbona-Reina, G. (2016). A two-phase two-layer model for fluidized granular flows with dilatancy effects. *J. Fluid Mech.*, 801:166221.

Bouzid, M., Trulsson, M., Claudin, P., and Andreotti, B. (2013). Non-local rheology for granular flows across yield conditions. *Phys. Rev. Lett.*, 111:238301.

Boyer, F., Guazzelli, E., and Pouliquen, O. (2011). Unifying suspension and granular rheology. *Phys. Rev. Lett.*, 107(18):188301.

Brewster, R., Grest, G. S., Landry, J. W., and Levine, A. J. (2005). Plug flow and the breakdown of bagnold scaling in cohesive granular flows. *Physical Review E*, 72(6):061301–.

Brown, R. L. and Richards, J. C. (1965). Kinematics of the flow of dry powders and bulk solids. *Rheologica Acta*, 4(3):153–165.

Brown, R. L. and Richards, J. C. (1970). *Principles of Powder Mechanics*. Pergamon Press, Oxford.

Cassar, C., Nicolas, M., and Pouliquen, O. (2005). Submarine granular flows down inclined planes. *Physics of Fluids*, 17(10):103301.

Chang, C. S., Converse, H. H., and Steele, J. L. (1991). Flow rates of grain through various shapes of vertical and horizontal orifices. *Trans. Am. Soc. Agr. Eng.*, 34(1789).

Chauchat, J. and Médale, M. (2010). A three-dimensional numerical model for incompressible two-phase flow of a granular bed submitted to a laminar shearing flow. *Computer Methods in Applied Mechanics and Engineering*, 199(9–12):439 – 449.

Chauchat, J. and Médale, M. (2014). A three-dimensional numerical model for dense granular flows based on the rheology. *Journal of Computational Physics*, 256:696 – 712.

Cheng, X., Varas, G., Citron, D., Jaeger, H. M., and Nagel, S. R. (2007). Collective behavior in a granular jet: Emergence of a liquid with zero surface tension. *Phys. Rev. Lett.*, 99:188001.

Courrech du Pont, S., Gondret, P., Perrin, B., and Rabaud, M. (2003). Granular avalanches in fluids. *Phys. Rev. Lett.*, 90:044301.

Crewdson, B. J., Ormond, A. L., and Nedderman, R. M. (1977). Air-impeded discharge of fine particles from a hopper. *Powder Technol.*, 16(2):197 – 207.

Cumberland, D. and Crawford, R. (1987). Handbook of powder technology. *The Packing of particles*, 6.

da Cruz, F., Emam, S., Prochnow, M., Roux, J.-N., and Chevoir, F. (2005). Rheophysics of dense granular materials : Discrete simulation of plane shear flows. *Phys. Rev. E*, 72:021309.

Dalloz-Dubrujeaud, B., Faure, R., Tadrist, L., and Giraud, G. (2000). Perte de pression et vitesse minimum de fluidisation dans un lit de particules 2D. *C. R. Acad. Sci. Paris*, 328:231–236.

Davier, G. and Bertails-Descoubes, F. (2016). Nonsmooth simulation of dense granular flows with pressure-dependent yield stress. *Journal of Non-Newtonian Fluid Mechanics*, 234:15–35.

de Jong, J. (1969). Vertical air-controlled particle flow from a bunker through circular orifices. *Powder Technol.*, 3(1):279 – 286.

de Jong, J. and Hoelen, Q. E. J. J. M. (1975). Cocurrent gas and particle flow during pneumatic discharge from a bunker through an orifice. *Powder Technol.*, 12(3):201 – 208.

de Ryck, A. (2008). Granular flows down inclined channels with a strain-rate dependent friction coefficient. part II: cohesive materials. *Granular Matter*, 10(5):361–367.

Doppler, D., Gondret, P., Loiseleux, T., Meyer, S., and Rabaud, M. (2007). Relaxation dynamics of water-immersed granular avalanches. *Journal of Fluid Mechanics*, 577:161–181.

Dubois, F., Jean, M., Renouf, M., Mozul, R., Martin, A., and Bagneris, M. (2011). Lmgc90. *10e colloque national en calcul des structures, May 2011, Giens, France.*

Dunatunga, S. and Kamrin, K. (2015). Continuum modelling and simulation of granular flows through their many phases. *Journal of Fluid Mechanics*, 779:483– 513.

Duran, J. (1997). *Sables, poudres et grains introduction à la physique des milieux granulaires.* Eyrolles, Paris. Avec bibliographie et index.

Duru, P., NICOLAS, M., HINCH, J., and GUAZZELLI, É. (2002). Constitutive laws in liquid-fluidized beds. *Journal of Fluid Mechanics*, 452:371–404.

Ergun, S. (1952). Fluid flow through packed columns. *Chemical Engineering Progress*, 48(2):89–94.

Forchheimer, P. (1901). Wasserbewegung durch boden. *Z. Ver. Deutsch, Ing.*, 45:1782–1788.

Forterre, Y. (2006). Kapiza waves as a test for three-dimensional granular flow rheology. *J. Fluid Mech.*, 563:123–132.

Forterre, Y. and Pouliquen, O. (2003). Long-surface-wave instability in dense granular flows. *J. Fluid Mech.*, 486:21–50.

Forterre, Y. and Pouliquen, O. (2008). Flows of dense granular media. *Annu. Rev. Fluid Mech.*, 40:1–24.

Fuketa, T., Sasajima, H., Mori, Y., and Ishijima, K. (1997). Fuel failure and fission gas release in high burnup pwr fuels under ria conditions. *J. Nucl. Mat.*, 248:249–256.

Gu, Y., Chialvo, S., and Sundaresan, S. (2014). Rheology of cohesive granular materials across multiple dense-flow regimes. *Physical Review E*, 90(3):032206–.

Gu, Z. and Wang, H. (1991). Gravity waves over porous bottoms. *Coastal Engineering*, 15(5):497–524.

Guyon Etienne, T. J.-P. (1994). *Du sac de bille au tas de sable*. Odile Jacob.

Hagen, G. (1852). Über den Druck und die Bewegung des trocknen Sandes. *Bericht über die zur Bekanntmachung geeigneten Verhandlungen der Königlich Preussischen Akademie der Wissenschaften zu Berlin*, pages 35–42.

Hall, K. R., Smith, G. M., and Turcke, D. J. (1995). Comparison of oscillatory and stationary flow through porous media. *Coastal Engineering*, 24(3):217–232.

Hassanizadeh, S. M. and Gray, W. G. (1987). High velocity flow in porous media. *Transport in Porous Media*, 2(6):521–531.

Hilton, J. E. and Clearly, P. W. (2011). Granular flow during hopper discharge. *Phys. Rev. E*, 84:011307.

Hirshfeld, D. and Rapaport, D. (2001). Granular flow from a silo: Discrete-particle simulations in three dimensions. *Eur. Phys. J. E*, 4:193–199.

Hsiau, S.-S., Hsu, C.-C., and Smid, J. (2010). The discharge of fine silica sands in a silo. *Phys. Fluids*, 22:043306.

Ishikawa, M. and Shiozawa, S. (1980). A study of fuel behavior under reactivity initialed accident conditions - review. *J. Nucl. Mat.*, 95:1–30.

Jackson, R. (2000). *The dynamics of fluidized particles*. Cambridge University Press.

Jaeger, H., Nagel, S., and Behringer, R. (1996). Granular solids, liquids, and gases. *Rev. Mod. Phys.*, 68(4):1259–1273.

Janda, A., Maza, D., Garcimartin, A., Kolb, E., Lanuza, J., and Clément, E. (2009). Unjamming a granular hopper by vibration. *Eur. Phys. Lett.*, 87:24002.

Janda, A., Zuriguel, I., Garcimartín, A., Pugnaloni, L. A., and Maza, D. (2008). Jamming and critical outlet size in the discharge of a two-dimensional silo. *EPL (Europhysics Letters)*, 84(4):44002.

Janda, A., Zuriguel, I., and Maza, D. (2012). Flow rate of particles through apertures obtained from self-similar density and velocity profiles. *Phys. Rev. Lett.*, 108:248001.

J.Bear (1972). *Dynamics of fluids in porous media / Jacob Bear*. American Elsevier.

Jop, P., Forterre, Y., and Pouliquen, O. (2005). Crucial role of sidewalls in granular surface flows: consequences for the rheology. *J. Fluid Mech.*, 541:167–192.

Jop, P., Forterre, Y., and Pouliquen, O. (2006). A constitutive law for dense granular flows. *Nature*, 441:727–730.

Kamrin, K. (2010). Nonlinear elasto-plastic model for dense granular flow. *Int. J. Plast.*, 26:167–188.

Karb, E. H., Pruessmann, M., Sepold, L., Hofmann, P., and Schanz, G. (1983). Lwr fuel rod behavior in the fr2 in-pile tests simulating the heatup phase of a loca. Technical report, Germany.

Lacaze, L. and Kerswell, R. R. (2009). Axisymmetric granular collapse: A transient 3D flow test of viscoplasticity. *Phys. Rev. Lett.*, 102:108305.

Lagrée, P.-Y., Staron, L., and Popinet, S. (2011). The granular column collapse as a continuum: validity of a two-dimensional navier–stokes model with a $\mu(I)$-rheology. *J. Fluid Mech.*, 686:378–408.

Lowe, R. J., Shavit, U., Falter, J. L., Koseff, J. R., and Monismith, S. G. (2008). Modeling flow in coral communities with and without waves: A synthesis of porous media and canopy flow approaches. *Limnology and Oceanography*, 53(6):2668–2680.

Mankoc, C., Garcimartín, A., Zuriguel, I., Maza, D., and Pugnaloni, L. A. (2009). Role of vibrations in the jamming and unjamming of grains discharging from a silo. *Phys. Rev. E*, 80:011309.

Mankoc, C., Janda, A., Arévalo, A., Pastor, J. M., Zuriguel, I., Garcimartín, A., and Maza, D. (2007). The flow rate of granular materials through an orifice. *Granul. Matter*, 9:407–414.

Meunier, P. and Leweke, T. (2003). Analysis and treatment of errors due to high velocity gradients in particle image velocimetry. *Experiments in fluids*, 35(5):408–421.

MIDI, G. (2004). On dense granular flows. *Eur. Phys. J. E*, 14:341–365.

Nakamura, T., Sasajima, H., Nakamura, J., and Uetsuka, H. (2002). NSRR high burnup fuel tests for RIAs and BWR power oscillations without scram. In *Nuclear Safety Research Conference 2002 in Washington, DC on October 28-30, 2002*.

Nedderman, R., Tūzūn, U., and Thorpe, R. (1983). The effect of interstitial air pressure gradients on the discharge from bins. *Powder Technology*, 35(1):69 – 81.

Nedderman, R. M. (1992). *Statics and kinematics of granular materials*. Cambridge University Press.

Nedderman, R. M., Tuzün, U., Savage, S. B., and Houlsby, G. T. (1982). The flow of granular materials-I. *Chem. Eng. Sci.*, 11:1597–1609.

Nield, D. A. and Bejan, A. (2006). *Convection in Porous Media*. Springer.

Ouriemi, M., Aussillous, P., and Guazzelli, E. (2009). Sediment dynamics. Part 1. Bed-load transport by laminar shearing flows. *J. Fluid Mech.*, 636:2955–319.

Ovarlez, G., C.Fond, and Clément, E. (2003). Overshoot effect in the janssen granular column: A crucial test for granular mechanics. *Phys. Rev. E*, 67(060302).

Pailha, M. and Pouliquen, O. (2009). A two-phase flow description of the initiation of underwater granular avalanches. *J. Fluid Mech.*, 633:115–135.

Peirano, E., Delloume, V., Johnsson, F., Leckner, B., and Simonin, O. (2002). Numerical simulation of the fluid dynamics of a freely bubbling fluidized bed: influence of the air supply system. *Powder Technol.*, 122(1):69 – 82.

Pennec, T. L., Måløy, K. J., Hansen, A., and Ammi, M. (1996). Ticking hour glasses: Experimental analysis of intermittent flow. *Phys. Rev. E*, 53:2257–2264.

Percier, B. (2013). *Dynamique d'un empilement granulaire : instabilité de tôle ondulée et fluage d'une colonne de grains*. Thesis, Université Lyon I – ENS de Lyon.

Perge, C., Aguirre, M. A., Gago, P. A., Pugnaloni, L. A., Tourneau, D. L., and Géminard, J.-C. (2012). Evolution of pressure profiles during the discharge of a silo. *Phys. Rev. E*, 85:021303.

Pitman, E. B. and Le, L. (2005). A two-fluid model for avalanche and debris flows. *Phil. Trans. R. Soc. A*, 363:1573–1601.

Pouliquen, O. and Forterre, Y. (2002). Friction law for dense granular flows: application to the motion of a mass down a rough inclined plane. *J. Fluid Mech.*, 453:133–151.

Pouliquen, O. and Forterre, Y. (2009). A non-local rheology for dense granular flows. *Phil. Trans. R. Soc. A*, 367:5091–5107.

Radjai, F. and Dubois, F. (2011). *Discrete-element modeling of granular materials*. Wiley-Iste.

Rajagopal, K. R. (2007). On a hierarchy of approximate models for flows of incompressible fluids through porous solids. *Mathematical Models and Methods in Applied Sciences*, 17(02):215–252.

Rao, K. K. and Nott, P. R. (2008). *An Introduction to Granular Flow*. Cambridge University Press, Cambridge.

Resnick, W., Heled, Y., Klein, A., and Palm, E. (1966). Effect of differential pressure on flow of granular solids through orifices. *Ind. Eng. Chem. (Fundam.)*, 5(3):392.

Revil-Baudard, T. and Chauchat, J. (2013). A two-phase model for sheet flow regime based on dense granular flow rheology. *Journal of Geophysical Research*, 118:619 619 – 634.

Roche, O., Montserrat, S., Niño, Y., and Tamburrino, A. (2008). Experimental observations of water-like behavior of initially fluidized, dam break granular flows and their relevance for the propagation of ash-rich pyroclastic flows. *Journal of Geophysical Research: Solid Earth*, 113(B12).

Rondon, L. (2011). *Effondrement granulaire : Couplages fluide-grains*. PhD thesis, Aix-Marseille University.

Rubio-Largo, S., Janda, A., Maza, D., Zuriguel, I., and Hidalgo, R. (2015). Disentangling the free-fall arch paradox in silo discharge. *Phys. Rev. Lett.*, 114:238002.

Ruyer, P. (2012). Interaction combustible réfrigérant suite à une rupture de gaine lors d'un accident d'insertion de réactivité. État de l'art des connaissances. Technical Report PSN/SEMIA/2012-00394, IRSN.

Rycroft, C. H., Bazant, M. Z., Grest, G. S., and Landry, J. W. (2006). Dynamics of random packings in granular flow. *Phys. Rev. E*, 73:051306.

Saingier, G. (2018). *Mécanismes et dynamiques d'interactions entre grains et liquide: du matériau granulaire sec au mélange saturé*. PhD thesis, Sorbonne Université.

Simonin, O., Chevrier, S., Audard, F., and Fede, P., editors (2016). *Drag force modelling in dilute to dense particle-laden flows with mono-disperse or binary mixture of solid particles*. 9th International Conference on Multiphase Flow.

Sollitt, C. K. and Cross, R. H. (1972). *Wave Transmission through Permeable Breakwaters*, pages 1827–1846. Coastal Engineering.

Sperl, M. (2006). Experiments on corn pressure in silo cells. Translation and comment of Janssen's paper from 1895. *Granul. Matter*, 8(2):59–65.

Staron, L., Lagrée, P.-Y., and Popinet, S. (2012). The granular silo as a continuum plastic flow: The hour-glass vs the clepsydra. *Phys. Fluids*, 24:103301.

Staron, L., Lagrée, P.-Y., and Popinet, S. (2014). Continuum simulation of the discharge of the granular silo. *The European Physical Journal E*, 37(1):1–12.

Sundaresan, S. (2003). Instabilities in fluidized beds. *Annual Review of Fluid Mechanics*, 35(1):63–88.

Tanzawa, S. and Fujishiro, T. (1987). Effects of waterlogged fuel rod rupture on adjacent fuel rods and channel box under RIA conditions. *Journal of Nuclear Science and Technology*, 24(1):23–32.

Tighe, B. and Sperl, M. (2007). Pressure and motion of dry sand: translation of Hagen's paper from 1852. *Granul. Matter*, 9:141 – 144.

To, K., Lai, P.-Y., and Pak, H. (2001). Jamming of granular flow in a two-dimensional hopper. *Phys. Rev. Lett.*, 86:71.

Tüzün, U., Houlsby, G. T., Nedderman, R. M., and Savage, S. B. (1982). Flow of granular materials - 2. Velocity distributions in slow flow. *Chem. Eng. Sci.*, 37(12):1691–1709.

Vanel, L., Claudin, P., Bouchaud, J.-P., Cates, M. E., Clément, E., and Wittmer, J. P. (2000). Stresses in silos: Comparison between theoretical models and new experiments. *Phys. Rev. Lett.*, 84:1439–1442.

W.B. Russel, D. S. . W. S. (1989). *Colloidal Dispersion*. Cambridge University Press.

Zhivomirov, H. (2019). On the development of STFT-analysis and ISTFT-synthesis routines and their practical implementation. *TEM Journal*.

Zhou, Y. (2016). *Ejection de gaz et de grains suite à la rupture d'un crayon de combustible nucléaire : modélisation de la dynamique*. PhD thesis, Aix-Marseille University. 2016AIXM4731.

Zhou, Y., Lagrée, P. Y., Popinet, S., Ruyer, P., and Aussillous, P. (2017). Experiments on, and discrete and continuum simulations of, the discharge of granular media from silos with a lateral orifice. *Journal of Fluid Mechanics*, 829:459–485.

Zhou, Y., Ruyer, P., and Aussillous, P. (2015). Discharge flow of a bidisperse granular media from a silo: Discrete particle simulations. *Phys. Rev. E*, 92:062204.

Zhu, T., Waluga, C., Wohlmuth, B., and Manhart, M. (2014). A study of the time constant in unsteady porous media flow using direct numerical simulation. *Transport in Porous Media*, 104(1):161–179.

Zuriguel, I., Garcimartín, A., Maza, D., Pugnaloni, L. A., and Pastor, J. M. (2005). Jamming during the discharge of granular matter from a silo. *Phys. Rev. E*, 71:051303.

Zuriguel, I., Parisi, D. R., Hidalgo, R. C., Lozano, C., Janda, A., Gago, P. A., Peralta, J. P., Ferrer, L. M., Pugnaloni, L. A., Clément, E., D. Maza, I. P., and Garcimartín, A. (2014). Clogging transition of many-particle systems flowing through bottlenecks. *Sci. Rep.*, 4(7324).

Résumé - Nous considérons un scénario hypothétique d'accident initié par une insertion de réactivité dans une centrale nucléaire entrainant la rupture de la gaine d'un crayon de combustible. La violence du contact entre le combustible et le fluide caloporteur dépendrait alors fortement du débit de fragment combustible sortant hors du crayon qui est initialement confiné avec le gaz pressurisé. Ce travail de thèse a consisté à étudier cette dynamique en la modélisant par la vidange d'un milieu granulaire hors d'un silo pressurisé. Les paramètres de contrôle sont la taille, la densité et la forme des particules ainsi que la taille de l'orifice et la pression initiale d'air imposée dans le silo, tandis que les débits d'air et du milieu granulaire et la pression d'air le long du silo sont mesurés. Les résultats expérimentaux ont été confrontés avec des simulations numériques discrètes et continues avec une rhéologie visco-plastique pour le milieu granulaire.

Afin d'étudier le rôle du confinement dans la géométrie d'intérêt, nous nous sommes d'abord concentrés sur la vidange d'un silo rectangulaire d'épaisseur W, avec une sortie latérale de taille D et un fond dont nous varions l'inclinaison. Pour un faible angle d'inclinaison, l'orientation de l'écoulement granulaire (et donc le débit) est contrôlée par la friction pariétale et dépend du rapport d'aspect de l'orifice D/W, tandis qu'un grand angle d'inclinaison détermine entièrement cette orientation.

Nous nous sommes ensuite intéressés au rôle du gaz pressurisé d'abord en imposant une surpression d'air constante en haut du silo puis en considérant un cas plus transitoire dans lequel une surpression initiale importante provoque la rupture de l'orifice. Le débit granulaire augmente significativement avec le débit d'air, d'autant plus que les particules sont fines. Dans les deux configurations, le débit granulaire est mis à l'échelle par une loi de Beverloo modifiée où le gradient de pression du gaz près de l'orifice agit comme une force motrice supplémentaire. De plus le gradient de pression est bien décrit par une loi de résistance de Forchheimer à travers le milieu granulaire. Nous proposons donc un modèle quasi-stationnaire pour la description transitoire du débit granulaire. Les deux configurations ont été reproduites avec succès par la simulation continue basée sur un modèle multiphasique. Pour les plus forts débits, nous observons une instabilité du jet granulaire, initiée par des oscillations de pression dans la zone près de l'orifice. Nous avons varié le milieu environnant et montré que la présence d'eau autour du silo n'agit que par un effet de pression hydrostatique supplémentaire.

Mots clés : milieux granulaires, vidange de silo, rhéologie d'un milieu granulaire dense, interaction fluide-grains, simulation discrète et continue, instabilité.

Abstract - We consider a hypothetical scenario of reactivity initiated accident in a nuclear power plant. The violence of the so-called fuel-coolant interaction phenomena, that we arbitrarily assume to occur during the accident, depends strongly on the flow rate of particles out of the gas pressurized rod in which they were initially confined. The aim of this thesis was to study how this discharge rate is driven by the internal geometry and the pressurized gas. Fuel particles were experimentally simulated by a dense granular material discharging out of a confined and pressurized silo. The controlled parameters were the particle size, density and shape, the outlet size and the gas pressure, whereas the granular and gas flow rates and the pressure along the silo are measured. Discrete and continuous numerical simulations were performed on similar configurations.

We focused firstly on the discharge of a rectangular silo of thickness W, with a lateral outlet of size D and an inclined bottom with a parametric angle. For a small inclination angle, the granular flow orientation depends on the aspect ratio D/W due to the wall friction, whereas a large inclination angle fully determines this orientation. These results were successfully reproduced by numerical simulations.

Secondly, we focused on two configurations with pressurized gas : a case with constant gas overpressure at the top of the silo and a more transient case for which an initial larger overpressure initiates the rupture of an orifice. The granular flow rate increases significantly with the gas flow, especially for the finer particles and the large overpressures. In both cases, the flow rate scales with a modified Beverloo law where the gas pressure gradient near the outlet acts as an additional driving force. The pressure gradient is well described by a Forchheimer resistance law through the granular medium. We therefore propose a quasi-steady model for the transient description of the granular flow rate. The two configurations were successfully reproduced by numerical simulations based on a continuum multiphase model. For the larger flow rates, instabilities of the granular jet were found to be initiated by pressure oscillations in the outlet region. The presence of water surrounding the silo only acts through an additional hydrostatic pressure effect.

Keywords : granular media, discharge, rheology, air flow, discrete simulation, continuous simulation, instability